Structure Sensitivity of Alkanes Hydrogenolysis & Alkynes Hydrogenation on Supported Ir Catalysts

Xiwen Zhang

Dissertation submitted to the Faculty of the Virginia Polytechnic Institute and State University in partial fulfillment of the requirements for the degree of

Doctor of Philosophy
In
Chemical Engineering

Ayman M. Karim
David F. Cox
Hongliang Xin
Dick A. Nagaki

Feb 18th, 2021
Blacksburg, VA

Keywords: Supported metal catalysts, Structure sensitivity, Operando characterization, Kinetic study, Alkanes hydrogenolysis, Alkynes hydrogenation

Structure Sensitivity of Alkanes Hydrogenolysis & Alkynes Hydrogenation on Supported Ir Catalysts

Xiwen Zhang

Abstract

In many catalytic systems, the activity and selectivity of supported metal catalysts or extended metal surface catalysts would be affected by the metal surface structure, and this phenomenon is called structure sensitivity. Generally, structure sensitivity is led by the change of geometric and electronic properties of the metal on the surface. The variation of metal nuclearity and metal-support interactions are effective ways to change the geometric and electronic properties of the supported metal catalyst, leading to different types of the active sites exposing on the support that would take effect on catalyzing the reaction.

In this work, a series of supported Ir catalysts (on $MgAl_2O_4$ and SiO_2) with different particle sizes less than 3 nm were utilized for hydrogenolysis of n-butane and ethane to study the structure sensitivity as well as the potential reaction pathways. The results indicate that the activity of n-butane hydrogenolysis increases as Ir particle size increases in the small particle size range (0.7–1.4 nm) and then drops when the Ir particle size further increases and the Ir single atoms might be inactive for hydrogenolysis after the post-reaction analysis. The selectivity of n-butane hydrogenolysis is dominated by central and one terminal C–C bond cleavage on the n-butane molecules at low temperature range. The selectivity to central C–C bond cleavage is highly dependent on the size of Ir and increases with a decrease in particle size down to ~1.4 nm but remains constant with further decrease in size. The hydrogenolysis of ethane shows a similar trend

in the small size range but the activity is much lower than n-butane, which supports the low level of series reaction pathway in the case of n-butane hydrogenolysis.

In addition to Ir nuclearity, the effect of electronic properties was also studied on another series of Ir catalysts supported on $ZnAl_2O_4$, in which zinc replace the magnesium within the same spinel structure. The characterization results including HAADF-STEM and volumetric CO chemisorption show the difference of Ir nuclearity in the subnanometer regime and nanoparticles (~1.4 nm), while XPS and DRIFTS indicate the difference of electronic properties from metal-support interaction on the two Ir catalysts with the same nuclearity but reduced at different temperatures. Acetylene hydrogenation is structure sensitive on $Ir/ZnAl_2O_4$ catalysts and the activity and selectivity are mainly determined by Ir nuclearity instead of the difference in electronic properties. The Ir single atoms and subnanometer clusters are more selective to the target product of C_2H_4 but less active than large Ir nanoparticles as there might be more π-bonded adsorption than di-σ bonded adsorption for C_2H_2 on the Ir single atoms and subnanometer clusters.

Structure Sensitivity of Alkane Hydrogenolysis & Alkynes Hydrogenation on Supported Ir Catalysts

Xiwen Zhang

General Audience Abstract

The supported metal catalyst is a kind of effective substance that could help increase the reaction rate when being properly utilized in the reaction. From the industry point of view, the best thing is to maximize the catalyst productivity and minimize the expense so that the economic benefit could be magnified. The catalyst effectiveness in a certain reaction might be different when the surface structure of the catalyst varies. Usually, only the fraction of the surface metals could take effect. As the particle size of the catalyst decreases, the fraction of the surface atoms that contain active sites drastically changes, leading to a different catalytic performance and probably lower cost with improved efficiency for metal utilization. Therefore, it is very significant for the researchers to study the reaction structure sensitivity on the same series of catalysts with different particle sizes. Also, by understanding the reaction mechanism and fundamentals of the catalytic system, it would be possible for the researchers to rationally design the catalysts aiming at higher efficiency and lower cost.

In this work, the reaction of hydrogenolysis that cleaves the C–C bonds within the alkanes molecules was studied on the supported Ir catalysts (Ir/$MgAl_2O_4$ and Ir/SiO_2) with different particle sizes ranging from mostly single atoms, subnanometer clusters to nanoparticles. For n-butane hydrogenolysis, it is found that the selectivity to the target product of ethane is weakly

dependent on particle size when smaller than 1.4 nm but decreases as the size further increases. Meantime, the activity is highest on the catalyst with surface-average particle size of 1.4 nm. Therefore, Ir size of ~1.4 nm is optimum for activity and selectivity to ethane.

The series of Ir/$ZnAl_2O_4$ catalysts was tested for structure sensitivity by another probe reaction, semi-hydrogenation of acetylene. The adsorbed acetylene molecules could be hydrogenated by adding two hydrogen to form the adsorbed ethylene before desorption or further hydrogenation to form ethane. Our results show the Ir single atoms and subnanometer clusters are more selective to the target product of ethylene but less active than the large nanoparticles. With the understanding of structure sensitivity, researchers are able to rationally design the catalysts based on their necessity for certain reactions.

Acknowledgement

Firstly, I would like to express my sincerest gratitude and highest respect to my advisor Prof. Ayman M. Karim, a real scientist and enthusiastic catalysis researcher, for his endless patience and support throughout my Ph.D. study. I thank him for always giving me chances and guidance again and again when I encountered difficulties, getting me to ask hard questions and training me with critical thinking and problem-solving skills.

Next, I can never fully convey my appreciation to my committee members, Prof. Hongliang Xin, Prof. David F. Cox and Dr. Dick Nagaki for their time and valuable feedbacks on my research and dissertation. Prof. Hongliang Xin taught me a lot of data analysis skills that would greatly benefit my future career. Prof. David F. Cox provided important insights and encouraged me to overcome difficulties during this hard journey. Special thanks to Dr. Dick Nagaki for his contributions and suggestions on my research in the hydrogenolysis study. During the week of my defense, Houston was suffering power and water outage from a rare and severe winter storm. I really appreciate his endless help on my dissertation and defense during such tough time.

Also, I would like to thank all the scientists and researchers who have provided generous help on my research: Dr. Xu Feng in Surface Chemistry Lab at Virginia Tech, Dr. Libor Kovarik at Pacific Northwest National Laboratory, Dr. Chris Whitehead at Colorado States University, Dr. Prasanna Dasari at SABIC, Dr. Christopher Winkler and Dr. Mitsu Murayama in ICTAS Nanoscale Characterization and Fabrication Laboratory at Virginia Tech. I am also grateful to all our collaborators and funding support from SABIC.

Furthermore, many thanks to the staff in our department: Diane Cannaday, Andrea Linkous, Tina Russell, Stacey Ratcliffe, Kevin Holshouser, Michael Vaught, Brad Reed and Riley Chan. I would like to express my sincerest gratitude for your help on communications, shipping, traveling, and all the other necessary works. Without their support, I could not successfully complete the research and study here.

I would like to thank all my former and current labmates and dear friends, Dr.Yubing Lu, Dr.Wenhui Li, Dr.Wendi Guo, Dr.Chun-Te Kuo, Coogan Thompson, Malik Abraham, Eric Husman, Dr.Saeed Mozaffari, Dr.Peiguang Hu. We spent so much time being stronger together, working inside the lab or having fun outside, helping each other on the research or making suggestions on the future life and career. I will never forget our impressive lives in Blacksburg.

Lastly, I would like to thank my family for their unconditional support and encouragement. Thank you for always being with me whenever I need to stay up for work, driving me to or picking me up from the lab in the midnights. Thanks to all my family members on the other side of the earth. I would not succeed in this journey without your encouragement and support.

Table of Contents

Chapter 1 Background and Literature Review

1.1 Structure Sensitivity / Insensitivity

For decades, it is of great interest for the modern researchers to investigate the details of reaction mechanism on the surface of the metal catalysts and correlate the catalytic performance with the structure of different catalysts. By understanding the surface reaction mechanism, it allows the researchers to rationally design the catalysts for specific reactions and control over the reaction pathways, activity and selectivity [1, 2]. It is found that for some of the reactions, the structure of the metal catalysts has a large effect on the reactivity and product distribution. This could be explained by the different interactions of the chemical species with surface sites of the metal catalysts as the geometric properties and electronic properties change for different atom configurations. The reactions that have different catalytic performance with varying structures of the catalysts are called structure sensitive reactions, e.g. ammonia synthesis on iron [3] and ruthenium catalysts [4], and ethane hydrogenolysis over Cu-Ni alloys [5], while the reactions that are generally accepted being independent of catalyst structure change are ascribed as structure insensitive reactions, e.g. CO oxidation on Pd/Al_2O_3 catalysts [6], and ethylene hydrogenation on Pt/silica catalysts [7]. Recently, the ethylene hydrogenation was also reported as structure sensitive reaction on the Pt/MgO catalysts in the subnanometer regime [8].

Basically, for metal catalysts in heterogeneous catalysis, the study of structure sensitivity / insensitivity mainly focuses on the two aspects, single crystal metal catalysts with different crystal facets and supported metal catalysts with different particle sizes and shapes.

1.1.1 Single crystal catalysts with different crystal facets

The first proposed evaluation of structure sensitivity / insensitivity is mainly based on the catalytic performance on the single crystal catalysts with different crystal facets. In general, the surface structures of the metal single crystal catalysts are distinguished as various crystal facets, depending on the arrangement of atoms. Since the spatial environment of the surface atoms on the different facets are distinctive, their ability of adsorbing and dissociating molecules is different, leading to unique catalytic performance. Moreover, most of the surface structures of the single crystal catalysts are not ideal and contain a lot of defects in practice. As shown in the diagram below, in addition to the stable planes of terraces, there are also steps, kinks, adatoms, vacancies existing on the surface. For some of the hydrocarbon reactions on Pt metal catalysts, the kinks and steps have higher efficiency in breaking and formation of C–C bonds, resulting in the structure sensitivity of the reaction [2].

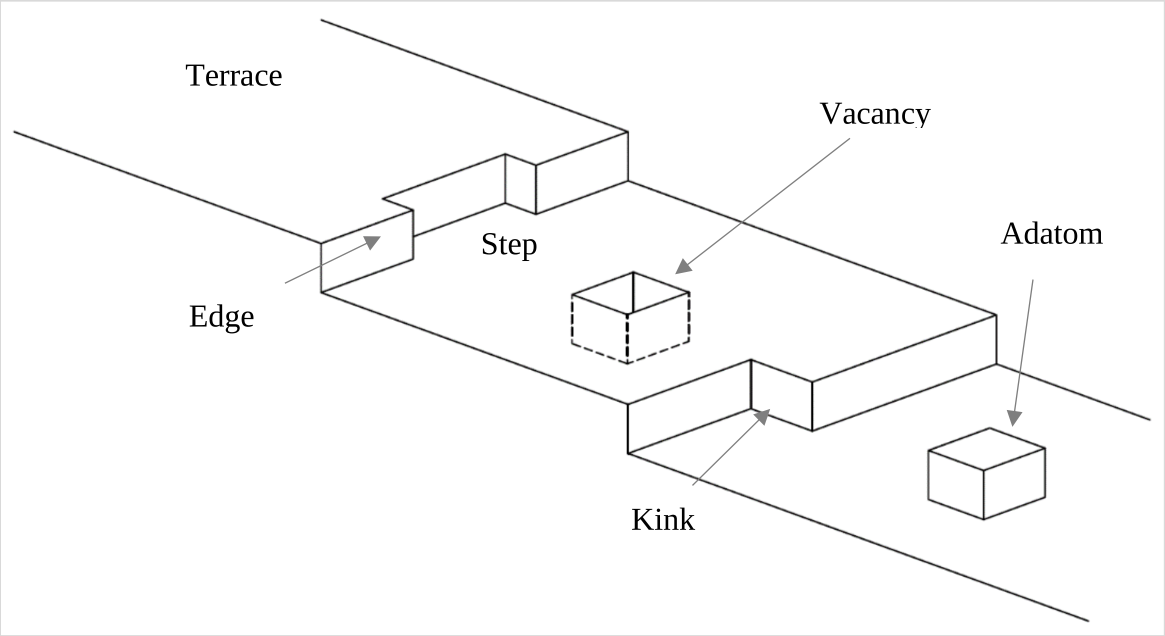

Figure 1. 1. 1 Schematic diagram of the single crystal surface with defects based on Figure 5.1.4 of the open source reference [9].

One example of the structure sensitive reaction on single crystal catalysts is the ethane hydrogenolysis on Ni catalysts. Goodman did a series kinetic measurements of ethane hydrogenolysis on Ni (100) and Ni (111) surfaces and made the comparison plot in Arrhenius form as shown in Figure 1.1.2 [10].

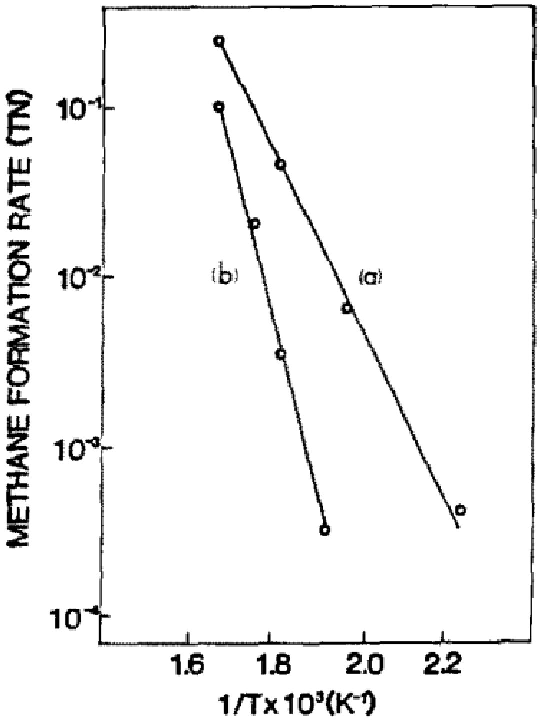

Figure 1. 1. 2 A comparison of methane formation rate from ethane hydrogenolysis on (a). Ni (100) and (b). Ni (111) catalyst in the Arrhenius form at a total pressure of 100 Torr, $H_2/C_2H_6=100$ [10]. (Reproduced with permission from Surface Science Volume 123 Issue1 (1982) Page: 7, D.Wayne Goodman, Ethane hydrogenolysis over single crystals of nickel: Direct detection of structure sensitivity. Copyright (1982), with permission from Elsevier)

From the plot, the activation barrier of ethane hydrogenolysis on Ni (100) (plot a) is obviously smaller than on Ni (111) (plot b), which is consistent with the speculation of other researchers that the (111) surface is less active than the (100) surface [11]. They also analyzed the reason for the difference in activity on these 2 crystal surfaces. One possible reason is the difference of electronic properties between the 2 crystal surfaces. If the activity is related to the back-bonding of the metal to the unfilled σ-orbital of ethane molecule, the better back-bonding ability of Ni (100) may lead to the higher activity of ethane hydrogenolysis than Ni (111). The other probability is the different atom arrangement between Ni (111) and Ni (100). As shown in the schematic diagram below, the distance between 2 four-fold hollow sites on Ni (100) is 2.5 Å, while the distance between 2 three-fold hollow sites on Ni (111) is only 1.4 Å, which is at the same level of the C–C bond length, 1.3-1.5 Å. So the C-C bonds adsorbed on the Ni (100) surface are hard to remain intact and more easily to be broken than on the Ni (111) surface, resulting in the activity difference of ethane hydrogenolysis on the 2 Ni crystal surface [10].

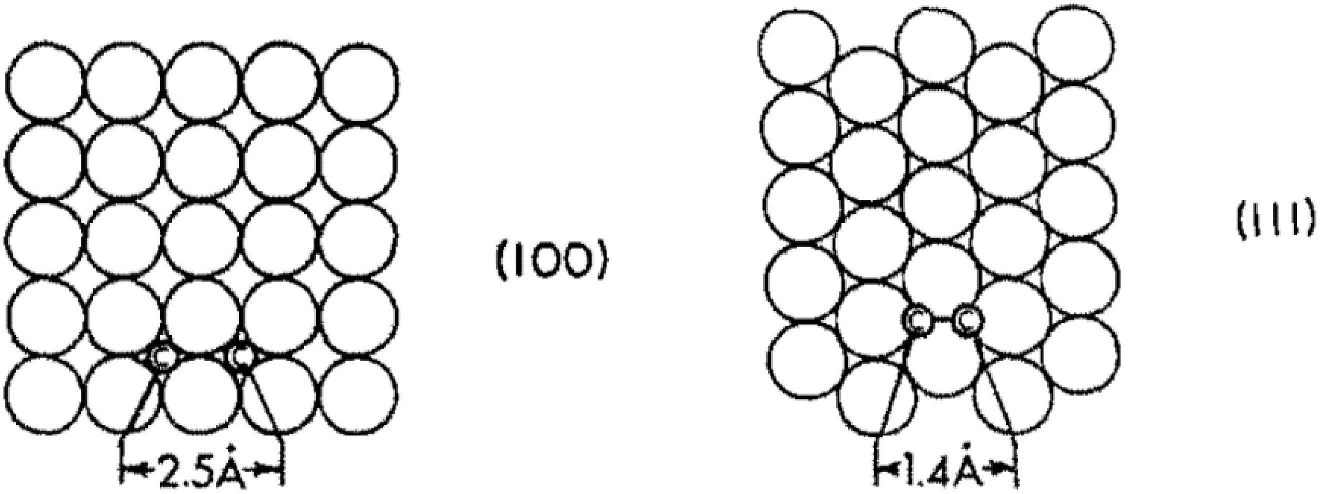

Figure 1. 1. 3 Schematic diagram of the structure on (100) surface with four-fold hollow sites and on (111) surface with three-fold hollow sites [10]. (Reproduced with permission from Surface Science 123.1 (1982): L679-L685, D.Wayne Goodman, Ethane hydrogenolysis over single crystals of nickel: Direct detection of structure sensitivity. Copyright (1982), with permission from Elsevier)

1.1.2 Particle size effects in supported metal catalysts

During the recent decades, tremendous efforts has been devoted towards the improvements of catalytic performance of supported metal catalysts. It is already known that for many catalytic systems, decreasing the particle size of the supported metal catalysts is very effective in the improvement of catalytic performance. For supported metal nanoparticle catalysts, only the surface atoms could serve as active sites for reaction, while the atoms in the bulk that do not have any opportunity to get access to the reactant species are wasted and the fraction of these bulk atoms should be minimized. Besides, among all the surface atoms, those at corners and edges called under-coordinated sites might be especially active for some particular reactions because of the higher chance and better interaction with the chemical species for adsorption, comparing with the well-coordinated atoms at the terrace sites. This could be explained by the difference of electronic properties of the atoms at different positions, which means the binding strength of the metal atoms at different surface sites with the reactant species and reaction intermediates would vary, thereby leading to different product distributions [12]. As a result, when the particle size of the nanoparticles decreases, the fraction of unsaturated surface atoms in the particle would drastically increase, especially the percentage of corner and edge site atoms.

Figure 1.1.4 shows the trend of the atomic ratios of surface atoms to total atoms and the corner and edge atoms to total atoms for FCC nanoparticles with cuboctahedron shape. As we can see from the figure, when the particle size gradually decreases, the fraction of unsaturated sites greatly increases. Specifically, the increase of the fraction of corner and edge atoms is much sharper [13].

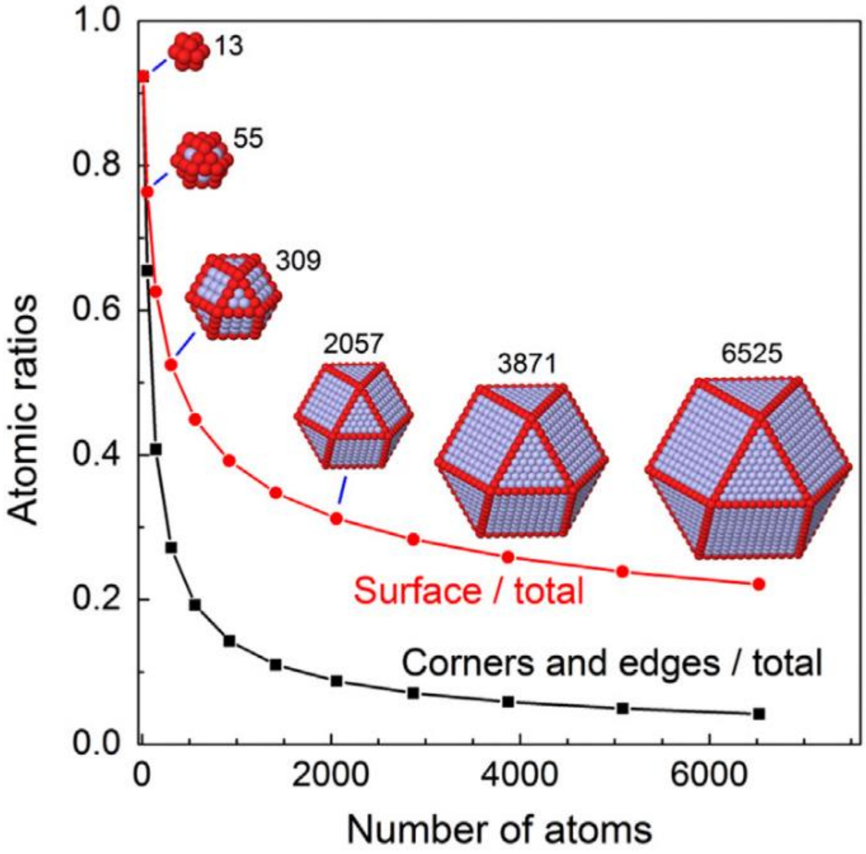

Figure 1. 1. 4 The size dependence of atomic ratios of surface atoms to total atoms and corner and edge atoms to total atoms for FCC NPs with cuboctahedron shape[13]. (Reproduced with permission from Surface Science Reports 70.2 (2015): 135-187, Beatriz Roldan Cuenya, Farzad Behafarid, Nanocatalysis: size-and shape-dependent chemisorption and catalytic reactivity. Copyright (2015), with permission from Elsevier)

The saturation level of the surface atoms could be evaluated by the coordination number, which is the number of closest neighbored atoms that are bonded to a certain atom. In terms of the active surface atoms, usually only the first shell of coordination number of the surface atoms needs to be considered. Generally, the atoms at terrace sites have larger coordination number, while those at corner and edge sites have smaller coordination number. The coordination number could be determined by advanced synchrotron x-ray techniques, in particular the extended X-ray adsorption fine structure (EXAFS) and X-ray adsorption near-edge structure (XANES). Nowadays, the researchers have already successfully correlated the average first-shell coordination number of the surface atoms with the particle diameter [14].

As was mentioned above, downsizing the particle size could increase the fraction of active surface atoms with low coordination number, thereby changing the catalytic performance. Thus, it becomes more and more important to precisely control the particle size of the supported metal catalysts. In recent years, the discovery of the isolated metal atoms dispersed on support shed new lights on heterogeneous catalysis. Theoretically, all the isolated metal atoms on the surface of the support would participate in the reactions, maximizing the efficiency of the novel metal utilization in catalysis [15]. However, the influence on the activity is uncertain. In general, the metal nanoparticles would allow multiple molecules to adsorb closely to each other, while the number of molecules adsorbed on the single atoms would be very limited. Also, the binding type between a certain reactant molecule to the nanoparticles or the single atoms might be different. In the case that the adjacent sites are required for different reactant molecules to adsorb prior to reaction, the single atom catalyst may not be the best choice to maximize the reactivity.

1.1.3 Particle shape effects in supported metal catalysts

In addition to the particle size, the shape of the catalyst particles also has an influence on the catalytic performance. Generally, it is not easy to synthesize the catalyst that have different particle shapes for comparison with the same particle size. In 2010, Mostafa, S., et al. [16] reported the shape-dependence of catalytic properties of 2-propanol oxidation over a series of Pt nanoparticles supported on γ-Al_2O_3 with different particle shapes as shown below in Figure 1.1.5.

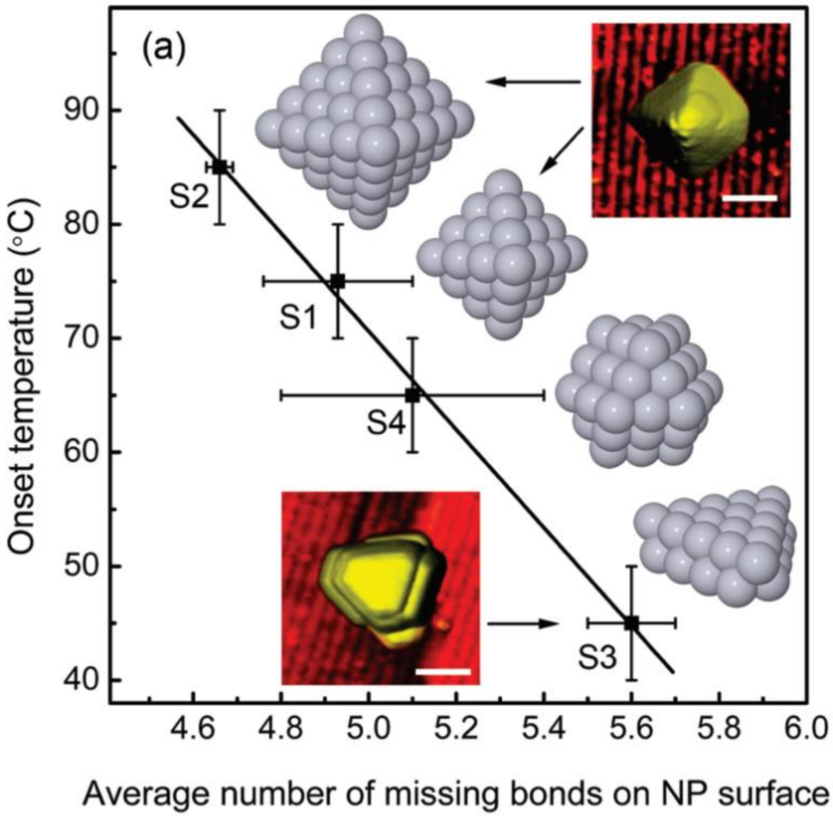

Figure 1. 1. 5 Onset temperature for 2-propanol oxidation over Pt NPs / γ-Al_2O_3 versus the average number of missing bonds on the NP surface [16]. **(**Reprinted with permission from (Mostafa, Simon, et al. "Shape-dependent catalytic properties of Pt nanoparticles." Journal of the American Chemical Society 132.44 (2010): 15714-15719.). Copyright (2010) American Chemical Society.)

In this paper, the authors synthesized 3 catalysts with the particle size of 1 nm but with 3 different shapes, octahedron (S2), cuboctahedron (S4) and 2D structure (S3). Additionally, they also synthesized one catalyst with octahedron shape (S1) with a lower particle size of 0.8 nm comparing with S2. After the reaction, they plotted the onset temperature versus the average number of missing bonds on the nanoparticle surface in Figure 1.1.5. The onset temperature could reflect the activity of 2-propanol oxidation on the catalysts. The lower the onset temperature, the higher the activity of the reaction on that catalyst. The average number of missing bonds on the nanoparticle surface could also be correlated with the average coordination number. The more missing bonds on the nanoparticle surface means the lower level of surface atom saturation, thereby resulting in the lower average coordination number. Therefore, the reactivity of 2-propanol oxidation is correlated with the average coordination number of the Pt nanoparticles. Details of the relationship between the reactivity and the fraction of surface atoms and corner / edge atoms could also be learned from the plots in Figure 1.1.6.

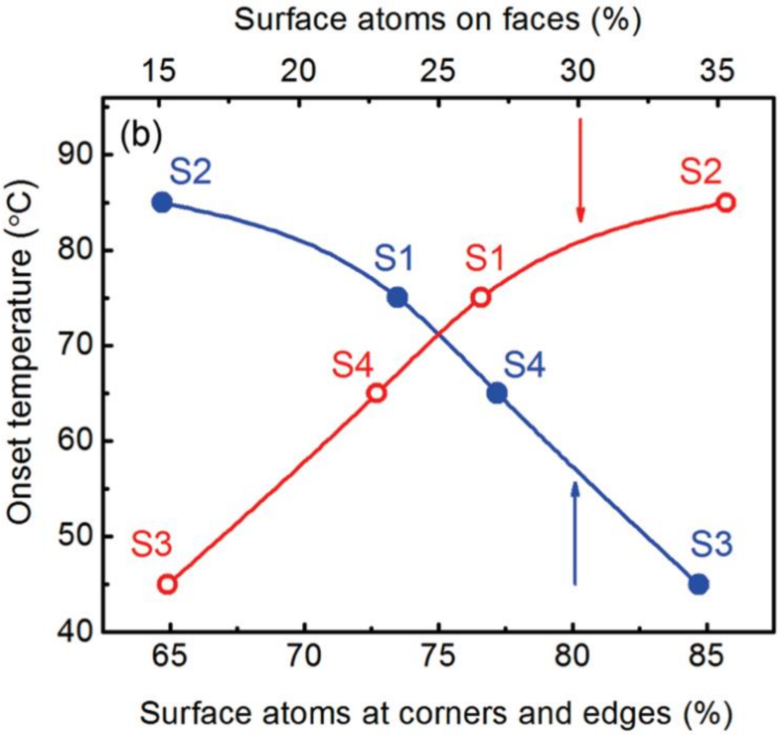

Figure 1. 1. 6 Onset temperature for 2-propanol oxidation over Pt NPs / γ-Al_2O_3 versus the percentage of atoms at corners / edges and faces on the NP surface [16]. (Reprinted with permission from (Mostafa, Simon, et al. "Shape-dependent catalytic properties of Pt nanoparticles." Journal of the American Chemical Society 132.44 (2010): 15714-15719.). Copyright (2010) American Chemical Society.)

The coordination number of the corner/edge atoms is 4 – 7, while those at faces is as large as 8 – 9. From the plot in Figure 1.1.6, the catalyst of cuboctahedron shape (S3) with the highest percentage of corner/edge atoms and lowest percentage of face atoms is the most active for 2-propanol oxidation reaction, while the catalyst of octahedron shape (S2) with the largest fraction of face atoms but smallest fraction of corner / edge atoms is the least active. As a result, the under-coordinated atoms at the corners / edges of Pt nanoparticles are more active for 2-propanol oxidation reaction than the well-coordinated atoms. Therefore, the particle shape effect on the supported metal catalysts could be ascribed by the difference of the fraction of under-coordinated atoms on the nanoparticle surface.

1.2 Hydrogenolysis of Alkanes

The selective C–C bond cleavage on metal catalysts is a very helpful way for decreasing the chain length of n-alkanes and for the ring opening of cycloalkanes. Moreover, it would also be responsible to the yield losses during hydrocarbon reforming or isomerization. As mentioned, the hydrogenolysis of ethane and n-butane are considered as prototypical structure sensitive reactions on supported metal catalysts [17-24]. Therefore, the hydrogenolysis of alkanes reactions are very worthwhile for us to study as a model for the structure sensitivity effects in catalysis especially in the subnanometer regime that has never been reported previously, so that we can rationally design the catalysts to realize the highest activity and largest selectivity to target products during chain length decreasing reactions and hydrocarbon reforming or isomerization.

1.2.1 N-butane hydrogenolysis on metal catalysts

As we can see from the chemical formula below, the reaction of n-butane hydrogenolysis includes a combination of parallel and series reaction pathways during which the target product of ethane could be an intermediate that undergoes further hydrogenolysis to methane.

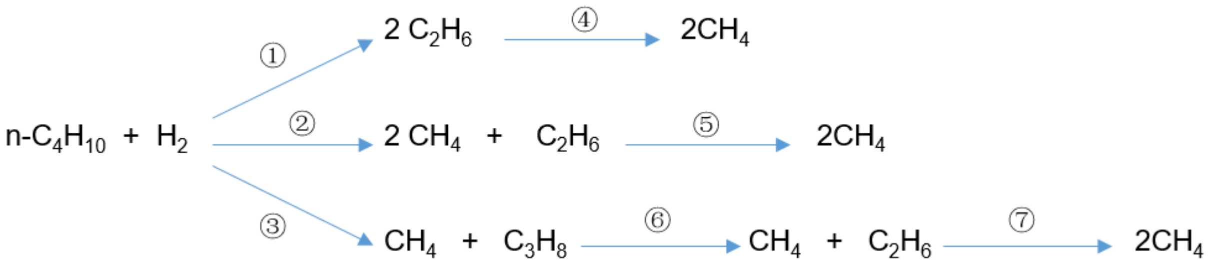

After adsorbing on the surface of the metal catalyst, the n-butane molecule would go through the process of central C–C bond cleavage (step ①) or terminal C-C bond cleavage (step ② and ③), producting two ethane molecules by step ①, two methane molecules and one ethane molecule by step ② or one methane molecule and one propane molecule by step ③. Then, based on the property of the metal catalysts and reaction conditions, the C–C bonds in the product of propane molecules might be further cleaved to form one methane and one ethane (step ⑥). Meanwhile, the C–C bonds in the product of ethane molecules could also be cleaved into two methane molecules as shown in step ④, ⑤ and ⑦, which, as a consequence, further decreases the selectivity to ethane from the whole reaction. Therefore, it is of great interest to study the reaction mechanism of n-butane hydrogenolysis that would help maximize the selectivity to ethane and minimize the costs for the separation of ethane from other products.

J.R. Engstrom, D.W. Goodman and W.H. Weinberg [23] studied the hydrogenolysis of n-butane on closed-packed (111) and corrugated (110)-(1×2) surfaces of Ir metal. The reconstructed (110) surfaces displayed as (1×2) superstructure have a large fraction of edge atoms with low coordination number in this configuration, and the ratio of edge atoms to the face atoms is 1/2 per unit cell. While on the (111) surface structure, the ratio of edge atoms to the face atoms is several times smaller than that on the (110)-(1×2) surface and only a few under-coordinated atoms exist in this kind of surface structure. In addition, by assuming that the shape of the supported metal catalysts is either octahedron or square-pyramidal as shown in the Figure 1.2.1, the effective particle size is about 16.6 or 8.1 nm for (111) surface, and 2.4 or 1.3 nm for (110)-(1×2) surface, respectively. Therefore, after performing the reaction on these two catalysts, it is convenient to determine whether n-butane hydrogenolysis is structure sensitive or insensitive reaction on iridium catalysts.

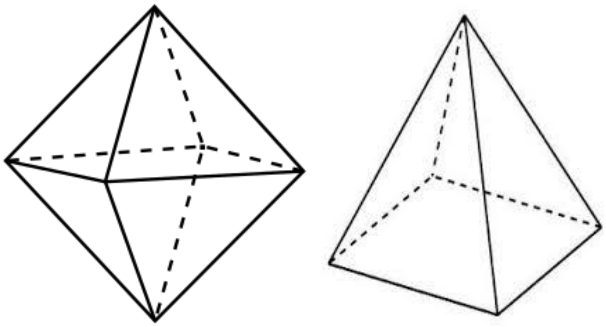

Figure 1. 2. 1 Images of the shape of octahedron and square-pyramidon.

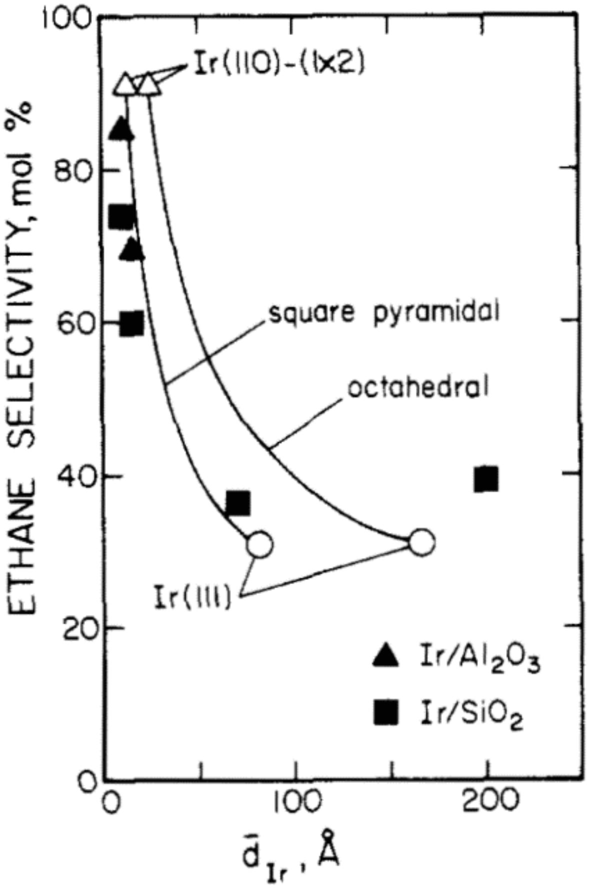

Figure 1. 2. 2 Selectivity to ethane product as a function of particle size from n-butane hydrogenolysis on Ir (111) and Ir (110)-(1×2) surface (normalized by particle size), as well as the supported catalysts of Ir/Al_2O_3 and Ir/SiO_2 (data from Foger and Anderson[25]).The solid curves represent the theoretical interpolations between the two single crystal catalysts. The reaction temperature in all cases is approximately 475K. The ratio of hydrogen to n-butane is 100 with the partial pressure of 1 torr for n-butane [23]. (Reprinted with permission from (Engstrom, J. R., D. W. Goodman, and W. H. Weinberg. "Hydrogenolysis of n-butane over the (111) and (110)-(1×2) surfaces of iridium: a direct correlation between catalytic selectivity and surface structure." Journal of the American Chemical Society 108.15 (1986): 4653-4655.). Copyright (1986) American Chemical Society.)

The authors also compared their results on the iridium single crystal catalysts with those on the supported iridium catalysts published by Foger and Anderson [25] in Figure 1.2.2. From the plot, there is an obvious correlation between the particle size and the selectivity to ethane which caused by the central C–C bond cleavage. And the observed improvement of the ethane selectivity with the decreased particle size could be explained by the higher fraction of under-coordinated surface atoms that participate in the reaction, as the steric hindrance for reactant adsorption on the under-coordinated atoms in the Ir (110)-(1×2) surface structure would be smaller than that on the intact Ir (111) surface. The plot shows that the selectivity to ethane is only about 30% on Ir (111) surface, but even close to 100% on Ir (110)-(1×2) surface. The major reaction pathway might be n-$C_4H_{10} + H_2 \rightarrow 2\ CH_4 + C_2H_6$ on the Ir (111) surface and n-$C_4H_{10} + H_2 \rightarrow 2\ C_2H_6$ on the Ir (110)-(1×2) surface, suggesting the potentially different intermediates during the reaction.

In 1990s, D. Kalakkad et al. [22] studied the structure sensitivity of n-butane hydrogenolysis on a series of Rh catalysts. They studied the n-butane hydrogenolysis on the synthesized Rh metal supported on alumina and silica supports with different particle sizes (from < 1 to > 5 nm) by changing the metal loadings. They compared and correlated the particle size effect as well as the pretreatment methods with single crystals to study the selectivity difference.

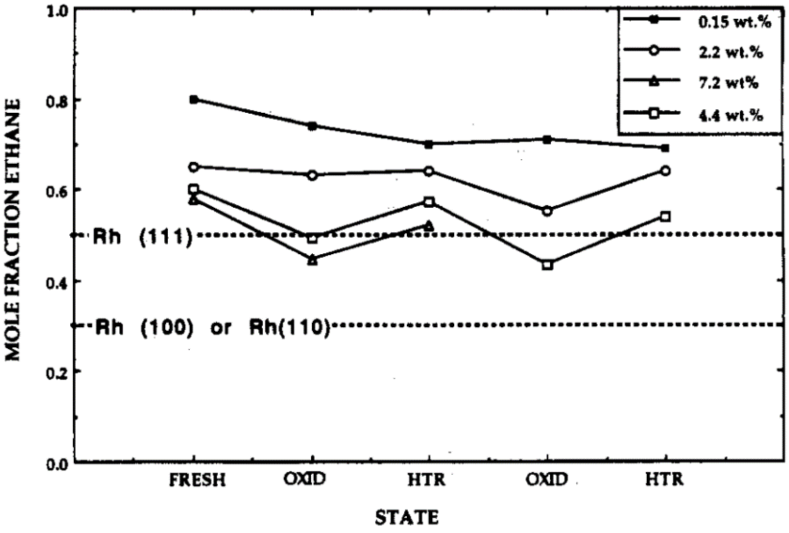

Figure 1. 2. 3 Comparison of mole reaction of ethane of n-butane hydrogenolysis on Rh/Al_2O_3 catalysts with different metal loadings by a cycle of pretreatment methods. (The ratio of hydrogen to n-butane is 20:1 with the total pressure of 630 Torr, the reaction temperature is 175°C.) [22] (Reprinted with permission from (Kalakkad, D., et al. "n-Butane hydrogenolysis as a probe of surface sites in rhodium metal particles: correlation with single crystals." The Journal of Physical Chemistry 97.7 (1993): 1437-1444.). Copyright (1993) American Chemical Society.)

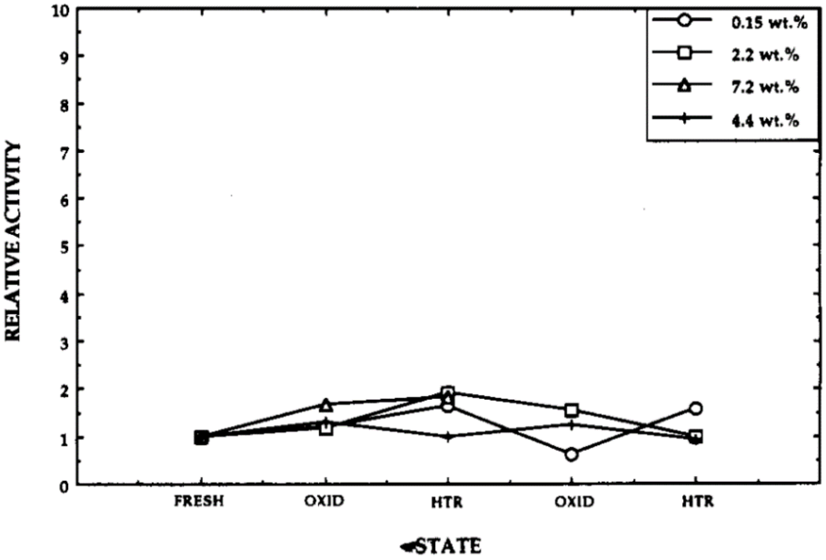

Figure 1. 2. 4 Comparison of reaction activity of n-butane hydrogenolysis on Rh/Al_2O_3 catalysts with different metal loadings by a cycle of pretreatment methods. (The ratio of hydrogen to n-

butane is 20:1 with the total pressure of 630 Torr, the reaction temperature is 175°C.) [22] (Reprinted with permission from (Kalakkad, D., et al. "n-Butane hydrogenolysis as a probe of surface sites in rhodium metal particles: correlation with single crystals." The Journal of Physical Chemistry 97.7 (1993): 1437-1444.). Copyright (1993) American Chemical Society.)

As the example shown in Figure 1.2.3, the selectivity to ethane from n-butane hydrogenolysis on Rh/Al_2O_3 is generally sensitive to the particle size while the activity does not vary greatly on these catalysts as shown in Figure 1.2.4. When the particle size of Rh/Al_2O_3 is so small that it is even undetectable by TEM at that time (0.15% Rh/Al_2O_3), the selectivity to ethane from n-butane hydrogenolysis is about 80%, which is much higher than the selectivity of 50% on Rh (111) surface or the selectivity of 30% on Rh (100) and Rh (110) surfaces. As the metal loading and particle size increase, the selectivity to ethane keeps decreasing. In the Rh/Al_2O_3 catalyst series, when the metal loadings are 4.4% and 7.2%, while the particle sizes are 2.5 and 3.0 nm characterized by TEM, the selectivity to ethane is about 50%, which is at the same level as the Rh (111) single crystal surface, but still larger than that on the Rh (100) and Rh (110) surfaces. The authors tested the effect of pretreatment methods (fresh as prepared, oxidation, reduction) on these Rh catalysts with different weight loading and average particle size. In general, the dependence of selectivity to ethane and reactive activity on different pretreatment methods showing in Figure 1.2.3 and Figure 1.2.4 is not very clear.

The authors also investigated the relationship between the ethane selectivity and the surface structure of the supported rhodium catalysts with different particle sizes and plotted the fraction of different types of surface atom as a function of particle diameter. The types of the surface atom in the Rh cuboctahedron are presented based on the equations developed by Van Hardeveld and

Hartog [26]. The symbol C_j is denoted as a surface atom with j nearest neighbors. To differentiate the atoms with the same number of nearest neighbors but different arrangements, a set of superscripts is also introduced to specify the position of the atom in a particular structure, which, in this case, signifies the rhodium cuboctahedral particles.

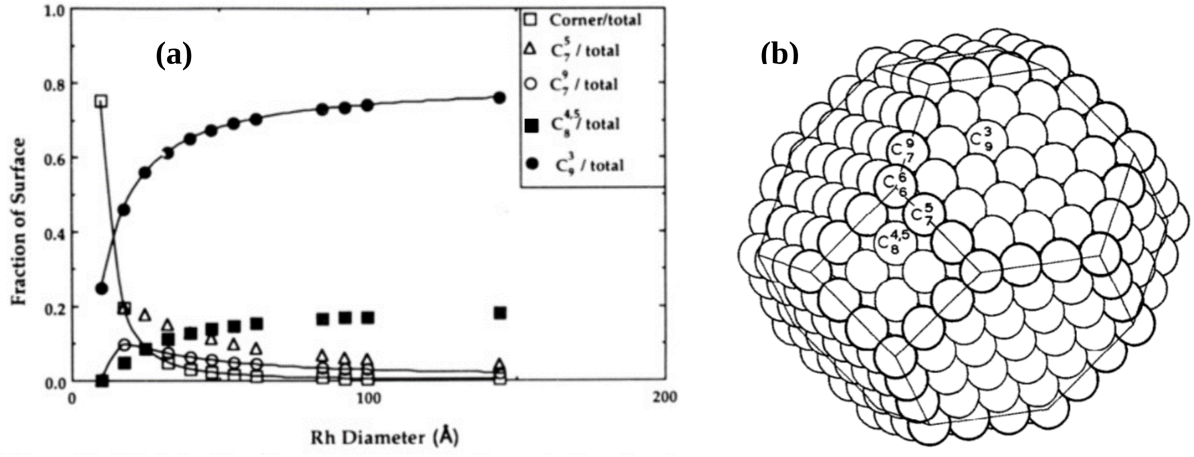

Figure 1. 2. 5 (a) Statistics of surface atoms for Rh cuboctahedron, based on the equation presented in reference 26 [22]. (Reprinted with permission from (Kalakkad, D., et al. "n-Butane hydrogenolysis as a probe of surface sites in rhodium metal particles: correlation with single crystals." The Journal of Physical Chemistry 97.7 (1993): 1437-1444.). Copyright (1993) American Chemical Society.) (b) Schematic illustration on the positions of C_j^i in the cuboctahedron structure [26]. (Reproduced with permission from Surface Science 15.2 (1969): 189-230, R. Van Hardeveld, F. Hartog, The statistics of surface atoms and surface sites on metal crystals. Copyright (1969), with permission from Elsevier.)

From the plot in Figure 1.2.5-(a), as the Rh particle size decreases, the fraction of terrace atoms (C_9^3 and $C_8^{4,5}$) decreases and the fraction of edge atoms (C_7^5 and C_7^9) and corner atoms (C_6^6) increases, and the trends go sharper in the very small diameter range. Combining with the TEM observations, the authors concluded that the surface structure of larger Rh particles resembles the Rh (111) surface. However, as the particle size decreases, the surface configuration with more C_7 atoms could not be simply analogized with unreconstructed Rh (110) surface. If the high selectivity on the highly dispersed metal catalyst is ascribed to the formation of metallocycle intermediates, the tightly arranged neighboring C_7 atoms in the Rh (110) structure, as shown in the red circle of the surface structure in Figure 1.2.6-(a), would sterically hinder the formation of the intermediates, leading to lower selectivity to ethane comparing with the results on the catalyst with Rh (110)-(1×2) structure shown in Figure 1.2.6-(b) without neighboring C_7 atoms [22]. Similarly, it could also help explain the higher selectivity to ethane on the Ir (110)-(1×2) single crystal catalysts comparing with the Ir (111) in Engstrom, Goodman and Weinberg's work [23].

Table 1. 1 A brief summary of n-butane hydrogenolysis results from literature.

Literature Author and publish year	Catalyst	T (°C)	H_2 / C_4 Ratio	Conversion	Selectivity to C_2H_6
Bond and Garcia 2017 [27]	Ru/13X	134	10/1	1.3%	45.7%
Bond and Yide 1984 [24]	Pt/Silica (O873+R773)	335	20/1	1%	41.5%
Kalakkad, Anderson et al. 1993 [22]	0.15%Rh/Al_2O_3	175	20/1	0.1-10%	80%
Bond and Slaa 1995 [28]	RuEC1	160	10/1	-	65.6%
Engstrom, Goodman et al. 1986 [23]	Ir(110)-(1×2)	202	100/1	<1%	90%
Foger and Anderson. 1979 [25]	2.5% Ir/Al_2O_3	170-212	20/1	-	85.4%
	0.9% Ir/SiO_2	180	20/1	7%	76.5%

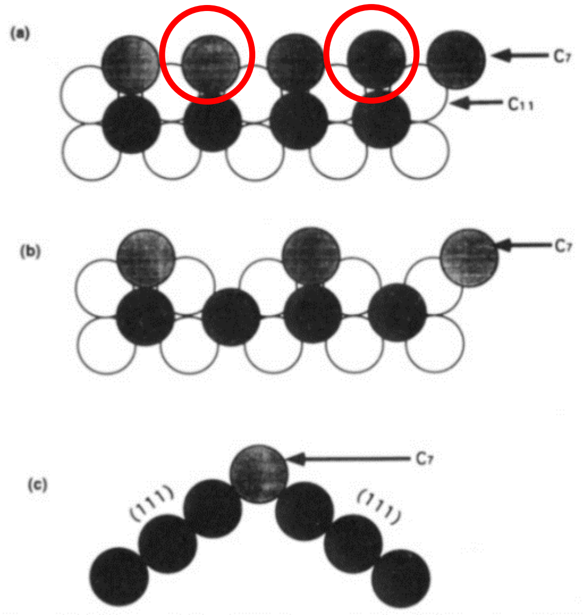

Figure 1. 2. 6 Schematic illustration of C_7 atoms on (a) fcc (110) surface, (b) fcc (110)-(1×2) surface, (c) edge atom in cuboctahedron [22]. (Reprinted with permission from (Kalakkad, D., et al. "n-Butane hydrogenolysis as a probe of surface sites in rhodium metal particles: correlation with single crystals." The Journal of Physical Chemistry 97.7 (1993): 1437-1444.). Copyright (1993) American Chemical Society.)

Table 1.1 is a brief summary of n-butane hydrogenolysis results from literature for comparison. For kinetic study, most of them have the conversion controlled under 1%. From the table we can see that the highest selectivity to ethane, which is 90%, reported among the listed literature was realized when the reaction was performed on the single crystal catalyst Ir (110)-(1×2) at the H_2/n-butane ratio of 100/1, at 202°C [23]. Among the metal supported catalysts, the Rh/Al_2O_3 catalyst reported by Kalakkad, Anderson et al. [22] has the selectivity as high as 80% at a lower temperature of 175°C with the H_2/n-butane ratio of 20/1. Similarly, Foger, K., and J. R. Anderson [25] tested n-butane hydrogenolysis on Ir/Al_2O_3 and Ir/SiO_2, and the best selectivity to ethane is about 85.4%

and 76.5%, respectively. However, the conversion is always less than 10% which is intentionally controlled for kinetic study in these cases, but extremely low for industry.

The plot of conversion and selectivity to methane, ethane and propane products versus the reciprocal flow rate on the oxidizing ‘decomposed’ Ru / 13X zeolite catalyst with the loading of 0.6% is shown in Figure 1.2.7. From the upper plot, as the flow rate decreases, which means the increase of the reciprocal flow rate in the plot, the conversion gradually increases as expected until 45% (temperature is 160°C and constant). Nevertheless, the selectivity to the 3 products does not change at all with the changing flow rate, which is rarely seen in practice. The carbon-based selectivity to ethane (defined in section 2.4.2) is about 25.8% after recalculating based on the data provided in the plot. After comparing with other results in Table 1.1, the Ru catalyst with 25.8% of the selectivity to ethane at 45% conversion may not be optimal.

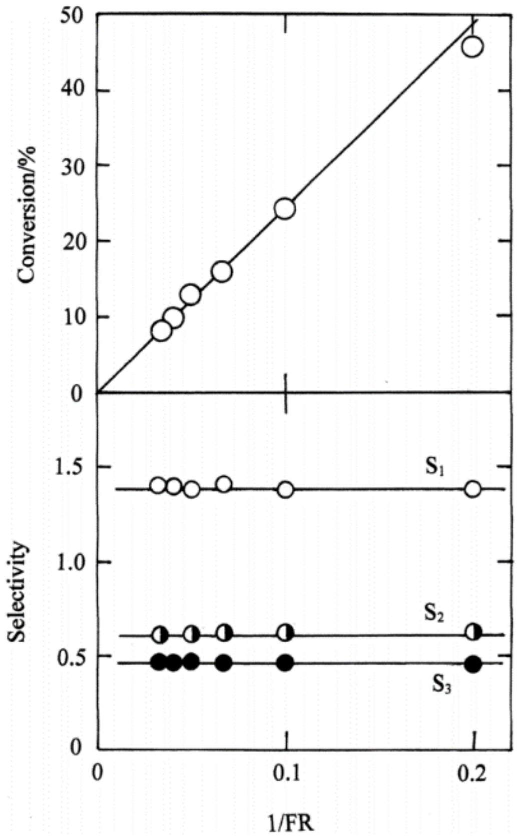

Figure 1. 2. 7 N-butane hydrogenolysis results of conversion and selectivity versus reciprocal flow rate on 0.6%Ru /13X zeolite catalyst at 160 °C published by Bond, G.C. and Garcia, J.J. in 2017 [27]. **(**Reproduced (in part) from (Bond, Geoffrey C., and Juan J. Garcia. "Hydrogenolysis of alkanes: reactions of n-butane on Ru/zeolite catalysts." Catalysis Science & Technology 7.22 (2017): 5294-5300.) with permission of The Royal Society of Chemistry.)

1.2.2 Ethane hydrogenolysis on the metal catalysts

Recall the chemical formula of n-butane hydrogenolysis mentioned above, the n-butane hydrogenolysis reaction is a combination of parallel and series reactions. To optimize the selectivity to the target product of ethane and minimize the side products of methane and propane, it is very important to minimize the parallel reaction pathway of terminal C–C bond cleavage ③ as well as the following series reactions of step ④, ⑤, ⑥ and ⑦. As the target product and important intermediate during the series reaction, ethane is the key factor for the selectivity in the hydrogenolysis environment. Therefore, the study of ethane hydrogenolysis provides important details in understanding the series reaction mechanism during n-butane hydrogenolysis on the same series of catalysts and offers good solutions to optimize the selectivity to ethane. Ethane hydrogenolysis is an exothermic reaction as shown in the following equation,

$$C_2H_6 + H_2 \longrightarrow 2CH_4 \qquad \Delta H^{\circ}_{298K} = -65.2\text{kJ/mol}$$

Somorjai, G.A. et al. [29] reported that ethane hydrogenolysis is structure sensitive reaction on Pt supported on SBA-15 Silica. In their work, they first synthesized a series of Pt/SBA-15 with different particle sizes by nanoparticle encapsulation method as well as Pt supported on SiO_2 by ion-exchange method with smaller particle sizes, then running ethane hydrogenolysis reactions on these silica supported Pt catalysts as well as Pt powder with extraordinarily large particle size of 287 nm. As a consequence, they showed that the catalytic activity and the measured apparent activation energy of ethane hydrogenolysis were highly dependent on the particle size of the catalysts as shown in Figure 1.2.8. As the particle size increases, the catalytic activity of ethane hydrogenolysis, expressed as the turnover frequency of methane formation in the plot, linearly decreases by about 2 orders of magnitude over the size range of 1-3.6 nm. After that, further increase in the particle size had small effect on the activity as we can see from the comparison of the Pt powder with the size of 287 nm with those supported Pt catalysts with the size lower than 10 nm. Oppositely, the measured apparent activation energy sharply increases as the particle size increases to 3.6 nm, after which the apparent activation energy flattens out.

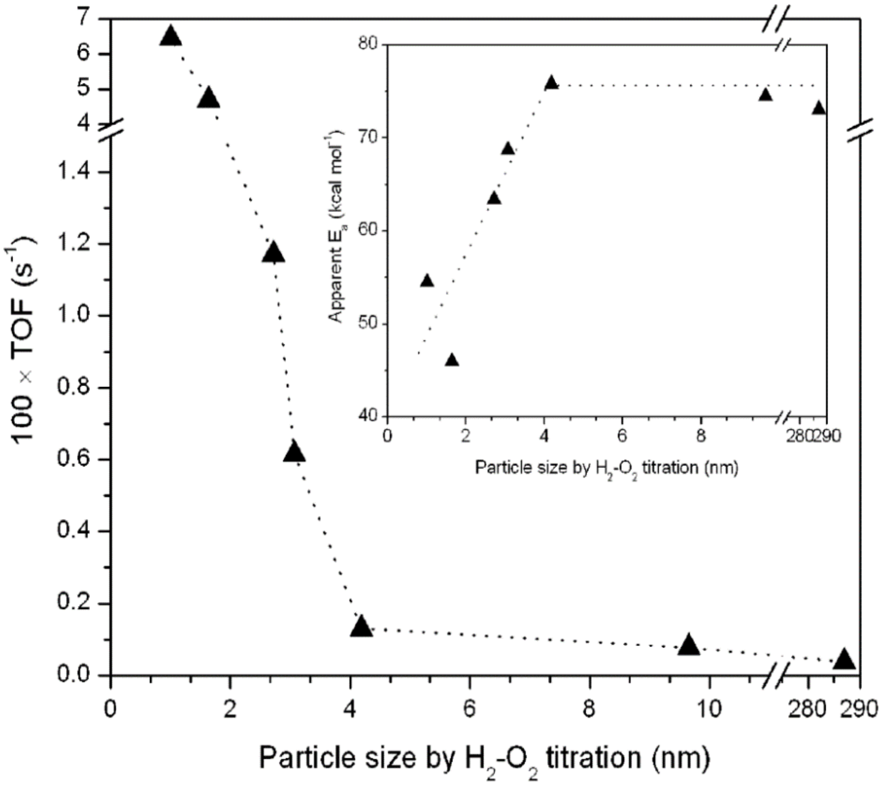

Figure 1. 2. 8 Dependence of ethane hydrogenolysis turnover frequency and apparent activation energy on Pt particle size. The turnover frequencies were measured at 20 torr C_2H_6, 200 torr H_2, and 658 K. (Reprinted with permission from (Song, Hyunjoon, et al. "Hydrothermal growth of mesoporous SBA-15 silica in the presence of PVP-stabilized Pt nanoparticles: synthesis,

characterization, and catalytic properties." Journal of the American Chemical Society 128.9 (2006): 3027-3037.). Copyright (2006) American Chemical Society.)

The details of the catalytic activity and reaction orders of ethane hydrogenolysis on Pt nanoparticles corresponding to different particle sizes are tabulated in Table 1.2. On one hand, the authors believed that the ethane molecules and C_2 intermediates are very likely to bond with multiple Pt atoms of the particles, making large Pt nanoparticles with several adjacent sites necessary for the adsorption of reactant. On the other hand, the saturation level of the surface atoms is also significant for the catalytic activity in addition to large particle size. Smaller size particles resemble the crystal surfaces that are comprised of more steps, kinks, and other special sites which increase the surface roughness and lower the saturation level of surface atoms. While larger size particles resemble the flat crystal surfaces such as (111) that are mostly comprised of terrace sites with high coordination numbers. In the case of ethane hydrogenolysis, the ethane molecules are more probably bound to multiple atoms served as different sites instead of one or two atoms on the flat surface. Also, the adsorption energy of the intermediates binding with the atoms in different surface structure are different. For instance, the activation barrier of the most active C_2H_5 species on the Pt (211) surface is much lower than that on the more flat Pt (111) surface, resulting in the different ability of C-C bond cleavage [31, 32]. These factors might be responsible for the trends that we can see from the plot in Figure 1.2.8. Surface roughness of the Pt particles is a very important parameter to weigh the fraction of active sites that usually determines the reactivity.

Table 1. 2 Ethane hydrogenolysis turnover frequencies and kinetic parameters measured on the series of Pt catalysts [29]. Adapted with permission from (Song, Hyunjoon, et al. "Hydrothermal growth of mesoporous SBA-15 silica in the presence of PVP-stabilized Pt nanoparticles: synthesis,

characterization, and catalytic properties." Journal of the American Chemical Society 128.9 (2006): 3027-3037.). Copyright (2006) American Chemical Society.)

Catalyst	**Dispersion**	**Particle size (Chemisorption)**	**TOF 100×(s^{-1})**	**Ea(kJ/mol)**	**Reaction orders**	
					C_2H_6	**H_2**
3.2% Pt/SiO_2-IE	1	1.0	6.5	228.03	0.99	-2.8
6.3% Pt/SiO_2-(EUROPT-1)	0.69	1.6	4.7	192.46	0.9	-1.8
0.6% Pt(1.7nm)/SBA-15	0.41	2.7	1.2	265.27	0.97	-2.4
0.77% Pt(2.9nm)/SBA-15	0.36	3.1	0.6	287.44	1	-3.1
0.6% Pt(3.6nm)/SBA-15	0.27	4.2	0.1	317.15	1.1	-3.0
0.62% Pt(7.1nm)/SBA-15	0.11	9.5	0.08	311.71	0.97	-2.9
Pt powder	0.004	287	0.04	294.97	0.99	-2.6

In the most recent 5 years, David W. Flaherty, Enrique Iglesia et.al. [32] investigated the reaction mechanism of ethane hydrogenolysis by performing experiments on Ir/SiO_2 particles with the size of 7 nm and by the computational study of DFT calculations using Vienna *ab initio* simulation package. They proposed a sequence of elementary reaction steps as potential reaction mechanisms as shown in scheme 1.1, and then confirmed the intermediate that went through the C–C bond cleavage by the combination of experimental reaction rates and reaction orders with DFT results.

$$H_2 + 2\,* \rightleftharpoons 2\,H^* \qquad (1)$$

$$C_2H_6 + * \rightleftharpoons C_2H_6^* \qquad (2)$$

$$C_2H_6^* + * \rightleftharpoons C_2H_5^* + H^* \qquad (3)$$

$$C_2H_5^* + 2\,* \rightleftharpoons {}^*C_2H_4^* + H^* \qquad (4)$$

$$\longrightarrow$$

$$\rightarrow$$

$$\cdots$$

$$^{*}C_2H^{*}_{6-(y-1)} + * \rightleftharpoons \ ^{*}C_2H^{*}_{6-y} + H^{*} \qquad (5)$$

$$^{*}C_2H^{*}_{6-y} \xrightarrow{k_{CC,y}} CH^{*}_{a} + CH^{*}_{b} \qquad (6)$$

$$CH^{*}_{a} + xH^{*} \rightleftharpoons CH_4 + (x+1)* \qquad (7)$$

Scheme 1. 1 Proposed sequence of elementary steps and intermediates during ethane hydrogenolysis reaction on Ir/SiO_2 particles. (* denotes one single site; *-* denotes an intermediate bound to two neighboring sites; "k_x" and "k_{-x}" are reaction constants that correspond to the forward and reverse reaction of the specific step) [32] (Reproduced with permission from Journal of Catalysis 311 (2014): 350-356, Flaherty, David W. et al., Theoretical and kinetic assessment of the mechanism of ethane hydrogenolysis on metal surfaces saturated with chemisorbed hydrogen. Copyright (2014), with permission from Elsevier)

In the proposed sequence of elementary steps shown in scheme 1.1, the C–H bonds of ethane are gradually replaced by C-metal bonds after the ethane molecules adsorb on the metal. During this process, the C–C bonds are simultaneously weakened as the electron density of C–C bonds are transferred to the metal surface atoms. The H_2 dissociation step (1), ethane adsorption step (1.2) and the dehydrogenation of adsorbed ethane steps (3-5) are assumed as quasi-equilibrated steps based on the H/D exchange experiments during ethane hydrogenolysis process elsewhere and the calculation of activation barriers by DFT study [34], so the C–C bond cleavage step (6) is the only rate determining step in this case. Macroscopically, the observed hydrogenolysis reaction rate should be proportional to the partial pressure of H_2 and C_2H_6 with the exponent of respective reaction order. Microscopically, the observed hydrogenolysis reaction rate should be the summation of the rates of each elementary C–C bond cleavage step for the intermediates with (6-

y) H atoms, written in the equation form of $r_{obs} = \sum_{y=0}(r_y) = \sum_{y=0}(k_{CC,y}[\,^*C_2H^*_{6-y}])$. Therefore, the rate equation derived from the sequence of elementary steps with the C-C bond cleavage of intermediate ($^*C_2H^*_{6-y}$) as the rate determining step becomes

$$r_y = k_{CC,y} \cdot \frac{(\prod_{n=1}^{y} K_{CH,n}) \cdot K_{C_2H_6} \cdot (C_2H_6)}{K_{H_2}^{\lambda} \cdot (H_2)^{\lambda}} \cdot [L]$$

$$y+\gamma=2\lambda$$

(γ is the number of H-atoms that desorb from the surface, y is the number of H atoms that lose from* C_2H_6 *molecule to form the intermediate that being cleaved the C–C bond,* $K_{CH,n}$ *is the equilibrium constant of H removal steps)*

(Note: there is no index of λ on the rate constant of K_{H_2} highlighted in red in the denominator in the original text of reference 32. After recalculating based on the same methods and combining with other literatures published by the same author, it is considered as a mistake of the missing index, which is the same as the partial pressure of H_2.)

The authors also tabulated the thermodynamic parameters for all the potential elementary steps based on the DFT calculations. The reaction enthalpy for C–H bond cleavage of intermediate ($^*C_2H^*_{6-y}$) is always smaller than C–C bond cleavage until y equals 4. For intermediate ($^*CHCH^*$), the activation barrier for C–H bond cleavage is 70 kJ·mol^{-1} higher than C–C bond cleavage. Therefore, the intermediate ($^*CHCH^*$) is determined as the one that goes through the C–C bond cleavage. In this case, the number of H atoms that lost from C_2H_6 molecule is 4 (y=4), and the H*atoms that desorb from the surface to makeup the methane molecule is 2 (γ=2). Therefore, according to the relationship of $y+\gamma=2\lambda$, the value of λ should be 3. The results from

DFT calculations are consistent with those coming from the experiments. From experiments, they determined that the C_2H_6 reaction order is 1, which is the same as the index of C_2H_6 term in the numerator of the rate equation. While the H_2 reaction order is -3.3, the approximation and absolute of which is exactly the same as the λ value of 3 coming from the rate equation derived by DFT calculations.

1.3 Selective Hydrogenation of Acetylene

Ethylene is one of the most important raw chemicals serving as the building block of polyethylene, which is the basic composition of multiple downstream products and polymer materials. During the olefin polymerization process, trace amount of acetylene may result in the poisoning of the catalyst (e.g. Ziegler-Natta) and hence lower polymerization efficiency [35]. The selective hydrogenation of acetylene to ethylene without further hydrogenation to ethane becomes significant to improve the efficiency and productivity.

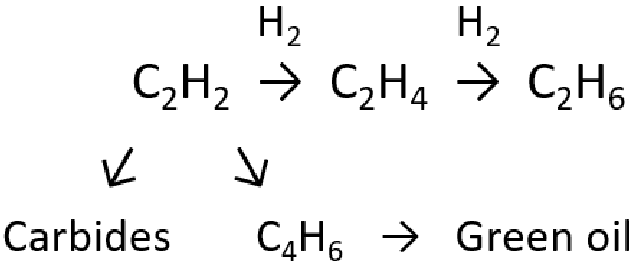

Above is the complete reaction pathway that possibly happened during selective hydrogenation of acetylene [36]. Firstly, the C_2H_2 and H_2 molecules adsorb on the surface of the metal catalyst. Basically, the adsorbed C_2H_2 molecules and H species react to form C_2H_4. The adsorbed C_2H_4 molecules can experience either desorption to produce C_2H_4 or further hydrogenation to form C_2H_6. To increase the selectivity to ethylene, the adsorption energy of C_2H_4 on the metal catalyst must be low. Otherwise, the adsorbed C_2H_4 molecules would be hard to desorb from the surface and the surrounding H species could further hydrogenate the unsaturated C_2H_4 to C_2H_6, resulting in a lower selectivity to ethylene. In addition to the main hydrogenation pathway, there are side reactions that decrease the productivity. One is the cracking of C_2H_2 molecules to form coke on the surface to deactivate the catalyst, the other one is the C–C coupling of C_2H_2 molecules helps the formation of higher hydrocarbons (e.g. C_4H_6) and finally some green oil. Both cause severe issues in industry, like the catalyst poisoning and the necessity for regeneration. To increase the selectivity of acetylene hydrogenation to ethylene, all the three pathway, further hydrogenation of C_2H_4, cracking and C–C coupling of C_2H_2 molecules should be avoided. Therefore, it is significant to understand the reaction mechanism and explore more efficient catalyst for selective hydrogenation of acetylene.

From literature, the selective hydrogenation of alkynes and hydrogenation of alkenes generally follow Horiuti−Polanyi mechanism [37, 38]. The hydrogen molecules are first activated dissociatively and adsorb on the surface of the metal, either heterolytically or homolytically. Then the C_2H_2 molecules adsorb and react with the surface H species to form adsorbed C_2H_4 (or saturated C_2H_6 molecules). Finally, the adsorbed C_2H_4 (or C_2H_6) molecules desorb from the surface as product in gas phase. The method of H_2 activation and C_2H_2 adsorption is dependent on the metal and the structure of the catalyst.

On VIII group metals like Pt, Rh, Pd, H_2 molecules can be dissociated homolytically, forming two hydrides on the surface of the catalyst. Because of the partially occupied d orbitals, these metals are able to accept σ electrons donated by H_2, and in the meantime donate the d-electrons to the H_2, the H–H bond can be weakened and then homolytic H–H bond cleavage happens. Therefore, active sites with high electron density are necessary for the hydrogenation reaction. When there are πacceptors such as CO, S and Cl containing in the feed, the catalysts would be poisoned and the H_2 dissociation might be suppressed [36]. In recent years, some literature also reported the heterolytic dissociation of H_2 on VIII group metals in heterogeneous catalysis. For example, Au/CeO_2 nanoparticles [39] and Pd/TiO_2 single atoms [40]. In these cases, as the supports are reducible, the interface sites of metal-support interaction are mostly electron deficient, therefore, heterolytic dissociation of H_2 likely to happen and form H^+ and H^-. After H_2 dissociatively adsorb on the catalyst surface, the H atoms on the metal nanoparticles can migrate on the support, this process has been widely observed and called as “spillover” [41]. In some cases, the H atoms can also penetrate the metal particles and form sublayer of hydride, and thus, increase the following reactivity by decreasing the stability of the hydrogen species on the surface of the catalyst. Doyle, Aidan M., et al. compared the alkenes hydrogenation on Pd nanoparticles and Pd crystal surface. The hydrogenation of alkenes can be observed on Pd nanoparticles but not on Pd crystals, as the subsurface hydrogen species on Pd nanoparticles are easier to access than the Pd crystals [42].

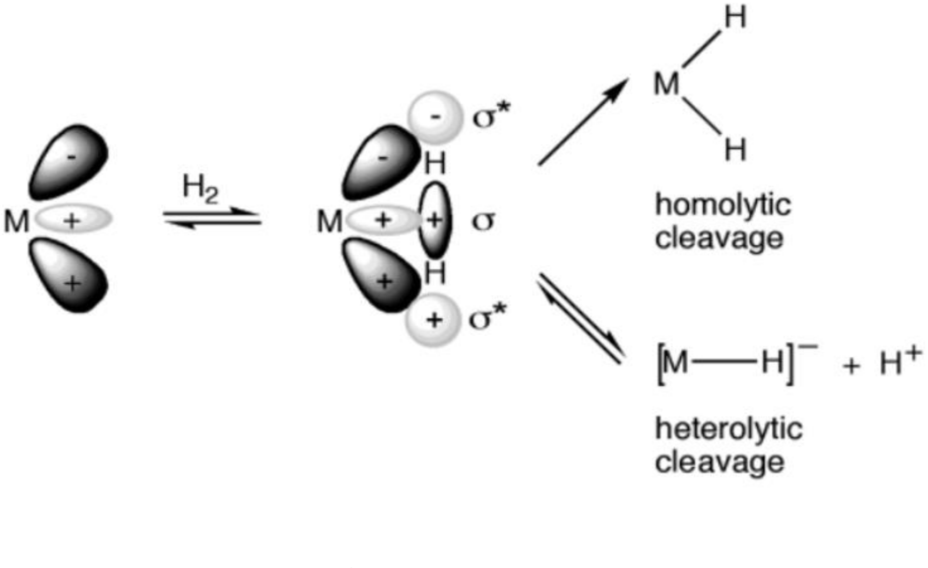

Figure 1.3.1 Schematic illustration of H_2 dissociation (homolytic vs. heterolytic) modes on transition metal active site [43]. (Reprinted with permission from (Frey, Guido D., et al. "Facile splitting of hydrogen and ammonia by nucleophilic activation at a single carbon center." Science

316.5823 (2007): 439-441.). Copyright (2007) The American Association for the Advancement of Science.)

The adsorption modes of acetylene on the catalyst surface are one of the key factors that determine the selectivity of acetylene hydrogenation. The adsorption modes are strongly dependent on the ensemble of the metal, emphasizing the significance of the structure sensitivity. Previously, it is found that ethylene could have three adsorption modes on the metal catalysts as shown in the example of Pd catalysts in Figure 1.3.2 below. When the particle size is large, there can be ethylidyne forming on 3-fold sites or di-σ bonded C_2H_4 on 2-fold sites. However, when there are only Pd single atoms isolated on the support, it is likely to form π-bonded C_2H_4. The ethylidyne mode has higher adsorption energy than di-σ bonded mode, while the π-bonded mode has the lowest adsorption energy. Therefore, on isolated sites the semi-hydrogenated C_2H_4 molecules are easier to desorb compared with clusters or nanoparticles, resulting in higher selectivity.

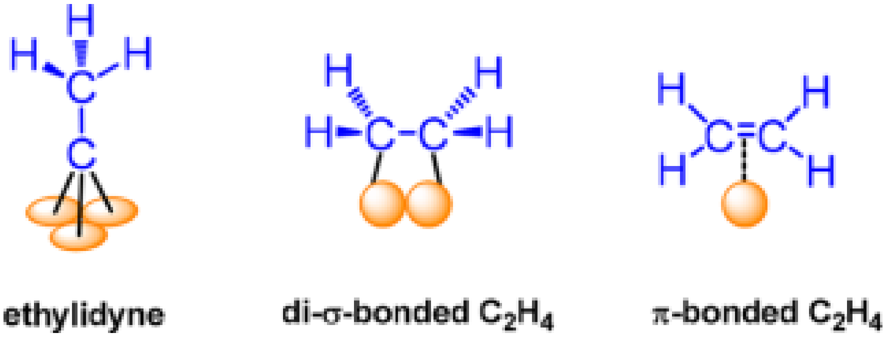

Figure 1.3.2 Three adsorption modes on supported Pd catalysts [36]. (Reprinted with permission from (Zhang, Leilei, et al. "Selective hydrogenation over supported metal catalysts: from nanoparticles to single atoms." Chemical Reviews 120.2 (2019): 683-733.). Copyright (2020) American Chemical Society.)

1.4 Objective of this work

In general, the conversion of n-butane hydrogenolysis would increase with temperature, but concomitantly the selectivity to the target product, ethane, would also decrease. To our knowledge, the highest selectivity to ethane reported is about 90% with the conversion of about 1% at 202 °C on the Ir(110)-(1×2) surface. However, the activity and selectivity on the metal catalysts in the subnanometer regime is missing. For industrial applications, a high selectivity at higher conversion range is desired to maximize the yield of the target product. To fill the gap, it is demanded to study the structure sensitivity of n-butane hydrogenolysis on the catalysts with different particle size in the subnanometer regime. The study of particle size is significant for understanding the fundamentals of the adsorption and desorption of reactant molecules and the preferred surface structure for the particular reaction to help the rational design of the catalysts.

In addition to particle size, other factors like temperature and conversion, the level of series reaction pathway from $C_3 \rightarrow C_2$ and $C_2 \rightarrow C_1$ are also significant to determine the selectivity to the target product of ethane. Therefore, it is of great importance to study ethane hydrogenolysis on the same series of catalysts in order to understand the reactivity for ethane at similar conditions. And it would be best to find ways to block the series reaction of C–C bond cleavage on the ethane intermediate during n-butane hydrogenolysis after fully understand the factors that control the reaction pathways in n-butane hydrogenolysis. In this study, the results of structure sensitivity / insensitivity of n-butane hydrogenolysis and ethane hydrogenolysis reactions on the series of supported Ir catalysts with different particle size distributions is presented. The first objective is to understand the pathway of alkanes hydrogenolysis on the supported Ir catalysts with different structures or sizes and find out the factors that determine the selectivity. After that the information of particle size / surface structure of the catalysts and the optimal conditions can help maximize the reactivity and magnify the commercial value for industry.

Considering the high demand of ethylene in the downstream chemical industry, the selective hydrogenation of acetylene to ethylene is of great importance for polyethylene manufacturing to avoid catalyst poisoning by removing trace of acetylene and ethane in the ethylene feed. The second objective is to study the structure sensitivity of acetylene hydrogenation on supported Ir catalysts to optimize the reactivity and selectivity.

In general, the following scientific questions are answered in this work.

I. How does the metal nuclearity in the subnanometer regime affect the behavior of C–C bond cleavage of alkanes (i.e. ethane, n-butane)?

II. What are the main factors that influence the level of parallel and series reaction pathway on supported metal catalysts in the subnanometer regime?

III. Are the hydrogenolysis of ethane and n-butane structure sensitive on supported Ir catalysts (regarding activity and selectivity)? How to optimize the structure based on the results?

IV. What is the reaction mechanism of hydrogenolysis on supported Ir catalysts based on the results of kinetic measurements?

V. What is the factor that determines the structure sensitivity in the catalytic performance of acetylene hydrogenation? Geometric properties or electronic properties?

1.5 Approach to this work

In this work, to study the structure sensitivity of alkanes hydrogenolysis and alkynes hydrogenation, we chose spinel structure support $MgAl_2O_4$ to stabilize Ir in the small size range of 0.7–1.3 nm to understand the effect of Ir nuclearity on the reaction. Because of the strong interfacial interaction between the facets of the $MgAl_2O_4$ spinel support and Ir that limits sintering [44], we were unable to prepare Ir nanoparticles larger than ~1.5 nm on $MgAl_2O_4$. Therefore, the inert SiO_2 was chosen as the support to prepare some larger sized Ir nanoparticles for comparison.

Wet impregnation and incipient wetness impregnation were used to synthesize the catalysts, as the operations are very simple without specific tools. To optimize the interaction between the metal and support, proper conditions (e.g. pH, weight loading, metal precursor) and different pretreatments (oxidation / reduction / sintering) were chosen so that the catalytic efficiency was promoted.

To understand reaction pathway hydrogenolysis, the catalysts were tested at high conversion range and in kinetic regime. The hydrogenolysis of ethane was tested in kinetic regime for activation energies and reaction orders to deduce the reaction mechanism and provide the hints for C–C bond cleavage in higher chain length alkanes. To understand the main factors that can be used to tune the reaction pathway, the effect of reaction conditions such as temperature and conversion were studied.

In order to investigate the effect of electronic properties, another series of Ir catalysts was also prepared on $ZnAl_2O_4$, as the metal-support interactions can tune the electronic properties of Ir. The hydrogenolysis on Ir/$ZnAl_2O_4$ is much lower because of unknown reasons, we chose acetylene hydrogenation as the probe reaction to continue the structure sensitivity study on Ir/$ZnAl_2O_4$ catalysts. Both the activity and selectivity were measured on Ir/$ZnAl_2O_4$ catalysts with different Ir nuclearity. We also synthesized two Ir catalysts with the same surface-average particle size but with different weight loadings (0.2% vs. 1%) and pretreated at different reduction temperatures

(400 °C vs. 600 °C) so that the electronic properties of Ir can be distinguished. Through this way the effect of the geometric properties and electronic properties could be decoupled for structure sensitivity study of acetylene hydrogenation on Ir/$ZnAl_2O_4$ catalysts.

References

[1] C. Vogt, E. Groeneveld, G. Kamsma, M. Nachtegaal, L. Lu, C.J. Kiely, P.H. Berben, F. Meirer, B.M. Weckhuysen, Unravelling structure sensitivity in CO 2 hydrogenation over nickel, Nature Catalysis, (2018) 1.

[2] G.A. Somorjai, J. Carrazza, Structure sensitivity of catalytic reactions, Industrial & engineering chemistry fundamentals, 25 (1986) 63-69.

[3] N.D. Spencer, R.C. Schoonmaker, G.A. Somorjai, Iron single crystals as ammonia synthesis catalysts: effect of surface structure on catalyst activity, Journal of Catalysis, 74 (1982) 129-135.

[4] C.J.H. Jacobsen, S. Dahl, P.L. Hansen, E. Törnqvist, L. Jensen, H. Topsøe, D.V. Prip, P.B. Møenshaug, I. Chorkendorff, Structure sensitivity of supported ruthenium catalysts for ammonia synthesis, Journal of Molecular Catalysis A: Chemical, 163 (2000) 19-26.

[5] J.H. Sinfelt, J. Carter, D.J.C. Yates, Catalytic hydrogenolysis and dehydrogenation over copper-nickel alloys, Journal of Catalysis, 24 (1972) 283-296.

[6] S. Ladas, H. Poppa, M. Boudart, The adsorption and catalytic oxidation of carbon monoxide on evaporated palladium particles, Surface Science, 102 (1981) 151-171.

[7] T.A. Dorling, M.J. Eastlake, R.L. Moss, The structure and activity of supported metal catalysts: IV. Ethylene hydrogenation on platinum/silica catalysts, Journal of Catalysis, 14 (1969) 23-33.

[8] A.S. Crampton, M.D. Rotzer, C.J. Ridge, F.F. Schweinberger, U. Heiz, B. Yoon, U. Landman, Structure sensitivity in the nonscalable regime explored via catalysed ethylene hydrogenation on supported platinum nanoclusters, Nat Commun, 7 (2016) 10389.

[9] M.E. Davis, R.J. Davis, Fundamentals of chemical reaction engineering, Courier Corporation, 2012.

[10] D.W. Goodman, Ethane hydrogenolysis over single crystals of nickel: Direct detection of structure sensitivity, Surface Science, 123 (1982) L679-L685.

[11] G.A. Martin, The kinetics of the catalytic hydrogenolysis of ethane over Ni/SiO2, Journal of Catalysis, 60 (1979) 345-355.

[12] J. Liu, Catalysis by supported single metal atoms, ACS Catalysis, 7 (2016) 34-59.

[13] B.R. Cuenya, F. Behafarid, Nanocatalysis: size-and shape-dependent chemisorption and catalytic reactivity, Surface Science Reports, 70 (2015) 135-187.

[14] A.I. Frenkel, C.W. Hills, R.G. Nuzzo, A view from the inside: complexity in the atomic scale ordering of supported metal nanoparticles, in, ACS Publications, 2001.

[15] X.-F. Yang, A. Wang, B. Qiao, J. Li, J. Liu, T. Zhang, Single-Atom Catalysts: A New Frontier in Heterogeneous Catalysis, Accounts of Chemical Research, 46 (2013) 1740-1748.

[16] S. Mostafa, F. Behafarid, J.R. Croy, L.K. Ono, L. Li, J.C. Yang, A.I. Frenkel, B.R. Cuenya, Shape-dependent catalytic properties of Pt nanoparticles, Journal of the American Chemical Society, 132 (2010) 15714-15719.

[17] D.J.C. Yates, W.F. Taylor, J.H. Sinfelt, Catalysis over supported metals. I. Kinetics of ethane hydrogenolysis over nickel surfaces of known area, Journal of the American Chemical Society, 86 (1964) 2996-3001.

[18] W.F. Taylor, D.J.C. Yates, J.H. Sinfelt, Catalysis over supported metals. II. The effect of the support on the catalytic activity of nickel for ethane hydrogenolysis, The Journal of Physical Chemistry, 68 (1964) 2962-2966.

[19] J.H. Sinfelt, W.F. Taylor, D.J.C. Yates, Catalysis over supported metals. III. Comparison of metals of known surface area for ethane hydrogenolysis, The Journal of Physical Chemistry, 69 (1965) 95-101.

[20] W.F. Taylor, J.H. Sinfelt, D.J.C. Yates, Catalysis over Supported Metals. IV. Ethane Hydrogenolysis over Dilute Nickel Catalysts, The Journal of Physical Chemistry, 69 (1965) 3857-3863.

[21] D.J.C. Yates, J.H. Sinfelt, An investigation of the dispersion and catalytic properties of supported rhenium, Journal of Catalysis, 14 (1969) 182-186.

[22] D. Kalakkad, S.L. Anderson, A.D. Logan, J. Pena, E.J. Braunschweig, C.H.F. Peden, A.K. Datye, n-Butane hydrogenolysis as a probe of surface sites in rhodium metal particles: correlation with single crystals, The Journal of Physical Chemistry, 97 (1993) 1437-1444.

[23] J.R. Engstrom, D.W. Goodman, W.H. Weinberg, Hydrogenolysis of n-butane over the (111) and (110)-(1. times. 2) surfaces of iridium: a direct correlation between catalytic selectivity and surface structure, Journal of the American Chemical Society, 108 (1986) 4653-4655.

[24] G.C. Bond, X. Yide, Hydrogenolysis of alkanes. Part 1.—Hydrogenolysis of ethane, propane and n-butane on 6% Pt/SiO 2 (EUROPT-1), Journal of the Chemical Society, Faraday Transactions 1: Physical Chemistry in Condensed Phases, 80 (1984) 969-980.

[25] K. Foger, J.R. Anderson, Hydrocarbon reactions on supported iridium catalysts, Journal of Catalysis, 59 (1979) 325-339.

[26] R. Van Hardeveld, F. Hartog, The statistics of surface atoms and surface sites on metal crystals, Surface Science, 15 (1969) 189-230.

[27] G.C. Bond, J.J. Garcia, Hydrogenolysis of alkanes: reactions of n-butane on Ru/zeolite catalysts, Catalysis Science & Technology, 7 (2017) 5294-5300.

[28] G.C. Bond, J.C. Slaa, Catalytic and structural properties of ruthenium bimetallic catalysts: effects of pretreatment on the behaviour of various RuAl2O3 catalysts in alkane hydrogenolysis, Journal of Molecular Catalysis A: Chemical, 101 (1995) 243-253.

[29] H. Song, R.M. Rioux, J.D. Hoefelmeyer, R. Komor, K. Niesz, M. Grass, P. Yang, G.A. Somorjai, Hydrothermal growth of mesoporous SBA-15 silica in the presence of PVP-stabilized Pt nanoparticles: synthesis, characterization, and catalytic properties, Journal of the American Chemical Society, 128 (2006) 3027-3037.

[30] R.M. Rioux, H. Song, J.D. Hoefelmeyer, P. Yang, G.A. Somorjai, High-surface-area catalyst design: synthesis, characterization, and reaction studies of platinum nanoparticles in mesoporous SBA-15 silica, The Journal of Physical Chemistry B, 109 (2005) 2192-2202.

[31] R.D. Cortright, R.M. Watwe, J.A. Dumesic, Ethane hydrogenolysis over platinum: Selection and estimation of kinetic parameters, Journal of Molecular Catalysis A: Chemical, 163 (2000) 91-103.

[32] D.W. Flaherty, D.D. Hibbitts, E.I. Gürbüz, E. Iglesia, Theoretical and kinetic assessment of the mechanism of ethane hydrogenolysis on metal surfaces saturated with chemisorbed hydrogen, Journal of Catalysis, 311 (2014) 350-356.

[33] D.D. Hibbitts, D.W. Flaherty, E. Iglesia, Effects of Chain Length on the Mechanism and Rates of Metal-Catalyzed Hydrogenolysis of n-Alkanes, The Journal of Physical Chemistry C, 120 (2016) 8125-8138.

[34] R.S. Dowie, D.A. Whan, C. Kemball, Hydrogenolysis of saturated hydrocarbons on evaporated platinum films, Journal of the Chemical Society, Faraday Transactions 1: Physical Chemistry in Condensed Phases, 68 (1972) 2150-2162.

[35] O.B. Ayodele, S. Vinati, E. Barborini, L. Boddapati, K. El Hajraoui, J. Kröhnert, F.L. Deepak, A. Trunschke, Y.V. Kolen'ko, Selectivity boost in partial hydrogenation of acetylene via atomic dispersion of platinum over ceria, Catalysis Science & Technology, 10 (2020) 7471-7475.

[36] L. Zhang, M. Zhou, A. Wang, T. Zhang, Selective hydrogenation over supported metal catalysts: from nanoparticles to single atoms, Chemical Reviews, 120 (2019) 683-733.

[37] I. Horiuti, M. Polanyi, Exchange reactions of hydrogen on metallic catalysts, Transactions of the Faraday Society, 30 (1934) 1164-1172.

[38] R.D. Cortright, S.A. Goddard, J.E. Rekoske, J.A. Dumesic, Kinetic study of ethylene hydrogenation, Journal of catalysis, 127 (1991) 342-353.

[39] T. Whittaker, K.B.S. Kumar, C. Peterson, M.N. Pollock, L.C. Grabow, B.D. Chandler, H2 oxidation over supported Au nanoparticle catalysts: evidence for heterolytic H2 activation at the metal–support interface, Journal of the American Chemical Society, 140 (2018) 16469-16487.

[40] P. Liu, Y. Zhao, R. Qin, S. Mo, G. Chen, L. Gu, D.M. Chevrier, P. Zhang, Q. Guo, D. Zang, Photochemical route for synthesizing atomically dispersed palladium catalysts, Science, 352 (2016) 797-800.

[41] R. Prins, Hydrogen spillover. Facts and fiction, Chemical reviews, 112 (2012) 2714-2738.

[42] A.M. Doyle, S.K. Shaikhutdinov, S.D. Jackson, H.J. Freund, Hydrogenation on metal surfaces: why are nanoparticles more active than single crystals?, Angewandte chemie international edition, 42 (2003) 5240-5243.

[43] G.D. Frey, V. Lavallo, B. Donnadieu, W.W. Schoeller, G. Bertrand, Facile splitting of hydrogen and ammonia by nucleophilic activation at a single carbon center, Science, 316 (2007) 439-441.

[44] W.-Z. Li, L. Kovarik, D. Mei, M.H. Engelhard, F. Gao, J. Liu, Y. Wang, C.H.F. Peden, A General Mechanism for Stabilizing the Small Sizes of Precious Metal Nanoparticles on Oxide Supports, Chemistry of Materials, 26 (2014) 5475-5481.

Chapter 2. Structure Sensitivity of n-Butane Hydrogenolysis on Supported Ir Catalysts

This work has been published in *Journal of Catalysis* and is available online. Reprinted (adapted) with permission from Zhang, X., Lu, Y., Kovarik, L., Dasari, P., Nagaki, D., & Karim, A. M. (2020). Structure Sensitivity of n-Butane Hydrogenolysis on Supported Ir Catalysts. Journal of Catalysis. Copyright Elsevier Journal of Catalysis (2020).

Author Affiliation:

[1]Department of Chemical Engineering, Virginia Polytechnic Institute and State University, Blacksburg, VA 24060, USA.

[2]Pacific Northwest National Laboratory, Richland, WA 99352, USA.

[3]Corporate Research and Development, SABIC, Sugar Land, Texas, 77478 USA

*Correspondence to: Ayman M. Karim amkarim@vt.edu.

KEYWORDS Alkane hydrogenolysis, structure sensitivity, heterogeneous catalyst, supported iridium nanoparticles, infrared spectroscopy

Attribution

Xiwen Zhang performed catalyst synthesis and all the catalytic tests, including data analysis, reaction mechanism analysis and wrote the manuscript. Yubing Lu conducted the synthesis of catalysts and characterizations (DRIFTS, chemisorption) for Ir/$MgAl_2O_4$ catalysts. Libor Kovarik performed the HAADF-STEM analysis for Ir/$MgAl_2O_4$. Roy Geiss at Colorado State University conducted the STEM analysis for Ir/SiO_2 catalysts with the assistance of Professor Richard G.Finke and his research group. Ayman M Karim conceived the idea and directed the project. Prasanna Dasari and Dick Nagaki provided important suggestions on the projects. All the authors discussed the results and provided comments on the projects.

2.1 Abstract

Hydrogenolysis of alkanes has been widely reported as structure sensitive reaction on transition metal heterogeneous catalysts with metal particle sizes ranging between 1–20 nm. In this work, a series of Ir/$MgAl_2O_4$ and Ir/SiO_2 catalysts with different Ir particle sizes ranging from subnanometer clusters (<1 nm) to nanoparticles (1–3 nm) were prepared and tested for n-butane hydrogenolysis. Our results show that the activity towards n-butane hydrogenolysis increases as Ir particle size increases in the lower particle size range, goes through a maximum at ~1.4–1.6 nm and then drops with a further increase in particle size. The product distribution at low temperature (170–190 °C) is dominated by central and terminal C–C bond cleavage of n-butane, and less by two C–C bond cleavage or further hydrogenolysis of the propane and ethane products. The selectivity to central C–C bond cleavage is highly dependent on the size of Ir and increases with a decrease in particle size down to ~1.4 nm but remains constant with further decrease in size. The results show that an Ir size of ~1.4 nm is optimum for n-butane hydrogenolysis activity and selectivity towards ethane.

2.2 Introduction

Hydrogenolysis of alkanes is a prototypical structure-sensitive reaction on supported noble metal catalysts and is used widely in many hydrocarbon processes to make smaller carbon chain molecules [1-3]. The selectivity (e.g. C–C cleavage of terminal vs. non-terminal C–C bonds) affects the energy density and fuel quality of molecules derived from fossil or biomass resources [4]. To study the fundamentals of hydrogenolysis of saturated alkanes, n-butane is the simplest molecule for investigating how the location of the C–C bond cleavage depends on temperature, reactant pressure and the structure of the catalyst.

Hydrogenolysis of n-butane has been reported to be structure sensitive on Ir, Rh and Ru catalysts [1, 5-10]. Kalakkad et al. showed that Rh(111) is more selective to the cleavage of the central C–C bond than Rh(100) or Rh(110) resulting in a selectivity to ethane of 50% on Rh(111) and 30% on Rh(100) and Rh(110) [1]. However, the selectivity to ethane on SiO_2 and Al_2O_3 supported Rh nanoparticles was higher than that on the Rh single crystals. Specifically, while larger Rh nanoparticles are expected to expose mostly (111) facets and show a similar selectivity to Rh(111), their selectivity was higher, ~60% on 3 and 6 nm Rh nanoparticles supported on Al_2O_3 and SiO_2 , respectively. Additionally, the ethane selectivity increased as the size decreased and reached ~80–90% on highly dispersed Rh (< 2nm) on both supports indicating that small Rh clusters have different properties than the more open/under-coordinated Rh surfaces, i.e. Rh(100) and Rh(110) [1]. On the other hand, the results on Ir single crystals and supported Ir catalysts were more consistent. Foger and Anderson reported that decreasing the particle size from 10 nm to 2 nm on Ir/Al_2O_3 and Ir/SiO_2 increases the selectivity of n-butane hydrogenolysis to ethane [5]. Engstrom et al. studied n-butane hydrogenolysis on Ir single crystals and found that ethane selectivity was much higher on the corrugated Ir (110) – (1×2) surface compared with the flat Ir (111) surface. The much higher selectivity on the roughened Ir surface was attributed to an increase in the fraction of under-coordinated sites (e.g. corner and edge atoms), on which the formation of metallacycle intermediates is proposed to be much easier [11, 12]. This is also a potential reason for the increased selectivity to ethane as the Ir size decreased from 10 nm to 2 nm on SiO_2 and Al_2O_3. Although a lot of studies focused on particle size effects in the nanometer range, the effect of size in the lower nanometer (< 2nm) and subnanometer ranges is not well understood.

As the metal particle size decreases and reaches the subnanometer regime, the fraction of under-coordinated sites increases significantly [13, 14]. Additionally, the electronic properties of subnanometer clusters are quite different from larger nanoparticles and are strongly affected by the interactions with the support [15, 16]. Different trends of activity and selectivity in the subnanometer regime has been reported in the case of alkenes / alkynes hydrogenation reactions. For example, Crampton et al. tested ethylene hydrogenation on MgO supported Pt clusters with 7 to 40 Pt atoms and reported that the catalyst with 13 Pt atoms (~0.8 nm) resulted in the highest activity [17]. In another study, Kuo et al. reported that the activity for acetylene hydrogenation on Pt/TiO_2 decreases as the particle size decreases from 2.1 nm all the way to single atoms, while the selectivity to ethylene increased from 50 to 100% [16]. Vajda et al. studied oxidative dehydrogenation of propane and reported that the activity and selectivity to propylene of Pt subnanometer clusters with more under-coordinated sites is much higher than Pt surface with more highly coordinated Pt sites. This was explained by the significant charge transfer from C–H bonds in propane to Pt subnanometer clusters that could efficiently weaken the C–H bond [18]. Argo et al. studied the size effect of alkenes hydrogenation on small Ir clusters and large Ir aggregates. The results show that the Ir_4 clusters on MgO are slightly more active than the Ir_6 clusters and Ir aggregates, while on γ-Al_2O_3 Ir_6 clusters are much less active than Ir_4 and Ir aggregates [19]. These reports show that it is still not clear how the size in the nanometer and subnanometer regimes influence the adsorption of the hydrocarbons, especially molecules as large as n-butane, and hence the activity and selectivity.

To investigate the structure sensitivity of n-butane hydrogenolysis on small nanoparticles and subnanometer clusters, we studied the activity and selectivity on Ir subnanometer clusters supported on $MgAl_2O_4$ and compared the results with nanoparticles. Because of the strong interfacial interaction between the facets of the $MgAl_2O_4$ spinel support and Ir that limits sintering [20], we were unable to prepare Ir nanoparticles larger than ~1.5 nm on $MgAl_2O_4$. Therefore, in addition to Ir/$MgAl_2O_4$ catalysts with varying average size below 1.3 nm, a series of SiO_2-supported Ir nanoparticles with larger particle sizes (1.4–2.9 nm) were also synthesized for comparison. The catalysts were characterized by high-angle annular dark-field (HAADF) aberration-corrected scanning transmission electron microscopy (STEM) and in-situ diffuse reflectance infrared Fourier transform spectroscopy (DRIFTS) of adsorbed CO. The results show that the selectivity to ethane is weakly dependent on particle sizes smaller than 1.4 nm and decreases with increasing particle size above 1.4 nm. On the other hand, ~1.4–1.6 nm nanoparticles were the most active while the activity was lower on the subnanometer clusters and larger nanoparticles. The reaction pathway of n-butane hydrogenolysis was analyzed based on the dependence of selectivity on temperature and conversion. The results indicate that the product distribution during hydrogenolysis of n-butane on these catalysts is dominated by the location of the initial C–C bond cleavage. The Ir particle size and to a lesser extent the reaction temperature controls the extent of central vs. terminal C–C bond cleavage in reactant n-butane and consequently the selectivity.

2.3 Experimental Methods

2.3.1 Synthesis and pretreatments

Three Ir/ $MgAl_2O_4$ catalysts with 1, 0.2, and 0.05 Ir weight % were prepared to achieve different Ir particle sizes between 0.7 and 1.3 nm (see results). The 1% Ir/ $MgAl_2O_4$ catalyst was synthesized by incipient wetness impregnation. The $MgAl_2O_4$ support (Puralox MG30, Sasol, calcined at 500 °C before use) was weighed and poured into a 250 mL Pyrex bottle. The iridium nitrate (aqueous solution, 8.7 wt. % Ir, Furuya Metal CO. Ltd.) precursor was diluted in deionized water to achieve 1% weight loading on the $MgAl_2O_4$ support. The diluted iridium nitrate solution was added to the support dropwise, then dried overnight in air at room temperature before reduction at 800 °C for 2 h (15 °C/min) in 50 kPa H_2 (99.999%, Airgas, with balance He, Airgas, 99.999%, equipped with high-capacity moisture and oxygen traps (Cat. # 21997 and Cat. # 20601, Restek), 100 sccm of total flow rate) in a tube furnace. Before the catalytic measurement, the catalyst was re-reduced at 800°C for 2 h (15 °C/min) in 20 kPa H_2 (balance He, 100 sccm of total flow rate).

The 0.2% Ir/ $MgAl_2O_4$ catalyst was synthesized by wet impregnation using $Ir(CO)_2(acac)$ (Sigma Aldrich) precursor dissolved in toluene (Sigma Aldrich). The precursor solution was added to the $MgAl_2O_4$ support (Puralox MG28, Sasol, calcined 500 °C before use) under N_2 flow to avoid exposure to air. The catalyst was then dried in flowing N_2 at room temperature under stirring (500 rpm) overnight to evaporate the solvent. The CO and acetylacetonate (acac) ligands were removed by treatment in 20 kPa H_2 (balance He, 100 sccm of total flow rate) at 500 °C for 2 h (10 °C/min). The reason for using a different Ir precursor for this catalyst is that it allowed us to minimize the interaction with the support and prepare ~1nm Ir nanoparticles with a narrow size distribution [21].

The 0.05% Ir/ $MgAl_2O_4$ was prepared by wet impregnation using iridium nitrate (aqueous solution, 8.7 wt% Ir, Furuya Metal Co. Ltd.) precursor. 200 mL deionized water was added into the 250 mL Pyrex bottle followed by the addition of iridium nitrate precursor diluted with appropriate amount of deionized water. The $MgAl_2O_4$ support (Puralox MG30, Sasol, calcined 500 °C before use) was then added to the solution under stirring. After 2 hours of stirring, the solution was filtered out and the solid sample was dried at room temperature in air overnight. The sample was dried at 80 °C and 100 °C (0.5 °C/min) before calcination in air at 500 °C for 4 h (5 °C/min). Finally, the sample was reduced in-situ in a flow of 20 kPa H_2 (balance He, 50 sccm of total flow rate) at 700 °C (10 °C/min) for 2 h. The Ir in the solution after filtration was measured by inductively coupled plasma-atomic emission spectroscopy (ICP-AES) on a Spectro ARCOS II Multi-View ICP Model FHM22 with CETAC Autosampler instrument and no Ir was detected. Details of all the Ir/$MgAl_2O_4$ catalysts synthesis and pretreatments are summarized in Supplementary Information Table S2.1.

As discussed in the introduction, due to the high metal support interaction between Ir and $MgAl_2O_4$, we were not able to synthesize Ir nanoparticles larger than ~1.5 nm on $MgAl_2O_4$. Instead, SiO_2 was chosen as support to synthesize larger Ir particles because of being inert (absence of acid sites). Three Ir/SiO_2 catalysts with different Ir particle sizes were prepared by incipient wetness impregnation. SiO_2 support (0.075–0.250 mm, 150 Å, Sigma Aldrich) was ground to fine powder and weighed in a 200 mL beaker. Appropriate amount of H_2IrCl_6 precursor (99.9%, Strem Chemicals) was dissolved in deionized water under ultrasonication. The diluted triethanolamine (TEOA, 98%, Sigma Aldrich) solution was injected into the precursor solution for ligand exchange with different ratios (TEOA : Ir=40, 20 and 10) without exposure to air. The precursor solution was then added to the SiO_2 support dropwise. After a day, the Ir/SiO_2 powder samples were heated at 120 °C for 12 h (1 °C/min) and another hour at 300 °C (1 °C/min) in 20 kPa O_2 (certified grade, Airgas, balance He, 50 total flow rate), then reduced at 400 °C for 3 h (2°C/min) in 50 kPa H_2 (99.999%, Airgas, balance He, 50 total flow rate) to remove the ligands before cooling down to room temperature. The He and H_2 gas was purified using high-capacity moisture and oxygen traps

(Cat. # 21997 and Cat. # 20601, Restek). Finally, the catalysts were passivated for 6 hours at 30 °C in 0.5 kPa O_2 (certified grade, Airgas, balance He, 100 sccm total flow rate) before exposure to air. Before characterization and catalytic measurements, the TEOA:Ir=40 and 20 Ir/SiO_2 catalysts were further oxidized at 300 °C for 1 h (5 °C/min) and reduced at 600 °C for 3 h (5 °C/min), while the TEOA:Ir=10 Ir/SiO_2 catalyst was oxidized at 400 °C for 1 h (5 °C/min) and reduced at 450 °C for 3 h (5 °C/min). Details of all the Ir/SiO_2 catalysts synthesis and pretreatments are summarized in Supplementary Information Table S2.1. The metal content of each sample was measured by inductively coupled plasma optical emission spectroscopy (ICP-OES) (Galbraith Laboratories, Inc.) and is listed in Supplementary Information Table S2.3.

2.3.2 Atomic resolution characterization (HAADF-STEM)

High-angle annular dark-field scanning transmission electron microscopy (HAADF-STEM) characterization for Ir/$MgAl_2O_4$ catalysts was conducted on an FEI TITAN 80–300 in STEM mode. The resolution is 0.1 nm, with the CEOS GmbH double-hexapole aberration corrector. The STEM characterization for Ir/SiO_2 catalysts was taken on JEOL JEM2100F transmission electron microscope. The particle size of all the catalysts was estimated based on horizontal line across the particle in multiple images (at least 7 images containing ~50-300 nanoparticles) by ImageJ, and the surface-average particle diameters were calculated using $d_{SA} = \frac{\sum n_i d_i^3}{\sum n_i d_i^2}$ [22], where n_i is the number of clusters with a diameter d_i. The total number of atoms per particle was estimated with the equation $N_T = \frac{\pi D^3 \rho N_A}{6 M_w}$ [23], where D is the nanoparticle diameter measured by STEM, ρ is the bulk density of Ir (22560 $kg \cdot m^{-3}$), N_A is Avogadro’s number (6.02×10^{23} mol^{-1}), and M_W is the molecular weight of Ir (0.192217 $kg \cdot mol^{-1}$). The particle size distribution shown in Supplementary

Information Figures S2.1 and S2.2 was calculated based on the percentage of atoms in each particle size range.

2.3.3 In-situ diffuse reflectance infrared Fourier transform spectroscopy (DRIFTS)

In-situ diffuse reflectance infrared Fourier transform spectroscopy (DRIFTS) experiments using CO chemisorption were performed using a Thermo Scientific IS-50R Fourier transform infrared spectrometer equipped with a mercury cadmium telluride (MCT-A) detector. The resolution for collecting the spectra was 4cm^{-1}. Each reported spectrum is an average of 32 scans and reported in Kubelka-Munk (K-M) units. Approximately 50 mg sample (25–90 µm diameter particles) was loaded in the Harrick Praying Mantis high temperature DRIFTS reaction chamber. All DRIFTS experiments were conducted at ambient pressure. The Ir catalysts were pretreated *in-situ* in the DRIFTS cell before collecting the spectra, and pretreatment details are summarized in Supplementary Information Table S2.1. After pretreatment, a spectrum under N_2 at 35 °C was collected as the background for each sample followed by flowing 1 kPa CO through the sample for 5 minutes then purged with pure N_2 to remove physisorbed CO while a series of spectra were collected every 20 s. Unless otherwise mentioned, the spectra recorded after 5 minutes of N_2 purge are reported. The N_2 gas was supplied from house-liquid N_2 boil-off and then further purified using high-capacity moisture and oxygen traps (Cat. # 21997 and Cat. # 20601, Restek). The CO (5% CO, balance N_2, certified grade, Airgas) gas line was equipped with a metal carbonyl purifier (Matheson, NanoChem Metal-X) to remove trace amount of metal carbonyls. The O_2 and moisture levels in the CO gas line were monitored using a mass spectrometer connected to the outlet of the DRIFTS cell and there was no measurable increase in the level of O_2 or H_2O (above baseline) when CO was turned on. All feed gas flows were controlled by mass flow controllers (5850EM, Brooks Instrument).

2.3.4 Volumetric CO chemisorption

The percentage of the exposed Ir sites was measured by volumetric CO chemisorption (Micromeritics 3Flex) using an adsorption stoichiometry of CO : Ir = 1. The Ir/$MgAl_2O_4$ samples were pressed and sieved into 425–710 μm particles. The Ir/SiO_2 samples were first diluted 5 times by weight with γ-Al_2O_3 as a binding agent and then pressed and sieved to 250–425 μm particles. 0.6 gram of Ir/$MgAl_2O_4$ samples and 0.5–0.8 gram of Ir/SiO_2 samples (after 5× dilution) were packed in a quartz U-tube and pretreated with the same procedure summarized in Supplementary Information Table S2.1. The total flow rate was 80 sccm for each step in the case of Ir/$MgAl_2O_4$ and 50 sccm in the case of Ir/SiO_2. After pretreatment, the samples were evacuated to 10^{-3} mmHg at 35 °C for 1 hour before CO (99.999%, Airgas) chemisorption analysis.

2.3.5 N-butane hydrogenolysis rate and selectivity measurements

The catalytic measurements were carried out in a packed-bed quartz tubular reactor (3/8 in. O.D. and 1/4 in. O.D. for integral measurements, i.e. selectivity versus conversion, and differential measurements in the kinetic regime, respectively). The reactor was placed in a heated furnace and the bed temperature was measured by a K-type thermocouple mounted on the outer wall of reactor with the tip at the catalytic bed center. The partial pressure of the reactants was controlled by individual mass flow controllers (Brooks mass flow controllers SLA5800 series) connected to n-C_4H_{10} (10%, balance He, certified standard, Airgas), pure H_2 (99.999%, Airgas) and He (Airgas, 99.999%, equipped with high-capacity moisture and oxygen traps (Cat. # 21997 and Cat. # 20601, Restek)). The composition of the effluent gases was measured by a gas chromatograph (Agilent

Micro GC 490) equipped with a TCD detector, with Mol Sieve 5A PLOT column and Pora PLOT U column to quantify H_2 and CH_4, respectively, and an Al_2O_3 column to quantify C_2H_6 and n-C_4H_{10}. Turn over frequency (TOF) was calculated by normalizing the reaction rate ($\mathrm{mol_{butane}\ g_{cat}^{-1}}$ $\mathrm{s^{-1}}$) to the number of Ir sites ($\mathrm{mol_{Ir}\ g_{cat}^{-1}}$, based on the quantity of CO adsorbed from volumetric CO chemisorption assuming a CO : Ir stoichiometry of 1), and all TOFs were measured in the kinetic regime (conversion < 3 %). The selectivity was calculated on mole- and carbon-basis (details in the Supplementary Information Table S2.4). The comparison of the activity trend on the whole series of catalysts has excluded the influence of transport limitations. The 0.05% Ir/$MgAl_2O_4$ was used without dilution. The 0.2% Ir/$MgAl_2O_4$ (~1.0nm) was tested without dilution and with 10 times dilution with SiO_2 and there was no difference in TOF. The 1% Ir/$MgAl_2O_4$ was diluted 20 times with SiO_2. The 1% Ir/SiO_2 (TEOA : Ir=40) (with the average particle size of 1.4 nm) was tested without dilution and with 20 times dilution with SiO_2 and there was no difference in TOF. Lastly, the 1% Ir/SiO_2 (TEOA : Ir=20 and 10) were used without dilution. Our calculations of the heat and mass transfer criterion show that the kinetic measurements were not affected by transport limitations (see SI for details).

2.4 Results

2.4.1 Atomic-resolution characterization

The Ir/$MgAl_2O_4$ and Ir/SiO_2 catalysts were characterized by scanning transmission electron microscopy (STEM) after reduction (pretreatment details in Supplementary Information Table S2.1) and representative images are shown in Figure 2.1. Despite the high calcination (500 °C) and reduction (700 °C) temperatures, the 0.05% Ir/$MgAl_2O_4$ catalyst (Figure 2.1-(a)) is mainly comprised of single atoms and subnanometer clusters, and the surface-average particle size is ~0.7

nm. The 0.2% Ir/$MgAl_2O_4$ catalyst (Figure 2.1-(b)) consists of subnanometer clusters and nanoparticles slightly larger than 1 nm, and the surface-average particle size is 1.0 nm. For the higher metal loading of 1%Ir/$MgAl_2O_4$ (Figure 2.1-(c)), the size was still limited to less than 2 nm after reduction at 800 °C without calcination, and the surface-average particle size is ~1.3 nm. The results are consistent with the ability of $MgAl_2O_4$ to stabilize Ir and Rh against sintering even at elevated temperatures [20, 21, 24]. We note that even though the 1%Ir/$MgAl_2O_4$ catalyst was reduced at the high temperature of 800 °C, the quantity of adsorbed CO was consistent with the size from STEM. Additionally, the quantity of adsorbed CO was similar to reduction at 500 °C. Therefore, the results suggest that strong-metal support interaction, i.e. encapsulation of Ir by $MgAl_2O_4$, should not be an issue for this catalyst.

For the series of catalysts supported on SiO_2, the estimated surface-average particle size of 1%Ir/SiO_2 (TEOA:Ir=40) (Figure 2.1-(d)) and 1% Ir/SiO_2 (TEOA:Ir=20) (Figure 2.1-(e)) catalysts is 1.4 and 1.6 nm, respectively. The surface-average particle diameter of 1% Ir/SiO_2 (TEOA:Ir=10) (Figure 2.1-(f)) catalyst is 2.9 nm, but the catalyst is mostly comprised of small particles with the average size of 1.4 nm and some larger 4–7 nm particles that constitute ~50% of atomic percentage as shown in Supplementary Information Figure S2.2-(c). The STEM results are summarized in Table 2.1, which lists the surface-average diameter for all the catalysts. In the following sections, the catalysts will be referred to by an abbreviation to depict the size of Ir as listed in Table 2.1.

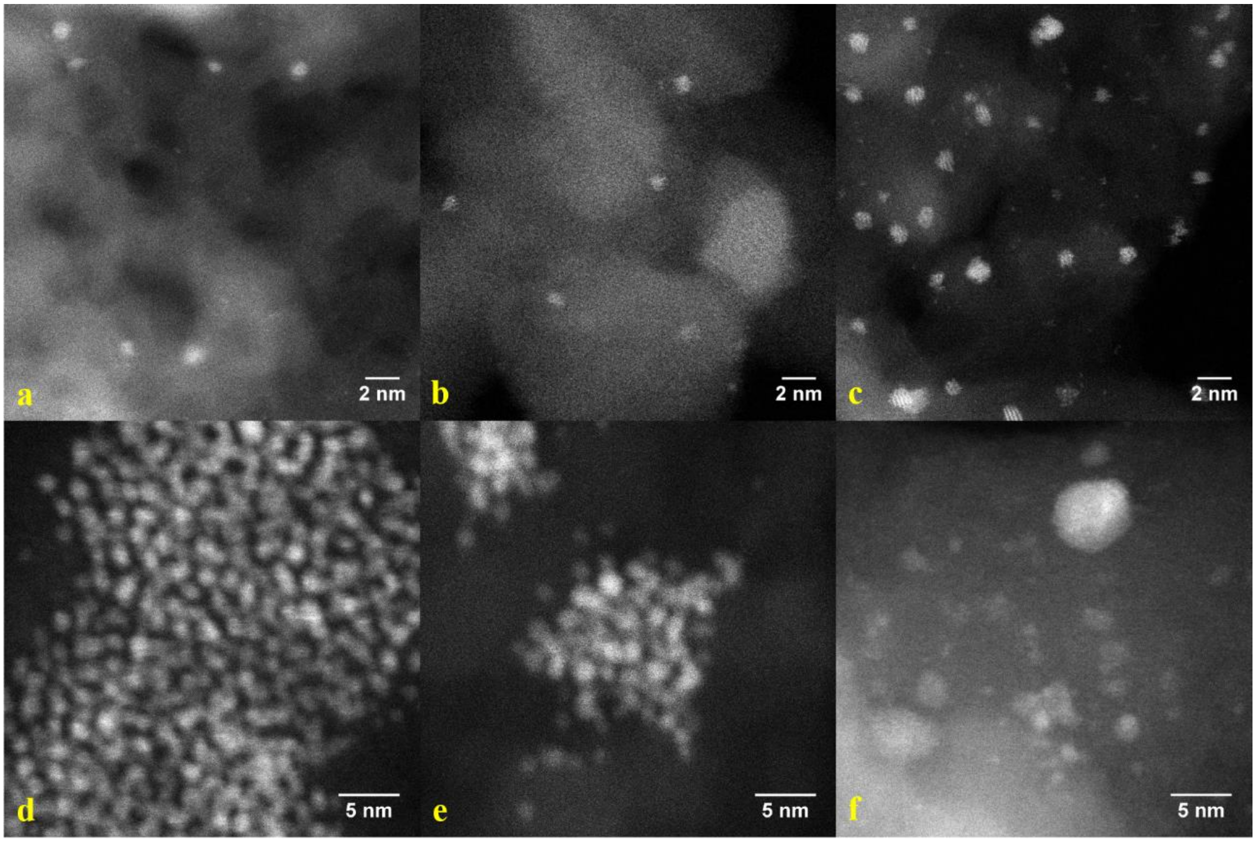

Figure 2.1 HAADF-STEM images of Ir/$MgAl_2O_4$ and Ir/SiO_2 catalysts with different particle size after pretreatment. (a) 0.05% Ir/$MgAl_2O_4$ ($Ir_{0.7nm}$) with average size of 0.7 nm, (b) 0.2%Ir/$MgAl_2O_4$ ($Ir_{1.0nm}$) with average size of 1 nm, (c) 1% Ir/$MgAl_2O_4$ ($Ir_{1.3nm}$) with average size of 1.3 nm, (d) 1% Ir/SiO_2 ($Ir_{1.4nm}$) with TEOA:Ir ratio of 40 and average size of 1.4 nm, (e) 1% Ir/SiO_2 ($Ir_{1.6nm}$) with TEOA:Ir ratio of 20 and average size of 1.6 nm, and (f) 1%Ir/SiO_2 ($Ir_{2.9nm}$) with TEOA:Ir ratio of 10 and average size of 2.9 nm.

Table 2.1 Average particle size of all the supported Ir catalysts used in the n-butane hydrogenolysis study from the analysis of STEM images.

Weight Loading	Support	Surface-average diameter (nm)	Abbreviation of Catalyst
0.05%	$MgAl_2O_4$	0.7 ± 0.2	$Ir_{0.7nm}/MgAl_2O_4$
0.2%	$MgAl_2O_4$	1.0 ± 0.2	$Ir_{1.0nm}/MgAl_2O_4$
1%	$MgAl_2O_4$	1.3 ± 0.24	$Ir_{1.3nm}/MgAl_2O_4$
1%	SiO_2	1.4 ± 0.22	$Ir_{1.4nm}/SiO_2$
1%	SiO_2	1.6 ± 0.32	$Ir_{1.6nm}/SiO_2$
1%	SiO_2	2.9 ± 0.8	$Ir_{2.9nm}/SiO_2$

2.4.2 In-situ DRIFTS characterization of CO adsorption

DRIFTS of adsorbed CO was used to characterize the surface Ir species of the supported Ir catalysts. The vibrational bands of linearly bound CO on Ir are typically located between 2030 and 2090 cm^{-1} for different Ir particle sizes and supports [15, 21, 23, 25-27]. The CO band for the $Ir/MgAl_2O_4$ catalysts with average particle size of 0.7, 1.0 and 1.3 nm was centered at 2033, 2034 and 2050 cm^{-1}, respectively, as shown in Figure 2.2-(a). The location of the CO band for $Ir_{0.7nm}/MgAl_2O_4$ and $Ir_{1.0nm}/MgAl_2O_4$ is similar. However, the band for $Ir_{0.7nm}/MgAl_2O_4$ is narrow indicating similar Ir sites, while the $Ir_{1.0nm}/MgAl_2O_4$ shows a broader band indicating the presence of different Ir sizes (with different distribution of sites). The results are consistent with the size distribution measured from the HAADF-STEM images (see Supplementary Information Figure S2.1. for detailed size distribution) which show that the $Ir_{0.7nm}/MgAl_2O_4$ consists of a more uniform size distribution around 0.7 nm while the $Ir_{1.0nm}/MgAl_2O_4$ shows a broader (relative to $Ir_{0.7nm}/MgAl_2O_4$) size distribution where subnanometer clusters and nanoparticles slightly larger than 1 nm co-exist. For the $Ir_{1.3nm}/MgAl_2O_4$ catalyst, the CO band is centered at 2050 cm^{-1} and is consistent with the larger Ir size compared to the other catalysts [23].

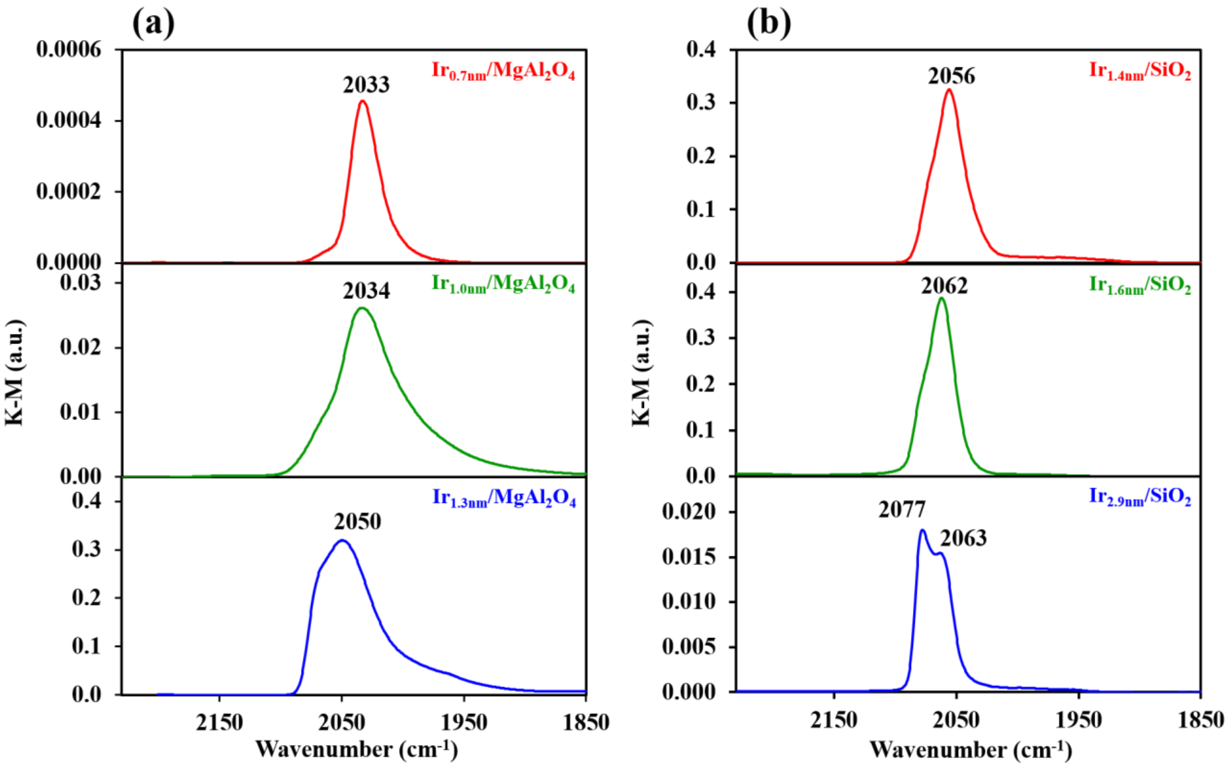

Figure 2.2 DRIFTS spectra of CO chemisorbed after 5 min exposure to 1 kPa CO at 35 °C on (a) $Ir/MgAl_2O_4$ catalysts ($Ir_{0.7nm}/MgAl_2O_4$, $Ir_{1.0nm}/MgAl_2O_4$ and $Ir_{1.3nm}/MgAl_2O_4$) and (b) 1% Ir/SiO_2 catalysts ($Ir_{1.4nm}/SiO_2$, $Ir_{1.6nm}/SiO_2$, and $Ir_{2.9nm}/SiO_2$).

On SiO_2, the linearly bound Ir-CO band on the $Ir_{1.4nm}/SiO_2$ catalyst is located at a slightly higher wavenumber position as the $Ir_{1.3nm}/MgAl_2O_4$ catalyst, at 2050cm^{-1}, which is consistent with their similar surface-average size. This is an important result as it shows that at this ~1.3–1.4 nm average particle size, the support has a small effect on the properties of Ir. While their surface-average size and Ir-CO peak position are similar, the differences in peak shape between the $Ir_{1.3nm}/MgAl_2O_4$ and the $Ir_{1.4nm}/SiO_2$ catalysts is likely due to the differences in size distribution where subnanometer clusters and single atoms contribute to the broader peak of the former (see a comparison of the peak widths in Table S2.3). This can have an effect on the activity and selectivity as shown below. On $Ir_{1.6nm}/SiO_2$, the main CO band shifts to higher wavenumber with a peak at 2062 cm^{-1} and a shoulder at 2077 cm^{-1} which can be assigned to under-coordinated and well-coordinated sites, respectively. Consistent with this assignment, the larger average size of the $Ir_{2.9nm}/SiO_2$ catalyst results in a much higher intensity of the CO band at 2077 cm^{-1} compared with the band at 2063 cm^{-1} due to the increased fraction of well-coordinated sites on the larger 4–7 nm nanoparticles [28]. The trend of increasing wavenumber of the CO band as the nanoparticle size increases is consistent with previous reports in the literature [29]. Deconvolution of the main CO band into two bands, one band representing CO adsorbed on well-coordinated (2074-2078 cm^{-1}) and a second for under-coordinated (2056-2062 cm^{-1}) Ir sites are also consistent with the size distribution from STEM for the $Ir_{1.4nm}/SiO_2$, $Ir_{1.6nm}/SiO_2$ and $Ir_{2.9nm}/SiO_2$ catalysts. The resolved DRIFTS spectra (Supplementary Information Figure S2.3) clearly show that the intensity ratio of the well-coordinated/under-coordinated Ir sites increases in the following order: $Ir_{1.4nm}/SiO_2$, < $Ir_{1.6nm}/SiO_2$ < $Ir_{2.9nm}/SiO_2$.

2.4.3 Structure sensitivity of n-butane hydrogenolysis

The $Ir/MgAl_2O_4$ and Ir/SiO_2 catalysts were tested for n-butane hydrogenolysis to study the structure sensitivity. Figure 2.3-(a) shows a comparison of the activity (TOF) and selectivity to ethane as a function of Ir particle size. The results show that the intermediate particle sizes of 1.4 and 1.6 nm on Ir/SiO_2 resulted in the highest activity while the activity drops as the particle size increases to 2.9 nm, or decreases to 0.7 nm. We acknowledge that the TOF trend in Figure 2.3-(a) can be dependent on how the activity is normalized, especially that smaller clusters and single atoms have a different CO:Ir stoichiometry. To determine if this affects the results, we normalized the activity (TOF) based on the dispersion from STEM instead of CO chemisorption and the trend was not strongly affected (Supplementary Information Figure S2.4). The results show that while the exact size for the maximum in TOF might change slightly, the trend in Figure 2.3-(a) does not seem to be strongly affected by the normalization method or by the overlap in size distribution between the catalysts. Additionally, the trend in TOF with Ir size was not affected by the H_2/C_4 ratio between 10-20 or temperatures form 170-190 °C. We note that the activity was lower on $Ir_{1.3nm}/MgAl_2O_4$ than on $Ir_{1.4nm}/SiO_2$. It is possible that the support (SiO_2 vs. $MgAl_2O_4$) affects the electronic properties of the 1–1.5 nm Ir nanoparticles in those catalysts. However, this effect is likely small since the main Ir-CO band was in a similar location on both catalysts as shown by the DRIFT spectra in Figure 2.2 (see also below for discussion on the catalyst selectivity). Interestingly, the difference between $Ir_{1.3nm}/MgAl_2O_4$ and $Ir_{1.4nm}/SiO_2$ becomes significantly smaller when the activity is normalized using dispersion calculated from STEM (Supplementary Information Figure S2.4). Therefore, the normalization method can partly explain the difference in TOF between the $Ir_{1.3nm}/MgAl_2O_4$ and $Ir_{1.4nm}/SiO_2$ catalysts. Additionally, the difference in the size distribution can also contribute to the lower activity on the $Ir_{1.3nm}/MgAl_2O_4$ since it shows a larger fraction of small clusters and single atoms which exhibit lower activity. In summary, the results show that while the differences in TOF between the catalysts might slightly change, the overall trend in TOF as a function of size in Figure 2.3-(a) does not seem to be strongly affected by the normalization method, by the overlap in size distributions of the different catalysts, or by the reaction conditions (within the partial pressures and temperatures tested in our work).

It is known that as the metal particle size decreases, the fraction of under-coordinated sites increases [13], and it is plausible that these under-coordinated sites (e.g. corner, edge atoms) are more active [1, 12], which can explain the increase in activity on Ir/SiO_2 with a decrease in Ir particle size from 2.9 to 1.4 nm. This trend on Ir/SiO_2 is also consistent with that for ethane hydrogenolysis on Pt/SBA-15 where the activity increased with a decrease in Pt particle size down to ~1 nm [30]. However, the reason for the decreasing activity trend in the subnanometer regime on Ir/$MgAl_2O_4$ is not clear. It is possible that a certain ensemble size is needed for alkane hydrogenolysis since the alkane molecule is more likely to bind with multiple metal sites before the cleavage of C–C bonds and adjacent sites are required for H adsorption [30]. Therefore, as the particle size decreases below a critical diameter having the optimum ensemble size, the activity for hydrogenolysis could drop significantly [31]. For example, Kawi et al. reported that the activity of propane hydrogenolysis on Ir_4/MgO is two orders of magnitude lower than that on large Ir particles (size was not reported) supported on MgO [32]. Additionally, while the activity trend on intermediate particle sizes was not reported, Flaherty et al. reported that for Ir/SiO_2, 0.7 nm nanoparticles were ~500x less active than 7 nm nanoparticles for hydrogenolysis of ethane [33]. There is no agreement in the literature on the minimum number of atoms required for alkane hydrogenolysis and whether it depends on alkane chain length [3, 30, 34, 35]. While the minimum ensemble size required for hydrogenolysis is not known, it likely consists of 4–8 atoms depending on the level of dehydrogenation required before the first C–C bond cleavage. Therefore, in the subnanometer regime, smaller Ir clusters with limited adjacent atoms can result in lower overall hydrogenolysis activity.

It is worth noting that there are conflicting literature reports for the effect of Ir size on hydrogenolysis activity. For example (not a comprehensive review), hydrogenolysis of n-butane and cyclopentane ring opening showed almost no dependence on Ir size [5, 36] while ethane and propane hydrogenolysis showed a decrease in activity with a decrease in size [32, 33]. On the other hand, hydrogenolysis of cyclohexane on Ir/SiO_2 with Ir dispersions between 0.01–0.65 exhibited a minimum TOF at Ir dispersion of ~0.4–0.5 [37]. We note that our reaction conditions are very different from those studies (lower temperature and atmospheric pressure vs. 250–300 °C and 0.5–1 MPa total pressure). We suspect that the different trends could be due to differences in the coverages of hydrogen and carbon species on Ir at those various conditions. However, our results were not sensitive to the range of experimental conditions we used and show that the activity increases with a decrease in Ir size until a maximum at ~1.4–1.6 nm, then the activity decreases on sizes below 1.4 nm and in the subnanometer regime.

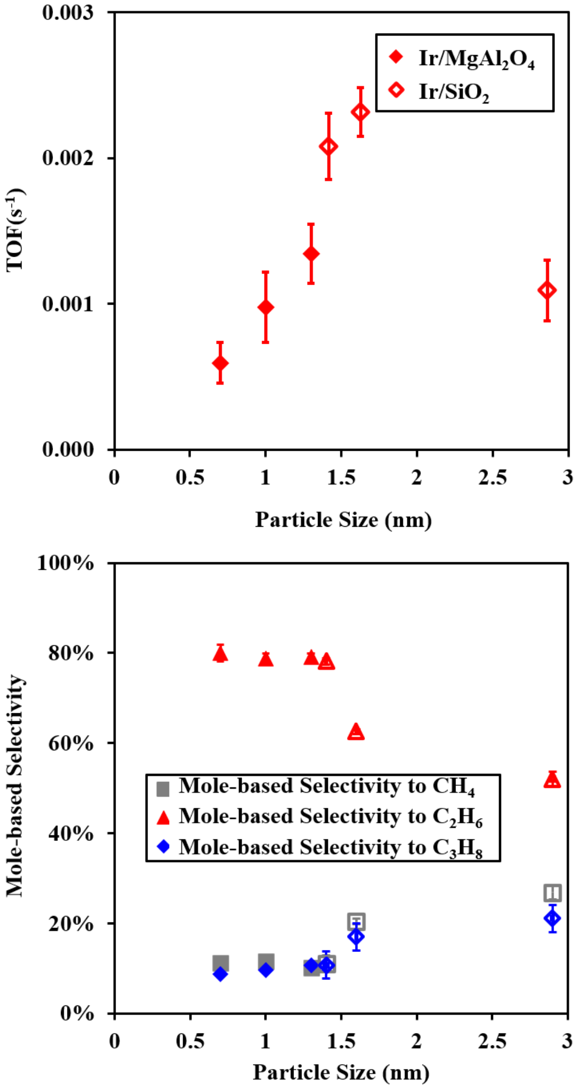

Figure 2.3 (a) Initial TOF (s^{-1}) and (b) mole-based selectivity (product distribution) to methane, ethane, and propane as a function of surface-average Ir particle size (nm) during n-butane hydrogenolysis on Ir/$MgAl_2O_4$ (solid) and Ir/SiO_2 (hollow). Reaction conditions: 10.13 kPa H_2 and 1.01 kPa n-C_4H_{10} at 170 °C and the conversion was 0.1–1%. The initial TOFs were measured within the first 10 minutes of time on stream. The error bars represent the standard deviation from averaging at least three experiments. The error bars for the selectivity are small and mostly covered by the data symbols in panel b.

The effect of size on mole-based selectivity (product distribution) to ethane at 170 °C is shown in Figure 2.3-(b) (the carbon-based selectivity is shown in Supplementary Information Figure S2.5 and the definitions for mole-based and carbon-based selectivity are listed in Supplementary Information Table S2.4). The selectivity to ethane was close to 80% (mole- and carbon-basis) and almost independent of size on the Ir/$MgAl_2O_4$ catalysts. Additionally, the selectivity to ethane was very close (~78 %) on the similar sized $Ir_{1.3nm}$/$MgAl_2O_4$ and $Ir_{1.4nm}$/SiO_2 catalysts as shown in Figure 2.3-(b). We note that while the presence of larger fraction of small clusters and single atoms on the $Ir_{1.3nm}$/$MgAl_2O_4$ compared with the $Ir_{1.4nm}$/SiO_2 catalyst is likely the reason for the difference in activity (Figure 2.3-(a) and discussion above), this had little effect on selectivity. The negligible effect on selectivity is consistent with the trend in Figure 2.3-(b) where the selectivity is almost independent of size below ~1.4 nm. Additionally, the similar selectivity on these two catalysts is consistent with the similar location of the linearly bound Ir-CO band as shown by the DRIFTS spectra in Figure 2.2, further indicating that the effect of support on Ir electronic properties in the 1–1.5 nm nanoparticles is not significant as discussed above. As the Ir size further increases above 1.4 nm, the selectivity to ethane decreases from 78% on $Ir_{1.4nm}$/SiO_2 to 52% on $Ir_{2.9nm}$/SiO_2 as seen in Figure 2.3-(b). Similar trend has been reported by Foger and Anderson [5] on Ir/SiO_2 with particle sizes ranging between 2 and 20 nm. They reported that the mole-based selectivity to ethane at 200 °C was ~73% on 2 nm nanoparticles then decreased to ~40% as the particle size increased to 7 nm and remained almost constant as the size further increased to 20 nm [5]. The higher selectivity on smaller particles was attributed to the increase in fraction of under-coordinated surface sites. Consistent with these results, later studies using Ir(111) and Ir (110)–(1×2) by Engstrom et al. [11, 12]. showed that the high selectivity to ethane originates from the increase in percentage of corner and edge sites as the size decreases.

2.4.4 Effect of Ir size on the reaction pathways

It is important to understand what controls the location of the C–C bond cleavage (i.e. terminal vs central) in n-butane and whether the propane and ethane products undergo further hydrogenolysis. The hydrogenolysis of n-butane is comprised of three parallel reaction pathways: central C–C bond cleavage, single terminal C–C bond cleavage, and the cleavage of two (two terminal or terminal and central) C–C bonds. Additionally, the propane and ethane products may undergo further hydrogenolysis to produce more methane, as shown in Scheme 2.1. The molar ratio of methane to propane was close to 1 at 170 °C (the ratio resulting from one terminal C–C bond scission of n-butane) for all the catalysts (Supplementary Information Figure S2.6, Table S2.5 and associated discussion). Additionally, the fragmentation factor [38, 39] which measures the number of fragmented molecules (shorter chain length products) per molecule of butane was ~2 for all the catalysts (Table S2.6 and associated discussion). The results indicate that the product distribution is dictated by the central and single terminal C–C bond cleavage of n-butane while further hydrogenolysis of propane and ethane was negligible at this low temperature with the conversion controlled below 1%. Therefore, in the case of negligible propane and ethane hydrogenolysis, the selectivity to the cleavage of the central C–C bond in n-butane becomes equivalent to the molar percentage of ethane in the products shown in Figure 2.3-(b). Similarly, the selectivity to the terminal C–C bond cleavage is equal to the addition of methane and propane. Figure 2.4 shows the selectivity to central and terminal C–C bond cleavage of butane at 170 °C, which shows that the difference in selectivity on the small and large particles due to the difference in their preference for cleaving the central or terminal C–C bond. Specifically, cleavage of the central C–C bond in n-butane is much more favored than the terminal C–C bond on the smaller sized Ir nanoparticles (<1.6 nm) and subnanometer clusters. In contrast, on the larger nanoparticles (2.9 nm) the selectivity to both central and terminal C–C bonds was almost equal.

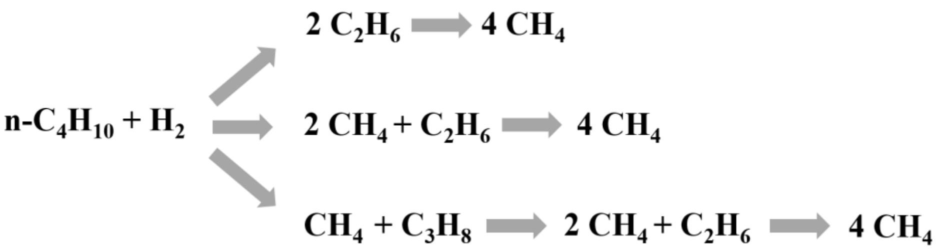

Scheme 2.1 Complete reaction pathway of n-butane hydrogenolysis. The n-butane molecules could be cleaved at the central C–C bond and one or two terminal C–C bond as initial parallel reaction pathways, and then the C_3 and C_2 products could be further cleaved as a series reaction pathway.

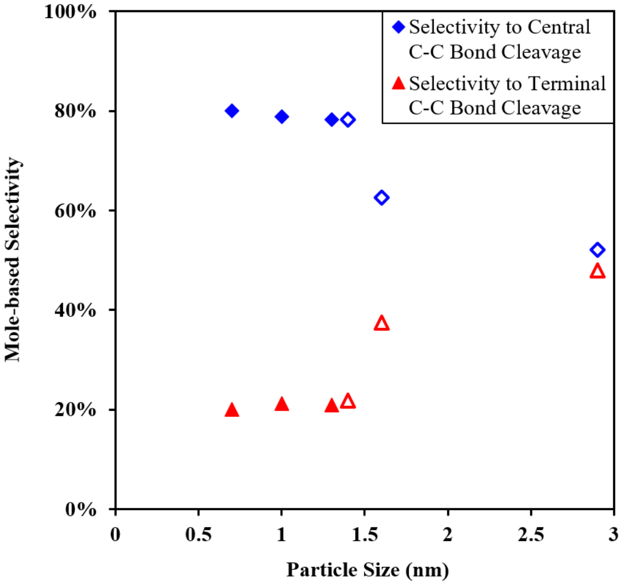

Figure 2.4 Mole-based selectivity to central C–C bond cleavage (blue diamonds) and terminal C–C bond cleavage (red triangles) during n-butane hydrogenolysis as a function of the surface-average Ir particle size (nm) on Ir/$MgAl_2O_4$ (solid) and Ir/SiO_2 (hollow). Reaction conditions: 10.13 kPa H_2 and 1.01 kPa n-C_4H_{10} at 170 °C and the conversion was 0.1–1%.

To provide insights on the selectivity towards central versus terminal C–C bond cleavage of n-butane as a function of Ir size, the hydrogenolysis of n-butane was measured at different temperatures. As shown in Figure 2.5, the effect of particle size on product distribution at all temperatures is similar to the results at 170 °C (Figure 2.4). Specifically, for smaller particle sizes (≤ 1.4 nm) the mole-based selectivity (carbon-based selectivity is shown in Supplementary Information Figure S2.7) is weakly dependent on size and all catalysts in this size range show high selectivity to ethane. However, as the temperature increases, a decrease in the selectivity to ethane can be observed on all the catalysts regardless of Ir size, although the extent of the decrease is slightly lower on the large nanoparticles ($Ir_{2.9nm}/SiO_2$). The decrease in selectivity to ethane at higher temperatures is accompanied by an increase in selectivity to methane and a slight decrease in selectivity to propane (more noticeable on the larger size, e.g. $Ir_{2.9nm}/SiO_2$), resulting in an increase in the C_1/C_3 molar ratio as shown in Supplementary Information Figure S2.8. At even a higher temperature of 300 °C, the selectivity to ethane decreased and that to methane increased on all sizes. However, the trend in selectivity with Ir size remained similar to that in Figure 2.4. Interestingly, at 300 °C the mole-based selectivity to ethane on small sized Ir catalysts, $Ir_{0.7nm}/MgAl_2O_4$ and $Ir_{1.3nm}/MgAl_2O_4$ was similar (56-58%) and much higher than the largest Ir nanoparticles, $Ir_{2.9nm}/SiO_2$ (5.4%) which produced mostly methane.

The lower selectivity to ethane and higher C_1/C_3 molar ratio at higher temperatures could be due to further hydrogenolysis of propane and ethane, i.e. the series reaction pathways in Scheme 2.1. However, it is known the rate of hydrogenolysis decreases as the alkane chain length decreases [3, 33]. Additionally, since the results in Figure 2.5 were collected in the kinetic regime (conversion <3%), the influence of series reaction pathway on the product distribution should be negligible given the lower reactivity of propane and ethane. To confirm this point, we measured the rate of ethane hydrogenolysis at 190 °C on the $Ir_{1.3nm}/MgAl_2O_4$ catalyst and it was ~15 times lower than that of butane (not shown). Furthermore, the fragmentation factor remained close to 2 under all conditions in Figures 2.4 and 2.5 (Table S2.6 and associated discussion). Therefore, the contribution of propane and ethane hydrogenolysis to the increase in methane selectivity is small under these reaction conditions. The results strongly suggest that the cleavage of two C–C bonds of n-butane ($C_4 \rightarrow 2C_1 + C_2$, see Scheme 2.1) is a third parallel pathway that contributes to the higher methane selectivity. We should emphasize that this parallel pathway ($C_4 \rightarrow 2C_1 + C_2$) does not have to be the result of simultaneous cleavage of two C–C bonds that would require the unfavorable binding of either 3 or 4 carbon atoms with the Ir surface [3, 33]. However, the second C–C bond needs to be cleaved before hydrogenation of the C_2/C_3 intermediate and its desorption as ethane/propane, otherwise it would be equivalent to the series pathways in Scheme 2.1, e.g. hydrogenolysis of butane to propane and methane, followed by re-adsorption and hydrogenolysis of propane. Consistent with this interpretation, increasing the H_2/C_4H_{10} ratio resulted in a lower C_1/C_3 molar ratio on the different catalysts, likely due to increased H_2 coverage which favors hydrogenation and desorption of the dehydrogenated intermediates after the first C–C cleavage (see Supplementary Information Table S2.7 and discussion in the Supplementary Information for the effect of H_2 partial pressure on selectivity for $Ir_{1.3nm}/MgAl_2O_4$). It is worth noting that the H_2/C_4

ratio between 10-20 did not affect the trend in selectivity shown in Figure 2.3-(b). However, further studies should be performed over a larger range of hydrogen partial pressures and temperatures to investigate the effect on the primary selectivities.

More importantly, in addition to n-butane hydrogenolysis proceeding via the three proposed parallel pathways in Scheme 2.1, the results indicate that they have different reaction barriers where the cleavage of two C–C bonds has the highest barrier followed by one terminal then central C–C bond. To summarize, the difference in selectivity to ethane between the catalysts is mainly due to the difference in the barriers between the parallel pathways in Scheme 1 rather than further hydrogenolysis of propane or ethane.

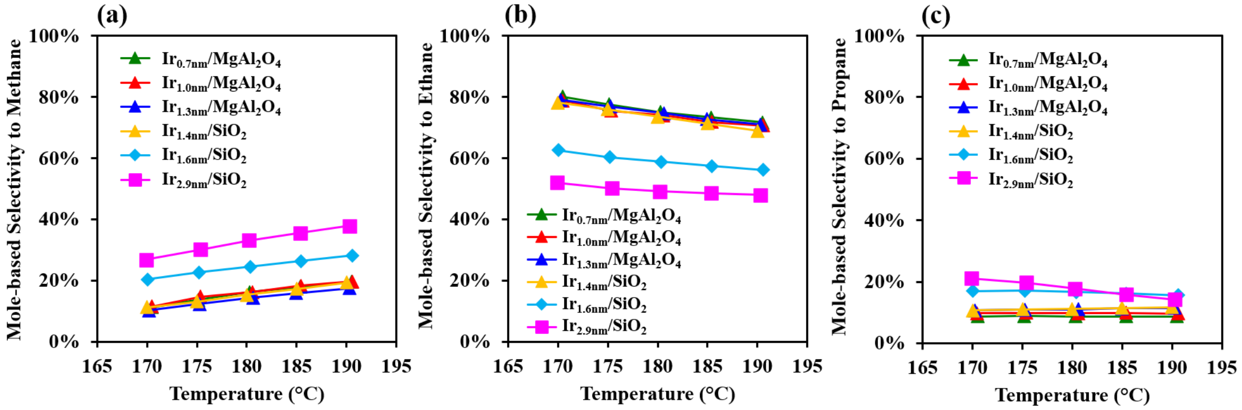

Figure 2.5 Mole-based selectivity (product distribution) to methane (a), ethane (b) and propane (c) as a function of temperature between 170 and 190 °C. Reaction conditions: 10.13 kPa H_2 and 1.01 kPa n-C_4H_{10} and the conversion was 0.1–3%.

To explore the effect of conversion on the selectivity and contribution from the series reaction pathways, the weight hourly space velocity (WHSV, $g_{n\text{-butane}}\cdot g_{cat}^{-1}\cdot h^{-1}$) was varied on $Ir_{1.3nm}/MgAl_2O_4$ and the results are shown in Figure 2.6 and Supplementary Information Figure

S2.9-(a) for mole- and carbon-based selectivity, respectively (similar trend was found on $Ir_{1.4nm}/SiO_2$, see Supplementary Information Figures S2.10-(a) and S2.10-(b)). As shown in Figure 2.6, over the entire conversion range (27 to 99%), the selectivity (mole- and carbon-based) to ethane was almost constant. Additionally, the selectivity to methane and propane were almost constant up to ~90% conversion. In fact, the C_1/C_3 molar ratio and fragmentation factor are weakly dependent on conversion in this range as shown in Supplementary Information Figures S2.9-(b) and Table S2.8. This is consistent with the lower reactivity of propane and ethane resulting in a negligible contribution of the series reaction pathways at low conversions as discussed above. The hydrogenolysis of propane starts to become important only after most of the n-butane has been converted and ethane hydrogenolysis is almost negligible until both n-butane and propane have been fully converted (see Supplementary Information Figures S2.11-(a) and S2.11-(b) and discussion in the Supplementary Information). Therefore, the results in Figure 2.6 further confirm that the selectivity on $Ir_{1.3nm}/MgAl_2O_4$ catalyst is controlled by the relative rates of the three parallel pathways in Scheme 2.1 and not by further hydrogenolysis of propane and ethane.

Furthermore, we note that the weak dependence of selectivity on n-butane conversion was also observed on all Ir sizes including subnanometer clusters ($Ir_{0.7nm}/MgAl_2O_4$) and larger nanoparticles ($Ir_{2.9nm}/SiO_2$) as shown in Supplementary Information Figures S2.12 and S2.13. The results indicate that the major reaction pathways for n-butane hydrogenolysis are very similar on the different sized Ir nanoparticles. On all the Ir catalysts, hydrogenolysis of n-butane proceeds mainly by the three parallel pathways in Scheme 2.1 while the series hydrogenolysis of propane and ethane affects the selectivity only at very high conversions. The difference in product distribution between different particle sizes originates from the effect of Ir size on the relative rates of the three parallel pathways in Scheme 1. Small nanoparticles ≤ 1.4 nm exhibit higher initial selectivity to central C–

C bond cleavage (higher rate relative to the other two pathways) resulting in higher selectivity to ethane compared to the large nanoparticles (2.9 nm).

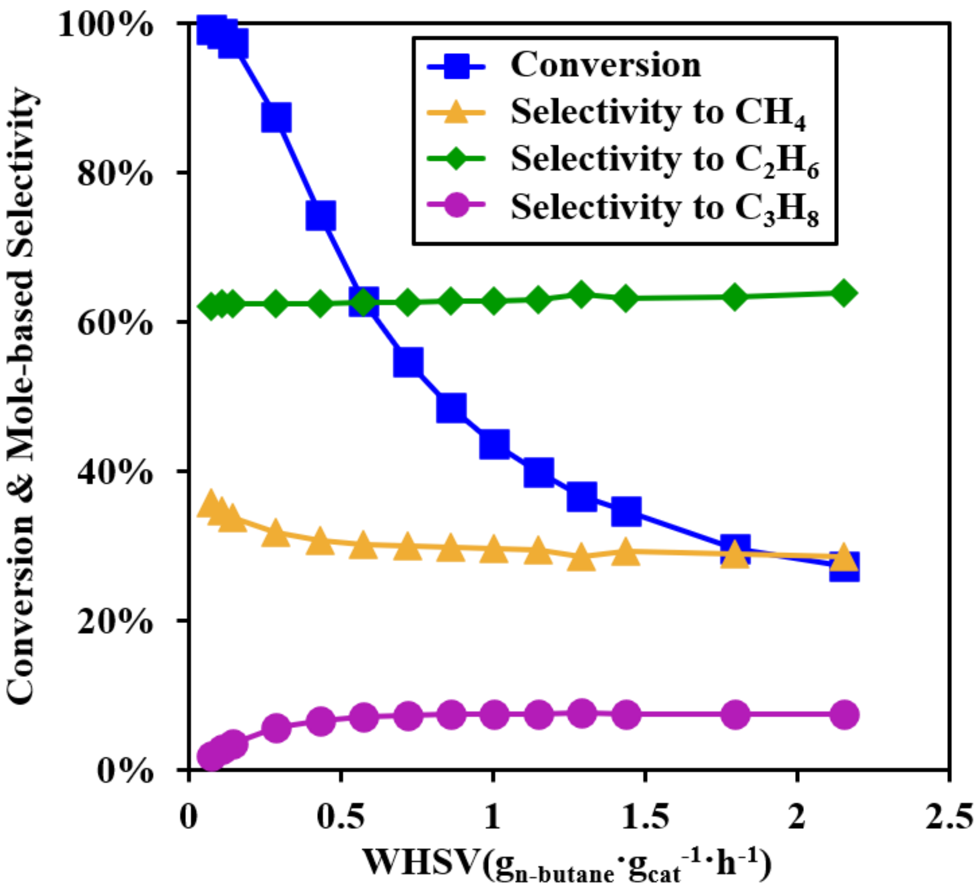

Figure 2.6 Effect of weight hourly space velocity (WHSV, $g_{n\text{-butane}}\cdot g_{cat}^{-1}\cdot h^{-1}$) on conversion (blue squares) and mole-based product distribution during n-C_4H_{10} hydrogenolysis on $Ir_{1.3nm}/MgAl_2O_4$. Reaction conditions: 10.13 kPa H_2 and 1.01 kPa n-C_4H_{10}, balance He at 190 °C. The WHSV was varied by adjusting the total gas flowrate. The fragmentation factor (ξ) at highest and lowest conversion is 2.41 and 2.24, respectively.

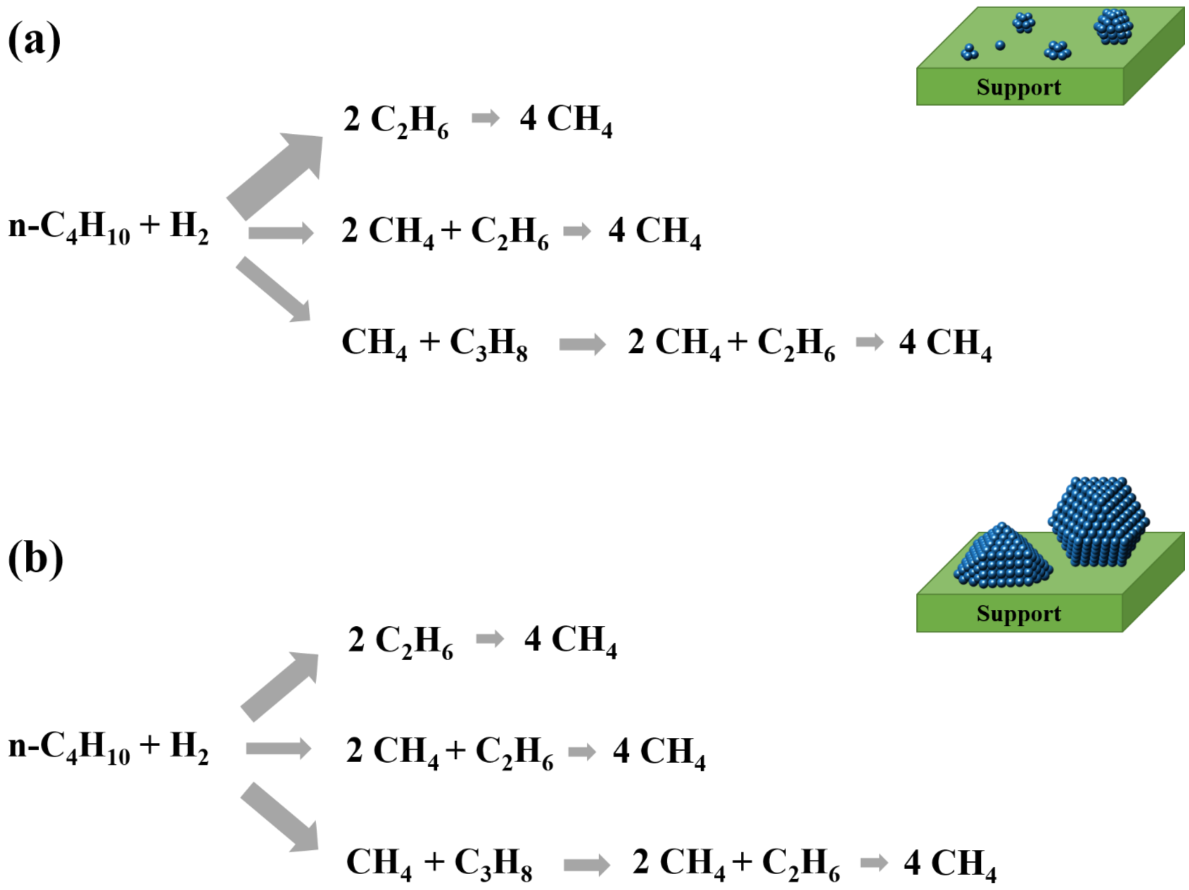

Scheme 2.2 Proposed reaction pathway of n-butane hydrogenolysis on subnanometer clusters and nanoparticles smaller than 1.4 nm (a) and nanoparticles larger than 1.4 nm (b), where the width of the arrow symbolically represents the favorability of the reaction pathway.

2.4 Discussion

The hydrogenolysis of n-butane on supported Ir is shown to be structure sensitive. The selectivity to ethane increases with a decrease in Ir nanoparticle size down to 1.4 nm then remains constant as the size further decreases to 1 nm and in the subnanometer regime (Figures 2.3-(b)). The product distribution as a function of conversion and temperature (Figures 2.5 and 2.6 and associated discussion above) clearly show that the selectivity is governed by the relative rates of the parallel pathways, i.e. cleavage of central vs. terminal vs. two C–C bonds, which depend on the size of Ir as shown in Scheme 2.2. On the other hand, the series reaction pathways, i.e. further hydrogenolysis of propane and ethane, start to have a significant effect on the selectivity only at high conversions due to their lower reactivity compared with n-butane. We propose that due to the lower reactivity of propane and ethane, the pathway involving cleavage of two C–C bonds in reactant n-butane is necessary to account for C_1/C_3 molar ratios higher than 1 especially in the lower conversion windows. A similar pathway was proposed for hydrogenolysis of propane on Ni/SiO_2 where the cleavage of two C–C bonds was required to explain the high C_1/C_2 ratio in the products [34]. This is consistent with ensemble theory, where large particles have large ensembles that favor multiple C-C cleavage [40, 41].

While two C–C bonds cleavage of n-butane is necessary to account for the observed product distribution (specifically $C_1/C_3 > 1$), the rate of this pathway is lower than the other two parallel pathways. For example, at low temperature of ~170 °C, the C_1/C_3 molar ratio was close to 1, which indicates a lower/negligible rate for the pathway with two C–C bond cleavage of n-butane ($C_4 \rightarrow 2C_1 + C_2$, see Scheme 2.2) compared to the cleavage of a single terminal or central C–C bond. Additionally, the significant increase in C_1/C_3 molar ratio at higher temperatures (Supplementary Information Figures S2.8 and S2.14) suggests a higher barrier for the $C_4 \rightarrow 2C_1 + C_2$ pathway than that for central or terminal C–C bond cleavage. This is consistent with DFT calculations on Ir(111) where the activation barrier of α,β-bound intermediates was lower than all others intermediates including those bound with 3 or 4 C atoms [42].

The cleavage of two C–C bonds, $C_4 \rightarrow 2C_1 + C_2$, is shown to be a minor pathway on all sizes, especially at low temperatures. Additionally, all the Ir catalysts had similar C_1/C_3 molar ratios making it difficult to determine how the Ir size affects the rate of this pathway relative to the cleavage of central and terminal C–C bonds. Therefore, for the purpose of discussing the effect of size on selectivity, we will neglect the $C_4 \rightarrow 2C_1 + C_2$ pathway and focus on the C–C cleavage of the central vs. terminal bonds in n-butane. On small Ir nanoparticles (≤ 1.4 nm) and subnanometer clusters, the cleavage of central C–C bond is favored with a selectivity of ~80% at 170 °C compared to ~50% on the large nanoparticles (Figure 2.4). This is even more pronounced at 300 °C where the larger nanoparticles ($Ir_{2.9nm}/SiO_2$) are much less selective than Ir subnanometer clusters and small nanoparticles ($Ir_{0.7nm}/MgAl_2O_4$ and $Ir_{1.3nm}/MgAl_2O_4$) to the central C–C bond cleavage (low ethane selectivity 5.4% vs. 56-58%, respectively). The results suggest that lower Ir nuclearity (increase in fraction of under-coordinated sites) plays a critical role in favoring a specific adsorption mode of the intermediates (e.g. $^2C–^2C$ vs. $^1C–^2C$) and could also lower the barrier for central C–C bond cleavage ($^2C–^2C$). However, there appears to be a limit as the size decreases to ~1.4 nm and smaller (in the subnanometer regime), where no further effect on selectivity was observed. This could be due to reaching the intrinsic reactivity of the under-coordinated sites where both adsorption modes co-exist ($^2C–^2C$ and $^1C–^2C$) and the selectivity is determined by the relative coverages and difference in the barriers for C–C bond cleavage. However, larger particles are more selective to the cleavage of the terminal C–C bond than small clusters. Therefore, we cannot rule out that a small fraction of large nanoparticles could contribute to higher selectivity to terminal C–C cleavage even as the average Ir size decreases.

In contrast to the selectivity to central C–C bond cleavage that increased with a decrease in Ir size and remained almost constant below 1.4 nm, the activity showed a maximum at a size of ~1.4–1.6 nm. Specifically, as the Ir average size decreased from 2.9 nm, the activity increased until ~1.4–1.6 nm and then decreased, albeit to a small extent, as the size decreased below ~1.4 nm. Hydrogenolysis of alkanes has been reported to require an ensemble of metal atoms, likely 4–8 metal atoms, but there is no agreement on the minimum number of atoms [30-32, 34, 35, 43-47].

The lack of large metal ensembles on the smaller size nanoparticles, and especially the subnanometer clusters is likely responsible for the lower hydrogenolysis activity. Our results are consistent with work by Kawi et al. where Ir_4/MgO was less active for hydrogenolysis of propane compared with large nanoparticles on the same support [32]. The lower activity could also be due to stronger interaction with the support that affects the Ir electronic properties as the Ir size decreases. We note that for sizes ~1–1.5 nm, our results show that the support does not appear to have a strong influence on the activity/selectivity. However, separating the effects of the support and metal nuclearity on the reactivity for butane hydrogenolysis in the subnanometer regime requires the synthesis of similar sized clusters on different supports. This work is currently in progress and will be published in due time. Our results show that on $MgAl_2O_4/SiO_2$ an optimum for Ir size of ~1.4 nm is needed to maximize both n-butane hydrogenolysis activity and selectivity to ethane (central C–C bond cleavage).

2.5 Conclusions

In this work, we investigated the structure sensitivity of n-butane hydrogenolysis on supported Ir catalysts with different particle sizes ranging between 0.7–2.9 nm. Our results show that the activity of n-butane hydrogenolysis slightly increases as the size increases from 0.7 nm to 1.4 nm and then decreases on larger sized nanoparticles. On the other hand, the product distribution is affected by particle size and temperature. The selectivity to ethane was weakly dependent on size between 0.7–1.4nm (~80% at 170 °C) and then decreased (to 50% at 170 °C) as the size increased to 2.9 nm. In the kinetic regime, the molar ratio of methane/propane was ~1, indicating that the location of the initial cleavage of C–C bond determines the product distribution. Therefore, the cleavage of central C–C bond is more favored on the subnanometer clusters and smaller sized nanoparticles (below ~1.4 nm), while on larger nanoparticles the cleavage of the central and terminal C–C bonds becomes competitive. The hydrogenolysis of propane and ethane was shown to proceed at very low rates and only become relevant at high conversions of n-butane where the effect was similar for all particle sizes of Ir. In addition to particle size, temperature had a strong effect on the product distribution. Increasing temperature resulted in a drop in selectivity to central C–C bond cleavage and a third parallel pathway consisting of two C–C bonds cleavage is shown to increase the selectivity to methane. Our results show that lower reaction temperature and Ir size of ~1.4 nm are optimum for activity and selectivity to ethane (central C–C bond cleavage).

Acknowledgement

This research was primarily sponsored by SABIC. STEM imaging was performed at the William R. Wiley Environmental Molecular Science Laboratory (EMSL) sponsored by the U.S. Department of Energy, office of Biological and Environmental Research located at Pacific Northwest National Laboratory (PNNL) under science theme proposal 49326. STEM images for Ir/SiO_2 were obtained at Colorado State University by Roy Geiss and with the assistance of Professor Richard G. Finke and his research group.

References

[1] D. Kalakkad, S.L. Anderson, A.D. Logan, J. Pena, E.J. Braunschweig, C.H.F. Peden, A.K. Datye, n-Butane hydrogenolysis as a probe of surface sites in rhodium metal particles: correlation with single crystals, The Journal of Physical Chemistry, 97 (1993) 1437-1444.

[2] G.C. Bond, J.C. Slaa, Catalytic and structural properties of ruthenium bimetallic catalysts: hydrogenolysis of propane and n-butane on RuAl2O3 catalysts modified by a Group 14 element, Journal of Molecular Catalysis A: Chemical, 106 (1996) 135-149.

[3] D.W. Flaherty, E. Iglesia, Transition-state enthalpy and entropy effects on reactivity and selectivity in hydrogenolysis of n-alkanes, J Am Chem Soc, 135 (2013) 18586-18599.

[4] G.C. Bond, Metal-catalysed reactions of hydrocarbons, Springer, 2005.

[5] K. Foger, J.R. Anderson, Hydrocarbon reactions on supported iridium catalysts, Journal of Catalysis, 59 (1979) 325-339.

[6] A.K. Datye, B.F. Hegarty, D.W. Goodman, Butane hydrogenolysis over single-crystal rhodium catalysts, Faraday discussions of the Chemical Society, 87 (1989) 337-344.

[7] D. Kalakkad, S.L. Anderson, A.K. Datye, The Effect of Rhodium Particle Size on n-BUTANE Hydrogenolysis Activity and Selectivity, in: Studies in Surface Science and Catalysis, Elsevier, 1993, pp. 2411-2414.

[8] G.C. Bond, X. Yide, Hydrogenolysis of alkanes. Part 1.—Hydrogenolysis of ethane, propane and n-butane on 6% Pt/SiO 2 (EUROPT-1), Journal of the Chemical Society, Faraday Transactions 1: Physical Chemistry in Condensed Phases, 80 (1984) 969-980.

[9] R.J. Lobo-Lapidus, B.C. Gates, Rhenium complexes and clusters supported on γ-Al2O3: Effects of rhenium oxidation state and rhenium cluster size on catalytic activity for n-butane hydrogenolysis, Journal of Catalysis, 268 (2009) 89-99.

[10] G.C. Bond, R.R. Rajaram, R. Burch, Hydrogenolysis of propane, n-butane, and isobutane over variously pretreated ruthenium/titanium dioxide catalysts, The Journal of Physical Chemistry, 90 (1986) 4877-4881.

[11] J.R. Engstrom, D.W. Goodman, W.H. Weinberg, Hydrogenolysis of ethane, propane, n-butane, and neopentane on the (111) and (110)-(1. times. 2) surfaces of iridium, Journal of the American Chemical Society, 110 (1988) 8305-8319.

[12] J.R. Engstrom, D.W. Goodman, W.H. Weinberg, Hydrogenolysis of n-butane over the (111) and (110)-(1. times. 2) surfaces of iridium: a direct correlation between catalytic selectivity and surface structure, Journal of the American Chemical Society, 108 (1986) 4653-4655.

[13] B.R. Cuenya, F. Behafarid, Nanocatalysis: size-and shape-dependent chemisorption and catalytic reactivity, Surface Science Reports, 70 (2015) 135-187.

[14] K. An, G.A. Somorjai, Size and shape control of metal nanoparticles for reaction selectivity in catalysis, ChemCatChem, 4 (2012) 1512-1524.

[15] J. Lu, P. Serna, B.C. Gates, Zeolite-and MgO-supported molecular iridium complexes: support and ligand effects in catalysis of ethene hydrogenation and H–D exchange in the conversion of H2+ D2, ACS Catalysis, 1 (2011) 1549-1561.

[16] C.-T. Kuo, Y. Lu, L. Kovarik, M.H. Engelhard, A.M. Karim, Structure Sensitivity of Acetylene Semi-Hydrogenation on Pt Single Atoms and Subnanometer Clusters, ACS Catalysis, (2019).

[17] A.S. Crampton, M.D. Rotzer, C.J. Ridge, F.F. Schweinberger, U. Heiz, B. Yoon, U. Landman, Structure sensitivity in the nonscalable regime explored via catalysed ethylene hydrogenation on supported platinum nanoclusters, Nat Commun, 7 (2016) 10389.

[18] S. Vajda, M.J. Pellin, J.P. Greeley, C.L. Marshall, L.A. Curtiss, G.A. Ballentine, J.W. Elam, S. Catillon-Mucherie, P.C. Redfern, F. Mehmood, P. Zapol, Subnanometre platinum clusters as highly active and selective catalysts for the oxidative dehydrogenation of propane, Nat Mater, 8 (2009) 213-216.

[19] A.M. Argo, J.F. Odzak, J.F. Goellner, F.S. Lai, F.S. Xiao, B.C. Gates, Catalysis by oxide-supported clusters of iridium and rhodium: Hydrogenation of ethene, propene, and toluene, The Journal of Physical Chemistry B, 110 (2006) 1775-1786.

[20] W.-Z. Li, L. Kovarik, D. Mei, M.H. Engelhard, F. Gao, J. Liu, Y. Wang, C.H.F. Peden, A General Mechanism for Stabilizing the Small Sizes of Precious Metal Nanoparticles on Oxide Supports, Chemistry of Materials, 26 (2014) 5475-5481.

[21] Y. Lu, J. Wang, L. Yu, L. Kovarik, X. Zhang, A.S. Hoffman, A. Gallo, S.R. Bare, D. Sokaras, T. Kroll, V. Dagle, H. Xin, A.M. Karim, Identification of the active complex for CO oxidation over single-atom Ir-on-$MgAl_2O_4$ catalysts, Nature Catalysis, 2 (2019) 149-156.

[22] J.M. Thomas, Handbook Of Heterogeneous Catalysis. 2., completely revised and enlarged Edition. Vol. 1–8. Edited by G. Ertl, H. Knözinger, F. Schüth, and J. Weitkamp, Angewandte Chemie International Edition, 48 (2009) 3390-3391.

[23] Y. Lu, C.-T. Kuo, L. Kovarik, A.S. Hoffman, A. Boubnov, D.M. Driscoll, J.R. Morris, S.R. Bare, A.M. Karim, A versatile approach for quantification of surface site fractions using reaction kinetics: The case of CO oxidation on supported Ir single atoms and nanoparticles, Journal of Catalysis, 378 (2019) 121-130.

[24] W.-Z. Li, L. Kovarik, D. Mei, J. Liu, Y. Wang, C.H.F. Peden, Stable platinum nanoparticles on specific MgAl2O4 spinel facets at high temperatures in oxidizing atmospheres, Nature Communications, 4 (2013).

[25] M. Mihaylov, E. Ivanova, F. Thibault-Starzyk, M. Daturi, L. Dimitrov, K. Hadjiivanov, New types of nonclassical iridium carbonyls formed in Ir-ZSM-5: a Fourier transform infrared spectroscopy investigation, The Journal of Physical Chemistry B, 110 (2006) 10383-10389.

[26] P. Gélin, A. Auroux, Y.B. Taarit, P.C. Gravelle, Infrared and calorimetric studies of the adsorption of carbon monoxide on zeolite-supported iridium catalysts, Applied Catalysis, 46 (1989) 227-240.

[27] F. Solymosi, E. Novak, A. Molnar, Infrared spectroscopic study on carbon monoxide-induced structural changes of iridium on an alumina support, Journal of physical chemistry, 94 (1990) 7250-7255.

[28] Y. Lu, C. Thompson, D. Kunwar, A. Datye, A.M. Karim, Origin of the high CO oxidation activity on CeO2 supported Pt nanoparticles: weaker binding of CO or facile oxygen transfer from the support?, ChemCatChem.

[29] M.J. Kale, P. Christopher, Utilizing Quantitative in Situ FTIR Spectroscopy To Identify Well-Coordinated Pt Atoms as the Active Site for CO Oxidation on Al2O3-Supported Pt Catalysts, ACS Catalysis, 6 (2016) 5599-5609.

[30] H. Song, R.M. Rioux, J.D. Hoefelmeyer, R. Komor, K. Niesz, M. Grass, P. Yang, G.A. Somorjai, Hydrothermal growth of mesoporous SBA-15 silica in the presence of PVP-stabilized Pt nanoparticles: synthesis, characterization, and catalytic properties, Journal of the American Chemical Society, 128 (2006) 3027-3037.

[31] G.A. Martin, A quantitative approach to the ensemble model of catalysis by metals, Catalysis Reviews Science and Engineering, 30 (1988) 519-562.

[32] S. Kawi, J.R. Chang, B.C. Gates, Cluster Catalysis: Propane Hydrogenolysis Catalyzed by MgO-Supported Tetrairidium, The Journal of Physical Chemistry, 98 (1994) 12978-12988.

[33] D.W. Flaherty, D.D. Hibbitts, E. Iglesia, Metal-catalyzed C–C bond cleavage in alkanes: effects of methyl substitution on transition-state structures and stability, Journal of the American Chemical Society, 136 (2014) 9664-9676.

[34] M.F. Guilleux, J.A. Dalmon, G.A. Martin, Mechanism and structure sensitivity of propane hydrogenolysis over Ni/SiO2 catalysts, Journal of Catalysis, 62 (1980) 235-242.

[35] M. Boudart, G. Djéga-Mariadassou, Kinetics of heterogeneous catalytic reactions, Princeton University Press, 2014.

[36] J. Barbier, COMPARATIVE STUDY OF" STRUCTURE SENSITIVE" REACTIONS ON PT-AL2O3 AND IR-AL2O3 CATALYSTS, (1981).

[37] H. Shi, X. Li, G.L. Haller, O.Y. Gutiérrez, J.A. Lercher, Active sites and reactive intermediates in the hydrogenolytic cleavage of C–C bonds in cyclohexane over supported iridium, Journal of catalysis, 295 (2012) 133-145.

[38] B. Coq, A. Bittar, F. Figueras, Hydrogenolysis and isomerization of alkanes on Ru/Al2O3 catalysis of varying dispersions, Applied Catalysis, 59 (1990) 103-121.

[39] Z. Paál, P. Tétényi, A new classification of metal catalysts in skeletal reactions of hydrocarbons, Nature, 267 (1977) 234-236.

[40] F. Locatelli, D. Uzio, G. Niccolai, J.M. Basset, J.P. Candy, Hydrogenolysis of 1, 4-dimethylcyclohexane on silica supported iridium catalyst: influence of time on stream on activity and selectivity, Catalysis Communications, 4 (2003) 189-194.

[41] J.A. Dalmon, G.A. Martin, Hydrogenolysis of C2H6, C3H8 and n-C4H10 over silica-supported nickel-copper catalysts, Journal of Catalysis, 66 (1980) 214-221.

[42] D.D. Hibbitts, D.W. Flaherty, E. Iglesia, Effects of Chain Length on the Mechanism and Rates of Metal-Catalyzed Hydrogenolysis of n-Alkanes, The Journal of Physical Chemistry C, 120 (2016) 8125-8138.

[43] H. Song, R.M. Rioux, J.D. Hoefelmeyer, R. Komor, K. Niesz, M. Grass, P.D. Yang, G.A. Somorjai, Hydrothermal growth of mesoporous SBA-15 silica in the presence of PVP-stabilized

Pt nanoparticles: Synthesis, characterization, and catalytic properties, Journal of the American Chemical Society, 128 (2006) 3027-3037.

[44] R.M. Rioux, H. Song, J.D. Hoefelmeyer, P. Yang, G.A. Somorjai, High-surface-area catalyst design: Synthesis, characterization, and reaction studies of platinum nanoparticles in mesoporous SBA-15 silica, Journal of Physical Chemistry B, 109 (2005) 2192-2202.

[45] P.S. Kirlin, B.C. Gates, Activation of the C-C bond provides a molecular basis for structure sensitivity in metal catalysis, Nature, 325 (1987) 38-40.

[46] N.R. Peela, J.E. Sutton, I.C. Lee, D.G. Vlachos, Microkinetic Modeling of Ethane Total Oxidation on Pt, Industrial & Engineering Chemistry Research, 53 (2014) 10051-10058.

[47] Y. Chen, D.G. Vlachos, Hydrogenation of Ethylene and Dehydrogenation and Hydrogenolysis of Ethane on Pt(111) and Pt(211): A Density Functional Theory Study, Journal of Physical Chemistry C, 114 (2010) 4973-4982.

Supplementary Information

Supplementary Table S2.1 Summary of pretreatment methods for Ir/$MgAl_2O_4$ and Ir/SiO_2 catalysts before catalytic, DRIFTS and CO chemisorption measurements.

Catalyst	Surface Average Particle Size, d_{SA}	TEOA : Ir	Oxidation	Reduction
0.05% Ir/$MgAl_2O_4$	0.7 nm	-	5%O_2, 100°C, 0.5 h, 400 °C, 1 h	20% H_2, 700 °C, 2 h
0.2% Ir/$MgAl_2O_4$	1.0 nm	-	-	20% H_2, 500 °C, 2 h
1% Ir/$MgAl_2O_4$	1.3 nm	-	-	20% H_2, 800 °C, 2 h
1% Ir/SiO_2	1.4 nm	40	20%O_2, 300 °C, 1 h	50% H_2, 600 °C, 3 h
1% Ir/SiO_2	1.6 nm	20	20%O_2, 300 °C, 1 h	50% H_2, 600 °C, 3 h
1% Ir/SiO_2	2.9 nm	10	20%O_2, 400 °C, 1 h	50% H_2, 450 °C, 3 h

For reduction at temperatures higher than 500 °C, the catalysts were first pretreated ex-situ in the reactor, then transferred into the IR chamber and reduced again at the maximum temperature (the maximum temperature in IR chamber is 500 °C).

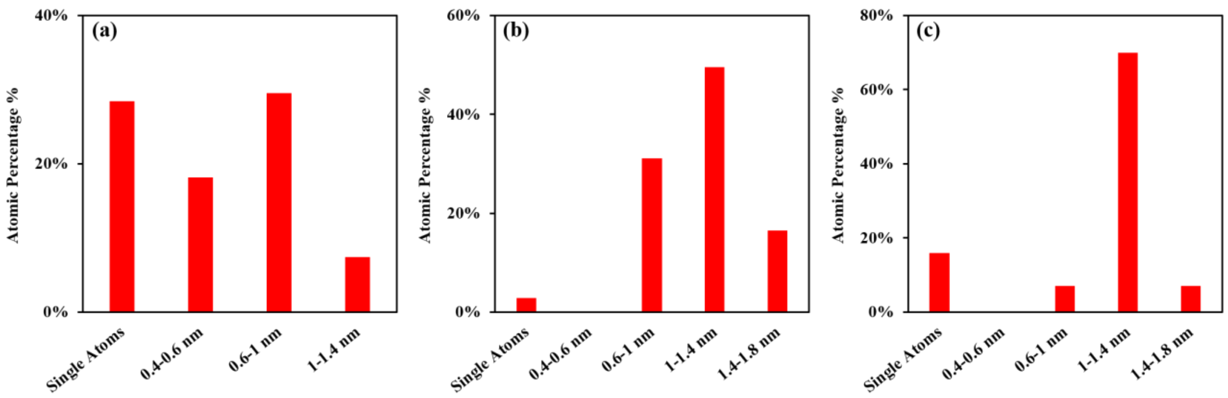

Supplementary Figure S2.1 Particle size distribution (atomic percentage calculated based on total atom number of each particle over total atom number of all the particles) for $Ir_{0.7nm}/MgAl_2O_4$ (0.05% $Ir/MgAl_2O_4$) catalyst with average particle size of 0.7 nm based on 422 single atoms and 50 nanoparticles (a), $Ir_{1nm}/MgAl_2O_4$ (0.2% $Ir/MgAl_2O_4$) catalyst with average particle size of 1 nm based on 55 single atoms and 59 nanoparticles (b) and $Ir_{1.3nm}/MgAl_2O_4$ (1% $Ir/MgAl_2O_4$) catalyst with average particle size of 1.3 nm based on 127 single atoms and 60 nanoparticles (c). The surface-average particle diameters were calculated by $<\boldsymbol{d_{TEM}}>=\frac{\sum \boldsymbol{n_i d_i^3}}{\sum \boldsymbol{n_i d_i^2}}$, where n_i is the number of clusters with a diameter d_i.

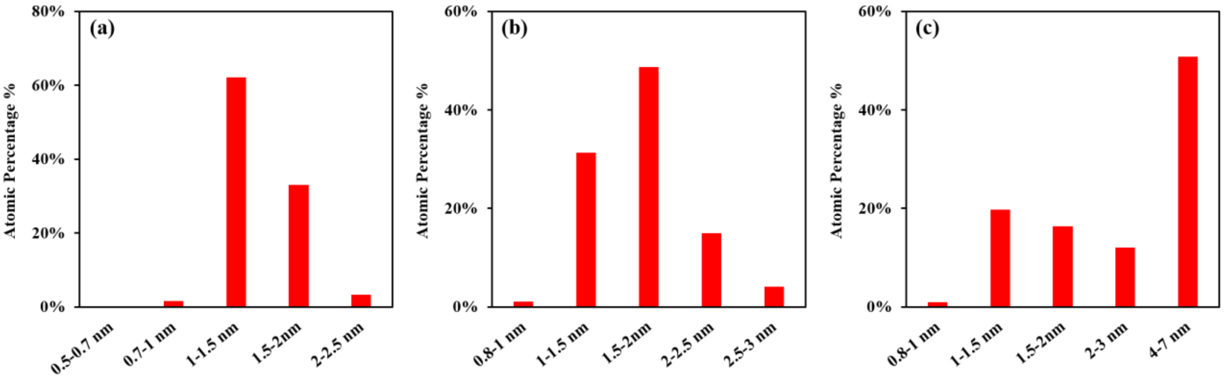

Supplementary Figure S2.2 Particle size distribution (atomic percentage calculated based on total atom number of each particle over total atom number of all the particles) for $Ir_{1.4nm}/SiO_2$ (1% Ir/SiO_2, TEOA:Ir=40) catalyst with average particle size of 1.4 nm based on 318 nanoparticles (a), $Ir_{1.6nm}/SiO_2$ (1% Ir/SiO_2, TEOA:Ir=20) catalyst with average particle size of 1.6 nm based on 317 nanoparticles (b) and $Ir_{2.9nm}/SiO_2$ (1% Ir/SiO_2, TEOA:Ir=10) catalyst with average particle size of 2.9 nm based on 153 nanoparticles (c). The surface-average particle diameters were calculated by $< \boldsymbol{d_{TEM}} >= \frac{\sum \boldsymbol{n_i d_i^3}}{\sum \boldsymbol{n_i d_i^2}}$, where n_i is the number of clusters with a diameter d_i.

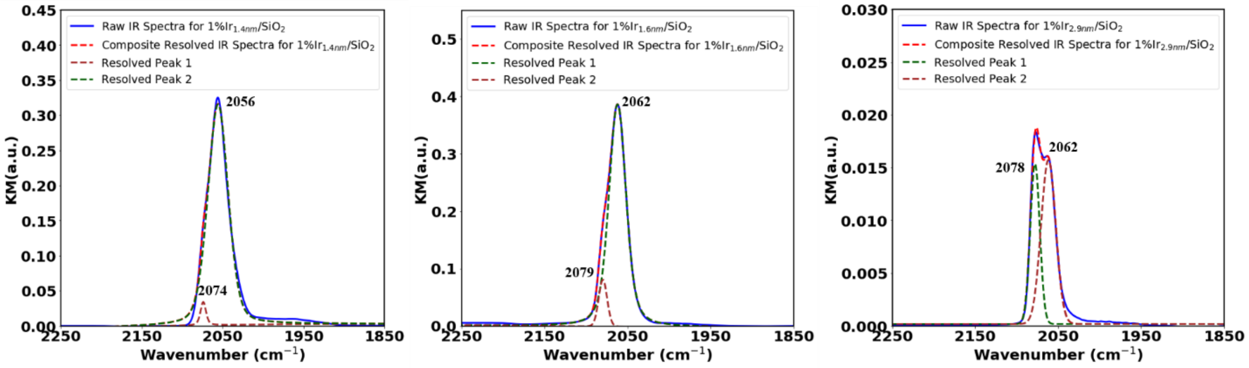

Supplementary Figure S2.3 Deconvolution of bands representing large and small sized nanoparticles for the IR spectrum of $Ir_{1.4nm}/SiO_2$, $Ir_{1.6nm}/SiO_2$ and $Ir_{2.9nm}/SiO_2$ catalysts.

Supplementary Table S2.2 FWHM (full width at half maximum) of DRIFT spectra for each catalyst.

Catalyst	FWHM (cm^{-1})
$Ir_{0.7nm}/MgAl_2O_4$	27
$Ir_{1.0nm}/MgAl_2O_4$	56
$Ir_{1.3nm}/MgAl_2O_4$	56
$Ir_{1.4nm}/SiO_2$	36
$Ir_{1.6nm}/SiO_2$	29
$Ir_{2.9nm}/SiO_2$	30

Supplementary Table S2.3 Summary of particle size from STEM and quantity of CO adsorbed from chemisorption on the $Ir/MgAl_2O_4$ and Ir/SiO_2 catalysts.

Weight loading	Weight loading from ICP	Catalyst	Surface-average diameter (nm)	Quantity of CO adsorbed (mmol/g)	CO/Ir (mol/mol) Chemisorption	Dispersion STEM*
0.05%	0.05%	$Ir_{0.7nm}/MgAl_2O_4$	0.7 ± 0.2	0.0023	0.88	0.96
0.2%	0.2%	$Ir_{1.0nm}/MgAl_2O_4$	1.0 ± 0.2	0.009	0.86	0.90
1%	-	$Ir_{1.3nm}/MgAl_2O_4$	1.3 ± 0.24	0.053	1.02	0.83
1%	0.9%	$Ir_{1.4nm}/SiO_2$	1.4 ± 0.22	0.026	0.55	0.75
1%	1.3%	$Ir_{1.6nm}/SiO_2$	1.6 ± 0.32	0.032	0.47	0.69
1%	1%	$Ir_{2.9nm}/SiO_2$	2.9 ± 0.8	0.013	0.25	0.37

***** dispersion calculated using the size distribution from STEM.

The quantity of CO adsorbed was measured by volumetric CO chemisorption, and the results are summarized in Supplementary Table S2.1. The particle size in the table is the surface-average particle size from STEM. Throughout this article, the turnover frequency (TOF) of reaction is calculated by the following equation with the assumption of a stoichiometry of CO : Ir of 1

$$\mathrm{TOF} = \frac{\text{Molar flow rate of } C_4H_{10} \times \text{Conversion}}{\text{Total amount of catalyst } \times \text{quantity of CO adsorbed}}$$

The surface-average size of $Ir_{1.3nm}/MgAl_2O_4$ and $Ir_{1.4nm}/SiO_2$ catalyst is very close, but the difference in CO dispersion on Ir is large from the CO chemisorption measurement. To unveil the difference in CO dispersion, an analysis based on the particle size distribution obtained by STEM was also conducted. Details of the estimation method was previously published [1]. In general, the number of surface atoms (based on hemispherical model) and total atoms for all the particles obtained from STEM, and the dispersion is estimated by the number of surface atoms over total atoms. The TOF can be calculated as

$$\mathrm{TOF} = \frac{\text{Mole Flow Rate of } C_4H_{10} \times \text{Conversion}}{\frac{\text{Total Amount of Catalyst } \times \text{Weight Loading}}{\text{Molecular Weight of Ir}} \times \text{Dispersion}}$$

After normalizing the TOF with the dispersion from STEM, the activity trend does not change much as shown by the comparison of TOF in Supplementary Figure S2.4, and the optimal TOF is still on $Ir_{1.6nm}/SiO_2$ catalyst.

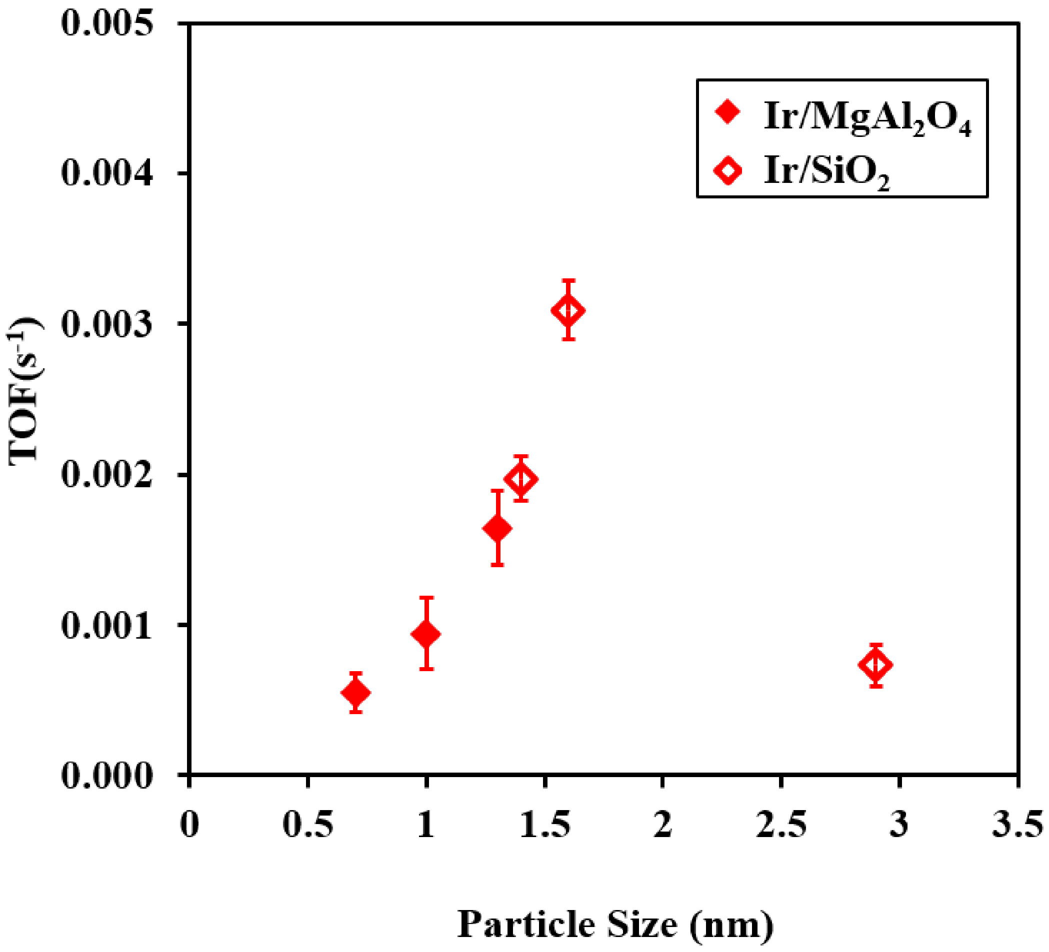

Supplementary Figure S2.4 TOF (s^{-1}) normalized by the dispersion from STEM with consideration of single atoms and as a function of surface-average Ir particle size (nm) during n-butane hydrogenolysis on Ir/$MgAl_2O_4$ (solid) and Ir/SiO_2 (hollow) as a comparison with the normalization method by CO chemisorption in Figure 2.3-(a). Reaction conditions: 10.13 kPa H_2 and 1.01 kPa n-C_4H_{10} at 170 °C and the conversion was 0.1–1%. Details of the calculation for dispersion from STEM were previously published [1].

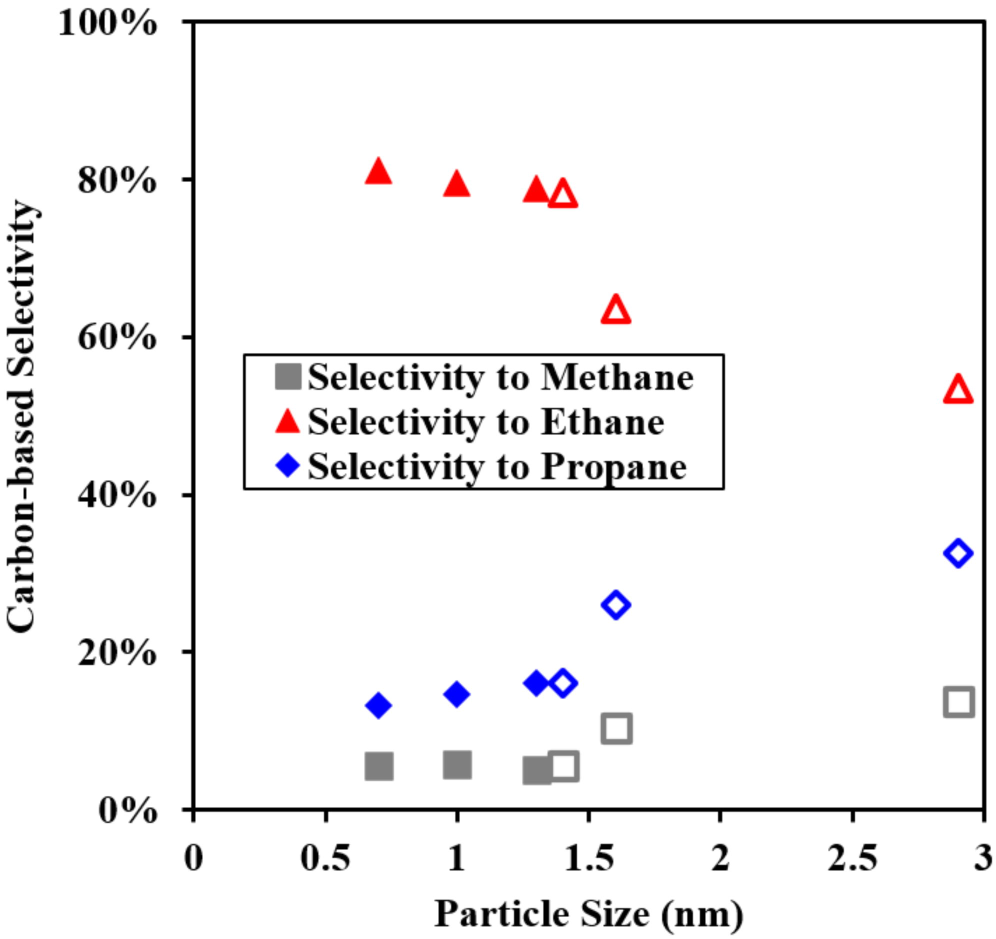

Supplementary Figure S2.5 Carbon-based selectivity to methane (gray squares), ethane (blue diamonds) and propane (red triangles) of n-butane hydrogenolysis as a function of the average Ir particle size (nm) on Ir/$MgAl_2O_4$ (solid) and Ir/SiO_2 (hollow). Reaction conditions: 10.13 kPa H_2 and 1.01 kPa n-C_4H_{10} at 170 °C, the conversion was 0.1–1%.

Supplementary Table S2.4 Equations for calculation of carbon-based selectivity and mole-based product distribution of n-butane hydrogenolysis using effluent moles of methane, ethane and propane.

	Methane	Ethane	Propane
Carbon-based selectivity	$\frac{CH_4}{CH_4 + 2C_2H_6 + 3C_3H_8}$	$\frac{2C_2H_6}{CH_4 + 2C_2H_6 + 3C_3H_8}$	$\frac{3C_3H_8}{CH_4 + 2C_2H_6 + 3C_3H_8}$
Mole-based selectivity (product distribution)	$\frac{CH_4}{CH_4 + C_2H_6 + C_3H_8}$	$\frac{C_2H_6}{CH_4 + C_2H_6 + C_3H_8}$	$\frac{C_3H_8}{CH_4 + C_2H_6 + C_3H_8}$

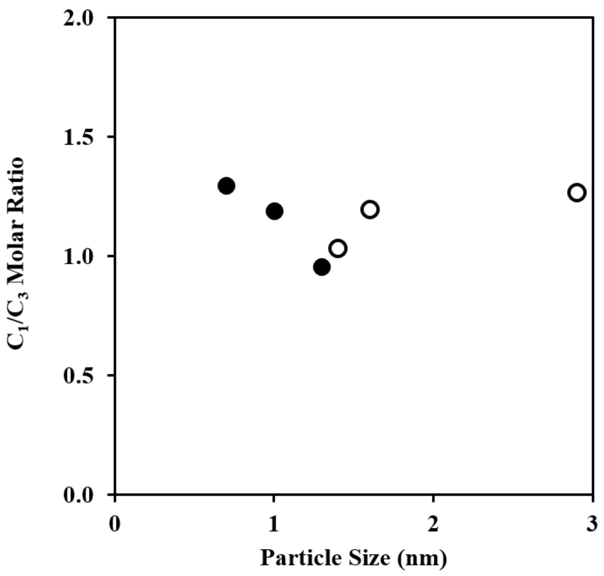

Supplementary Figure S2.6 The molar ratio of methane to propane in the products as a function of the average Ir particle size (nm) on Ir/$MgAl_2O_4$ (solid) and Ir/SiO_2 (hollow). Reaction conditions: 10.13 kPa H_2 and 1.01 kPa n-C_4H_{10} at 170 °C, the conversion was 0.1–1%.

From Supplementary Figure S2.6, the molar ratio of methane to propane on $Ir_{0.7nm}$/$MgAl_2O_4$, is about 1.3 at 170 °C, which is the highest. We can correct the molar ratio to 1 by assuming that the additional methane is coming from either the series reaction pathway of $C_3H_8 \rightarrow CH_4 + C_2H_6$ or the 3rd parallel pathway of two C–C bond cleavage and then do the calculation again. The corrected result of selectivity to central C–C bond cleavage is ~80% comparing with 79.8% without correction for both cases (the 3rd pathway takes only 2% from the pathway of one terminal C–C bond cleavage). Therefore, the extent of series reaction pathway and the products coming from the 3rd parallel pathway (two C–C bond cleavage) should be very limited at such conditions. The selectivity to central and terminal C–C bond cleavage shown in Figure 2.4 (main text) is accurate and minimally affected by other possible pathways. The size effect on ethane selectivity at 170 °C is indeed coming from the difference in initial extent of parallel reaction pathway.

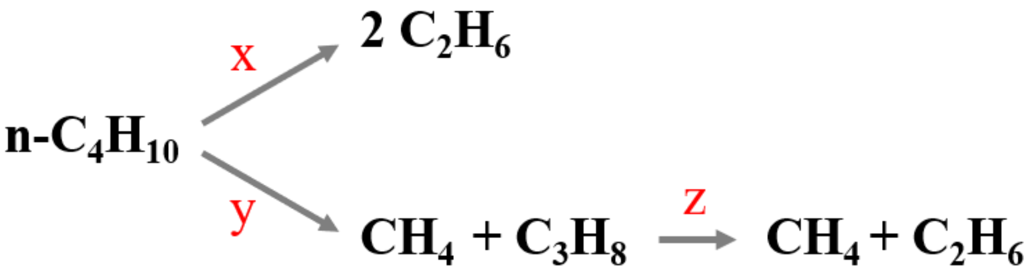

Supplementary Scheme S2.1 The reaction pathway excluding ethane hydrogenolysis and two C–C cleavage of butane.

In Supplementary Scheme S2.1, we assume x and y are moles of n-butane reacted by central and terminal C–C bond cleavage, z is the percentage of C_3 further reacted to produce C_1 and C_2. By fitting the mole-based selectivity from experiment, the x, y, and z could be calculated (x and y are normalized to display the mole-based selectivity to central and terminal C–C bond cleavage by x% and y%, while z represents the conversion of C_3). If we take $Ir_{1.3nm}/MgAl_2O_4$ catalyst as an example, at 190°C, the estimated conversion of C_3 (z) is 20.7%, which is much higher than the conversion of C_3 (1.1%) at this condition. This is contradictory to the higher reactivity of C_4 than C_3. The z calculated at 170°C is slightly negative, as the estimated C_1/C_3 molar ratio is ~0.96. The error of C_1/C_3 molar ratio is relatively large at very low conversion, since the selectivity to terminal C–C bond cleavage is very low and thereby very small concentration of methane and propane measured by the GC.

Supplementary Table S2.5 The results of x%, y% and z (mole-based selectivity to by central and terminal C–C bond cleavage and C_3 conversion) on $Ir_{1.3nm}/MgAl_2O_4$ catalyst when the reaction was assumed to proceed by the pathway in Supplementary Scheme 2.1.

Temperature (°C)	Conversion	x%	y%	z
170	0.3%	79.1%	20.9%	-2.2%
175	0.5%	76.7%	23.3%	5.8%
180	0.7%	74.2%	25.8%	13.1%
185	0.8%	72.1%	27.9%	16.5%
190	1.1%	70.1%	29.9%	20.7%

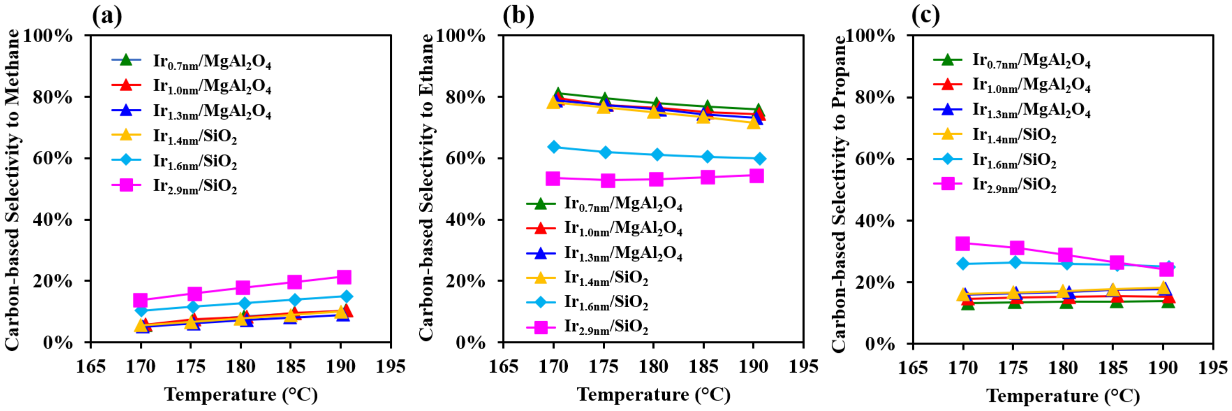

Supplementary Figure S2.7 Carbon-based selectivity to methane (a), ethane (b) and propane (c) on $Ir/MgAl_2O_4$ and Ir/SiO_2 between 170 and 190 °C. Reaction conditions: 10.13 kPa H_2 and 1.01 kPa $n\text{-}C_4H_{10}$ and the conversion was 0.1–3%.

Supplementary Table S2.6 Fragmentation factor (ξ) calculated for each catalyst between 170 - 190 °C shown in Figure 2.5 in the main text. As the temperature increases the fragmentation factor for each catalyst increases, indicating a deeper hydrogenolysis.

ξ at Temperature	**Ir$_{0.7nm}$**	**Ir$_{1.0nm}$**	**Ir$_{1.3nm}$**	**Ir$_{1.4nm}$**	**Ir$_{1.6nm}$**	**Ir$_{2.9nm}$**
170 °C	2.03	2.02	2.00	2.01	2.03	2.06
175 °C	2.05	2.05	2.01	2.02	2.06	2.11
180 °C	2.08	2.07	2.03	2.04	2.08	2.17
185 °C	2.10	2.09	2.05	2.06	2.11	2.22
190 °C	2.11	2.10	2.06	2.08	2.13	2.27

To simplify the comparison of C–C ruptures on different catalysts, we calculated the fragmentation factor which is a measure for the depth of hydrogenolysis. It is defined as the number of fragmented molecules (shorter chain length products) per molecule of the alkane as reactant [2], and the calculation follows the equation

$$\xi = \frac{\sum_{i}^{n-1} C_i}{\sum_{i}^{n-1} \frac{i}{n} C_i}$$

From Table S2.6, at 170 °C, the difference in fragmentation factor is very small. As the temperature increases from 170 °C to 190 °C, the fragmentation factor keeps increasing, even though the temperature window is small, the trend is still clear. The fragmentation factor trend as a function of temperature is consistent with that reported in the literature. For the case of hydrogenolysis of n-hexane, higher temperature favors multiple C–C ruptures rather than single C–C [3]. When the

WHSV effect was measured at high conversion range, the fragmentation factor for $Ir_{1.3nm}/MgAl_2O_4$ and $Ir_{1.4nm}/SiO_2$ catalysts at 190 °C was 2.1–2.4 between 20%-100% conversion as shown in Supplementary Table S2.8 and Table S2.9. Similarly, for $Ir_{2.9nm}/SiO_2$ the fragmentation factor increases with increase in conversion at 220 °C (Table S2.11). The results show that at the same temperature, larger Ir size and higher conversion favor deeper hydrogenolysis. Additionally, higher temperatures favor deeper hydrogenolysis on all Ir sizes.

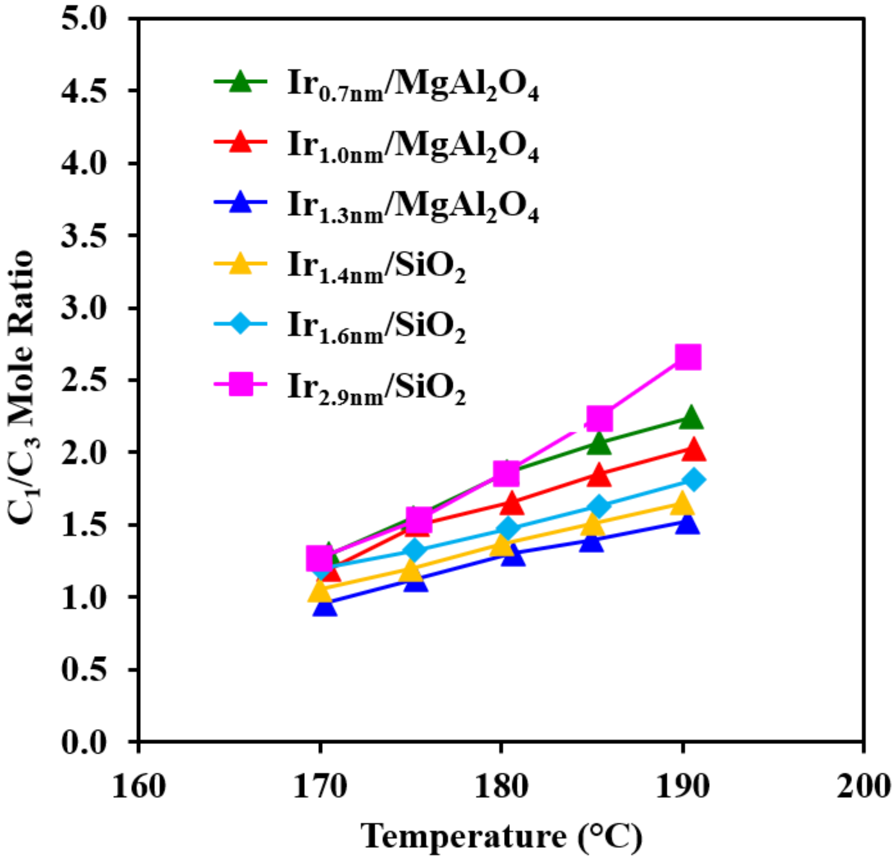

Supplementary Figure S2.8 Molar ratio of methane to propane in the products as a function of temperature between 170 and 190 °C. Reaction conditions: 10.13 kPa H_2 and 1.01 kPa $n\text{-}C_4H_{10}$ and the conversion was 0.1–3%.

Experiments at higher H_2/C_4H_{10} ratio on $Ir_{1.3nm}/MgAl_2O_4$ catalyst result in lower hydrogenolysis reaction rate and lower C_1/C_3 molar ratio (Supplementary Table S2.7). Since the hydrogenolysis of propane and ethane is very limited under these conditions, the higher H_2 partial pressure likely results in a higher H_2 coverage on the Ir surface which favors hydrogenation and desorption of the intermediate products from the first C–C bond cleavage instead of undergoing further dehydrogenation and C–C cleavage. A higher H_2 partial pressure (and H_2 coverage) could also make the adsorption of more than two carbon atoms in n-butane less favorable.

Supplementary Table S2.7 A summary of H_2 effect on the conversion and C_1/C_3 molar ratio on $Ir_{1.3nm}/MgAl_2O_4$ catalyst by changing the H_2 partial pressure from 35.5 to 60.8 kPa at fixed 1.01 kPa n-C_4H_{10} at 160 °C.

H_2/n-C_4H_{10} Molar Ratio	Conversion	C_1/C_3 Molar Ratio	Mole-based Selectivity to C_2H_6
20	16.7%	2	75.5%
25	11.1%	1.8	76.2%
30	7.6%	1.7	76.7%
35	5.3%	1.9	77.3%
40	3.8%	1.8	77.8%
45	2.8%	1.7	78.2%
50	2.1%	1.6	78.8%
60	1.3%	1.3	80.2%

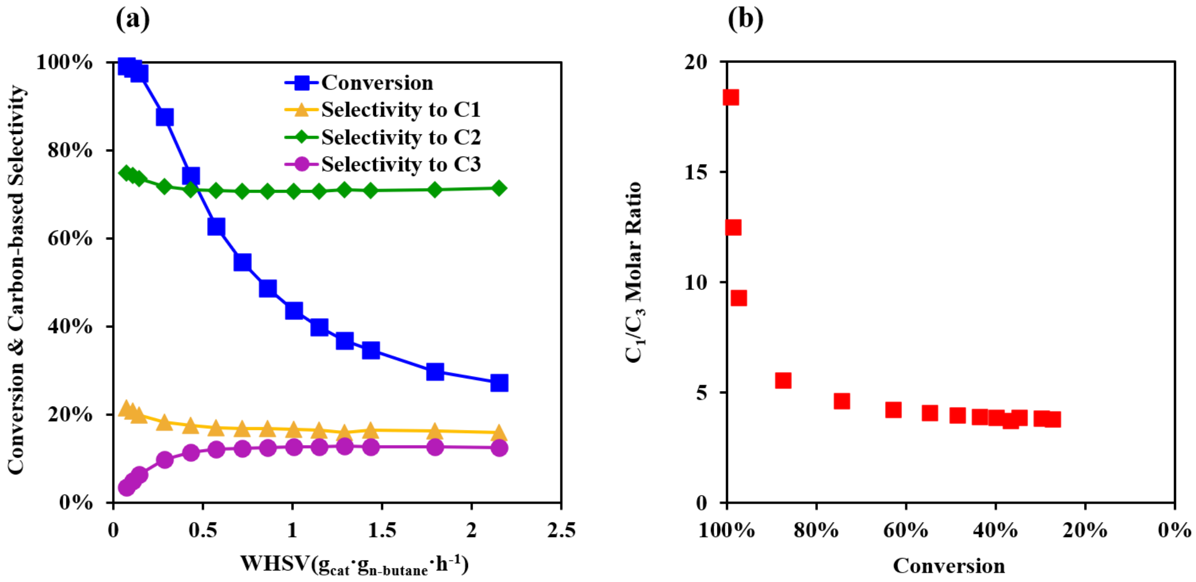

Supplementary Figure S2.9 Effect of weight hourly space velocity (WHSV, $g_{n\text{-butane}} \cdot g_{cat}^{-1} \cdot h^{-1}$) on conversion (blue squares) and carbon-based selectivity during n-C_4H_{10} hydrogenolysis on $Ir_{1.3nm}/MgAl_2O_4$ (a) and C_1/C_3 molar ratio as a function of conversion (b). Reaction conditions: 10.13 kPa H_2 and 1.01 kPa n-C_4H_{10}, balance He at 190 °C. The WHSV was varied by adjusting the total gas flowrate. The selectivity to methane (yellow triangles), ethane (green diamonds) and propane (purple circles) are calculated on carbon basis.

We note that the C_1/C_3 molar ratio reported in this figure was measured in an integral reactor (at high conversion without catalyst dilution) and was higher than that measured in the kinetic regime (at less than 1% conversion). The reason is likely due to heat transfer limitation, as the catalyst was not diluted in order to reach high conversions, in contrast to 20 times dilution for the kinetic measurements in Figures 2.4 and 2.5 in the main text. Since the C_1/C_3 molar ratio increases at higher temperature, we attribute the higher C_1/C_3 ratio in the integral reactor to a higher effective temperature resulting from the exothermicity of the reaction.

Supplementary Table S2.8 Fragmentation factor (ξ) calculated for effect of WHSV on $Ir_{1.3nm}/MgAl_2O_4$ catalyst at 190 °C. As the conversion increases, the fragmentation factor keeps increasing and reaches 2.4 when the conversion is close to 100% (data corresponding to Figure 2.6 and Supplementary Figure S2.9).

WHSV	Conversion	ξ
2.15	27.3%	2.24
1.79	29.8%	2.24
1.44	34.8%	2.24
1.29	36.8%	2.23
1.15	39.9%	2.25
1.00	43.7%	2.25
0.86	48.7%	2.25
0.72	54.8%	2.26
0.57	62.9%	2.26
0.43	74.4%	2.27
0.29	87.6%	2.30
0.14	97.5%	2.36
0.11	98.6%	2.38
0.07	99.2%	2.41

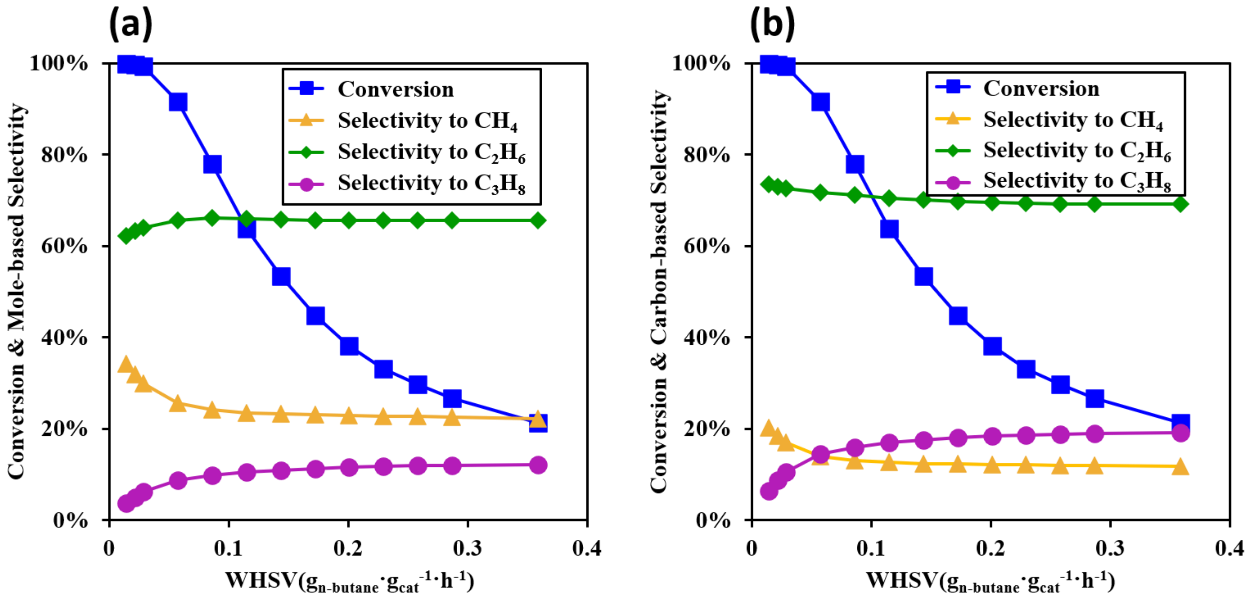

Supplementary Figure S2.10 Effect of weight hourly space velocity (WHSV, $g_{n\text{-}butane}\cdot g_{cat}^{-1}\cdot h^{-1}$) on conversion (blue squares) and selectivity during n-C_4H_{10} hydrogenolysis on $Ir_{1.4nm}/SiO_2$. Reaction conditions: 10.13 kPa H_2 and 1.01 kPa n-C_4H_{10}, balance He at 190 °C. The WHSV was varied by adjusting the total gas flowrate. The selectivity to methane (yellow triangles), ethane (green diamonds) and propane (purple circles) are calculated on mole basis (a) and carbon basis (b). The fragmentation factor (ξ) at highest and lowest conversion is 2.36 and 2.11, respectively.

Supplementary Table S2.9 Fragmentation factor (ξ) calculated for effect of WHSV on $Ir_{1.4nm}/SiO_2$ catalyst at 190 °C (data corresponding to Supplementary Figure S2.10).

WHSV	Conversion	ξ
0.36	21.2%	2.11
0.29	26.7%	2.11
0.26	29.7%	2.11
0.23	33.2%	2.12
0.20	38.1%	2.12
0.17	44.8%	2.13
0.14	53.3%	2.13
0.11	63.8%	2.14
0.09	77.9%	2.15
0.06	91.7%	2.18
0.03	99.4%	2.27
0.02	99.8%	2.31
0.01	99.8%	2.36

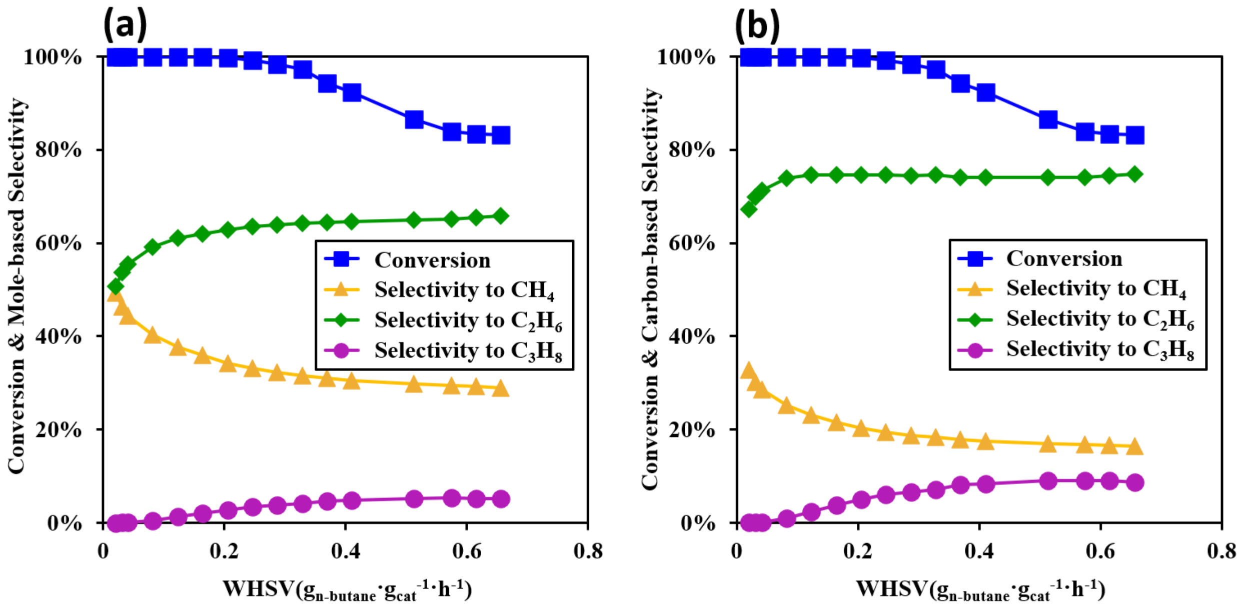

Supplementary Figure S2.11 Effect of weight hourly space velocity (WHSV, $g_{n\text{-butane}}$·g_{cat}^{-1}·h^{-1}) on conversion (blue squares) and selectivity during n-C_4H_{10} hydrogenolysis on $Ir_{1.3nm}$/$MgAl_2O_4$ at 100% conversion. Reaction conditions: 10.13 kPa H_2 and 1.01 kPa n-C_4H_{10}, balance He at 190 °C. The WHSV was varied by adjusting the total gas flowrate. The selectivity to methane (yellow triangles), ethane (green diamonds) and propane (purple circles) are calculated on mole basis (a) and carbon basis (b). The TOF of C–C bond cleavage for C_2H_6 is 0.00036 (s^{-1}) by calculating the ethane consumption changing from 0.04 to 0.02 $g_{n\text{-butane}}$·g_{cat}^{-1}·h^{-1}. A separate control experiment on the same catalyst was also performed for ethane hydrogenolysis, and the TOF of C–C bond cleavage was 0.0003 (s^{-1}). The TOF of $C_2H_6 \rightarrow 2CH_4$ in both cases is ~15 times lower than that on butane (0.0042 s^{-1}) at the same reaction conditions, confirming the extremely low level of series reaction pathway $C_2H_6 \rightarrow 2CH_4$ during n-butane hydrogenolysis. The fragmentation factor (ξ) at highest and lowest conversion was 2.65 and 2.27, respectively.

The product distribution was also studied using a larger bed of $Ir_{1.3nm}$/$MgAl_2O_4$ catalyst to reach 100% conversion at the same temperature (190 °C). The results indicate as the conversion increases, hydrogenolysis of propane and ethane proceed more but at lower rate than that of n-butane except at close to 100% conversion (vide infra). The rate of ethane hydrogenolysis on $Ir_{1.3nm}/MgAl_2O_4$ (at the same conditions in Figure 2.6, not shown) was ~15 times lower than that of n-butane. The much lower activity of ethane hydrogenolysis than longer chain alkanes (cycloalkanes) is consistent with literature where Locatelli et al. measured a much higher apparent activation energy for hydrogenolysis of ethane than cyclohexane on Ir/SiO_2 [4]. Additionally, a significant decrease in ethane selectivity was only observed with further decrease in space velocity after the conversion of n-butane reached 100% and all the propane was consumed (see Supplementary Figures S2.11-(a) and S2.11-(b)). From Table S2.10, the fragmentation factor reaches 2.6 only when the conversion is 100% and the ethane starts to be consumed. These results are consistent with the reported decrease in hydrogenolysis rate with decrease in alkane chain length [5].

Supplementary Table S2.10 Fragmentation factor (ξ) calculated for effect of WHSV on $Ir_{1.3nm}/MgAl_2O_4$ catalyst at 190 °C at very high conversion range close to 100% (data corresponding to Supplementary Figure S2.11).

WHSV	Conversion	ξ
0.66	83.3%	2.27
0.62	83.4%	2.27
0.57	84.0%	2.27
0.51	86.6%	2.28
0.41	92.4%	2.29
0.37	94.3%	2.30
0.33	97.3%	2.32
0.29	98.3%	2.33
0.25	99.2%	2.35
0.21	99.7%	2.37
0.16	99.9%	2.41
0.12	100.0%	2.45
0.08	100.0%	2.50
0.04	100.0%	2.57
0.03	100.0%	2.60
0.02	100.0%	2.65

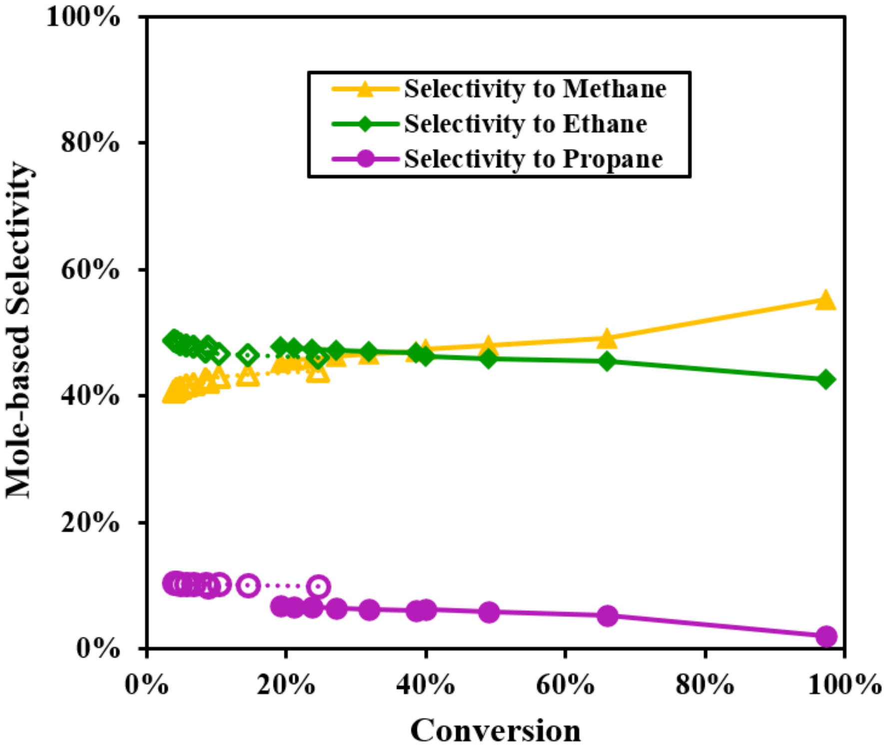

Supplementary Figure S2.12 Comparison of mole-based selectivity to methane (gray squares), ethane (blue diamonds) and propane (red triangles) of n-butane hydrogenolysis as a function of conversion by adjusting the total gas flowrate on $Ir_{1.3nm}/MgAl_2O_4$ (solid) and $Ir_{0.7nm}/MgAl_2O_4$ (hollow). Reaction conditions: 10.13 kPa H_2 and 1.01 kPa n-C_4H_{10}, balance He at 250 °C.

The amount of Ir in the reactor was the same for $Ir_{0.7nm}/MgAl_2O_4$ and $Ir_{1.3nm}/MgAl_2O_4$. Since the activity of $Ir_{0.7nm}/MgAl_2O_4$ is lower, the selectivity was measured in the lower conversion range than $Ir_{1.3nm}/MgAl_2O_4$ catalyst. The mole-based selectivity to ethane is weakly dependent on conversion on these two catalysts in similar conversion range. When the conversion is close to 100% on $Ir_{1.3nm}/MgAl_2O_4$, the mole-based selectivity to ethane decreases, showing the proceeding of series reaction pathway of $C_2H_6 \rightarrow 2\ CH_4$ at such high temperature.

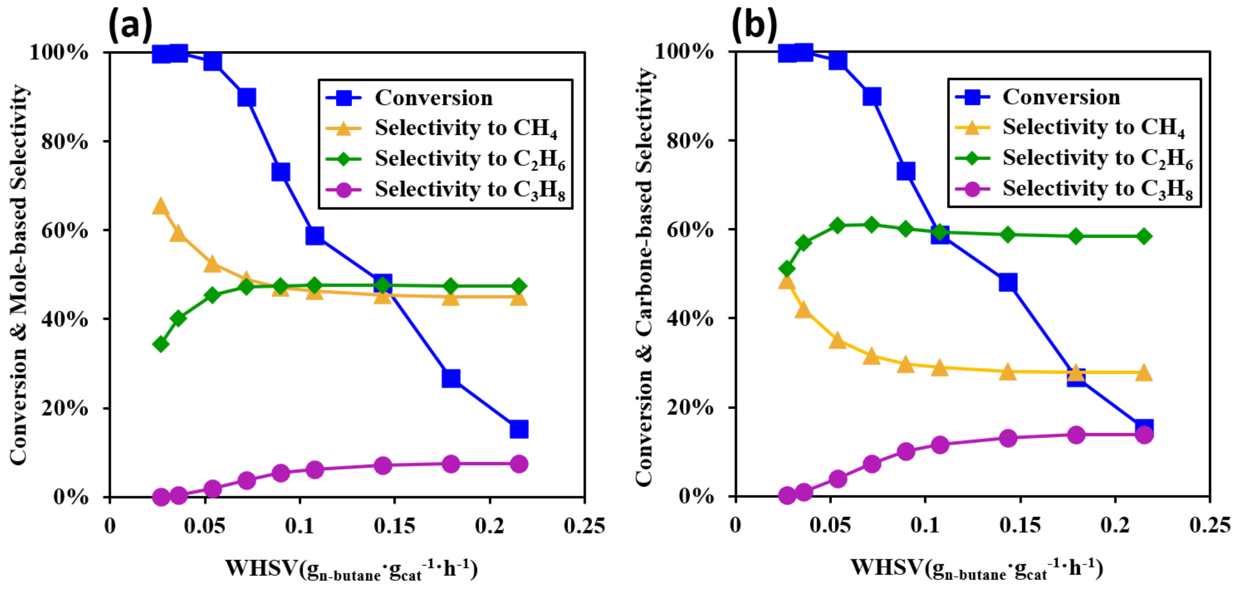

Supplementary Figure S2.13 Effect of weight hourly space velocity (WHSV, $g_{n\text{-butane}}\cdot g_{cat}^{-1}\cdot h^{-1}$) on conversion (blue squares) and selectivity during n-C_4H_{10} hydrogenolysis on $Ir_{2.9nm}/SiO_2$. Reaction conditions: 10.13 kPa H_2 and 1.01 kPa n-C_4H_{10}, balance He at 220 °C. The WHSV was varied by adjusting the total gas flowrate. The selectivity to methane (yellow triangles), ethane (green diamonds) and propane (purple circles) are calculated on mole basis (a) and carbon basis (b). The fragmentation factor (ξ) at highest and lowest conversion is 2.97 and 2.46, respectively.

As the WHSV decreases from 0.22 to 0.03 $g_{n\text{-butane}}\cdot g_{cat}^{-1}\cdot h^{-1}$, the conversion increases from 15 to 100%, but the mole-based selectivity to ethane stays between 34–47% and does not decrease until the conversion almost reaches 100%. The selectivity to methane increases while the selectivity to propane decreases as conversion reaches 100%, showing the evidence of series reaction pathway from propane to ethane and methane. The increasing fragmentation factor shown in Supplementary Table S2.11 could also reflect the deeper level of hydrogenolysis on $Ir_{2.9nm}/SiO_2$ catalyst, especially when conversion is close to 100%.

Generally, as the conversion increases, there is a balance between the less favored central C–C bond cleavage to produce less ethane and further hydrogenolysis of propane to produce more ethane. The C–C bond cleavage on the intermediate of ethane might happen, but the level must also be very low based on the almost constant selectivity before the conversion reaches 100%, which is similar with the case on $Ir_{1.3nm}/MgAl_2O_4$ as discussed in section 2.4.3 of main text. The selectivity trend with conversion is still similar with that on $Ir_{1.3nm}/MgAl_2O_4$ and $Ir_{1.4nm}/SiO_2$, but the selectivity to ethane is much lower, indicating that the particle size does affect the initial parallel reaction pathway, where the central C–C bond cleavage is less favored on the large particles.

Supplementary Table S2.11 Fragmentation factor (ξ) calculated for effect of WHSV on $Ir_{2.9nm}/SiO_2$ catalyst at 220 °C (data corresponding to Supplementary Figure S2.13).

WHSV	Conversion	ξ
0.22	15.3%	2.46
0.18	26.8%	2.46
0.14	48.3%	2.47
0.11	58.9%	2.50
0.09	73.2%	2.53
0.07	90.0%	2.58
0.05	98.1%	2.68
0.04	99.8%	2.83
0.03	99.7%	2.97

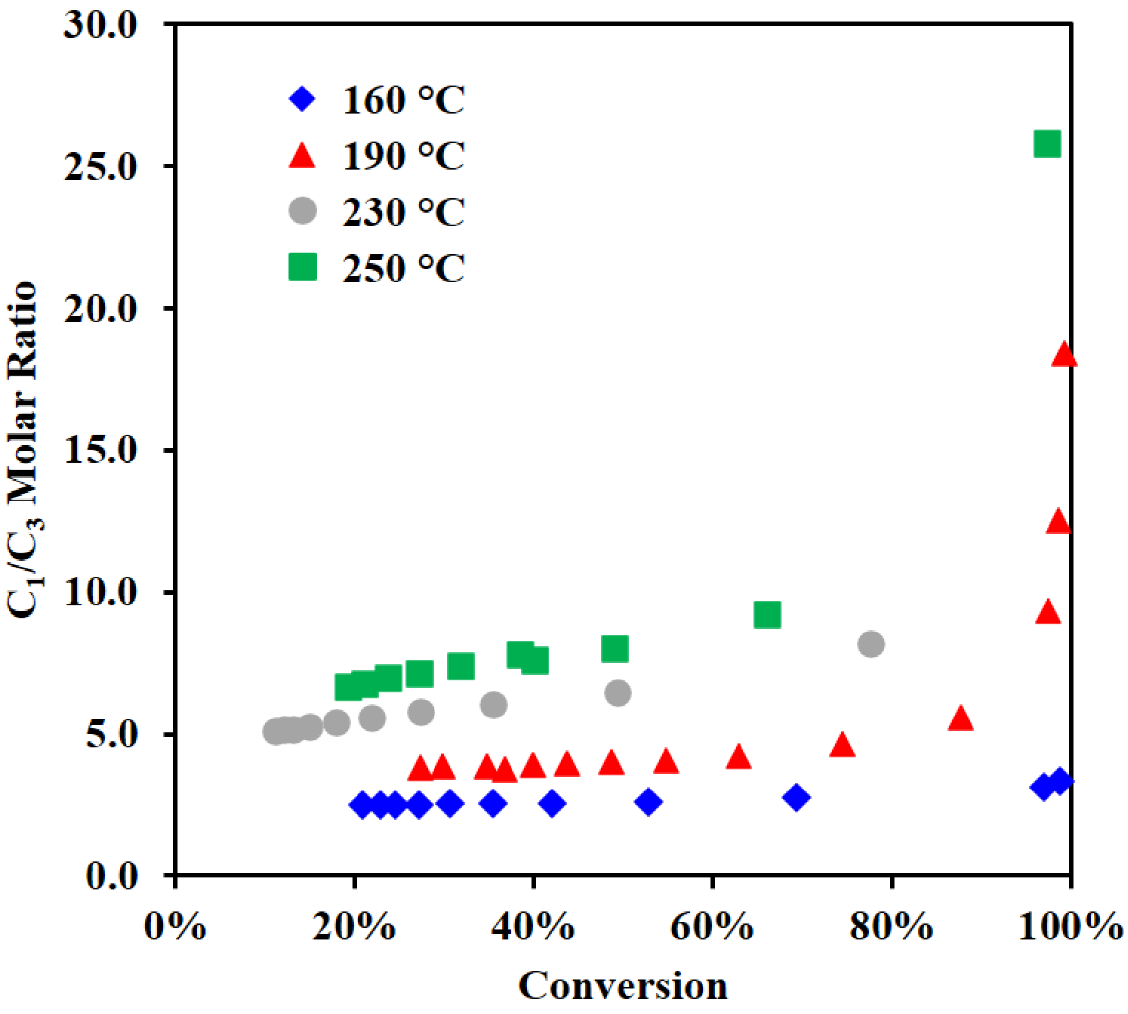

Supplementary Figure S2.14 Comparison of C_1/C_3 molar ratio at different temperatures on $Ir_{1.3nm}/MgAl_2O_4$ catalyst. Reaction conditions: 10.13 kPa H_2 and 1.01 kPa n-C_4H_{10}, balance He. The conversion was varied by adjusting the WHSV (total gas flowrate) at 160, 190, 230 and 250 °C.

Calculations of transport limitations for n-butane hydrogenolysis over $Ir_{1.3nm}/MgAl_2O_4$ catalyst [6, 7]

I. Mears Criterion for External Diffusion

The results of n-butane hydrogenolysis over $Ir_{1.3nm}/MgAl_2O_4$ catalyst are used for the following calculation.

The catalyst was diluted 20 times with SiO_2, the bed length is ~4.5 cm, total amount of catalyst (including diluent) is 0.4g, the inner radius of the reactor is 0.35cm.

The external mass transfer effects could be negligible when $\frac{-r'_A \rho_b R n}{k_C C_{Ab}} < 0.15$ (where $-r'_A$ is reaction rate).

TOF at 170 °C is ~ 0.0013 s^{-1}, which is 0.0013 $\frac{\text{mole of n}-C_4H_{10}}{\text{mole of Ir}\cdot s}$.

$$r'_A = \left[0.0013\,\frac{\text{mole of n} - C_4H_{10}}{\text{mole of Ir }\cdot s}\right]\left[\frac{\text{mole of Ir}}{192\text{ g Ir}}\right]\left[\frac{1\%\text{ loading of Ir}}{g_{cat}}\right]$$

$$= 6.8 \times 10^{-8}\ \frac{\text{mole of n} - C_4H_{10}}{g_{cat}\ \cdot s}$$

n = reaction order (use 1)

$R_p = 9 \times 10^{-5}$ m (catalyst particle radius)

$\rho_b = \frac{\text{Total amount of catalyst (including diluent)}}{\pi\times(\text{inner radius of reactor})^2\times\text{bed length}} = \frac{0.4\text{ g}}{\pi\times0.35^2\times4.5} = 0.23\text{ g cm}^{-3}$ (bulk density of catalyst bed)

$C_{Ab} = \frac{1\% \times 10^5\text{ Pa}}{\left[8.314\text{ Pa}\cdot\frac{m^3}{K}\cdot\text{mol}\right][443K]} = 0.27\text{ mol/m}^3$ (bulk gas concentration of reactant, mol/m^3)

$\mathrm{k_C = 2D_{AB}/R_p}$ (mass transfer coefficient, m/s)

$\mathrm{D_{AB}} = \frac{0.001\times \mathrm{T}^{1.75}\mathrm{M}_{\mathrm{AB}}^{0.5}}{\mathrm{P}[(\sum \mathrm{v})_{\mathrm{A}}^{\frac{1}{3}}+(\sum \mathrm{v})_{\mathrm{B}}^{\frac{1}{3}}]^2}$ (The Fuller-Schettler-Giddings equation for gas-phase diffusivity between A and B [8, 9])

Case 1. n-C_4H_{10} is in bath gas of He, then $\mathrm{D_{AB}} = 6.5 \times 10^{-5}\ \mathrm{m^2/s}$.

Case 2. H_2 is in bath gas of He, then $\mathrm{D_{AB}} = 3.3 \times 10^{-4}\mathrm{m^2/s}$.

We use the lower $\mathrm{D_{AB}}$ for the following calculation.

$$\mathrm{k_C} = \frac{2\mathrm{D_{AB}}}{\mathrm{R_p}} = \frac{2\times(6.5\times10^{-5}\,\frac{\mathrm{m}^2}{\mathrm{s}})}{9\times10^{-5}\ \mathrm{m}} = 1.44\ \mathrm{m/s}$$

$$\frac{-\mathrm{r}'_{\mathrm{A}}\ \rho_{\mathrm{b}}\mathrm{Rn}}{\mathrm{k_C C_{Ab}}} = \frac{\left[6.8\times10^{-8}\ \frac{\text{mole of n}-\mathrm{C_4H_{10}}}{\mathrm{g_{cat}}\ \cdot \mathrm{s}}\right][0.23\ \mathrm{g\ cm^{-3}}][\frac{\mathrm{cm}^3}{\mathrm{m}^3}]\times(9\times10^{-5}\ \mathrm{m})|1|}{\left[1.44\,\frac{\mathrm{m}}{\mathrm{s}}\right]\times[0.27\,\frac{\mathrm{mol}}{\mathrm{m}^3}]}$$

$$= 3.6\times10^{-6}$$

$$\frac{-\mathrm{r}'_{\mathrm{A}}\ \rho_{\mathrm{b}}\mathrm{R_p n}}{\mathrm{k_C C_{Ab}}} \ll \mathbf{0.15}$$

II. Weisz-Prater Criterion for Internal Diffusion

The internal mass transfer effects could be negligible when $\frac{-r'_A\ \rho_c\ R^2}{D_e C_{As}} < 1$.

TOF = 0.0013 $\frac{mole\ of\ n-C_4H_{10}}{mole\ of\ Ir\cdot s}$, at 170 °C.

$D_e = \frac{D_{AB}\phi_p\sigma_c}{\tau}$ (effective gas-phase diffusivity, m^2/s)

$D_{AB} = 6.5 \times 10^{-5}\ m^2/s$ (gas-phase diffusivity)

ϕ_p= 0.4 (pellet porosity)

σ_c=0.8 (constriction factor)

$\tau = 3$, tortuosity

$$\mathrm{D_e} = \frac{\mathrm{D_{AB}\phi_p\sigma_c}}{\tau} = \frac{6.5\times10^{-5}\ \mathrm{m^2/s} \times 0.4 \times 0.8}{3} = 6.9 \times 10^{-6}\ \mathrm{m^2/s}$$

$$\mathrm{C_{As}} = \frac{1\%\ \times 10^5\mathrm{Pa}}{\left[8.314\ \mathrm{Pa}\cdot\frac{\mathrm{m^3}}{\mathrm{K}}\cdot\mathrm{mol}\right][443\mathrm{K}]} = 0.27\ \mathrm{mol}\ /\mathrm{m^3}$$

$\rho_c = 2.65 g/cm^3$ (density of solid catalyst, in this case the density of diluent, since the catalyst was intraparticle diluted with SiO_2 by 20 times)

$$\frac{-\mathrm{r'_A}\ \rho_c\ \mathrm{R^2}}{\mathrm{D_e C_{As}}} = \frac{\left[6.8\times10^{-8}\ \frac{\mathrm{mole\ of\ n-C_4H_{10}}}{\mathrm{g_{cat}}\ \cdot \mathrm{s}}\right]\times[2.65\frac{\mathrm{g}}{\mathrm{cm^3}}]\left[\frac{\mathrm{cm^3}}{\mathrm{m^3}}\right]\times[9\times10^{-5}\ \mathrm{m}]^2}{\left[6.9\times10^{-6}\frac{\mathrm{m^2}}{\mathrm{s}}\right][0.27\ \frac{\mathrm{mol}}{\mathrm{m^3}}]}$$

$$= 7.8\ \times\ 10^{-4}$$

$$\frac{-\mathrm{r'_A}\ \rho_c\ \mathrm{R^2}}{\mathrm{D_e C_{As}}} \ll \mathbf{1}$$

III. Mears Criterion for Intraparticle Heat Transfer Limitation

The intraparticle heat transfer effects could be negligible when $\frac{|\Delta H_R|\Re R_p E_a}{\lambda_S T_0 R_g T_0} < 0.75$

Ea = 134000 J/mol (Use the highest Ea obtained from Arrhenius plot fitted by TOF data cooling down from 190 to 170 °C, including deactivation effect)

$T_0 = 443$ K (temperature of particle surface)

$$\Re = \left[6.8 \times 10^{-8}\ \frac{mole\ of\ n{-}C_4H_{10}}{g_{cat}\cdot s}\right]\left[2.65\,\frac{\mathrm{g}}{\mathrm{cm}^3}\right]\left[\frac{\mathrm{cm}^3}{\mathrm{m}^3}\right] = 0.18\,mol/m^3 \cdot s$$

ΔH_R=174000 J/mol/K (heat of reaction, assuming all the C–C bond has been cleaved and product is CH_4 only)

$\lambda_S = 1.3\ \mathrm{W/m \cdot K}$ (thermal conductivity of SiO_2, as the majority of the catalyst particles is diluent of SiO_2)

R_g = 8.314 $\mathrm{J/mol \cdot K}$ (ideal gas constant)

$$\frac{|\Delta H_R|\Re R_p E_a}{\lambda_S T_0 R_g T_0} = \frac{\left[174000\,\frac{\mathrm{J}}{\mathrm{mol}}\cdot \mathrm{K}\right]\left[0.18\,\frac{mol}{m^3}\cdot s\right][9 \times 10^{-5}\,m]^2\left[134000\,\frac{\mathrm{J}}{\mathrm{mol}}\right]}{\left[1.3\,\frac{\mathrm{W}}{\mathrm{m}}\cdot \mathrm{K}\right][443K]^2[8.314\ \mathrm{J/mol \cdot K}]} = 1.6 \times 10^{-5}$$

$$\frac{|\Delta \mathrm{H_R}|\Re \mathrm{R_p E_a}}{\lambda_\mathrm{S} \mathrm{T_0 R_g T_0}} \ll \mathbf{0.75}$$

IV. Mears Criterion for Radical (Interparticle) Heat Transfer Limitation

The interparticle heat transfer effects could be negligible when $\frac{|\Delta H_R|\Re R_t^2}{\frac{\lambda_{eff} T_w^2 R_g}{E_a}}(1 + \frac{4\lambda_{eff}}{R_t h_w}) < 0.4$

R_t = 0.35 cm (reactor radius)

T_w = 443K (wall temperature)

$h_w = \frac{2\lambda_g}{d_p}$ (heat transfer coefficient at the wall)

$d_p = 1.8 \times 10^{-4}\,m$ (catalyst particle diameter)

$$\lambda_g = y_{C_4H_{10}\times}\lambda_{C_4H_{10}} + y_{H_2\times}\lambda_{H_2} + y_{He\times}\lambda_{He} = 1\% \times 28 + 10\% \times 230 + 89\% \times 191$$

$$= 0.193\ \mathrm{W/m \cdot K}$$

$\lambda_{\mathrm{C_4H_{10}}} = 0.028\ \mathrm{W/m \cdot K}$ at 400K, 101.325 kPa.

$\lambda_{H_2} = 0.23\ \mathrm{W/m \cdot K}$ at 400K, 101.325 kPa.

$\lambda_{He} = 0.191\ \mathrm{W/m \cdot K}$ at 400K, 101.325 kPa.

$$\mathrm{h_w} = \frac{2\lambda_\mathrm{g}}{\mathrm{d_p}} = \frac{2 \times 0.193\ \mathrm{W/m \cdot K}}{1.8 \times 10^{-4}\ \mathrm{m}} = 2144\ \mathrm{W/m^2 \cdot K}$$

$$\lambda_{eff} = \lambda_g \beta \left(\frac{1-\phi}{\frac{\lambda_g}{\lambda_s} + \psi} \right) = 0.193\ \mathrm{W/m \cdot K} \times 1 \times \frac{1-0.4}{\frac{0.193\ \mathrm{W/m \cdot K}}{1.3\ \mathrm{W/m \cdot K}} + 0.04} = 0.61\ \mathrm{W/m \cdot K}$$

$where\ \beta = 1, \psi = 0.04, \phi = 0.4, \lambda_s = \lambda_{SiO_2} = 1.3\ \mathrm{W/m \cdot K}$

$$\frac{|\Delta H_R| \Re R_t^2}{\frac{\lambda_{eff} T_w^2 R_g}{E_a}} \left(1 + \frac{4\lambda_{eff}}{R_t h_w}\right)$$

$$= \frac{\left|174000 \frac{J}{mol} \cdot K\right| \left[0.18 \frac{mol}{m^3} \cdot s\right] [3.5 \times 10^{-4}\mathrm{m}]^2}{\frac{\left[0.61 \frac{\mathrm{W}}{\mathrm{m}} \cdot \mathrm{K}\right] [443\mathrm{K}]^2 \left[8.314 \frac{J}{K} \cdot mol\right]}{\left[134000 \frac{J}{mol}\right]}}$$

$$\times \left(1 + \frac{4 \times 0.61 \frac{\mathrm{W}}{\mathrm{m}} \cdot \mathrm{K}}{[3.5 \times 10^{-4}\mathrm{m}] \left[2144 \frac{\mathrm{W}}{\mathrm{m^2}} \cdot \mathrm{K}\right]}\right) = 2 \times 10^{-3}$$

$$\frac{|\Delta \mathrm{H_R}| \Re \mathrm{R_t^2}}{\frac{\lambda_\mathrm{eff} \mathrm{T_w^2 R_g}}{\mathrm{E_a}}} \left(1 + \frac{4\lambda_\mathrm{eff}}{\mathrm{R_t h_w}}\right) \ll \mathbf{0.4}$$

V. Mears Criterion for Interphase Heat Transfer Limitation

The interphase heat transfer effects could be negligible when $\left|\frac{-\Delta H_R(-\Re)RE_a}{hT^2R_g}\right| < 0.15$

$\mathrm{h} = 2144\ \mathrm{W/m^2 \cdot K}$ (heat transfer coefficient between gas and pellet)

$$\left|\frac{-\Delta H_R(-\Re)R_pE_a}{hT^2R_g}\right| = \left|\frac{\left[-174000\frac{J}{mol}\cdot K\right]\left[-0.18\frac{mol}{m^3}\cdot s\right][9\times10^{-5}\,m]\left[134000\frac{J}{mol}\right]}{[2144\frac{W}{m^2}\cdot K][443K]^2[8.314\,J/K\cdot mol]}\right|$$

$$= 1.1\times10^{-4}$$

$$\left|\frac{-\Delta H_R(-\Re)\rho_bRE_a}{hT^2R_g}\right| \ll \mathbf{0.15}$$

”

References

[1] Y. Lu, C.-T. Kuo, L. Kovarik, A.S. Hoffman, A. Boubnov, D.M. Driscoll, J.R. Morris, S.R. Bare, A.M. Karim, A versatile approach for quantification of surface site fractions using reaction kinetics: The case of CO oxidation on supported Ir single atoms and nanoparticles, Journal of Catalysis, 378 (2019) 121-130.

[2] Z. Paál, P. Tétényi, A new classification of metal catalysts in skeletal reactions of hydrocarbons, Nature, 267 (1977) 234-236.

[3] A. Majesté, S. Balcon, M. Guérin, C. Kappenstein, Z. Paál, Hydrogenolysis of n-hexane on Al2O3-supported Ir catalysts of various treatments, Journal of Catalysis, 187 (1999) 486-492.

[4] F. Locatelli, J.-P. Candy, B. Didillon, G.P. Niccolai, D. Uzio, J.-M. Basset, Hydrogenolysis of Cyclohexane over Ir/SiO2 Catalyst: A Mechanistic Study of Carbon− Carbon Bond Cleavage on Metallic Surfaces, Journal of the American Chemical Society, 123 (2001) 1658-1663.

[5] D.W. Flaherty, D.D. Hibbitts, E. Iglesia, Metal-catalyzed C–C bond cleavage in alkanes: effects of methyl substitution on transition-state structures and stability, Journal of the American Chemical Society, 136 (2014) 9664-9676.

[6] A.M. Karim, A comparison between packed bed and wall coated reactors for the steam reforming of methanol, (2003).

[7] C.-T. Kuo, Y. Lu, L. Kovarik, M.H. Engelhard, A.M. Karim, Structure Sensitivity of Acetylene Semi-Hydrogenation on Pt Single Atoms and Subnanometer Clusters, ACS Catalysis, (2019).

[8] E.N. Fuller, P.D. Schettler, J.C. Giddings, New method for prediction of binary gas-phase diffusion coefficients, Industrial & Engineering Chemistry, 58 (1966) 18-27.

[9] H.S. Fogler, M.N. Gürmen, Elements of Chemical Reaction Engineering. 2005, There is no corresponding record for this reference.[Google Scholar], (1999) 741-760.

Appendix N-Butane hydrogenolysis on Ir/$ZnAl_2O_4$

To understand the effect of the electronic property and metal-support interaction, one more 1%$Ir_{1.4nm}/ZnAl_2O_4$ catalyst was also tested for n-butane hydrogenolysis. The details for the catalyst will be discussed in Chapter 4. The surface-average particle size of the catalyst is 1.4 nm, which is very close to 1.3 nm for $Ir_{1.3nm}/MgAl_2O_4$ applied in this chapter. However, the activity of n-butane hydrogenolysis on 1%$Ir_{1.4nm}/ZnAl_2O_4$ catalyst is much lower than that on $Ir_{1.3nm}/MgAl_2O_4$ and it is impossible to measure the selectivity at the same temperature range (~190 °C) used for $Ir_{1.3nm}/MgAl_2O_4$. Supplementary Information Figure S2.15 shows the selectivity change as a function of the weight hourly space velocity (WHSV, $g_{n\text{-}butane}\cdot g_{cat}^{-1}\cdot h^{-1}$) as a comparison with that in Figure 2.6. Even though the reaction temperature increases from 190 to 300 °C, the mole-based selectivity to ethane on 1%$Ir_{1.4nm}/ZnAl_2O_4$ catalyst is about 55 %, which is very close to those on

Ir/$MgAl_2O_4$ series (~56-58 % at 300 °C, Supplementary Figure S2.12). Similar with $Ir_{1.3nm}$/$MgAl_2O_4$, the selectivity to the three products shows very weak dependence on conversion (WHSV). The selectivity to methane is much lower and the selectivity to propane is much higher than the results on $Ir_{1.3nm}$/$MgAl_2O_4$ in Figure 2.6, indicating a lower-level proceeding in the series reaction pathway of $C_3 \rightarrow C_1 + C_2$.

A lower activity on Ir catalysts supported on $ZnAl_2O_4$ was also observed for CO oxidation (0.2%$Ir_{0.8nm}$/$ZnAl_2O_4$ vs. 0.05%$Ir_{0.7nm}$/$MgAl_2O_4$). Details of the activity comparison will be published later elsewhere. The reason for the lower activity on $ZnAl_2O_4$ support is still unknown. Because of the lower activity, we are unable to study reaction pathway and product distribution of n-butane hydrogenolysis as compared with the work in Chapter 2. Therefore, we chose acetylene hydrogenation as the probe reaction to investigate the structure sensitivity on the series of Ir/$ZnAl_2O_4$ catalysts and the results are shown in Chapter 4.

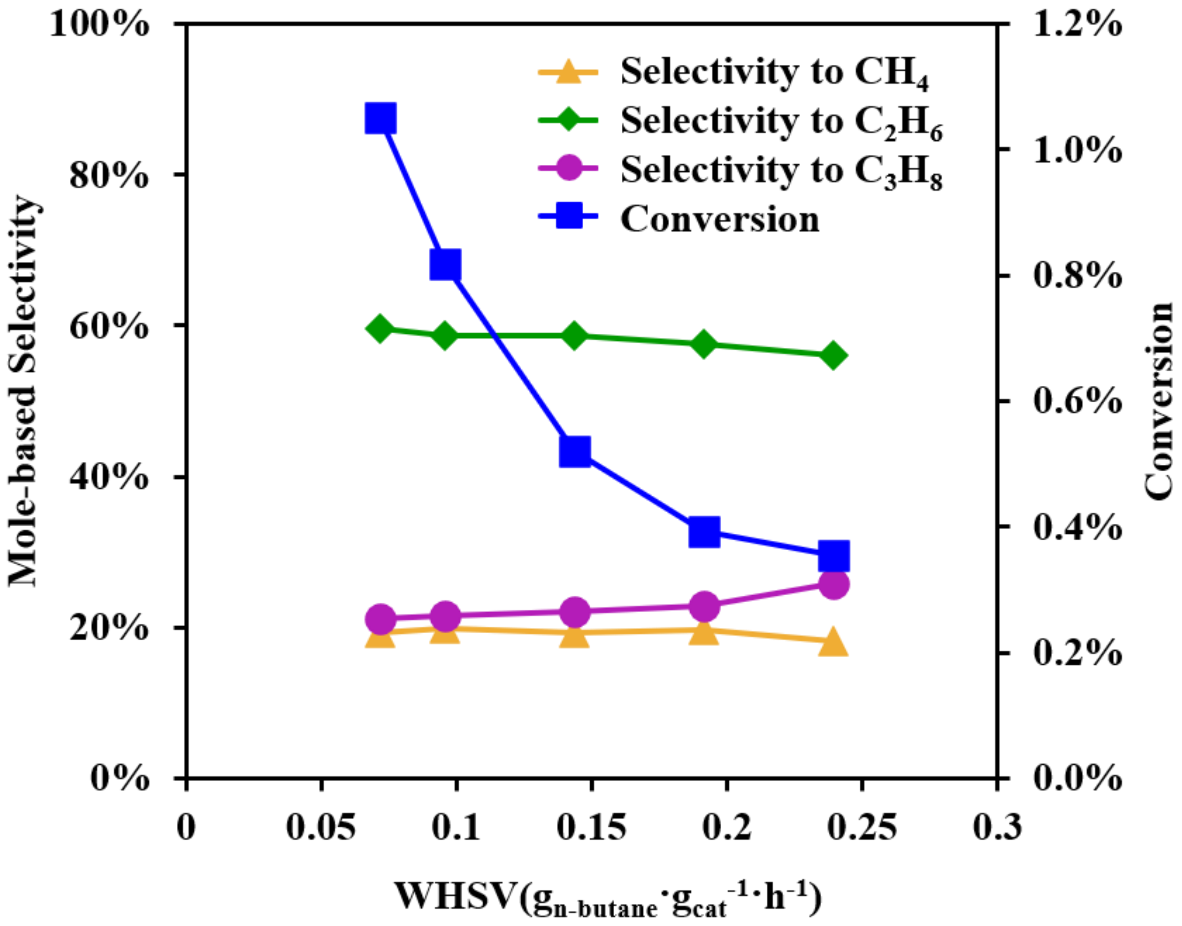

Supplementary Figure S2.15 Effect of weight hourly space velocity (WHSV, $g_{n\text{-butane}}\cdot g_{cat}^{-1}\cdot h^{-1}$) on conversion (blue squares) and selectivity during n-C_4H_{10} hydrogenolysis on 0.3g 1%$Ir_{1.4nm}$/$ZnAl_2O_4$ without any dilution at low conversion range (0.3-1.05%). Reaction conditions: 10.13 kPa H_2 and 1.01 kPa n-C_4H_{10}, balance He at 300 °C. The WHSV was varied by adjusting the total gas flow rate.

Chapter 3. Structure Sensitivity of Ethane Hydrogenolysis on Ir/$MgAl_2O_4$ Catalysts

This manuscript is still in preparation.

Attribution

Xiwen Zhang performed part of the catalyst synthesis and all the catalytic tests, including data analysis, reaction mechanism analysis and wrote the manuscript. Yubing Lu conducted the synthesis of catalysts and characterizations (DRIFTS, chemisorption). Libor Kovarik performed the HAADF-STEM analysis. Ayman M Karim conceived the idea and directed the project. All the authors discussed the results and provided important comments on the projects.

3.1 Abstract

Hydrogenolysis of alkanes has been widely reported as structure sensitive reaction on supported metal catalysts with particle size ranging between 1–20 nm. Among the alkanes, ethane is the simplest molecule with only one saturated C–C bond and performs as an important intermediate that related to the selectivity of n-butane hydrogenolysis. In this work, a series of Ir/$MgAl_2O_4$ catalysts in the small size range from mostly single atoms to nanoparticles (1–2 nm) were prepared and tested for ethane hydrogenolysis at 335–350 °C. Our results show that the activity of ethane hydrogenolysis decreases from nanoparticles to subnanometer clusters, and then increases again on the Ir/$MgAl_2O_4$ catalyst with mostly single atoms and small fraction of nanoparticles. The exclusive trend for the high activity on this catalyst might be because of the fraction of

nanoparticles. The reaction mechanism of ethane hydrogenolysis on these Ir/$MgAl_2O_4$ catalysts was also analyzed and it is highly possible that both hydrogen and hydrocarbon species are the most abundant surface intermediates on the supported Ir catalysts.

3.2 Introduction

Hydrogenolysis of n-alkanes and cycloalkanes is widely used in many hydrocarbon processes to decrease the chain length of the saturated alkanes [1-3]. From the industrial point of view, the selectivity to different products with shorter chain length affects the energy density and fuel quality of the alkanes extracted from fossil resources like natural gas or shale gas [4]. To study the fundamentals of hydrogenolysis of saturated alkanes, ethane is the simplest molecule to understand the mechanism of C–C bond cleavage dependent on the effect of temperature, pressure and particle size of the catalyst, since there is only one C–C bond within the ethane molecule.

Ethane hydrogenolysis has been reported to be structure sensitive on single crystal surfaces and supported metal catalysts such as Pt/SiO_2, Rh/SiO_2 and Ni/SiO_2 [5-10]. Goodman reported that the activity of ethane hydrogenolysis on Ni (100) surface is significantly much higher than that on Ni (111) surface because of the different spacing of available sites on the surface. Since the C–C bond of ethane could remain intact on the Ni (111) surface with spacing of 0.14 nm between the three-fold hollow sites, which approximately equals the C–C intermediate bond length of ethane (0.13 – 0.15 nm). While on Ni (100) surface, the bigger spacing of 0.25 nm between the four-fold hollow sites prevents the intact configuration of C–C intermediate of ethane and facilitates the bond cleavage and hence the higher activity [5]. In the case of SiO_2 supported Ni catalysts, Martin found the reaction rate of ethane hydrogenolysis gradually increases with particle size from 2.5 to 6.4 nm, then greatly drops when further increasing the particle size to 12 and 22 nm, and the much lower activity on larger sized particles is because of the presence of (111) surface [10]. Song et al. tested ethane hydrogenolysis over the SiO_2 supported Pt nanoparticles in the reduced size range between 1 and 10 nm and they found the TOF does not change much by decreasing the particle size from 10 to 4 nm but increases by 50-fold of magnitude when narrowing the size from 4 to 1 nm. In general, a certain size and good facets orientation of Pt ensembles is required for ethane hydrogenolysis. The C–C bond of the intermediate is likely to bond with multiple Pt atoms and meantime adjacent Pt atoms are demanded for H adsorption, but the required ensemble size of Pt might be reduced in their case since the surface atoms with low coordination number (steps, corner, etc.) also play a critical role to enhance the catalytic reactivity [7]. However, although a lot of work was done on the size effect in the nanometer size range of different transition metals, the effect of size on C–C bond cleavage of ethane in the very small size range (from single atoms to ~2 nm) was rarely reported.

As the metal particle size decreases in the low nanometer or subnanometer regime, the fraction of sites with low coordination number greatly increases [11, 12]. It is generally accepted that the electronic properties of these undercoordinated sites, especially the single atoms, are quite different from those on the large nanoparticles or the flat and intact metal surface [13]. Therefore, the catalytic performance is expected to be distinguished and strongly affected by the metal nuclearity because of the different surface roughness along with the requirement of ensemble size for a specific reaction aforementioned. For example, Crampton et al. tested ethylene hydrogenation over a series of Pt clusters with 7 to 40 Pt atoms supported on MgO and they found the activity on the catalyst with 13 Pt atoms (~0.8 nm) is the highest [14]. On the other hand, Wei et al. reported the FeO_x supported Pt single atoms are more active and selective for chemoselective hydrogenation of nitroarenes than the Pt nanoparticles with larger particle size [15], which is in contrast to Kuo et al.'s results on Pt/TiO_2 catalysts that the activity decreases with decreasing Pt size while the selectivity on the Pt single atoms is remarkably the highest [16]. These reports show that it is still not clear how the size in the subnanometer regimes influence the adsorption of the hydrocarbons, even for simplest alkenes / alkanes with only two carbons, and hence the activity and selectivity.

To study the structure sensitivity of ethane hydrogenolysis in the subnanometer regime, we tested the active on the Ir catalysts with mostly single atoms, subnanometer clusters and very small nanoparticles (~1.3 nm) supported on the $MgAl_2O_4$ spinel. As of the special properties of spinel structure support, it is much easier to prepare small sized Ir (<1.5 nm) than the very large particles. Because Ir is epitaxial metal, the strong interfacial interaction between the metal and support limits the sintering of Ir [17]. The catalysts were characterized by in-situ diffuse reflectance infrared Fourier transform spectroscopy (DRIFTS) by CO adsorption and high-angle annular dark-field (HAADF) aberration-corrected scanning transmission electron microscopy (STEM), the details were analyzed elsewhere [18, 19]. The results show the activity decreases with decreasing particle size below 1.3 nm and increases again on the catalyst with mostly single atoms. The higher activity might be because of the fraction of large particles within the catalyst. The reaction mechanism was also analyzed on Ir nanoparticles with surface-average particle size of 1.3 nm. The results of ethane hydrogenolysis shed a light on the selectivity and reaction pathway study on the hydrogenolysis of longer chain alkanes.

3.3 Methods

3.3.1 Synthesis of $Ir/MgAl_2O_4$ catalysts

Three $Ir/MgAl_2O_4$ catalysts with 1 and 0.05 Ir weight % were prepared to achieve different Ir particle sizes ranging from mostly single to ~1.3 nm (see results). The 0.05% $Ir/MgAl_2O_4$ catalyst with mostly single atoms (referred as $Ir_{SA-0.7nm}/MgAl_2O_4$) was prepared by liquid ion-exchange method using iridium nitrate (aqueous solution, 8.7 wt% Ir, Furuya Metal Co. Ltd.) precursor. 1 L of deionized water was added to the Pyrex bottle with pH adjusted to 2.8 by nitrate acid. Then the diluted iridium nitrate precursor was added into the acid solution. The fine powder of $MgAl_2O_4$ support (Puralox MG 28, Sasol) was calcined at 500 °C for 4 hours in the muffle furnace before adding to the precursor solution under stirring. After 4 hours of stirring, the pH was tested as 9.5. Then the solution was filtrated and the filter residue was dried in air overnight at room temperature. The weight loading of the catalyst was confirmed to be 0.05% since the Ir in the filtrate was measured by inductively coupled plasma-atomic emission spectroscopy (ICP- AES) on a Spectro ARCOS II Multi-View ICP Model FHM22 with CETAC Autosampler instrument and no Ir was detected (detection limit 0.015 mg/mL). The catalyst was then sent into the muffle furnace to dry at 80 °C for 12 hours and 100 °C for 4 hours before calcination at 500 °C for 4 hours in air. Finally, the sample was reduced in-situ in a flow of 20 kPa H_2 (99.999%, Airgas, with balance He, Airgas, 99.999%, equipped with high-capacity moisture and oxygen traps (Cat. # 21997 and Cat. # 20601, Restek), 50 sccm of total flow rate) at 500 °C (15 °C /min) for 2 hours before use.

The 0.05% $Ir/MgAl_2O_4$ with mostly subnanometer clusters (referred as $Ir_{0.7nm}/MgAl_2O_4$) was synthesized by wet impregnation using the same iridium nitrate precursor. 200 mL of deionized water was added into the Pyrex bottle before the addition of the diluted iridium nitrate precursor, and then the fine powder of $MgAl_2O_4$ support (Puralox MG30, Sasol) was added into the precursor solution under stirring. The $MgAl_2O_4$ support (Puralox MG30, Sasol) was calcined at 500 °C for 4 hours in the muffle furnace before use. After stirring for 4 hours, the solution was filtered out and the solid sample was dried in air overnight at room temperature. The weight loading of the catalyst was confirmed to be 0.05% since the Ir in the filtrate was measured by ICP- AES and no

Ir was detected. The catalyst was then sent into the muffle furnace to dry at 80 °C for 12 hours and 100 °C for 4 hours before calcination at 500 °C for 4 hours in air. Finally, the sample was reduced in-situ in a flow of 20 kPa H_2 (balance He, 50 sccm of total flow rate) at 700 °C (10 °C /min) for 2 hours before use.

The 1% Ir/$MgAl_2O_4$ catalyst with mostly small sized nanoparticles (referred as $Ir_{1.3nm}$/$MgAl_2O_4$) was prepared by incipient wetness. The fine powder of $MgAl_2O_4$ support (Puralox MG30, Sasol, calcined at 500 °C before use) was weighed and poured into a 150 mL beaker. The iridium nitrate precursor solution was diluted with appropriate amount of deionized water to achieve 1% weight loading on the $MgAl_2O_4$ support. Then the diluted iridium nitrate solution was dropped onto the support to fill the pores on the support surface and dried in air overnight at room temperature. The sample was reduced at 800 °C for 2 h (15 °C/min) in 50 kPa H_2 (balance He, 100 sccm of total flow rate) in a tube furnace. Finally, the catalyst was diluted and pelletized with appropriate amount of SiO_2 inert and then re-reduced in-situ at 800°C for 2 h (15 °C/min) in 20 kPa H_2 (balance He, 50 sccm of total flow rate) before use. Details of the pretreatment methods for all Ir/$MgAl_2O_4$ catalysts are summarized in Supplementary Information Table S3.1.

3.3.2 In-situ diffuse reflectance infrared Fourier transform spectroscopy (DRIFTS)

In-situ diffuse reflectance infrared Fourier transform spectroscopy (DRIFTS) was used to study the interaction between the supported Ir and CO adsorbent. The experiments were operated on a Thermo Scientific IS-50R Fourier transform infrared spectrometer equipped with a mercury cadmium telluride (MCT-A) detector. The spectral resolution was 4 cm^{-1} for collection and each spectrum reported is an average of 32 scans in Kubelka-Munk (K-M) units. After loading the catalyst sample (approximately 50 mg with pellet size of 25–90 μm), the chamber (Harrick Praying Mantis high temperature DRIFTS reaction chamber) was sealed and connected to a temperature control system and a gas flow system controlled by mass flow controllers (5850EM, Brooks Instrument). The catalysts were pretreated in-situ in the chamber at atmosphere pressure under the conditions listed in Supplementary Information Table S3.1. After the pretreatment, a background spectrum was collected at 35 °C under N_2 flow (supplied from house-liquid N_2 boil-off and then further purified using high-capacity moisture and oxygen traps (Cat. # 21997 and Cat. # 20601, Restek)) and then applied for each experiment. Then 1kPa CO (5% CO, balance N_2, certified grade, Airgas, equipped with a metal carbonyl purifier (Matheson, NanoChem Metal-X) to remove trace amount of metal carbonyls) was flowed for 5 minutes and then followed by a purge with N_2 only to remove the physisorbed CO during which period a series of continuous spectra were collected every 20 seconds. All spectra reported in this article were recorded right after 5 minutes purge with N_2.

3.3.3 Atomic resolution characterization (HAADF-STEM)

High-angle annular dark-field scanning transmission electron microscopy (HAADF-STEM) characterization was performed on an FEI TITAN 80–300 in STEM mode with a CEOS GmbH double-hexapole aberration corrector. The particle size of the catalyst was estimated by counting the single atoms and measuring the diameter of the nanoparticles from multiple images using ImageJ. Details of the analysis for particle size distribution has been reported elsewhere [19]. Basically, the surface-average particle size were estimated by $d_{SA} = \frac{\sum n_i d_i^3}{\sum n_i d_i^2}$ [20]， and the total number of atoms per particle was calculated by $N_T = \frac{\pi D^3 \rho N_A}{6M_w}$ [19]， where n_i is the number of clusters with a diameter d_i and D is the diameter of the particle measured based on STEM image.

The particle size distribution (atomic percentage) shown in Figure 3.1 was calculated based on 1160 Ir single atoms and 36 Ir nanoparticles for $Ir_{SA-0.7nm}/MgAl_2O_4$ catalyst, 422 single atoms and 50 nanoparticles for $Ir_{0.7nm}/MgAl_2O_4$ (0.05% $Ir/MgAl_2O_4$) catalyst and 127 single atoms and 60 nanoparticles for $Ir_{1.3nm}/MgAl_2O_4$ (1% $Ir/MgAl_2O_4$) catalyst. The abbreviation of each catalyst as referred based on particle size is listed in Table 3.1.

3.3.4 Volumetric CO chemisorption

The dispersion of Ir sites on the catalyst surface was measured by volumetric CO chemisorption (Micromeritics 3Flex). Approximately 0.3–1.0 gram of sample was used in total for each measurement. The $Ir/MgAl_2O_4$ samples were pressed and sieved into 425-710 μm particles before packing into the quartz tube and then pretreated with the same procedure listed in Supplementary Information Table S3.1. The total flow rate was 80 sccm for each step with pure gas for each pretreatment step. Finally, the sample was evacuated to 10-5 mmHg for 1 hour at 35 °C before CO (99.999%, Airgas) chemisorption. The adsorption of CO was conducted twice with an evacuation step between them and difference of the isotherms obtained by the 1st and 2nd adsorption is counted for the quantity of CO adsorbed on the catalyst and calculated for the dispersion of exposed Ir sites on the surface of the catalyst.

3.3.5 Ethane hydrogenolysis

The reaction of ethane hydrogenolysis was performed in a packed-bed quartz tubular reactor (3/8 in. O.D.) connected to a flow system and placed in a heat furnace. The gas flow system is fully PC automated connected with LabView software system and well controlled by the mass flow controller (Brooks Instrument 5850). The reactants are metered electronically by the mass flow controller with 20% C_2H_6 (balance He, certified standard, Airgas), pure H_2 (99.999%, Airgas) and

He (Airgas, 99.999%, equipped with high-capacity moisture and oxygen traps (Cat. # 21997 and Cat. # 20601, Restek)). An extra K-type thermocouple was mounted on the outer wall of the reactor with the tip centered at the catalyst bed to get accurate reaction temperature in the system. The gas composition was analyzed by a gas chromatography (Agilent Micro GC 490) at where the products will be sampled every 2.5 minutes and output the gas composition data to the PC. The GC was equipped with a TCD detector and 3 columns (Mol Sieve 5A PLOT to quantify H_2, Pora PLOT U column to quantify CH_4 and an Al_2O_3 column to quantify C_2H_6). The GC was calibrated with the calibration gas (certified standard, Airgas) before use, and the calibration of the mass flow controller was conducted by the flowmeter (Agilent ADM 2000) and the GC.

Turn over frequency (TOF) was measured in the kinetic regime (conversion < 3%). It was calculated by normalizing the reaction rate ($\mathrm{mol}_{C_2H_6}\ \mathrm{g}_{\mathrm{cat}}^{-1}\ \mathrm{s}^{-1}$) to the number of Ir sites ($\mathrm{mol}_{\mathrm{Ir}}\ \mathrm{g}_{\mathrm{cat}}^{-1}$, based on the quantity of CO adsorbed from volumetric CO chemisorption assuming a CO : Ir stoichiometry of 1). The comparison of the activity trend on the whole series of catalysts has excluded the influence of transport limitations. The $Ir_{1.3nm}/MgAl_2O_4$ was diluted 200 times with SiO_2. The details of the analysis and calculation for the transport limitation criterion are shown in the Supplementary Information.

3.4 Results

3.4.1 Particle size distribution by HAADF-STEM

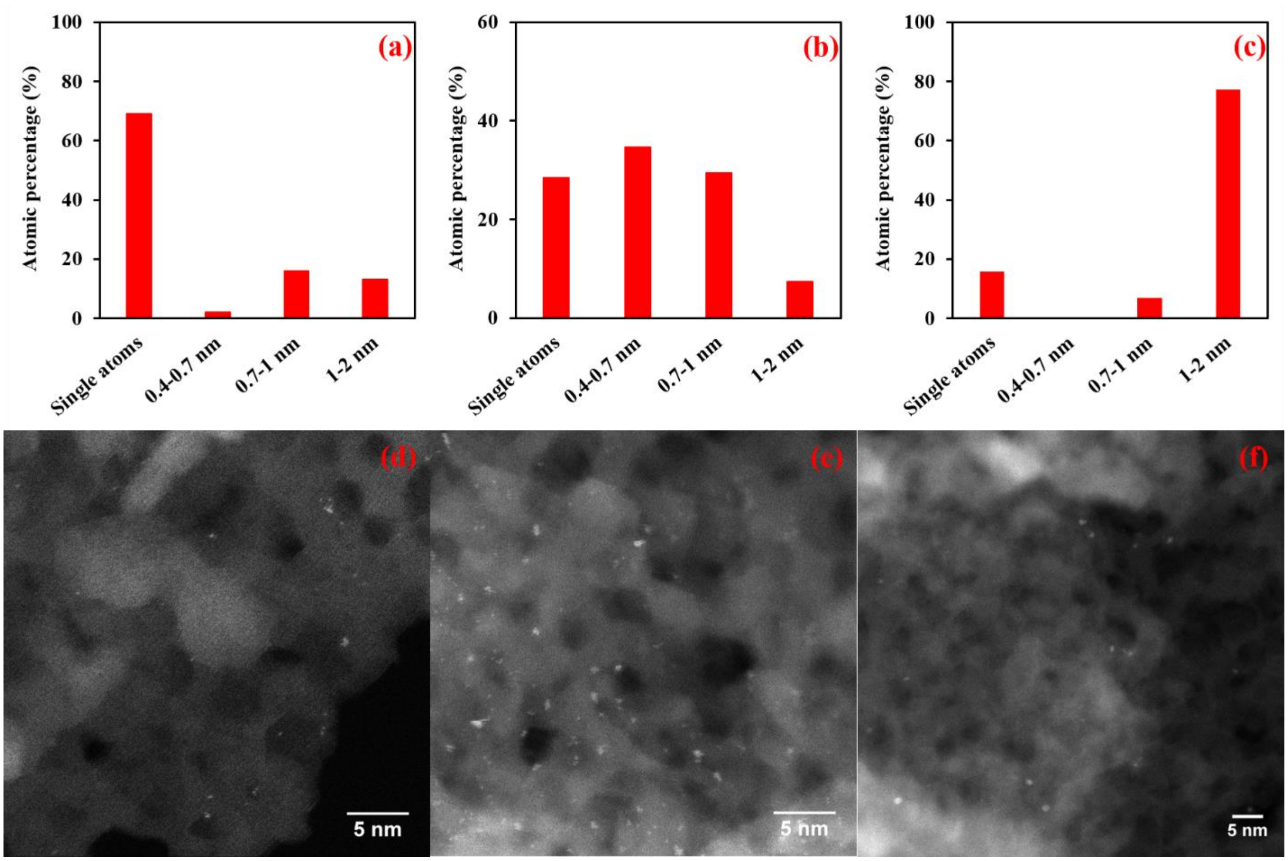

Figure 3.1 Particle size distribution (a–c) and HAADF-STEM images of Ir/$MgAl_2O_4$ catalysts after pretreatment. (a, d) $Ir_{SA\text{-}0.7nm}$/$MgAl_2O_4$ (0.05% Ir/$MgAl_2O_4$) with mostly single atoms and clusters with surface-average particle size of 0.7 nm, (b, e) $Ir_{0.7nm}$/$MgAl_2O_4$ (0.05% Ir/$MgAl_2O_4$) with mostly subnanometer clusters with surface-average particle size of 0.7 nm and (c, f) $Ir_{1.3nm}$/$MgAl_2O_4$ (1% Ir/$MgAl_2O_4$) with mostly nanoparticles with surface-average particle size of 1.3 nm.

The Ir/$MgAl_2O_4$ catalysts were characterized by scanning transmission electron microscopy (STEM) after reduction (pretreatment details in Supplementary Information Table S3.1) and representative images are shown in Figure 3.1. Despite the high calcination (500 °C) and reduction (500 °C) temperatures, the $Ir_{SA\text{-}0.7nm}$/$MgAl_2O_4$ catalyst (shown in Figure 3.1-(a) and 3.1-(d)) is mainly comprised of single atoms and a small fraction of nanoparticles (≤ 2 nm), and the surface-average size for the particles is ~0.7 nm. The $Ir_{0.7nm}/MgAl_2O_4$ (shown in Figure 3.1-(b) and 3.1-(e)) consists of some single atoms and mostly subnanometer clusters between 0.4 and 1 nm, and the surface-average particle size is 0.7 nm. For the higher metal loading of $Ir_{1.3nm}/MgAl_2O_4$ catalyst (shown in Figure 3.1-(c) and 3.1-(f)), the size of the particles centralized between 1–2 nm and the surface-average particle size is ~1.3 nm. There are also some single atoms, but the percentage is very low comparing to the other two catalysts. Even though the weight loading was improved by 20 times and the catalyst was pretreated at very harsh conditions (reduction at 800 °C for twice before use), we are still not able to get very large Ir particles. This is consistent with the results from experimental and computational study conducted by Li et al. that the strong interaction between the epitaxial metal (e.g. Pt, Ir and Rh) and the (111) facets of spinel structure support limits the metal sintering [17, 21]. Details of the particle size and abbreviation referred for each catalyst are listed in Table 3.1.

Table 3.1 Average particle size of all the supported Ir catalysts used for the study of ethane hydrogenolysis from the analysis of STEM images.

Weight Loading (%)	Surface-average diameter (nm)	Abbreviation of Catalyst
0.05%	Single atoms + 0.7	$Ir_{SA-0.7nm}/MgAl_2O_4$
0.05%	0.7 ± 0.15	$Ir_{0.7nm}/MgAl_2O_4$
1%	1.3 ± 0.24	$Ir_{1.3nm}/MgAl_2O_4$

3.4.2 In-situ DRIFTS characterization

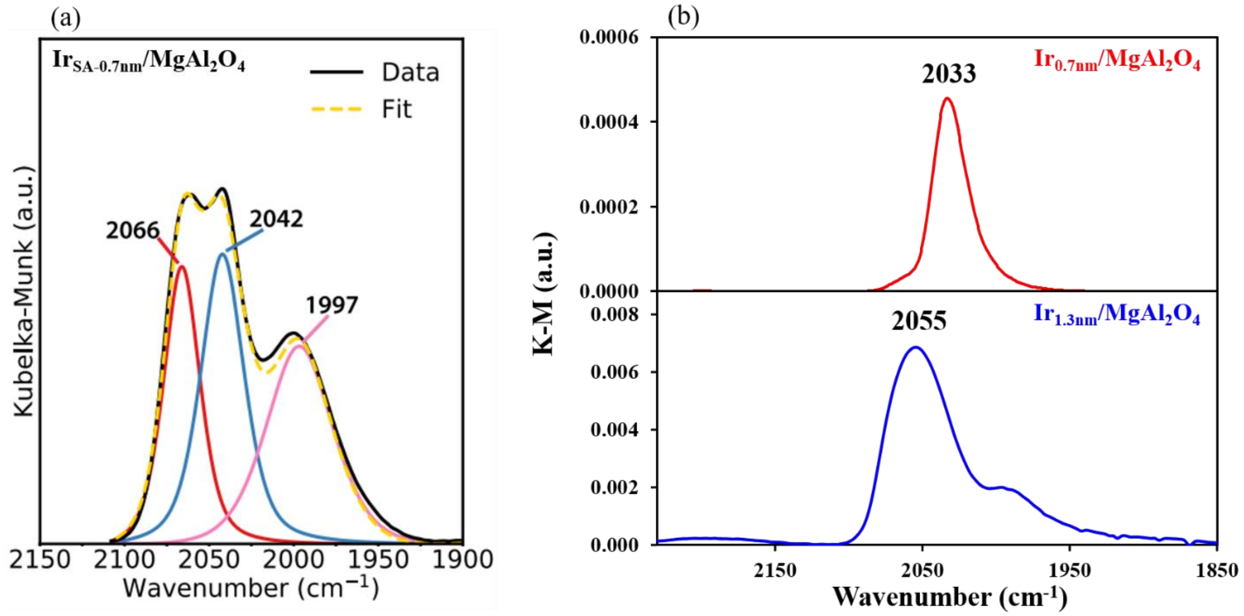

Figure 3.2 In-situ DRIFTS spectra of CO adsorption on the Ir$_{\text{SA-0.7nm}}$/MgAl$_2$O$_4$ (a), Ir$_{0.7\text{nm}}$/MgAl$_2$O$_4$ and Ir$_{1.3\text{nm}}$/MgAl$_2$O$_4$ (b) after 5 min exposure to CO at 35 °C. The DRIFTS spectra on Ir$_{\text{SA-0.7nm}}$/MgAl$_2$O$_4$ (a) [19] was reprinted with permission from (Lu, Yubing, et al. "A versatile approach for quantification of surface site fractions using reaction kinetics: The case of CO oxidation on supported Ir single atoms and nanoparticles." Journal of Catalysis 378 (2019): 121-130.). Copyright (2019) ELSEVIER. The DRIFTS spectra on Ir$_{0.7\text{nm}}$/MgAl$_2$O$_4$ and Ir$_{1.3\text{nm}}$/MgAl$_2$O$_4$ (b) [22] was reprinted with permission from (Zhang, Xiwen, et al. “Structure sensitivity of n-butane hydrogenolysis on supported Ir catalysts.” Journal of Catalysis (2020).). Copyright (2020) ELSEVIER.

CO chemisorption on the Ir/MgAl$_2$O$_4$ catalysts was characterized by DRIFTS, and the details of the analysis have been published elsewhere [19, 22]. In Figure 3.2-(a), the 2066 and 1997 cm^{-1} peaks are assigned to di-carbonyl on Ir single atoms, while the peak at 2042 cm^{-1} represents for the nanoparticles. The DRIFTS spectra for CO adsorption on single atoms and nanoparticles are consistent with the particle size distribution shown in Figure 3.1-(a) and (d). While Figure 3.2-(b) shows the spectra on Ir$_{0.7\text{nm}}$/MgAl$_2$O$_4$ and Ir$_{1.3\text{nm}}$/MgAl$_2$O$_4$. The linear CO adsorption band on the nanoparticles shift from 2033 to 2055 cm^{-1}. The blue shift is also consistent with the increasing surface-average particle size from 0.7 to 1.3 nm based on the statistic of particle size distribution in Figure 3.1-(e) and 3.1-(f).

3.4.3 Structure sensitivity of ethane hydrogenolysis

Three $Ir/MgAl_2O_4$ catalysts were tested for ethane hydrogenolysis to study the structure sensitivity. Figure 3.3 shows a comparison of the activation energy in an Arrhenius plot. From the figure, the $Ir_{1.3nm}/MgAl_2O_4$ with mostly large nanoparticles is the most active with the lowest activation barrier. Nevertheless, as the particle size decreases, the activity first drops slightly on $Ir_{0.7nm}/MgAl_2O_4$ subnanometer clusters and increases again on the mostly single atoms of $Ir_{SA-0.7nm}/MgAl_2O_4$ catalyst. The catalyst deactivation during the measurements for activation energy and reaction orders is summarized in Table 3.2. The level of deactivation is acceptable on the three catalysts. The activation energies were measured by both heating and cooling down between 335 and 350 °C, and the Ea results by cooling down were reported for comparison since the influence by deactivation is relatively low by cooling down. Details of analysis on the activation energy were shown in the Arrhenius plot in Supplementary Information Figure S3.1. The activation energies were measured 4 times on $Ir_{1.3nm}/MgAl_2O_4$ catalyst by increasing and decreasing the temperature between 335 and 350 °C. Because of the deactivation, the activation energy obtained by heating is always a little lower than that obtained by cooling down. The accurate results should be in the middle of them and from math closer to that obtained by cooling down. So the results of activation energy reported in this work are fitted from the activity data by cooling down from 350 °C to 335 °C.

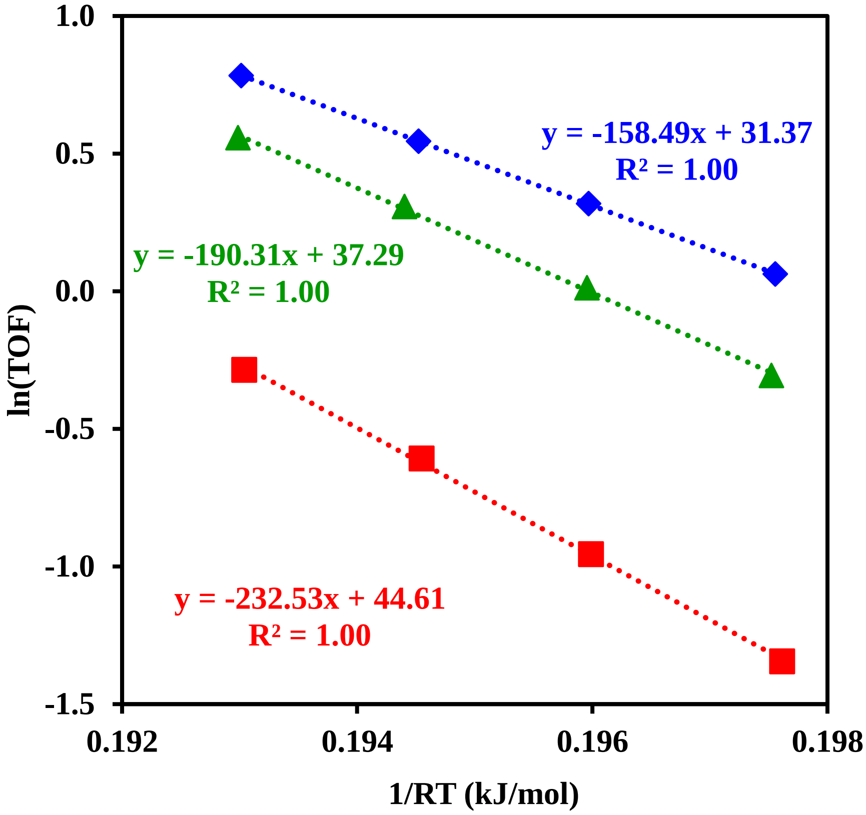

Figure 3.3 Comparison of the activation energy of ethane hydrogenolysis measured by cooling down from 350 to 335 °C on the catalyst of $Ir_{1.3nm}/MgAl_2O_4$ nanoparticles (blue diamonds) diluted by 200 times with SiO_2, the $Ir_{0.7nm}/MgAl_2O_4$ subnanometer clusters (red squares), and the $Ir_{SA-0.7nm}/MgAl_2O_4$ catalyst with mostly single atoms (green triangles).

The trend is not very consistent with that obtained by Song et al. on the series of Pt/SBA-15 catalyst between 1 – 10 nm. They found the activity monotonically increases as the average particle size of Pt keeps decreasing, especially when the size is smaller than 4 nm [7]. It is well known that the percentage of under-coordinated sites (e.g. corner, edge atoms within the particle) will increase as the metal particle size decreases. These under-coordinated sites greatly influence the adsorption of the reactant adsorbent on the metal because of their special electronic properties from the well-coordinated atoms on the flat surface. The theory works well in their case when the particle size is still larger than 1 nm. However, in our case, the opposite trend shown in Figure 3.3 from nanoparticles (~1.3 nm) to subnanometer clusters (~0.7nm) still could not be explicitly explained. Song et al. held that a large ensemble with multiple metal atoms align adjacently is necessary for the hydrogenolysis of ethane molecules, as the carbon atoms are likely bonding to multiple metal atoms with H atoms adsorbed at the neighbor sites [7]. Therefore, the number of sites for reactants adsorption might be determinant for the performance of structure sensitivity when the particle size is in the subnanometer regime. Goodman tested the ethane hydrogenolysis on the single crystal catalysts and the results show the Ni (100) surface is significantly more active than Ni (111) surface. On Ni (111) surface, the distance between the 3-fold hollow sites, which responds for the adsorption of ethane molecules, is approximately 0.14 nm and very close to the C–C bond length of an ethane molecule (0.13 – 0.15 nm); while on Ni (100) surface, the distance between the 4-fold hollow sites is about 0.25 nm, much larger than C–C bond length of ethane. That is possibly the reason that the ethane C–C bond is more easily to be broken on Ni (100) surface. Therefore, spatial distance between the atoms aligned on the surface is the factor that determines the reactivity, and it varies with different metals. In addition to the spatial distance, Martin, G. A. correlated the ensemble size and critical diameter to explain the structure sensitivity. When the size of metal particle decreases, the number of feasible metal atoms on the surface drops greatly as a unit of per size, and hence the activity would be close to zero when the particle size is smaller than a critical diameter. The particle with the least required number of adjacent atoms as critical diameter is an ensemble for the certain reaction. For example, 12 Ni adjacent atoms are necessary as an ensemble for ethane hydrogenolysis, while the ensemble for propane hydrogenolysis consists of 12 and 17 atoms for different reaction pathways of one and two C–C bond cleavage to produce $C_1 + C_2$ and $3C_1$ [10]. Kawi et al. got similar trend on Ir particles supported on MgO for propane hydrogenolysis and Ir_4/MgO catalyst is considerably less active than the large Ir nanoparticles (details of particle size was not reported) on the same support [23]. Thus, it is still under debate how many adjacent atoms are necessary for an ensemble to react with varying number of carbon atoms in the reactants.

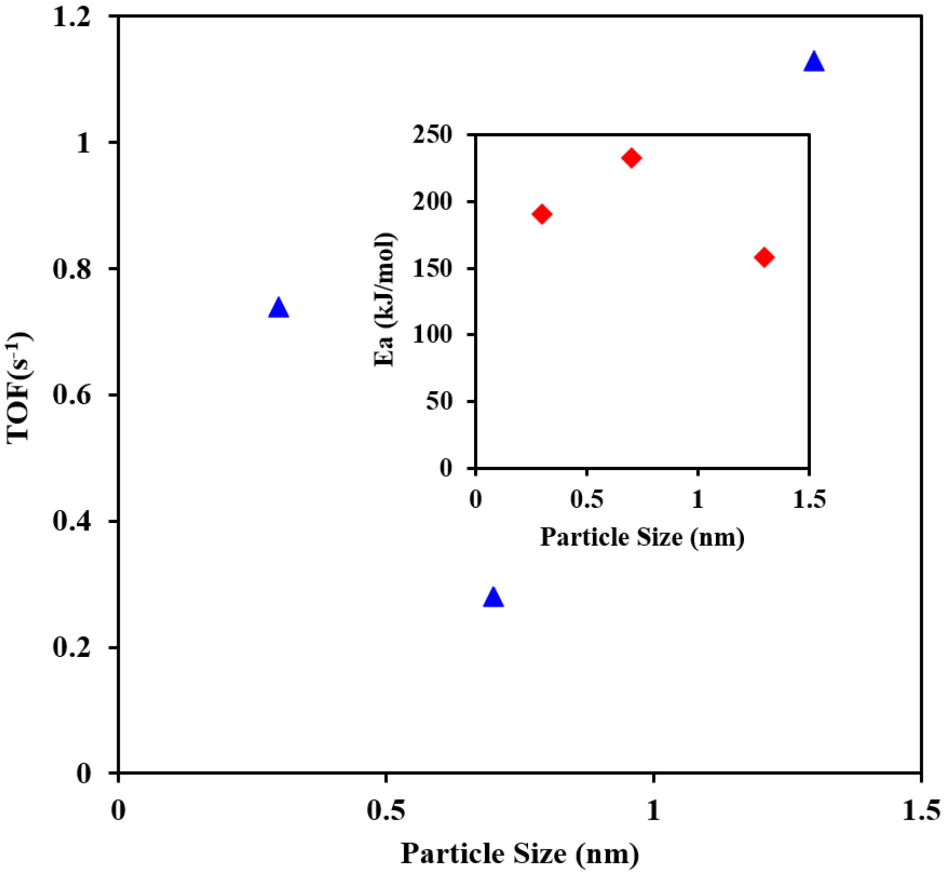

Figure 3.4 TOF(s^{-1}) and activation energy (inner plot) as a function of surface-average Ir particle size (nm) during ethane hydrogenolysis on Ir/$MgAl_2O_4$. Reaction conditions: 10.13 kPa H_2 and 1.01 kPa n-C_2H_6 at 335 °C and the conversion was < 3.5%.

From STEM analysis after n-butane hydrogenolysis and one cycle of regeneration (Supplementary Information Figure S3.2), the percentage of single atoms is much lower than that before the reaction. Due to the higher temperature used for ethane hydrogenolysis, it is highly possible that the higher activity on the $Ir_{SA-0.7nm}/MgAl_2O_4$ with mostly single atoms is because of the aggregation of Ir single atoms during the reaction. It is remaining unknown when the aggregation happens and why the single atoms become mobile under the reaction condition. We have confirmed the structure of $Ir_{SA-0.7nm}/MgAl_2O_4$ catalyst does not change at all after CO oxidation [19]. In this case, the mobility of Ir single atoms might be activated under the H_2 atmosphere, as the reaction temperature is as high as 350 °C, which is slightly lower than the reduction temperature of 500 °C. It is likely the Ir atoms restore mobility under such conditions but favors aggregation when there are hydrocarbon species.

Table 3.2 Comparison of activity and deactivation of ethane hydrogenolysis on each catalyst. The unit of TOF is s^{-1}.

Catalyst	**TOF, s^{-1} (initial)**	**TOF, s^{-1} (end)**	**Deactivation**	**Time**
$Ir_{1.3nm}/MgAl_2O_4$	1.13	0.91	19.5%	10.5 hours
$Ir_{0.7nm}/MgAl_2O_4$	0.28	0.24	13.4%	7 hours
$Ir_{SA-0.7nm}/MgAl_2O_4$	0.74	0.70	5.8%	6.5 hours

3.5 Possible Reaction Mechanism

Scheme 3.1 shows a possible sequence of elementary reaction steps of ethane hydrogenolysis from literature [24-26]. It is generally accepted that after flowing the reactants, the reaction would start from the dissociative adsorption of H_2 during hydrogenolysis. On Ir/SiO_2 particles (~7 nm), the C_2H_6 and H_2 order were reported as 1 and -3 with H* species as the most abundant surface intermediate and $*C_2H_2*$ as the intermediate that going through the C–C bond cleavage [24].

However, in this study, the reaction orders are quite different from their results, probably led by different reaction mechanism. Table 3.3 is the summary of all the kinetic parameters on the three catalysts with different particle sizes.

$$H_2 + 2 * \rightleftharpoons 2\, H^* \qquad (1)$$

$$C_2H_6 + * \rightleftharpoons C_2H_6^* \qquad (2)$$

$$C_2H_6^* + * \rightleftharpoons C_2H_5^* + H^* \qquad (3)$$

$$C_2H_5^* + 2 * \rightleftharpoons {}^*C_2H_4^* + H^* \qquad (4)$$

$$\longrightarrow$$

$$\rightarrow$$

$$\cdots$$

$${}^*C_2H_{6-(y-1)}^* + * \rightleftharpoons {}^*C_2H_{6-y}^* + H^* \qquad (5)$$

$${}^*C_2H_{6-y}^* \rightleftharpoons CH_a^* + CH_b^* \qquad (6)$$

$$CH_a^* + xH^* \rightleftharpoons CH_4 + (x+1)* \qquad (7)$$

Scheme 3.1 One possible sequence of elementary steps of ethane hydrogenolysis on Ir/$MgAl_2O_4$ catalysts.

Table 3.3 A summary of activation energies measured by cooling down from 350 to 335 °C (1.01kPa C_2H_6 and 10.13kPa % H_2 with 100 sccm total flow rate) and H_2 order (1.01kPa C_2H_6, 10.13– 19.25kPa H_2) and C_2H_6 order (10.13kPa H_2, 1.01–2.84kPa C_2H_6) at 335°C.

Catalyst	**Ea (kJ/mol)**	**Conversion**	**H_2 Order**	**C_2H_6 Order**
$Ir_{1.3nm}/MgAl_2O_4$	158.5	0.6 – 1.5%	-1.2	0.5
$Ir_{0.7nm}/MgAl_2O_4$	232.5	1 – 3%	-0.7	0.05
$Ir_{SA\text{-}0.7nm}/MgAl_2O_4$	190.3	3.5 – 9%	-0.3	0.1

Based on the elementary steps proposed in Scheme 3.1, the differential equations could be listed with the assumption that the H_2 dissociative adsorption and C_2H_6 adsorption with H progressive removal steps are quasi-equilibrated.

$$\frac{d\theta_H}{dt} = k_1^+ P_{H_2}\theta_*^2 - k_1^-\theta_H^2$$

$$\frac{d\theta_{C_2H_6}}{dt} = k_2^+ P_{C_2H_6}\theta_* - k_2^-\theta_{C_2H_6}$$

$$\frac{d\theta_{C_2H_5}}{dt} = k_3^+\theta_{C_2H_6}\theta_* - k_3^-\theta_{C_2H_5}\theta_H$$

$$\frac{d\theta_{C_2H_4}}{dt} = k_4^+\theta_{C_2H_5}\theta_*^2 - k_4^-\theta_{C_2H_4}\theta_H$$

$$\frac{d\theta_{C_2H_3}}{dt} = k_5^+\theta_{C_2H_4}\theta_* - k_5^-\theta_{C_2H_3}\theta_H$$

$$\frac{d\theta_{C_2H_2}}{dt} = k_6^+\theta_{C_2H_3}\theta_* - k_6^-\theta_{C_2H_2}\theta_H$$

…

$$\frac{d\theta_{CH_4}}{dt} = k^{+}_{CH_4}\theta_{CH_x}\theta_H^{4-x} - k^{-}_{CH_4}P_{CH_4}\theta_*^{5-x}$$

θ_H, $\theta_{C_2H_6}$, $\theta_{C_2H_5}$, … represent the fraction of each adsorbent on the surface of catalyst. The total coverage of all the adsorbent and the vacant sites is 1.

$$\theta_* + \theta_H + \theta_{C_2H_6} + \theta_{C_2H_5} + \theta_{C_2H_4} + \theta_{C_2H_3} + \theta_{C_2H_2} + \cdots = 1$$

As the partial pressure of hydrogen is much higher than ethane (H_2/C_2H_6 ratio = 10) and the dissociative adsorption of hydrogen on the surface is assumed to be very fast, the θ_H term ($\theta_H = \sqrt{K_{H_2}P_{H_2}}\,\theta^*$) would be much larger than all the other terms. Therefore, $\theta^* \sim (K_{H_2}P_{H_2})^{-0.5}$.

By assuming that "$*C_2H_2*$", "$*C_2H_3*$", "$*C_2H_4*$", "$*C_2H_5$" and "$*C_2H_6$" is the intermediate, respectively, that undergoes C–C bond cleavage and all the other steps are quasi-equilibrated steps (the correspondent differential equation equals zero), the derived hydrogen order would be -3, -2.5, -2, -1.5, -1, respectively, while the ethane order is always 1 for all these cases. However, the "$*C_2H_6$" species should not be considered as the intermediate that undergoes the C–C bond cleavage, as the adsorbed ethane species must dehydrogenate first before cleaving the C–C bonds. Therefore, the "-1" hydrogen order does not make sense and should be excluded from the list. Therefore, it seems that when the C–C bond cleavage on "$*C_2H_5$" is considered as the rate determining step and the adsorbed hydrogen is assumed to be the most abundant surface species, the derived order of -1.5 in H_2 and 1 in ethane is the closest to the experimental results of the reaction orders -1.2 in H_2 and 0.5 in ethane.

Another series of adsorbed hydrocarbon species could also be assumed as the most abundant surface intermediates. The derived reaction order results as well as the assumptions are summarized in Table 3.4.

Table 3.4 Possibilities for H_2 and C_2H_6 orders with different assumptions for the most abundant surface species and the intermediates that undergo the C–C bond cleavage. The rate determining step is always assumed to be C–C bond cleavage in the cases showing in this table.

Intermediate for C-C bond cleavage	MASI	H_2 Order	C_2H_6 Order
$*C_2H_5$	$*C_2H_6$	-0.5	-1
$*C_2H_4*$	$*C_2H_6$	-1	-1
$*C_2H_3*$	$*C_2H_6$	-1.5	-1
$*C_2H_2*$	$*C_2H_6$	-2	-1
$*C_2H_2*$	$*C_2H_3*$	1	-1
$*C_2H_2*$	$*C_2H_5$	-1	-1
$*C_2H_3*$	$*C_2H_5$	-0.5	-1

From Table 3.4, when the most abundant surface intermediate is assumed as "$*C_2H_6$" species, the ethane order is always -1 and the H_2 order changes between -0.5 and -2 as the intermediate for C–C bond cleavage changes from $*C_2H_5$ to $*C_2H_2*$. There are also some other possibilities listed in the table when the most abundant surface intermediates are assumed to be more dehydrogenated hydrocarbon species. In addition to the previous analysis when the surface hydrogen is the most abundant surface intermediate, the actual reaction mechanism is very likely showing as the combination of these two cases. In other words, the most abundant surface species might be surface hydrogen and adsorbed hydrocarbon species altogether. For example, if the rate determine step is the C–C bond cleavage on the intermediate of $*C_2H_5$ and both of surface hydrogen and adsorbed $*C_2H_6$ species are assumed to be the most abundant surface intermediates, the simplified surface terms could be written as "$\theta_H + \theta_{C_2H_6} \sim 1$". And if so, the θ_* term must be written as the combination of H_2 and C_2H_6 terms, and hence the rate equation need to be written as the equation below. Details of the derivation process are shown in Supplementary Information.

$$r = K_{C-C} \frac{K_{C_2H_5} K_{C_2H_6} P_{C_2H_6}}{(K_{H_2}P_{H_2})^{1.5} + 2 \times K_{H_2}P_{H_2} \times K_{C_2H_6}P_{C_2H_6} + \sqrt{K_{H_2}P_{H_2}} \times (K_{C_2H_6}P_{C_2H_6})^2}$$

Besides, in the following mechanism examples, by assuming "$^*C_2H_5^*$" as the intermediate that undergoes C–C bond cleavage, the derived hydrogen order is -1.5, while the ethane order would still be 1. In fact, Cortright, R. D., et al. also proposed in their paper that $^*C_2H_5^*$ is one of the two possible intermediates (the other one is "$CHCH_3$") for C–C bond cleavage on Pt (211) and Pt (111) slabs [24, 27].

$$H_2 + 2 * \rightleftharpoons 2\,H^* \qquad (1)$$

$$C_2H_6 + * \rightleftharpoons C_2H_6^* \qquad (2)$$

$$C_2H_6^* + \ 2 * \rightleftharpoons \ ^*C_2H_5^* + \ H^* \qquad (3)$$

$$^*C_2H_5^* \rightarrow CH_2^* + \ CH_3^* \qquad (4)$$

…

or

$$H_2 + 2 * \rightleftharpoons 2\,H^* \qquad (1)$$

$$C_2H_6 + 2 * \rightleftharpoons \ ^*C_2H_6^* \qquad (2)$$

$$^*C_2H_6^* + * \rightleftharpoons \ ^*C_2H_5^* + H^* \qquad (3)$$

$$^{*}C_2H_5^{*} \rightarrow CH_2^{*} + CH_3^{*} \qquad (4)$$

…

Scheme 3.2 Another two possible sequences of elementary steps of ethane hydrogenolysis with $^*C_2H_5^*$ and $^*C_2H_6^*$ adsorbing on two sites of the catalyst surface, respectively.

The only possibility to get the ethane order closer to or less than zero is to assume the hydrogen adsorption step as the rate limiting step. When assuming the $^*C_2H_6$ is the most abundant surface species and the dissociative adsorption of H_2 is the rate determining step, the H_2 order could be 1 and the ethane order could be -2. After comparing with the experiment results, the reaction on the nanoparticles is not very likely to take place under this mechanism. It has also been reported that the H–D exchange under deuterium and hydrocarbon atmosphere for the nanoparticles is very fast comparing with the hydrogenolysis rate [28], so the rate determine step is not likely to be the dissociative adsorption of H_2. However, on the single atom catalysts or very small clusters, it is possible that the dissociative hydrogen adsorption step is the rate determining step because of the very slow H–D exchange rate. For instance, the H–D exchange rate is very low on the MgO supported mononuclear Ir catalysts reported by Lu et al. [29], and when supported on TiO_2, it is about ten times lower on Pt catalyst with mostly single atoms than the nanoparticles with average particle size of 2.1 nm [16].

In this work, the ethane reaction order measured on all the three catalysts with different particle sizes is between 0-0.5, comparing with that always being 1 derived from a series of reasonable reaction mechanisms in the previous analysis. Except the aforementioned very slow rate of dissociate hydrogen adsorption, there are also other reasonable possibilities for the inconsistency.

One is that the experimental results of ethane order could be a combination effect of different sized particles as the particle size distribution is very broad. For ethane hydrogenolysis on the large nanoparticles in the size range of 1-2 nm, the reaction mechanism might follow the analysis above, while for those on the mostly single atoms, the reaction mechanism might be quite different, since an extra site on the support might be required when C_2H_x species bind with Ir single atoms (i.e. two carbon atoms of C_2H_x species bind with one oxygen atom of $MgAl_2O_4$ support and one Ir single atom at the same time). Besides, the C_2H_x species may also bind only with one site and form a π bond during hydrogenation steps, or both carbon atoms in the C_2H_x species form di-σ bonds on the Ir single atoms after binding and dehydrogenation. In these two cases, the intermediate corresponding to the C–C bond cleavage could only have less than 4 hydrogen atoms. If the dehydrogenated C_2H_x species could be adsorbed on single Ir atoms and form π bonds, the binding energy would be much weaker than that for the subnanometer clusters, which would more probably form a di-σ bond between the dehydrogenated hydrocarbon species and the neighbored Ir sites within the cluster. The adsorption of C_2H_x species on the surface of nanoparticles could also form di-σ bonds, but the binding energy of the di-σ bonds should be lower than that on the surface of subnanometer clusters because of the steric effect. These possibilities might be able to explain the higher activity of ethane hydrogenolysis on the nanoparticles and single atoms than that on the subnanometer clusters.

Another possible reason for the inconsistent ethane order is the H_2/C_2H_6 ratio during the ethane order measurement. The hydrogen partial pressure applied in the hydrogenation/hydrogenolysis reactions is always at least 10 times higher than the hydrocarbon reactant since the hydrogen species is more favorable to cover the surface of the catalyst and prevent carbon deposition from the hydrocarbon species. Meanwhile, one of the most important prerequisites for the derivation of ethane order is that the θ_H term is much larger than all the other surface coverage terms so that all the other surface coverage terms could be negligible for simplification. However, in this study, the H_2/C_2H_6 ratio decreases from 10 to 3.5 during the ethane reaction order measurement, and so the derived reaction order from the mechanism analysis does not fit the experimental result very well. As discussed in the previous analysis, it is very probable that both surface hydrogen and the hydrocarbon species are the most abundant surface intermediates, so that the experimental result of the ethane order is a combination of the reaction mechanisms with different intermediates as the most abundant surface species. Catalysts with more uniform particle size distribution would be helpful to explain the H_2/C_2H_6 ratio effect at higher range for the partial pressure of hydrogen. Furthermore, the study of H–D exchange rate on the same series of $Ir/MgAl_2O_4$ catalysts is a good way to determine if the dissociate hydrogen adsorption step is fast enough when making assumptions for quasi-equilibrated steps.

3.6 Conclusions

Three $Ir/MgAl_2O_4$ catalysts with different particle size ranging from single atoms to nanoparticles were tested for ethane hydrogenolysis for structure sensitivity study. The activity decreases from nanoparticles (~1.3nm) to subnanometer clusters (~0.7 nm) but increases again on the one with mostly single atoms. The high activity on $Ir_{SA\text{-}0.7nm}/MgAl_2O_4$ might be mostly coming from the fraction of large nanoparticles. The reaction mechanism of ethane hydrogenolysis was also analyzed. The results of H_2 and C_2H_6 reaction orders suggest a combination of different sites on these catalysts and both hydrogen and hydrocarbon species might be co-existent as the most abundant surface intermediates. Our results demonstrate the Ir catalysts in the subnanometer regime are not optimum from the activity of ethane hydrogenolysis comparing with the nanoparticles slightly larger than 1 nm.

Acknowledgement

This research was primarily sponsored by SABIC. STEM imaging was performed at the William R. Wiley Environmental Molecular Science Laboratory (EMSL) sponsored by the U.S. Department of Energy, office of Biological and Environmental Research located at Pacific Northwest National Laboratory (PNNL) under science theme proposal 49326.

References

[1] D.W. Flaherty, E. Iglesia, Transition-state enthalpy and entropy effects on reactivity and selectivity in hydrogenolysis of n-alkanes, J Am Chem Soc, 135 (2013) 18586-18599.

[2] D. Kalakkad, S.L. Anderson, A.D. Logan, J. Pena, E.J. Braunschweig, C.H.F. Peden, A.K. Datye, n-Butane hydrogenolysis as a probe of surface sites in rhodium metal particles: correlation with single crystals, The Journal of Physical Chemistry, 97 (1993) 1437-1444.

[3] G.C. Bond, J.C. Slaa, Catalytic and structural properties of ruthenium bimetallic catalysts: hydrogenolysis of propane and n-butane on RuAl2O3 catalysts modified by a Group 14 element, Journal of Molecular Catalysis A: Chemical, 106 (1996) 135-149.

[4] G.C. Bond, Metal-catalysed reactions of hydrocarbons, Springer, 2005.

[5] D.W. Goodman, Ethane hydrogenolysis over single crystals of nickel: Direct detection of structure sensitivity, Surface Science, 123 (1982) L679-L685.

[6] R.M. Rioux, H. Song, J.D. Hoefelmeyer, P. Yang, G.A. Somorjai, High-surface-area catalyst design: synthesis, characterization, and reaction studies of platinum nanoparticles in mesoporous SBA-15 silica, The Journal of Physical Chemistry B, 109 (2005) 2192-2202.

[7] H. Song, R.M. Rioux, J.D. Hoefelmeyer, R. Komor, K. Niesz, M. Grass, P. Yang, G.A. Somorjai, Hydrothermal growth of mesoporous SBA-15 silica in the presence of PVP-stabilized Pt nanoparticles: synthesis, characterization, and catalytic properties, Journal of the American Chemical Society, 128 (2006) 3027-3037.

[8] J.L. Carter, J.A. Cusumano, J.H. Sinfelt, Catalysis over supported metals. V. The effect of crystallite size on the catalytic activity of nickel, The Journal of Physical Chemistry, 70 (1966) 2257-2263.

[9] D.J. Yates, J.H. Sinfelt, The catalytic activity of rhodium in relation to its state of dispersion, Journal of Catalysis, 8 (1967) 348-358.

[10] G.A. Martin, Influence of the surface structure on the kinetics of ethane hydrogenolysis over Ni/SiO2 catalysts, Journal of Catalysis, 60 (1979) 452-459.

[11] K. An, G.A. Somorjai, Size and shape control of metal nanoparticles for reaction selectivity in catalysis, ChemCatChem, 4 (2012) 1512-1524.

[12] B.R. Cuenya, F. Behafarid, Nanocatalysis: size-and shape-dependent chemisorption and catalytic reactivity, Surface Science Reports, 70 (2015) 135-187.

[13] X.-F. Yang, A. Wang, B. Qiao, J. Li, J. Liu, T. Zhang, Single-Atom Catalysts: A New Frontier in Heterogeneous Catalysis, Accounts of Chemical Research, 46 (2013) 1740-1748.

[14] A.S. Crampton, M.D. Rotzer, C.J. Ridge, F.F. Schweinberger, U. Heiz, B. Yoon, U. Landman, Structure sensitivity in the nonscalable regime explored via catalysed ethylene hydrogenation on supported platinum nanoclusters, Nat Commun, 7 (2016) 10389.

[15] H. Wei, X. Liu, A. Wang, L. Zhang, B. Qiao, X. Yang, Y. Huang, S. Miao, J. Liu, T. Zhang, Feox-supported platinum single-atom and pseudo-single-atom catalysts for chemoselective hydrogenation of functionalized nitroarenes. Nat Commun 5: 5634–5641, in, 2014.

[16] C.-T. Kuo, Y. Lu, L. Kovarik, M.H. Engelhard, A.M. Karim, Structure Sensitivity of Acetylene Semi-Hydrogenation on Pt Single Atoms and Subnanometer Clusters, ACS Catalysis, (2019).

[17] W.-Z. Li, L. Kovarik, D. Mei, M.H. Engelhard, F. Gao, J. Liu, Y. Wang, C.H.F. Peden, A General Mechanism for Stabilizing the Small Sizes of Precious Metal Nanoparticles on Oxide Supports, Chemistry of Materials, 26 (2014) 5475-5481.

[18] Y. Lu, J. Wang, L. Yu, L. Kovarik, X. Zhang, A.S. Hoffman, A. Gallo, S.R. Bare, D. Sokaras, T. Kroll, Identification of the active complex for CO oxidation over single-atom Ir-on-MgAl2O4 catalysts, Nature Catalysis, 2 (2019) 149.

[19] Y. Lu, C.-T. Kuo, L. Kovarik, A.S. Hoffman, A. Boubnov, D.M. Driscoll, J.R. Morris, S.R. Bare, A.M. Karim, A versatile approach for quantification of surface site fractions using reaction kinetics: The case of CO oxidation on supported Ir single atoms and nanoparticles, Journal of Catalysis, 378 (2019) 121-130.

[20] J.M. Thomas, Handbook Of Heterogeneous Catalysis. 2., completely revised and enlarged Edition. Vol. 1–8. Edited by G. Ertl, H. Knözinger, F. Schüth, and J. Weitkamp, Angewandte Chemie International Edition, 48 (2009) 3390-3391.

[21] W.Z. Li, L. Kovarik, D. Mei, J. Liu, Y. Wang, C.H. Peden, Stable platinum nanoparticles on specific MgAl2O4 spinel facets at high temperatures in oxidizing atmospheres, Nat Commun, 4 (2013) 2481.

[22] X. Zhang, Y. Lu, L. Kovarik, P. Dasari, D. Nagaki, A.M. Karim, Structure Sensitivity of n-Butane Hydrogenolysis on Supported Ir Catalysts, Journal of Catalysis, (2020).

[23] S. Kawi, J.R. Chang, B.C. Gates, Cluster Catalysis: Propane Hydrogenolysis Catalyzed by MgO-Supported Tetrairidium, The Journal of Physical Chemistry, 98 (1994) 12978-12988.

[24] D.W. Flaherty, D.D. Hibbitts, E.I. Gürbüz, E. Iglesia, Theoretical and kinetic assessment of the mechanism of ethane hydrogenolysis on metal surfaces saturated with chemisorbed hydrogen, Journal of Catalysis, 311 (2014) 350-356.

[25] D.W. Flaherty, D.D. Hibbitts, E. Iglesia, Metal-catalyzed C–C bond cleavage in alkanes: effects of methyl substitution on transition-state structures and stability, Journal of the American Chemical Society, 136 (2014) 9664-9676.

[26] A. Almithn, D. Hibbitts, Comparing Rate and Mechanism of Ethane Hydrogenolysis on Transition Metal Catalysts, The Journal of Physical Chemistry C, (2019).

[27] R.D. Cortright, R.M. Watwe, J.A. Dumesic, Ethane hydrogenolysis over platinum: Selection and estimation of kinetic parameters, Journal of Molecular Catalysis A: Chemical, 163 (2000) 91-103.

[28] R.S. Dowie, D.A. Whan, C. Kemball, Hydrogenolysis of saturated hydrocarbons on evaporated platinum films, Journal of the Chemical Society, Faraday Transactions 1: Physical Chemistry in Condensed Phases, 68 (1972) 2150-2162.

[29] J. Lu, P. Serna, B.C. Gates, Zeolite-and MgO-supported molecular iridium complexes: support and ligand effects in catalysis of ethene hydrogenation and H–D exchange in the conversion of H2+ D2, ACS Catalysis, 1 (2011) 1549-1561.

Supplementary Information

Supplementary Table S3.1 Summary of pretreatment methods for Ir/$MgAl_2O_4$ before catalytic, DRIFTS and CO chemisorption measurements.

Catalyst	Weight Loading	Oxidation	Reduction
$Ir_{SA\text{-}0.7nm}/MgAl_2O_4$	0.05%	5% O_2, 100°C, 0.5 h, 400 °C, 1 h	20% H_2, 500 °C, 2 h
$Ir_{0.7nm}/MgAl_2O_4$	0.05%	5% O_2, 100°C, 0.5 h, 400 °C, 1 h	20% H_2, 700 °C, 2 h
$Ir_{1.3nm}/MgAl_2O_4$	1%	-	20% H_2, 800 °C, 2 h

When the reduction temperature is higher than 500 °C, the catalysts were pretreated in the reactor (ex-situ) before moving into the IR chamber, since the maximum temperature that could be reached in the IR chamber is ~ 500 °C. In these cases, the catalyst would be reduced again at the maximum temperature in the IR chamber right before the collection of spectra.

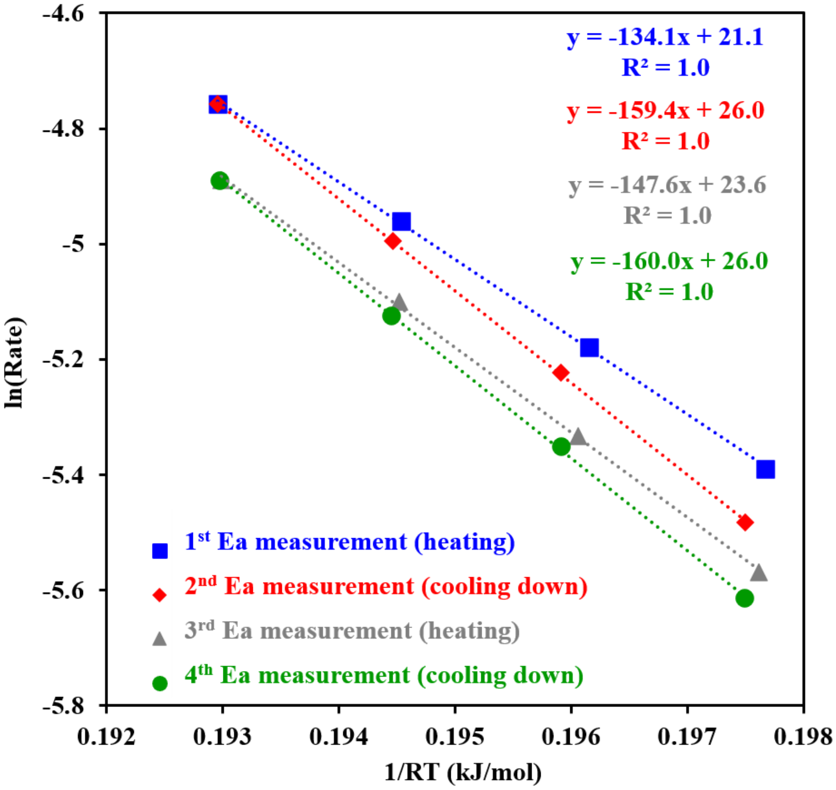

Supplementary Figure S3.1 Activation energy measured on $Ir_{1.3nm}/MgAl_2O_4$ catalyst by increasing and decreasing the temperature between 335 and 350 °C for 4 times to study the influence of deactivation on the activation energy results.

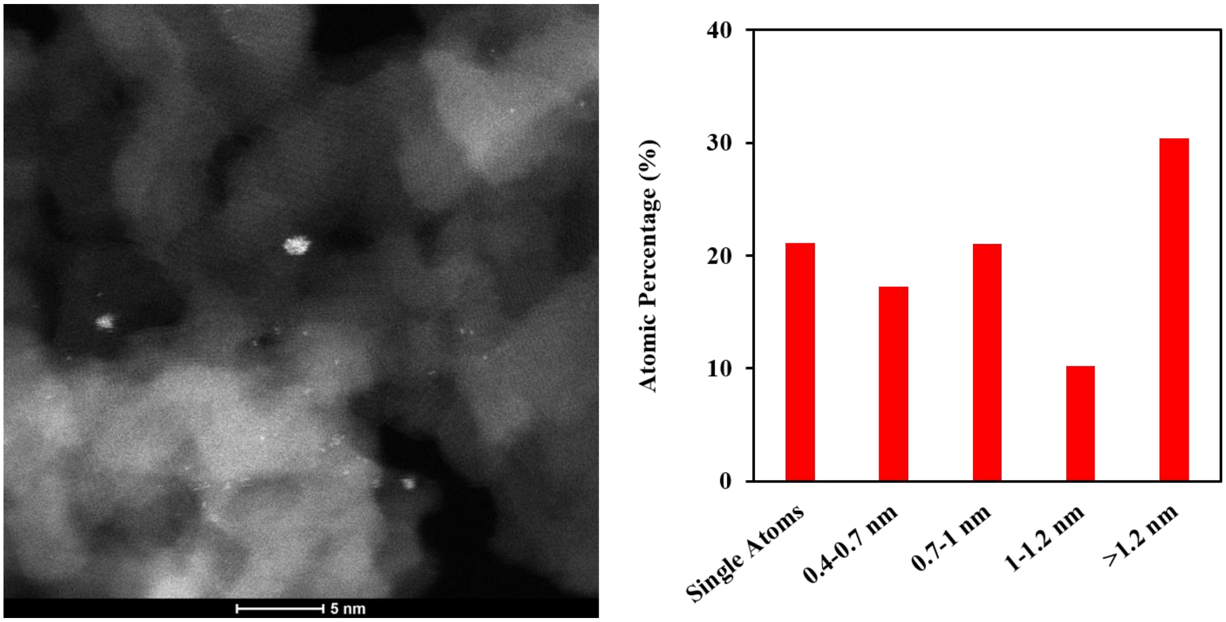

Supplementary Figure S3.2 HAADF-STEM and particle size distribution for $Ir_{SA\text{-}0.7nm}/MgAl_2O_4$ catalyst after 1 cycle of n-butane hydrogenolysis and regeneration. Reaction conditions: 10.13 kPa H_2 and 1.01 kPa n-C_4H_{10} between 170–220 °C, the conversion was controlled 0.1–10%.

The $Ir_{SA\text{-}0.7nm}/MgAl_2O_4$ catalyst was also tested for n-butane hydrogenolysis in addition to the 3 $Ir/MgAl_2O_4$ catalysts we already published earlier. The activity of n-butane hydrogenolysis shows similar trend with ethane hydrogenolysis on the series of $Ir/MgAl_2O_4$ catalysts. The activity decreases as the particle size decreases but exclusively increases on $Ir_{SA\text{-}0.7nm}/MgAl_2O_4$ with mostly single atoms. From the post-reaction STEM analysis, the fraction of single atoms decreases by two thirds and there are more subnanometer clusters between 0.4–0.7 nm and nanoparticles larger than 1.2 nm as compared with the particle size distribution in Figure 3.2. The results clearly indicate an aggregation of Ir atoms during the hydrogenolysis of n-butane. Therefore, the significant high activity of n-butane hydrogenolysis on $Ir_{SA\text{-}0.7nm}/MgAl_2O_4$ catalyst could be ascribed to the high activity coming from the fraction of large nanoparticles initially existed or the nanoparticles from the aggregation of the Ir single atoms. Here for ethane hydrogenolysis, the much higher activity on $Ir_{SA-0.7nm}/MgAl_2O_4$ catalyst is very likely the same case. Specifically, the reaction temperature for ethane hydrogenolysis (335–350°C) is much higher than n-butane hydrogenolysis (170–220 °C). The supported single atoms have more tendency to aggregate into large nanoparticles at elevated temperatures [1], indicating the possibility of more aggregation of Ir atoms in the case of ethane hydrogenolysis.

Experimental Analysis of Transport Limitation

A catalytic diffusion process includes the diffusion of the reactant molecules in the gas phase to the catalyst particle surface and the transport within the pores of the catalyst particles. This is called mass transport phenomena. When the diffusion rate is much higher than the reaction rate, the catalysts are utilized in the most effective way. In addition to the mass diffusion, heat transport phenomena also need to be considered as energy is another important factor that has great influence on the reactivity. For exothermic reactions, the excessive heat released during the reaction would cause the inner bed of catalyst or particle cores overheated; for endothermic reactions, the inadequate heat diffusion might limit the energy adsorbing and the reaction rate could be lower hence. Therefore, for kinetic parameter measurements, both of heat and mass diffusion should be well controlled so that the catalytic process would be considered as “reaction-limited” and thereby the kinetic study is meaningful [2]. This is the reason why we need to guarantee the reaction is free of transport limitations for the intrinsic kinetic study of ethane hydrogenolysis.

The most accurate method to determine if there are transport limitations is to study the dilution effect in that catalytic system. One typical example of dilution effect study for the calculation of criterion showing in the text below is ethane hydrogenolysis on the high loading catalyst of $Ir_{1.3nm}/MgAl_2O_4$ nanoparticles (the most active).

As the details shown in Supplementary Table S3.2, a series of $Ir_{1.3nm}/MgAl_2O_4$ catalysts was diluted (mass-based) with the diluent of SiO_2 powder before reaction. The SiO_2 powder was calcined in the muffle furnace at 850 °C for 5 hours with a ramp rate of 5°C/min before use. The post-calcined SiO_2 was confirmed as inert material through the SiO_2 blank test of ethane hydrogenolysis. After adding the post-calcined SiO_2 powder into $Ir_{1.3nm}/MgAl_2O_4$ catalyst by a certain mass-based ratio, the mixture was further ground and shaken on the shaker for better mixing. Then the mixed powder was pelletized in the size range of 106 – 250 μm. To minimize the heat transport limitation, the reactor applied in ethane hydrogenolysis study has the inner diameter as small as 0.4 cm. With such a thin reactor tube, the catalyst bed length must not be too long to avoid the pressure drop and the limitations for the throughput and conversion of the reaction [3]. Hence the total amount of catalyst utilized in these reactors was controlled between 50-100 mg (the catalyst bed length of 0.7 – 1.5 cm). For the first and second dilution trials in Supplementary Table S3.2, the total amount of the diluted catalyst is 50 mg since the dilution ratio of them is in the low range, while the total amount of the diluted catalyst is 100 mg for the third trial because of the higher dilution ratio.

Supplementary Table S3.2 Details of $Ir_{1.3nm}/MgAlO_4$ catalysts utilized for dilution effect experiments and a comparison of the activity results. The inner diameter of reactor utilized here is 0.4 cm. The total flow rate is 100 sccm with 1.01kPa ethane and 10.13kPa H_2 balanced with Helium.

No.	**Dilution times (SiO_2)**	**Pellet Size**	**Mole of Ir**	**Conversion % (335°C)**	**TOF, s^{-1} (335°C)**
1	200	0.106-0.250 mm	1.3 E-8	1.63%	1.13
2	20	0.106-0.250 mm	1.3 E-7	4.02%	0.28
3	1000	0.106-0.250 mm	5.2 E-9	0.54%	0.94
4	2000	Fine powder	2.6 E-9	0.35%	1.24

As we can see from Supplementary Table S3.2, the TOF is 1.13 when the dilution ratio is 200 times (No.1). As the dilution ratio increases 5 times (No.3), the TOF decreases by about 16%. The difference in TOF is within the reasonable error range. Therefore, the results show that the 200 times intraparticle dilution with SiO_2 is high enough to eliminate the heat transport limitation.

Moreover, increasing the dilution ratio could concurrently help decrease the mass transfer limitation. To make sure that 200 times dilution is not too large, a 20 times dilution was also examined. As we can see from Supplementary Figure S3.2, the TOF of the one with 20 times dilution is much smaller than the other three experiment results with 200–1000 times dilution. It is very likely that the one with only 20 times dilution has mass transfer issues. The reactant molecules could not easily travel in the porous catalyst pellets, which means many of the active sites sit on the surface of the pores inside the catalyst pellets do not take effects, leading to a much lower TOF. Therefore, 200 times intraparticle dilution ratio is optimum for ethane hydrogenolysis study on $Ir_{1.3nm}/MgAl_2O_4$ catalyst.

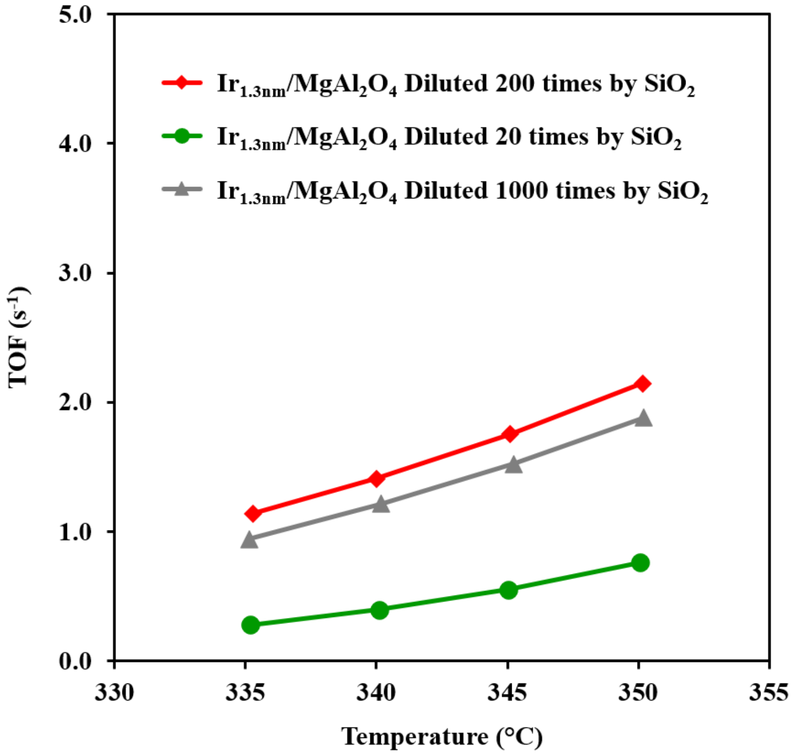

Supplementary Figure S3.3 Comparison of turnover frequency of ethane hydrogenolysis as a function of temperature on $Ir_{1.3nm}/MgAl_2O_4$ catalysts with different times of intraparticle dilution with SiO_2. The pellet diameter range of catalysts with 20-, 200- and 1000-times dilution was 0.106-0.250 milimeter.

The heat and mass transport limitations within the catalyst bed could also be determined by the calculation of the criterion. The example of the calculation procedure on the $Ir_{0.7nm}/MgAl_2O_4$ catalyst and the summary of the results based on the criterion would be provided in the following part.

Determination of Transport Limitation based on Theoretical Criterion [4]

In addition to the analysis based on experimental results of dilution effect, another fast way to determine the transport limitation is based on the criterion. In the following, one example of $Ir_{0.7nm}/MgAl_2O_4$ would be utilized to display the procedures of calculation to determine the transport limitations based on the criterion, and the calculation results of other experiments would also be summarized in a Supplementary Table S3.3.

Experiments conditions and results.

Catalyst amount: m = 50 mg = 5×10^{-5} kg

Particle size: 106-250 μm
- Average particle diameter $d_p = 1.78 \times 10^{-4}$ m.
- Average particle radius $R_p = 8.9 \times 10^{-5}$ m.

Total flow rate = 100 sccm, the percentage of ethane = 1%

$$\text{Mole flow rate of } C_2H_6 = \frac{(100\ \text{sccm}\times1\%)\times(101325\ Pa)\times(10^{-6}\ m^3)}{(60\ s)\times(8.314\ J\cdot K^{-1}\cdot mol^{-1})\times(273\ K)} = 7.44\times10^{-7}\ mol\cdot\ s^{-1}$$

(Note: at lab conditions, mass flow rate ≈ volumetric flow rate)

Activity Results.
- At 335°C (608K)
  - Conversion = 3.38% TOF=0.28 s^{-1}
  - Reaction rate = 5.02×10^{-7} mol / (g of cat ·s)
- At 350°C (623K)
  - Conversion = 8.82% TOF = 0.59 s^{-1}
  - Reaction rate = 1.32×10^{-6} mol / (g of cat ·s)

Reaction rate in the unit of m^3 / (kg · s):

$$\mathrm{r} = \frac{100 \times 1\%/10^6}{60}\ (m^3/s) \times\ conversion\ /\ catalyst\ amount\ in\ 'kg'$$

At 335°C, plug in the conversion and catalyst amount:

$$\mathrm{r} = \frac{10^{-6}}{60}(m^3/s) \times 3.38\%\ /\ (5 \times 10^{-5})kg = 1.13 \times 10^{-5}\ \ m^3/kg \cdot s$$

Mears criterion for external mass diffusion

In the ethane hydrogenolysis reaction system, there are C_2H_6 and H_2 served as reactants balanced with helium and also CH_4 as the only product. As we could learn from the CRC handbook of chemistry and physics [5], the smallest binary diffusion coefficient in the reaction system is the diffusion coefficient between methane and helium. $D_{CH_4-He}(673.15\mathrm{K}) = 2.784\ cm^2/s$.

Based on the temperature and pressure dependence equation for diffusion relationships for gases [3],

$$D_{AB}(T_2, P_2) =\ D_{AB}(T_1, P_1) \times \frac{P_1}{P_2} \times (\frac{T_2}{T_1})^{1.75}$$

In this case, at 335°C (608K),

$$D_{CH_4-He}(608\mathrm{K}) = D_{CH_4-He}(673.15\mathrm{K}) \times\ (\frac{608.15K}{673.15K})^{1.75} = 2.331\, cm^2/s = 2.331 \times\ 10^{-4}\, m^2/s.$$

Bulk density:

$$\rho_b =\ \frac{Total\ catalys\ amount\ in\ the\ reactor}{\pi \times (inner\ radius\ of\ the\ reactor) \times bed\ length}$$

$$= \frac{5 \times 10^{-5}kg}{\pi \times (0.2 \times 10^{-2}m)^2 \times (0.7 \times 10^{-2}m)} = 568.4\ kg/m^3$$

Granule density:

$$\rho_c = \frac{\rho_b}{1-\phi} = \frac{568.4\,kg}{1-0.4} = 947.35\,kg/m^3,$$

where the pellet porosity $\Phi = 0.4$

Mass transfer coefficient:

$$k_C = \frac{2 \cdot D_{CH_4-He}}{d_p} = \frac{2 \times (2.331 \times 10^{-4}\,m^2/s)}{1.78 \times 10^{-4}\,m} = 2.62\,m/s$$

k_1' is defined as the product of reaction rate in the unit of m^3 / (kg ·s) multiply the granule density:

$$k_1' = 1.127 \times 10^{-5}\,m^3/(kg \cdot s) \times 947.35\,kg/m^3 = 0.0107\,s^{-1}$$

Mears Criterion for External mass diffusion: $\frac{k_1' \cdot R_p}{k_C} < 0.15$

In this case,

$$\frac{k_1' \cdot R_p}{k_C} = \frac{0.0107\,s^{-1} \cdot (8.9 \times 10^{-5} m)}{2.62\,m/s} = 3.63 \times 10^{-7} \ll 0.15$$

Therefore, there is no external concentration gradients between the reactant's fluid bulk and the surface of the catalyst pellet.

Internal diffusion limitation by Weisz-Prater criterion

Effective diffusivity in the catalyst pellet:

$$De = \frac{D_{AB} \cdot \phi \cdot \sigma}{\tilde{\tau}} = \frac{D_{CH_4-He} \cdot \phi \cdot \sigma}{\tilde{\tau}} = \frac{2.331 \times 10^{-4} m^2/s \times 0.4 \times 0.8}{3},$$

where the constriction factor σ = 0.8;

the tortuosity $\tilde{\tau} = \frac{\text{Actual distance a molecule travels between 2 points}}{\text{Shortes distance between the 2 points}} \approx 3.$

Therefore, De $= \frac{2.331\times10^{-4}\ m^2/s\times0.4\times0.8}{3} = 2.5\times10^{-5}\ m^2/s$

Weisz-Prater Criterion: $\frac{k_1\cdot\rho_C\cdot R_p^2}{De} < 0.6$

In this case, $\frac{k_1\cdot\rho_C\cdot R_p^2}{De} = \frac{(1.127\times 10^{-5}\ m^3/(kg\cdot s))\times(947.35\ kg/m^3)\times(8.9\times10^{-5}m)^2}{(2.5\times10^{-5}m^2/s)} = 3.38\times10^{-6} \ll 0.6$

Therefore, there is no existing internal concentration gradients in the catalytic system.

Intraparticle heat transfer limitation

Heat of ethane hydrogenolysis reaction: $\Delta H_R = 65000\ J/mol$

Thermal conductivity of $MgAl_2O_4$: $\lambda_{MgAl_2O_4} = 0.1\ W/(cm\cdot K) = 10\ W/(m\cdot K)$

(Particle thermal conductivity of the catalyst λ_s *is estimated by the thermal conductivity of* $MgAl_2O_4$ *support, since the catalyst is mainly composed of the support at such a low loading iridium of 0.05%.)*

Concentration of ethane: $\frac{P_{C_2H_6}}{RT} = \frac{1\%\times101325Pa}{8.314\ J/(K\cdot mol)\times608K} = 0.2\ mol/m^3$

Measured reaction rate per unit particle volume:

$$\Re = \frac{k_1\cdot\rho_b\cdot C_{C_2H_6}}{1-\phi} = \frac{(1.127\times10^{-5}m^3/(kg\cdot s))\times(568kg/m^3)\times(0.2mol/m^3)}{1-0.4} = 2.134\times10^{-3}\ mol/(m^3\cdot s)$$

The criterion for intraparticle heat transfer limitation: $\frac{|\Delta H_R|\Re R_p^2 E_a}{\lambda_s R_g T_0^2} < 0.75$,

where Rg is the ideal gas constant in the unit of J/(mol·K); T_0 is the temperature at the surface of the particle, which, in our case, is the approximately the same as reaction temperature that measured by the additional thermocouple attached at the center of the catalyst bed; Ea is the activation energy in the unit of J/mol.

In this case,

$$\frac{|\Delta H_R|\Re R_p^2 Ea}{\lambda_{MgAl_2O_4}\cdot R_g\cdot T_0^2}$$

$$=\frac{(65000\,J/mol)\times(2.134\times10^{-3}\,mol/(m^3\cdot s)\times(89\times10^{-6})^2(230.4\times10^3\,J/mol)}{(10\ W/(m\cdot K))\times 8.314J/(mol\cdot K)\times(608K)^2}$$

$$=8.2\times10^{-9}\ll 0.75$$

Therefore, there is no intraparticle heat transfer limitation in the catalytic system.

Mears interphase heat transfer limitation

Gas-solid heat transfer coefficient: $\mathrm{h}=\frac{2\lambda_g}{d_p}$, where $\lambda_g = y_{He}\lambda_{He} + y_{H_2}\lambda_{H_2} + y_{C_2H_6}\lambda_{C_2H_6}$.

$\lambda_{H_2} = 317.6\ mW/(m\cdot K)$ at 600K, 0.1MPa;

$\lambda_{He} = 252.4\ mW/(m\cdot K)$ at 600K, 0.1MPa;

$\lambda_{C_2H_6} = 73.338\,mW/(m\cdot K)$ at 600K, 0.1MPa.

The condition of 600K, 0.1MPa is very close to our condition of 608K, 1atm, therefore, the thermal conductivity of the reaction components at the condition of 600K, 0.1MPa could be calculated by

$$89\%\times 0.2524\,W/(m\cdot K)+10\%\times0.3176\ W/(m\cdot K)+1\%\times0.073338\,W/(m\cdot K)=0.257\,W/(m\cdot K)$$

From above, $\mathrm{h}=\frac{2\lambda_g}{d_p}=\frac{2\times0.257W/(m\cdot K)}{178\times10^{-6}m}=2887.64\ W/(m^2\cdot K)$

Mears criterion for interphase heat transfer limitation: $\frac{|\Delta H_R|\Re R_p Ea}{R_g h T_0^2} < 0.15$

In this case,

0.15

Therefore, there is no interphase heat transfer limitation in the catalytic system.

Mears criterion for (interparticle) heat transfer limitation

The effective thermal conductivity of the bed:

$\lambda_{eff} = \lambda_g \cdot \beta \cdot \left(\frac{1-\phi}{\frac{\lambda_g}{\lambda_s} + \psi} \right)$, where β=1, ψ=0.04 when Φ=0.4, $\lambda_s \approx \lambda_{MgAl_2O_4} = 10\ W/(m \cdot K)$

Thus, $\lambda_{eff} = 0.257\mathrm{W/(m \cdot K)} \times \frac{1-0.4}{\frac{0.257 W/(m \cdot K)}{10\ W/(m \cdot K)} + 0.04} = 2.35 \frac{W}{m \cdot K}$

Wall heat transfer coefficient: $h_w = \frac{1.2\ \lambda_g}{d_p} = \frac{1.2 \times 0.257\ W/(m \cdot K)}{1.78 \times 10^{-4} m} = 1732.6\ \mathrm{W}/m^2 \cdot K$

Reactor radius: R_t = 0.2cm = (2×10^{-3}) m

Mears criterion for radial heat transfer limitation: $\frac{|\Delta H_R|\Re R_t^2}{\frac{\lambda_{eff} T_w^2 R_g}{Ea}} \left(1 + \frac{4\lambda_{eff}}{R_t h_w} \right) < 0.4$

In this case,

$$\frac{|\Delta H_R|\Re R_t^2}{\frac{\lambda_{eff}T_w^2R_g}{Ea}}\left(1+\frac{4\lambda_{eff}}{R_th_w}\right)$$

$$=\frac{(65000J/mol)\times(2.134\times10^{-3}mol/m^3\cdot s)\times(2\times10^{-3}m)^2}{\frac{2.35W/m\cdot K\ \times 608K^2\times 8.314}{230.4\times10^3J/mol}}$$

$$\cdot\left(1+\frac{4\times\frac{2.35W}{m\cdot K}}{(2\times10^{-3}m)\times1732.6W/(m^2\cdot K)}\right)=6.58\times10^{-5}\ll0.4$$

Therefore, there is no interparticle heat transfer limitation in the catalytic system.

A summary of transport limitation criterions for ethane hydrogenolysis on all catalysts

The results of ethane hydrogenolysis on other catalysts with or without dilution were also used to do the calculation for the transport limitation criterion. From the calculation results in the table shown below, we could learn that theoretically there is no existing transport limitation in these catalytic systems as the calculated numbers are all much smaller than the criterion. The criterion results are important reference for researchers to determine if there is transport limitation or the activity results are reliable or not.

Supplementary Table S3.3 A summary of the calculation results for transport limitation criterion of ethane hydrogenolysis on all catalysts with or without dilution.

Catalyst	External Mass Diffusion	Internal Mass Diffusion	Intraparticle Heat Transfer	Interphase Heat Transfer	Interparticle Heat Transfer
	$\frac{k_1' \cdot R_p}{k_C}$ < 0.15	$\frac{k_1 \cdot \rho_C \cdot R_p^2}{De}$ < 0.6	$\frac{\lvert\Delta H_R\rvert \Re R_p^2 E_a}{\lambda_s R_g T_0^2}$ < 0.75	$\frac{\lvert\Delta H_R\rvert \Re R_p Ea}{R_g h T_0^2}$ < 0.15	$\frac{\frac{\lvert\Delta H_R\rvert \Re R_t^2}{\lambda_{eff} T_w^2 R_g}}{Ea}\left(1 + \frac{4\lambda_{eff}}{R_t h_w}\right)$ < 0.4
$Ir_{1.3nm}/MgAl_2O_4$ ($D=200$ SiO_2)	1.7 E-7	1.6 E-6	2.7 E-9	1.1 E-7	2.2 E-5
$Ir_{SA\text{-}0.7nm}/MgAl_2O_4$ (no dilution)	9.5 E-7	8.9 E-6	1.8 E-8	6.9 E-7	1.4 E-4
$Ir_{0.7nm}/MgAl_2O_4$ (no dilution)	3.6 E-7	3.4 E-6	8.3 E-9	3.2 E-7	6.6 E-5

Derivations for the Rate Equation

The process of the derivations for the rate equation of ethane hydrogenolysis shown in section 3.3.5 would be presented in the following text.

Recall the proposed sequence of the steps and intermediates during ethane hydrogenolysis on 7 nm Ir/SiO_2 from Flaherty, David W., et al. [6].

$$H_2 + 2 * \rightleftharpoons 2\, H^* \qquad (1)$$

$$C_2H_6 + * \rightleftharpoons C_2H_6^* \qquad (2)$$

$$C_2H_6^* + * \rightleftharpoons C_2H_5^* + \ H^* \qquad (3)$$

$$C_2H_5^* + 2 * \rightleftharpoons \ {}^*C_2H_4^* + \ H^* \qquad (4)$$

$${}^*C_2H_4^* + \ {}^* \rightleftharpoons \ {}^*C_2H_3^* + H^* \qquad (5)$$

$${}^*C_2H_3^* + \ {}^* \rightleftharpoons \ {}^*C_2H_2^* + H^* \qquad (6)$$

$${}^*C_2H_2^* \rightleftharpoons \ CH^* + \ CH^* \qquad (6)$$

$$CH^* + \ 3H^* \rightleftharpoons CH_4 + 4 * \qquad (7)$$

The experimental results of the reaction orders in this study are unlikely to follow the same mechanism with the literature. Based on the analysis in section 3.3.5, if $*C_2H_5$ is the intermediate that undergoes the C–C bond cleavage, which is exactly the rate determining step.

The elementary steps could be presented as below.

$$H_2 + 2 * \rightleftharpoons 2\, H^* \qquad (1) \qquad \text{Quasi-equilibrium}$$

$$C_2H_6 + * \rightleftharpoons C_2H_6^* \qquad (2) \qquad \text{Quasi-equilibrium}$$

$$C_2H_6^* + * \rightleftharpoons C_2H_5^* + \ H^* \qquad (3) \qquad \text{Quasi-equilibrium}$$

$${}^*C_2H_5 + * \rightleftharpoons \ CH_2^* + \ CH_3^* \qquad (6) \qquad \text{Rate determining step}$$

$CH_2^* + 2H^* \rightleftharpoons CH_4 + 3^*$ (7-1) Quasi-equilibrium

$CH_3^* + H^* \rightleftharpoons CH_4 + 2^*$ (7-2) Quasi-equilibrium

The rate equation for each of the elementary step before C-C bond cleavage could also be listed as below.

$$\frac{d\theta_H}{dt} = k_1^+ P_{H_2} \theta_*^2 - k_1^- \theta_H^2$$

$$\frac{d\theta_{C_2H_6}}{dt} = k_2^+ P_{C_2H_6} \theta_* - k_2^- \theta_{C_2H_6}$$

$$\frac{d\theta_{C_2H_5}}{dt} = k_3^+ \theta_{C_2H_6} \theta_* - k_3^- \theta_{C_2H_5} \theta_H$$

As these steps are quasi-equilibrated, the terms of $\frac{d\theta_H}{dt}$, $\frac{d\theta_{C_2H_6}}{dt}$, and $\frac{d\theta_{C_2H_5}}{dt}$ approximately equal to zero.

$$k_1^+ P_{H_2} \theta_*^2 - k_1^- \theta_H^2 = 0 \quad \rightarrow \quad \theta_H = \sqrt{K_1 P_{H_2}}\, \theta_*$$

$$k_2^+ P_{C_2H_6} \theta_* - k_2^- \theta_{C_2H_6} = 0 \quad \rightarrow \quad \theta_{C_2H_6} = K_2 P_{C_2H_6} \theta_*$$

$$k_3^+ \theta_{C_2H_6} \theta_* - k_3^- \theta_{C_2H_5} \theta_H = 0 \quad \rightarrow \quad \theta_{C_2H_5} = \frac{K_3 \theta_{C_2H_6} \theta_*}{\theta_H} = \frac{K_3 K_2 P_{C_2H_6} \theta_*}{\sqrt{K_1 P_{H_2}}}$$

The rate equation for the reaction could be considered the same as the rate equation for the rate limiting step: $r = k_{C-C} \theta_{C_2H_5} \theta_*$

To solve θ_*, the most abundant surface intermediate needs to be assumed for simplification. First of all, if the surface hydrogen is the most abundant surface intermediate, which means that $\theta_H \gg$

θ_*, $\theta_{C_2H_6}$ and $\theta_{C_2H_5}$, then $\theta_H = \sqrt{K_1P_{H_2}}\theta_* \approx 1$. After solving it, $\theta_* = \frac{1}{\sqrt{K_1P_{H_2}}}$, and if the θ_* and $\theta_{C_2H_5}$ terms are plugged in the rate equation, then $r = k_{C-C}\frac{K_3\theta_{C_2H_6}\theta_*^2}{\theta_H} = k_{C-C}\frac{K_3K_2P_{C_2H_6}\theta_*^3}{\sqrt{K_1P_{H_2}}\theta_*} = k_{C-C}\frac{K_3K_2P_{C_2H_6}}{(K_1P_{H_2})^{1.5}}$. Therefore, the H_2 order is -1.5 and the ethane order is 1.

It could also be assumed that the most abundant surface intermediate is the $*C_2H_6$ species instead of the surface hydrogen. So in this case, $\theta_{C_2H_6} = K_2P_{C_2H_6}\theta_* \approx 1$, thus, $\theta_* = \frac{1}{K_2P_{C_2H_6}}$. So the rate equation could be expressed as $r = k_{C-C}\frac{K_3\theta_{C_2H_6}\theta_*^2}{\theta_H} = k_{C-C}\frac{K_3K_2P_{C_2H_6}\theta_*^2}{\sqrt{K_1P_{H_2}}} = k_{C-C}\frac{K_3K_2P_{C_2H_6}}{\sqrt{K_1P_{H_2}}\times(K_2P_{C_2H_6})^2} = \frac{k_{C-C}K_3}{\sqrt{K_1P_{H_2}}\times K_2P_{C_2H_6}}$. Therefore, the H_2 order is -0.5, and the ethane order is -1.

When it is assumed that the C–C bond cleavage on the $*C_2H_5$ is the rate determining step, and both of the surface hydrogen and adsorbed $*C_2H_6$ species are the most abundant surface intermediates, then $\theta_H + \theta_{C_2H_6} \sim 1$. This means that $\left(\sqrt{K_1P_{H_2}} + K_2P_{C_2H_6}\right) \times \theta_* = 1$, so $\theta_* = \frac{1}{\sqrt{K_1P_{H_2}} + K_2P_{C_2H_6}}$. Therefore, the rate equation could be presented as $r = k_{C-C}\frac{K_3K_2P_{C_2H_6}}{(K_1P_{H_2})^{1.5} + 2K_1P_{H_2}K_2P_{C_2H_6} + (K_2P_{C_2H_6})^2\sqrt{K_1P_{H_2}}}$. As there are more than one intermediate serving as the most abundant surface species, no simplification could be applied to the denominator of the rate equation in this case. Consequently, the reaction orders obtained from experiments are very likely a combination of different reaction mechanisms such as the coexisting surface intermediates, since the particle size distribution within the catalyst utilized in this study is not very uniform.

References

[1] J. Jones, H. Xiong, A.T. DeLaRiva, E.J. Peterson, H. Pham, S.R. Challa, G. Qi, S. Oh, M.H. Wiebenga, X.I.P. Hernández, Thermally stable single-atom platinum-on-ceria catalysts via atom trapping, Science, 353 (2016) 150-154.

[2] G.A. Martin, The kinetics of the catalytic hydrogenolysis of ethane over Ni/SiO2, Journal of Catalysis, 60 (1979) 345-355.

[3] H.S. Fogler, Essentials of chemical reaction engineering, Pearson Education, 2010.

[4] A.M. Karim, A comparison between packed bed and wall coated reactors for the steam reforming of methanol, (2003).

[5] W.M. Haynes, CRC handbook of chemistry and physics, CRC press, 2014.

[6] D.W. Flaherty, D.D. Hibbitts, E.I. Gürbüz, E. Iglesia, Theoretical and kinetic assessment of the mechanism of ethane hydrogenolysis on metal surfaces saturated with chemisorbed hydrogen, Journal of Catalysis, 311 (2014) 350-356.

Chapter 4. Structure Sensitivity of Acetylene Hydrogenation on Ir/$ZnAl_2O_4$ Catalysts

This manuscript is still in preparation.

Attribution

Xiwen Zhang performed catalyst synthesis, characterizations of DRIFTS and volumetric CO chemisorption and all the reactions for catalytic performance, including data analysis, reaction mechanism analysis and wrote the manuscript. Dr. Xu Feng, the manager of Surface Chemistry Lab at Virginia Tech, performed the XPS tests and assisted the data analysis. Researchers in Institute for Catalysis at Hokkaido University conducted the STEM characterization with the assistance of Dr. Abhijit Shrotri and his research group. Dr. Ayman M. Karim conceived the idea and directed the project. Dr. Yubing Lu and Dr. Chun-Te Kuo provided important suggestions on the analysis of DRIFTS and reaction mechanism of acetylene hydrogenation in this project. All the authors discussed the results and provided comments on the projects.

4.1 Abstract

Supported metal catalysts are widely used in industry because of their unique activity and selectivity for multiple reactions and high efficiency in novel metal utilization. Typically, the catalytic performance is strongly affected by the surface structure of the catalyst, especially the metal nuclearity. In this work, we tested the acetylene hydrogenation on a series of Ir catalysts with different particle size supported on $ZnAl_2O_4$. Systematic characterizations including HAADF-STEM and volumetric CO chemisorption were utilized to study the geometric property

difference of the Ir nuclearity, while DRIFTS and XPS were applied to establish the electronic property change on different Ir nuclearity. Three catalysts with different particle size were applied to understand the effect of geometric properties, while two catalysts with the same surface-average particle size were tested for the effect of electronic properties. The results indicate that the catalytic performance is mostly dependent on the geometric property difference (particle size effect) instead of electronic properties (e.g. the electron density of Ir after different Ir-Zn interactions) on the series of Ir catalysts supported on $ZnAl_2O_4$. The Ir single atoms and subnanometer clusters are more selective to target product of C_2H_4 but less active than large Ir nanoparticles. When the surface-average particle size is the same, the electronic properties are not essential for the selectivity to C_2H_4. Further analysis on kinetic study suggests a potential mechanism with two adsorption sites (π and di-σ) that went through the dissociative adsorption of H_2 and selective hydrogenation on C_2H_2 molecules.

4.2 Introduction

Hydrogenation is one of the most important themes in modern chemical industry [1, 2]. Semi-hydrogenation of alkynes is the direct route to remove the trace impurity of alkynes in alkenes to avoid catalyst poisoning in the downstream polymerization process. As one of the most essential organic chemicals and building blocks in the chemicals industry, ethylene and its derivatives are used to produce plastics, rubber, and other fine chemicals. However, it is very challenging to selectively hydrogenate acetylene to ethylene without further hydrogenation to ethane, as the thermodynamic stability of ethane is better than ethylene. When the adsorption energy of ethylene is strong, the adsorbed ethylene molecules tend to be further hydrogenated to form saturated ethane instead of desorbing from the metal surface as the product of ethylene. For example, some conventional supported metal catalysts, e.g. Pd, tend to over hydrogenate the acetylene to ethane. In the recent years, researchers explored to modify the electronic properties of the metal catalysts by adding a second metal (e.g. Ag [3], Cu [4, 5]), or modify the geometric properties (e.g. surface structure, particle size) so that the catalytic performance can be greatly promoted. Pei et al. tested acetylene hydrogenation on Cu-alloyed Pd single atom catalysts and they found the selectivity is improved comparing with pure Pd and Cu metal catalysts. They proposed the electron transfer from Cu to Pd can help increase the H_2 dissociation and spillover and meantime decrease the adsorption energy of C_2H_4 [4]. The electronic and geometric properties are typically linked and difficult to differentiate. Gates studied the ethylene hydrogenation on very small clusters comprised of 4 Ir atoms on DAY-zeolite and MgO so that the difference of geometric properties can be well excluded. The results show that the zeolite supported Ir catalysts are more electron-deficient so that the Ir_4/DAY-zeolite catalysts are able to bind more ligands than the Ir_4/MgO catalysts, leading to higher reactivity [6].

It has been widely reported the hydrogenation of acetylene is a structure sensitive reaction on supported Pt [7] and Pd [8, 9] catalysts. Kuo et al. studied the semi-hydrogenation of acetylene on a series of Pt/TiO_2 catalysts with different particle size ranging from single atoms to 2.1 nm and they found the activity of acetylene hydrogenation increases with increase particle size while the selectivity to ethylene is opposite. The higher selectivity to ethylene on the small sized Pt particles is because of the lower adsorption energy confirmed by the heat of adsorption from calorimetry results, which is consistent with the proposed adsorption modes on Pd catalysts in literature [7]. The ethylene molecules are most likely to form ethylidyne structure (three sites) or di-σ bonded structure (two sites) with high adsorption energy on large sized particles. While on the single atoms and subnanometer clusters, the ethylene molecules could adsorb weakly on the only one site in π

bonded mode [1]. Contradictory results have also been reported for hydrogenation reactions. For example, Ruta et al. reported both initial TOF and the selectivity of acetylene hydrogenation increases with particle size on Pd/CNF (carbon nanofibers) catalysts ranging between 8–13 nm [8]. On the other hand, Crampton et al. tested ethylene hydrogenation on a series of Pt/MgO clusters with 8–40 Pt atoms, and the activity shows a maximum on Pt_{13}/MgO and the catalysts are not active at all when the clusters are comprised with less than 10 Pt atoms (< 1 nm) [10]. These results indicate the effect of metal nuclearity and surface structure on the catalytic performance for hydrogenation reactions are still not well understood, especially for transition metal catalysts like Ir that has been rarely reported before.

In this work, we synthesized a series of Ir nanoparticles and subnanometer clusters with size smaller than 1.4 nm on $ZnAl_2O_4$. Spinel structure materials (e.g. metal aluminate with the structure of MAl_2O_4, M=Mg, Cu, Ni, …) have been widely used as support for metal catalysts. The computational study showed Ir nuclearity can be limited on $MgAl_2O_4$ spinel because of the strong interfacial interaction between the facets of $MgAl_2O_4$ and Ir [11]. It is hard to prepare very large Ir nanoparticles (>1.5nm) when supported on $MgAl_2O_4$ no matter how harsh the sintering conditions [12, 13]. This work is the first one applying $ZnAl_2O_4$ as the support for Ir catalysts to our best knowledge. The surface structure of the catalysts was characterized by High-angle annular dark-field scanning transmission electron microscopy (HAADF-STEM), CO chemisorption to study the geometric properties (particle size), then diffuse reflectance infrared Fourier transform spectroscopy (DRIFTS) and X-ray photoelectron spectroscopy (XPS) for electronic properties. The catalysts were tested for hydrogenation of acetylene. The results show a similar trend with the other catalysts like Pt/TiO_2 [7] that the activity increases with increase particle size while the selectivity to ethylene decreases with particle size. The particle size of Ir is the key factor that determines the activity and selectivity. When the particle sizes of $Ir/ZnAl_2O_4$ catalysts are the same, the difference in electronic properties has very small effect on the catalytic performance for acetylene hydrogenation.

4.3 Methods

4.3.1 Synthesis and pretreatments

The $ZnAl_2O_4$ support were synthesized with aluminium isopropoxide ($Al(O\text{-}i\text{-}Pr)_3$, 98+%, granular, Alfa Aesar) and zinc nitrate hexahydrate ($Zn(NO_3)_2 \cdot 6H_2O$, 99.0 – 101.0%, J.T.Baker) by sol-gel method. 0.05 mol zinc nitrate hexahydrate was dissolved in 150 mL ethanol under ultrasound. 0.1 mol aluminium isopropoxide fine powder and 150 mL ethanol were added into the Pyrex bottle, and then start to stir on the hotplate. The zinc nitrate solution was gradually dropped into the bottle and stirred for an hour and then the solution was heated at 120 °C for 12 hours under stirring. After that, the Pyrex bottle was sealed and put into the oven at 80 °C standing for stratification for 3 days and then the lid was removed to evaporate the upper layer of solvents and dry the $ZnAl_xO_y$ chucks. Finally, the $ZnAl_xO_y$ was ground and calcined at 700 °C for 12 hours to form the crystalline structure of $ZnAl_2O_4$, as shown by the XRD pattern in Supplementary Information Figure S4.2. The impregnation of Ir atoms does not affect the structure of $ZnAl_2O_4$ support since no extra Ir peaks are shown in the XRD pattern.

Four $Ir/ZnAl_2O_4$ catalysts with 0.2 and 1% weight loading were synthesized with Ir particle sizes between 0.7 and 1.4 nm. The $0.2\%Ir/ZnAl_2O_4$ catalysts were synthesized by wet impregnation method. Appropriate amount of dihydrogen hexachloroiridate(IV) hydrate (H_2IrCl_6, 99%, metal basis, Strem Chemicals, Inc.) was placed into an empty vial in the glove box and DI water was injected into the vial under ultrasound sonication to dissolve the Ir precursor. The calcined $ZnAl_2O_4$ support was weighed and added into a 1000 mL Pyrex bottle. By adding different amount of HCl, the pH was adjusted to 3 or 6.7 before adding the precursor solution into the support. After stirring for 6 hours, the solution was filtered under vacuum. The resulting powder was dried in a Muffle furnace at 80 °C for 12 hours and then 100 °C for 4 hours with a ramp rate of 0.5 °C/min before any further pretreatments. The filtrate was tested for Ir by inductively coupled plasma-atomic emission spectroscopy (ICP-AES) on a Spectro ARCOS II Multi-View ICP Model FHM22 with CETAC Autosampler instrument and no Ir was detected. For 0.2%Ir/$ZnAl_2O_4$ catalyst with mostly single atoms, the catalyst was reduced at 600 °C in-situ in a flow of 20 kPa H_2 (balance He, 50 sccm of total flow rate). For 0.2%Ir/$ZnAl_2O_4$ catalyst with mostly subnanometer clusters (~0.8 nm), the catalyst was calcined at 500 °C for 4 hours in the Muffle furnace and then reduced at 400 °C in-situ in a flow of 20 kPa H_2 (balance He, 50 sccm of total flow rate). For 0.2%Ir/$ZnAl_2O_4$ catalyst with mostly nanoparticles (~1.4 nm), the catalyst was freshly reduced at 400 °C in-situ in a flow of 20 kPa H_2 (balance He, 50 sccm of total flow rate).

The 1%Ir/$ZnAl_2O_4$ catalyst with mostly nanoparticles (~1.4 nm) was prepared by incipient wetness impregnation. The $ZnAl_2O_4$ support was weighed and added to a 150 mL beaker. The dihydrogen hexachloroiridate(IV) solution was added to the support dropwise, then dried overnight in air at room temperature and then in the Muffle furnace at 80 °C for 12 hours and 100 °C for another 4 hours with a ramp rate of 0.5 °C/min. Finally, the 1%Ir/$ZnAl_2O_4$ catalyst was reduced at 600 °C in-situ in a flow of 20 kPa H_2 (balance He, 50 sccm of total flow rate).

4.3.2 Catalyst characterizations

Atomic resolution characterization (HAADF-STEM)

High-angle annular dark-field scanning transmission electron microscopy (HAADF-STEM) characterization for the Ir/$ZnAl_2O_4$ catalysts were conducted ex-situ using an aberration corrected Nion UltraSTEM operating at 100 keV and on an aberration corrected JEOL JEM-ARM200F at an acceleration voltage of 200 kV. The particle size of all the catalysts was measured horizontally across the particles in various images (at least 10 images with ~200–500 nanoparticles for each catalyst) by ImageJ. The surface-average particle diameters were calculated by the equation of $d_{SA} = \frac{\sum n_i d_i^3}{\sum n_i d_i^2}$ [14], where n_i is the number of nanoparticles and d_i is the diameter of the nanoparticle. The total number of atoms within a nanoparticle can be calculated using $N_T = \frac{\pi D^3 \rho N_A}{6 M_W}$ [15], where D is the diameter of the nanoparticle obtained by HAADF-STEM, ρ is the bulk density of Ir (22560 $kg \cdot m^{-3}$), N_A is Avogadro's number (6.02 × 1023 mol^{-1}), and M_W is the molecular weight of Ir (0.192217 $kg \cdot mol^{-1}$). The histogram of atomic percentage for each particle size range for all the four samples are shown in Supplementary Information Figure S4.1.

In-situ DRIFTS characterization

In-situ diffuse reflectance infrared Fourier transform spectroscopy (DRIFTS) experiments were conducted on Thermo Scientific IS-50R Fourier transform infrared spectrometer using mercury cadmium telluride detector (MCT-A), CO was applied as the probe molecule to observe the adsorption on the surface. The resolution of the spectra was 4 cm^{-1} in Kubelka-Munk (K–M) units and the reported spectra are an average of 32 scans. All tests were performed at atmospheric pressure. For each test, about 50 mg catalyst (fine powder) was loaded into the high temperature DRIFTS reaction chamber (Harrick Praying Mantis). Because of the limitation of temperature controller in the DRIFTS chamber, the Ir/$ZnAl_2O_4$ catalysts needs to be pretreated ex-situ first for those with the high reduction temperature of 600 °C and then transferred into the DRIFTS chamber for a second in-situ reduction at 500 °C. For those with low reduction temperature of 400 °C, the catalysts were directly reduced in-situ in the DRIFTS chamber. The details of the pretreatment methods are listed in Supplementary Information Table S4.1. After pretreatment and cooling down in H_2, the catalysts were flushed with N_2 at 200 °C for 20 min and then a baseline spectrum was collected at 35 °C under N_2. Then 0.25 kPa, 1 kPa, and 2.5 kPa CO (balance N_2) were flowed through the sample for 5 minutes and then purged with pure N_2 for 5 min to remove the surface physisorbed CO. The reported spectra are those after 5 min purge in N_2. The N_2 gas was supplied from boil-off liquid N_2 stored in house and purified with oxygen and high-capacity moisture traps (Cat. # 20601 and Cat. # 21997, Restek) before flowing into the reaction chamber. The CO (5%, balance N_2, certified grade, Airgas) gas line was equipped with a metal carbonyl purifier (Matheson, NanoChem Metal-X) to remove the trace amount of metal carbonyls impurities in the stainless-steel cylinder. When operating the DRIFTS experiments, the mass spectrometer was also connected to the outlet of the DRIFTS reaction chamber. When CO was turned on there was no increase for O_2 or H_2O above baseline compared to pure N_2. All the gas flows were metered by mass flow controllers (Brooks Instrument, 5850EM).

Volumetric CO chemisorption

The quantity of CO adsorbed on the catalyst (mmol of CO adsorbed per weight of Ir) and the percentage of the exposed Ir sites was measured by volumetric CO chemisorption (Micromeritics 3 Flex). The adsorption stoichiometry of CO : Ir is assumed to be 1:1. The samples were sieved into size of 150-250 μm after pelletizing the powder catalysts. Approximately 0.2–0.3 gram of each sample was packed in a straight quartz tube and pretreated by the same procedure as listed in Supplementary Information Table S4.1. The pressure is set at 760 mmHg for saturation during the reduction at target temperature in pure H_2. Before and after pretreatment, the catalysts were evacuated for 1–2 hours until lower than 10^{-3}–10^{-4} mmHg pressure was achieved at 35 °C before the CO (99.999%, certificate grade, Airgas) chemisorption analysis. The CO chemisorption isotherms were conducted at 35 °C between 5 – 450 mmHg. There was an evacuation step between the measurements for the two isotherms in order to remove the physically adsorbed CO on top of chemisorbed CO. The first isotherm is for both chemisorbed and physisorbed CO, while the second isotherm represents for the physisorbed CO only. The amount of chemisorbed CO can be calculated by the difference of the two CO isotherms.

X-ray photoelectron spectroscopy

The X-ray photoelectron spectroscopy (XPS) analysis was performed right after the reduction without exposing to air. The samples were first pretreated in the center of a stainless-steel tube with Swagelok valves installed at the two ends. The inlet was connected to the mass flow controllers (SLA 5800 series, Brooks Instrument), while the outlet was connected to the fume hood. The tube was placed inside a stainless-steel block was heated by two 300 W heating cartridges connected to a PID temperature controller (Watlow). The thermocouple used to control the catalyst temperature was placed in the center of the catalyst bed in the tube for accurate temperature. After pretreatment following the procedure listed in Supplementary Information Table S4.1, the valves at the two ends of the tube were switched off to avoid exposure to air. The whole tube was then transferred into the glove box filled with N_2 and the samples were loaded onto the double-sided tape mounting on the sample holder. The holder was then sealed and moved out of the glove box and sent for the XPS measurements directly.

XPS was conducted on a PHI VersaProbe III scanning XPS microscope using monochromatic Al K-alpha X-ray source (1486.6 eV). XPS spectra were obtained over 200 µm × 200 µm sample area with pass energy of 26 eV, giving a full width at half maximum of 0.59 eV for $Ag3d_{5/2}$. All binding energies were referenced to Al2p peak at 74.2 eV. A Shirley background and Gaussian-Lorentzian peak shape were used for curve fitting. Quantification was accomplished using PHI MultiPak 9.9.0.8, using the appropriate corrected sensitivity factors.

4.3.3 Acetylene hydrogenation

The catalytic measurements of acetylene hydrogenation were performed in a packed-bed quartz tubular reactor (3/8 in. O.D.). The catalysts were pelletized and sieved into 125-250 μm pellets and then packed in the quartz reactor. The reactor was installed in the heating furnace and the bed temperature was measured by a K-type thermocouple mounted on the outer wall of the reactor at the center of the catalyst bed. The feed gases 5% C_2H_2 (balance He, certified standard), H_2 (99.999%) and He (99.999%) were purchased from Airgas Inc. The He gas line was equipped with high-capacity moisture and O_2 traps (Cat. # 21997 and Cat. # 20601, Restek) to eliminate O_2 and H_2O. All gases were metered by mass flow controllers (SAL 5800 series, Brooks Instrument) and the reactions were tested at atmosphere pressure. The concentration of the reactant and product gases from the outlet of the reactor was measured and analyzed by gas chromatography (Agilent Micro GC 490) equipped with an Al_2O_3 column and thermal conductivity detector to quantify C_2H_2, C_2H_4 and C_2H_6.

The conversion and selectivity of acetylene hydrogenation are calculated by the equations as followed:

$$Conversion = \frac{mole\ of\ (C_2H_4 + C_2H_6)_{outlet}}{mole\ of\ {C_2H_2}_{inlet}}$$

$$Selectivity = \frac{mole\ of\ C_2H_{4_{outlet}}}{mole\ of\ (C_2H_4 + C_2H_6)_{outlet}}$$

The turnover frequency (TOF) was calculated on the basis of the reaction rate ($\mathrm{mol}_{C_2H_2}\ \mathrm{g}_{\mathrm{cat}}^{-1}\ \mathrm{s}^{-1}$) per number of Ir sites ($\mathrm{mol}_{\mathrm{Ir}}\ \mathrm{g}_{\mathrm{cat}}^{-1}$), which is measured as quantity of CO adsorbed (mmol of CO / $\mathrm{g}_{\mathrm{cat}}^{-1}$) from volumetric CO chemisorption with the assumption of 1 : 1 for CO : Ir stoichiometry. All the results of activation energy (Ea) and reaction orders were measured in the kinetic regime (conversion < 1%). The 0.2% Ir/$ZnAl_2O_4$ catalysts were used without any dilution, while the 1% Ir/$ZnAl_2O_4$ catalyst was diluted by 5 times with SiO_2 (Silica gel, for chromatography, 0.075-0.250 mm, 150 Å, Sigma Aldrich) to control the conversion < 1%. The kinetic measurements have excluded the limitations from heat and mass transfer from the calculation results of criterion shown in the Supplementary Information. After pretreatment, the catalysts were cooled down in 20 kPa H_2 to room temperature (~25 °C) and then started to flow 0.5 kPa C_2H_2 and 5 kPa H_2 balanced He (100 sccm total flow rate) and heated until 50 °C. At 50 °C, the flowrate was lowered to 50 sccm with the same partial pressure for C_2H_2 and H_2 and stabilized overnight before the activation energy and reaction order measurements. The initial TOF reported is the average of TOF results within 10 minutes immediately when temperature reached 50 °C and the flowrate was changed to 50 sccm.

4.4 Results and Discussion

4.4.1 Characterization results

The Ir/$ZnAl_2O_4$ catalysts were characterized by high-angle annular dark-field scanning transmission electron microscopy (HAADF-STEM) to determine the particle size distribution of the catalysts after reduction (pretreatment methods are shown in Supplementary Information Table S4.1). Despite the higher reduction temperature of 600 °C, the 0.2%Ir/$ZnAl_2O_4$ catalyst prepared in neutral aqueous solution contains a large number of single atoms (> 40%) and some subnanometer clusters as shown in Figure 4.1-(a). When the 0.2%Ir/$ZnAl_2O_4$ catalyst was prepared in acidic solution (pH~3), lower reduction temperature of 400 °C results in larger particle size regardless of calcination, as shown in Figures 4.1-(b) and 4.1-(c). When the 0.2%Ir/$ZnAl_2O_4$ catalyst prepared in acidic solution (pH~3) was calcined at 500 °C before reduction at 400 °C, the majority of Ir is the subnanometer clusters with surface-average particle size of 0.8 nm. However, without calcination, a reduction at 400 °C will result in larger Ir nanoparticles with surface-average particle size of 1.4 nm. We noticed the results of particle size from STEM are consistent with the dispersion (CO/Ir) from volumetric CO chemisorption (Table 4.1). The last catalyst (Figure 4.1-(d)) has higher weight loading of 1% and was prepared by a different method (incipient wetness) from the rest three. After reduction at 600 °C, it is mainly comprised of nanoparticles and the surface-average particle size is the same as that 0.2%Ir/$ZnAl_2O_4$ freshly reduced at 400 °C. The results of Ir particle size (< 2 nm) on $ZnAl_2O_4$ shows the Ir nuclearity is still limited by the interaction of metal and support, which is consistent with Ir nanoparticles supported on $MgAl_2O_4$ (< 2 nm). The catalysts are referred with designation names for abbreviation showing in Table 4.1 in the following contents.

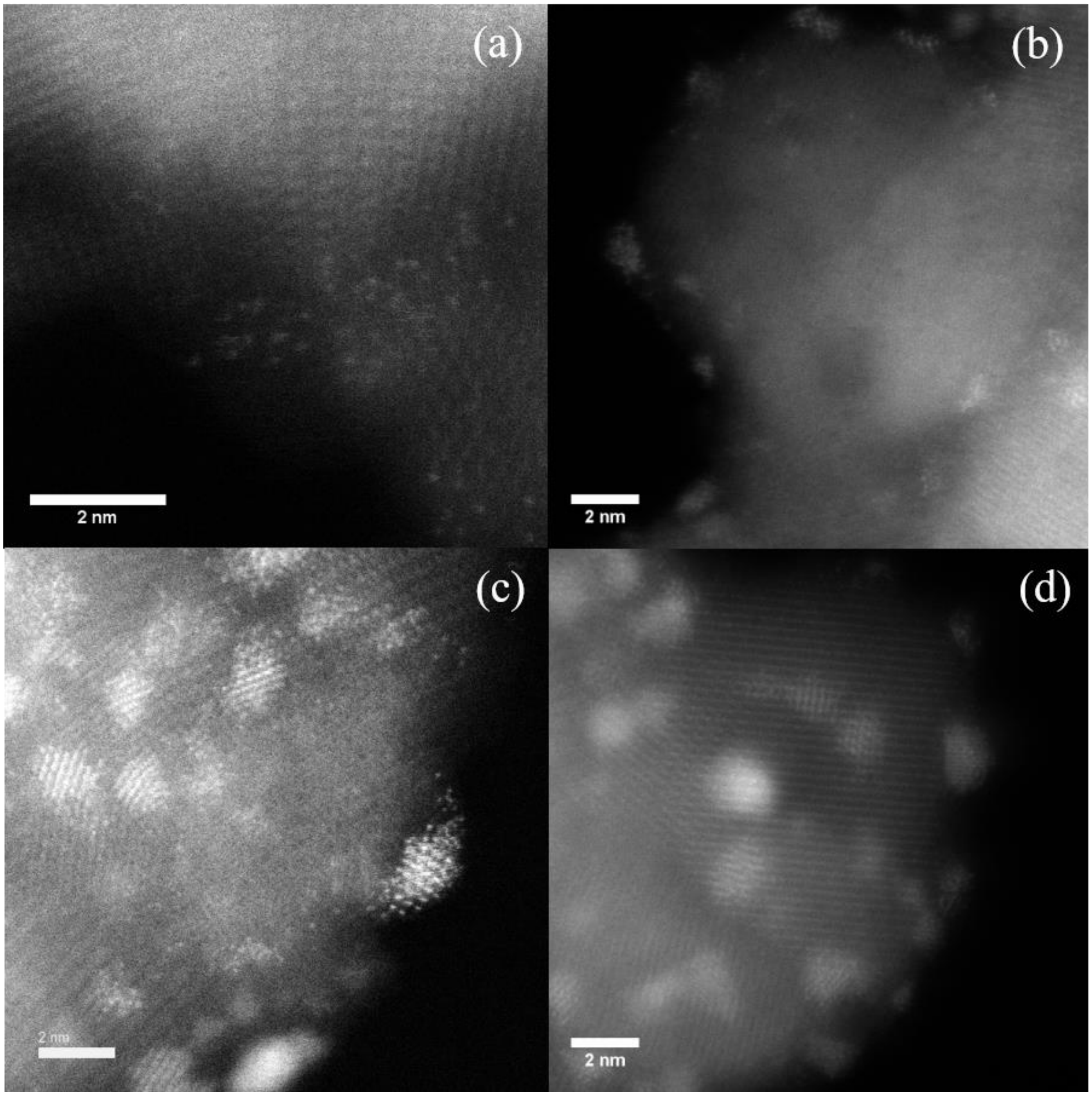

Figure 4.1 HAADF-STEM images of Ir/$ZnAl_2O_4$ catalysts with different particle size distribution after reduction. (a) 0.2%$Ir_{SA\text{-}0.7nm}$/$ZnAl_2O_4$ catalysts with mostly single atoms and subnanometer clusters with surface-average particle size of 0.7 nm, (b) 0.2%$Ir_{0.8nm}$/$ZnAl_2O_4$ subnanometer clusters with surface-average particle size of 0.8 nm, (c) 0.2%$Ir_{1.4nm}$/$ZnAl_2O_4$ nanoparticles with surface-average particle size of 1.4 nm and (d) 1%$Ir_{1.4nm}$/$ZnAl_2O_4$ nanoparticles with surface-average particle size of 1.4 nm.

Table 4.1 Surface-average particle size of all the Ir/$ZnAl_2O_4$ catalysts used in this work for acetylene hydrogenation after the analysis of STEM images.

Weight Loading	Preparation Method	Surface-average diameter (nm)	CO/Ir (mol/mol) Chemisorption	Abbreviation name	STEM Image
0.2%	pH~7, Wet Impregnation	SA-0.7	1.3 : 1	0.2%$Ir_{SA-0.7nm}/ZnAl_2O_4$	Fig. 1-(a)
0.2%	pH~3, Wet Impregnation	0.8	1.23 : 1	0.2%$Ir_{0.8nm}/ZnAl_2O_4$	Fig. 1-(b)
0.2%	pH~3, Wet Impregnation	1.4	0.7 : 1	0.2%$Ir_{1.4nm}/ZnAl_2O_4$	Fig. 1-(c)
1%	Incipient Wetness Impregnation	1.4	0.34 : 1	1%$Ir_{1.4nm}/ZnAl_2O_4$	Fig. 1-(d)

The results of volumetric CO chemisorption for all the catalysts are listed in Supplementary Information Table S4.1. The dispersion of CO : Ir is very consistent with the Ir particle size except 1%$Ir_{1.4nm}/ZnAl_2O_4$. Since the surface-average particle size of 1%$Ir_{1.4nm}/ZnAl_2O_4$ and 0.2%$Ir_{1.4nm}/ZnAl_2O_4$ is the same, the dispersion of CO : Ir is expected to be similar. We suspect that the much lower dispersion on 1%$Ir_{1.4nm}/ZnAl_2O_4$ is likely due to Zn reduction and migration on the surface of the nanoparticles at the high reduction temperature, thereby blocking surface Ir sites. The 1%$Ir_{1.4nm}/ZnAl_2O_4$ also displayed different DRIFTS spectra as shown in Supplementary Information Figure S4.3 with the 1979 cm^{-1} peak being assigned to Ir sites with nearby Zn.

From DRIFTS in Supplementary Information Figure S4.3, the CO adsorption bands located at much lower wavenumber of 1980 cm^{-1} when the catalysts (0.2%$Ir_{SA-0.7nm}/ZnAl_2O_4$ and 1%$Ir_{1.4nm}/ZnAl_2O_4$) were reduced at high reduction temperature of 600 °C. While the 2060 cm^{-1}

band has much higher intensity for the other two catalysts (0.2%$Ir_{0.8nm}$/$ZnAl_2O_4$ and 0.2%$Ir_{1.4nm}$/$ZnAl_2O_4$). The XPS results show the Ir 4f band shifts to lower binding energy as the particle size gets smaller and reduction temperature gets higher (Figure 4.2 (a) – (c)), indicating more electrons on small sized Ir subnanometer clusters. However, the 1%$Ir_{1.4nm}$/$ZnAl_2O_4$ catalyst with large nanoparticles shows a much lower binding energy than the 0.2%$Ir_{SA-0.7nm}$/$ZnAl_2O_4$ with the same surface-average particle size. The 1%$Ir_{1.4nm}$/$ZnAl_2O_4$ and 0.2%$Ir_{SA-0.7nm}$/$ZnAl_2O_4$ catalysts that both reduced at 600 °C have similar binding energy from XPS (Supplementary Information Figure S4.4-(a) and S4.4-(b) and CO adsorption band from DRIFTS, indicating a strong Ir-Zn interaction. At high reduction temperature, the Zn atoms in $ZnAl_2O_4$ can be reduced and probably interacts with Ir to form Ir-Zn structure [16]. While at lower reduction temperature of 400 °C, especially for 0.2%$Ir_{0.8nm}$/$ZnAl_2O_4$ catalyst that has been calcined at 500 °C before reduction, the main CO adsorption band is located at 2050 cm^{-1}, which is much higher than those at 1990-2000 cm^{-1}. It has been reported the interaction of Ir and Zn can be influenced by the oxidation atmosphere, at some special conditions (e.g. sputtering) the formation of Zn-Ir-Or structure can be easily achieved [17, 18]. In our case, EXAFS study is not feasible up to now since the coordination enviroment of Ir atoms could not be identified when supporting on $ZnAl_2O_4$ because of the strong influence of the Zn adsorption signals [16]. Details of the interaction between Ir and Zn is still not well understood and further work is required to elucidate the structure of Ir/$ZnAl_2O_4$ after different reduction conditions. From characterization results, it is feasible to study both the effect of geometric properties (on 0.2%$Ir_{SA-0.7nm}$/$ZnAl_2O_4$, 0.2%$Ir_{0.8nm}$/$ZnAl_2O_4$, and 0.2%$Ir_{1.4nm}$/$ZnAl_2O_4$) and electronic properties (0.2%$Ir_{1.4nm}$/$ZnAl_2O_4$ and 1%$Ir_{1.4nm}$/$ZnAl_2O_4$) in the following catalytic tests for acetylene hydrogenation.

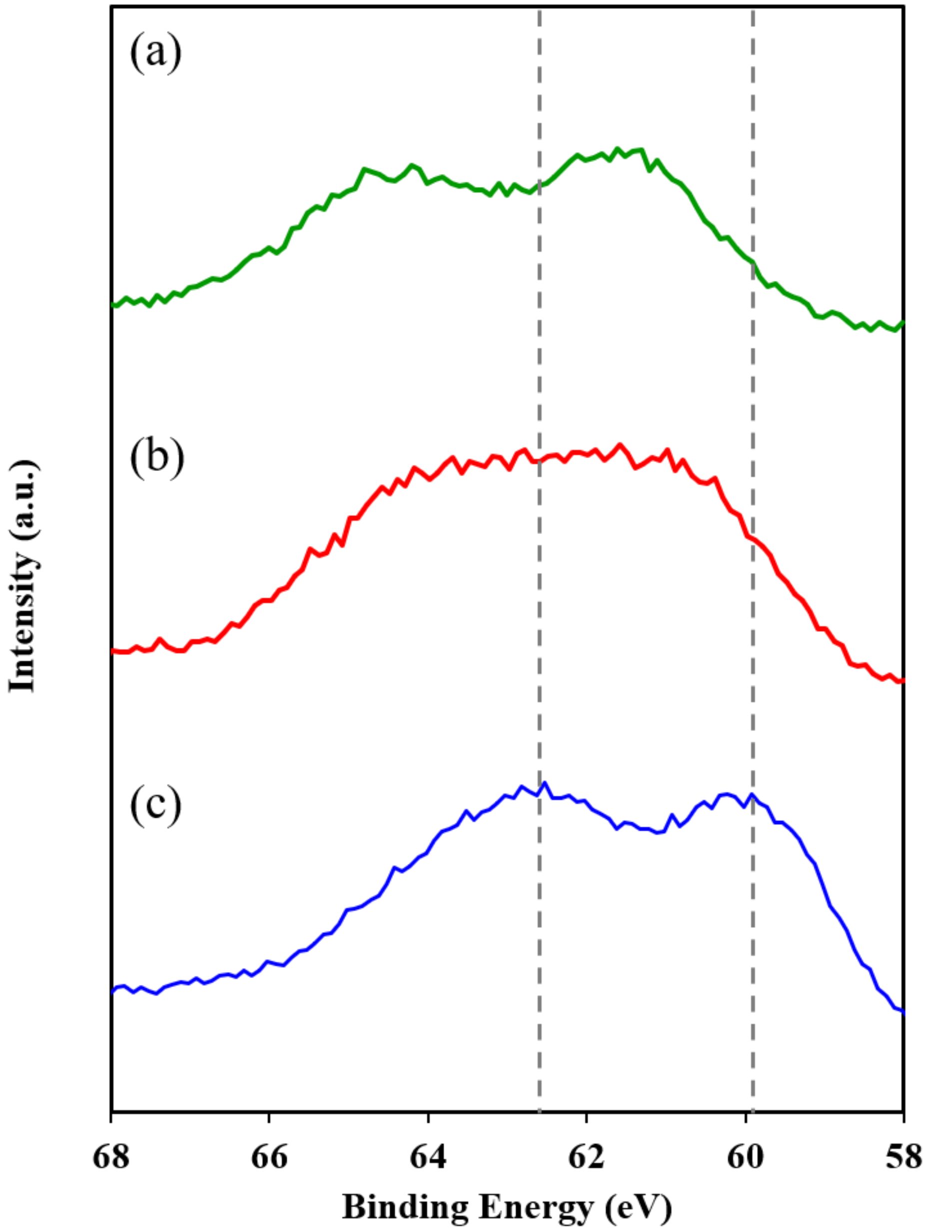

Figure 4.2 Ir 4f XPS spectra of (a) 0.2%$Ir_{1.4nm}$/$ZnAl_2O_4$, (b) 0.2%$Ir_{0.8nm}$/$ZnAl_2O_4$ and (c) 0.2%$Ir_{SA-0.7nm}$/$ZnAl_2O_4$ catalysts after reduction in H_2 at conditions listed in Supplementary Information Table S4.1. The dashed lines represent the raw Ir 4f peak positions for 0.2%$Ir_{SA-0.7nm}$/$ZnAl_2O_4$ (c). Starting from here, the Ir 4f peaks for 0.2%$Ir_{0.8nm}$/$ZnAl_2O_4$ (b) and 0.2%$Ir_{1.4nm}$/$ZnAl_2O_4$ (a) shifts to higher binding energy, indicating more oxidative states.

4.4.2 Catalytic performance and kinetic measurements of acetylene hydrogenation

Acetylene hydrogenation is an important probe reaction for structure sensitivity study on single crystal surfaces and supported metal catalysts in addition to its commercial value in industry. We tested acetylene hydrogenation on the four Ir/$ZnAl_2O_4$ catalysts ranging from mostly single atoms to nanoparticles with average size of 1.4 nm at mild conditions of atmosphere pressure and reaction temperatures of 50 – 70 °C. Figure 4.3 shows the comparison of initial TOF (s^{-1}) and selectivity to C_2H_4 at 50 °C within 10 minutes right after reaching 50 °C. As the particle size increases, the activity of acetylene hydrogenation keeps increasing while the selectivity to C_2H_4 is opposite, consistent with the trend on Pt/TiO_2 series of catalysts published earlier by our group [7]. As the particle size increases, the produced C_2H_4 intermediate after hydrogenation can be more difficult to desorb from the metal surface and further hydrogenated to ethane, resulting in lower selectivity to ethylene. This might be because of the higher heat of adsorption for ethylene on large sized particles, as ethylene can be more easily form and adsorb as ethylidyne (three sites) and di-σ bonded (two sites) structure comparing with the π-bonded structure on small sized clusters or single atoms with much lower binding energy mentioned in the introduction [1]. However, the lower heat of adsorption for C_2H_4 on small sized clusters also means lower binding energy for C_2H_2 based on the linear scaling relationship [19]. The C_2H_2 reactant molecules are more difficult to adsorb on the single atoms or small subnanometer clusters comparing with those large nanoparticles, resulting in a lower activity. The theory fits very well for the results we observed on the series of Ir/$ZnAl_2O_4$ catalysts as shown in Figure 4.3-(a) and 4.3-(b). Though from XPS, the Ir is electron rich on small subnanometer clusters, which should adsorb C_2H_4 stronger. Our results in the following text indicate the electronic properties have little effect on the selectivity. The results are mostly affected by the Ir nuclearity only.

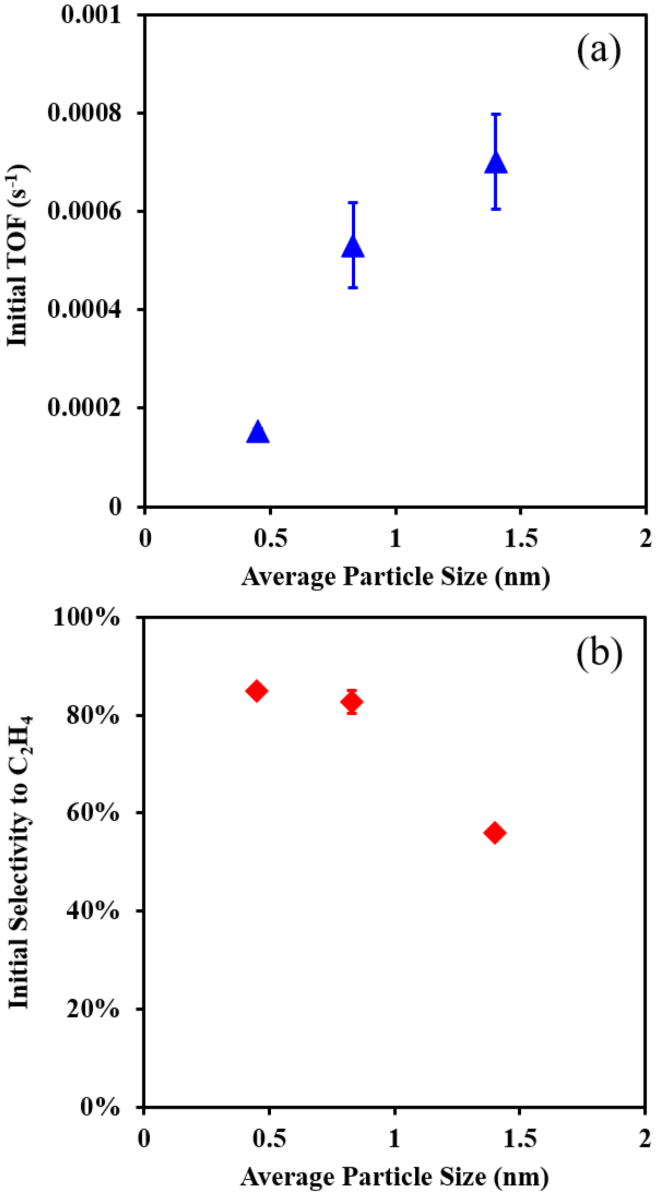

Figure 4.3 Comparison of (a) initial TOF (s^{-1}) and (b) selectivity to C_2H_4 as a function of surface-average Ir particle size (nm) for acetylene hydrogenation on supported 0.2%$Ir_{SA\text{-}0.7nm}/ZnAl_2O_4$, 0.2%$Ir_{0.8nm}/ZnAl_2O_4$ and 0.2%$Ir_{1.4nm}/ZnAl_2O_4$ catalysts. The initial TOFs and selectivities reported here are the data points collected within 10 minutes after reaching 50 °C at 0.51 kPa C_2H_2 and 5.1

kPa H_2 with 50 sccm total flow rate. The error bars represent the standard deviation of at least three experiments. The error bars for TOF on 0.2%$Ir_{SA-0.7nm}$/$ZnAl_2O_4$ and selectivities on 0.2%$Ir_{SA-0.7nm}$/$ZnAl_2O_4$ and 0.2%$Ir_{1.4nm}$/$ZnAl_2O_4$ catalysts are very small and mostly covered by the data symbols.

Figure 4.4 shows the activity (TOF) dependence on hydrogen and acetylene partial pressure on the four catalysts and the results of H_2 and C_2H_2 reaction orders are summarized in Table 4.2. In general, the H_2 order increases from ~0.5 to 1 from single atoms and subnanometer clusters to nanoparticles with surface-average particle size of 1.4 nm, while the C_2H_2 reaction order is ~0 for all the catalysts studied in this work. Kinetic studies for acetylene hydrogenation have been widely reported on extended metal surfaces and supported metal nanocatalysts [20-23]. For example, Bond et al reported the order of H_2 on Pd catalyst is 1.4 when Pd was in the hydrogen-depleted state when temperature is 125 °C, while exactly equals 1 when Pd was in hydrogen rich state when temperature is 0, 20 and 30 °C. The order of acetylene is ~0 and during this period the main product of the reaction is ethylene. Then the order of acetylene rapidly decreases to negative as the pressure of acetylene falls, and the selectivity to ethylene also decreases and further hydrogenation proceeds more as the pressure of acetylene decreases [21, 22]. A two sites mechanism was also reported to explain the first order in hydrogen partial pressure and zeroth order dependence on acetylene partial pressure between 30–70 °C for the reaction of acetylene and ethylene hydrogenation on Pd/Al_2O_3 without CO. On A-type sites the adsorption of acetylene is much stronger than ethylene in the form of di-σ adsorption and then di-σ adsorption transfers into π-adsorption upon the second hydrogenation step to form π-bonded C_2H_4 right before desorption, while on B-type sites the acetylene and ethylene compete to adsorb in the form of π-bonded structure [23]. In this work, the Ir particle size range is from single atoms to ~ 2 nm, so there might be both two sites within all these catalysts but the percentage is different. The lower H_2 order on smaller sized Ir suggests dissociative H_2 adsorption is important and the reaction may proceed via a competitive mechanism. While on large particles, the reaction may proceed via a non-competitive two site mechanism similar with literature. As H_2 partial pressure increases, the selectivity to C_2H_4 slightly decreases (Supplementary Information Figure S4.6-(a)), which means the H_2 might be preferably adsorb on π-adsorption sites. When the particle size decreases, the percentage of π-adsorption sites increases, resulting in less dependence of H_2 partial pressure, consistent with the slightly smaller H_2 reaction order of 0.5 on the 0.2%$Ir_{SA\text{-}0.7nm}$/$ZnAl_2O_4$ catalysts. Since the H_2/C_2H_2 ratio in this study is very high and there are no other hydrocarbon reactant molecules competing with C_2H_2 to adsorb on these sites, the C_2H_2 partial pressure is not important to tune the selectivity under such conditions. The dependence of selectivity to C_2H_4 on H_2 and C_2H_2 partial pressure shows the H_2 might adsorb in preference on π-bonded sites.

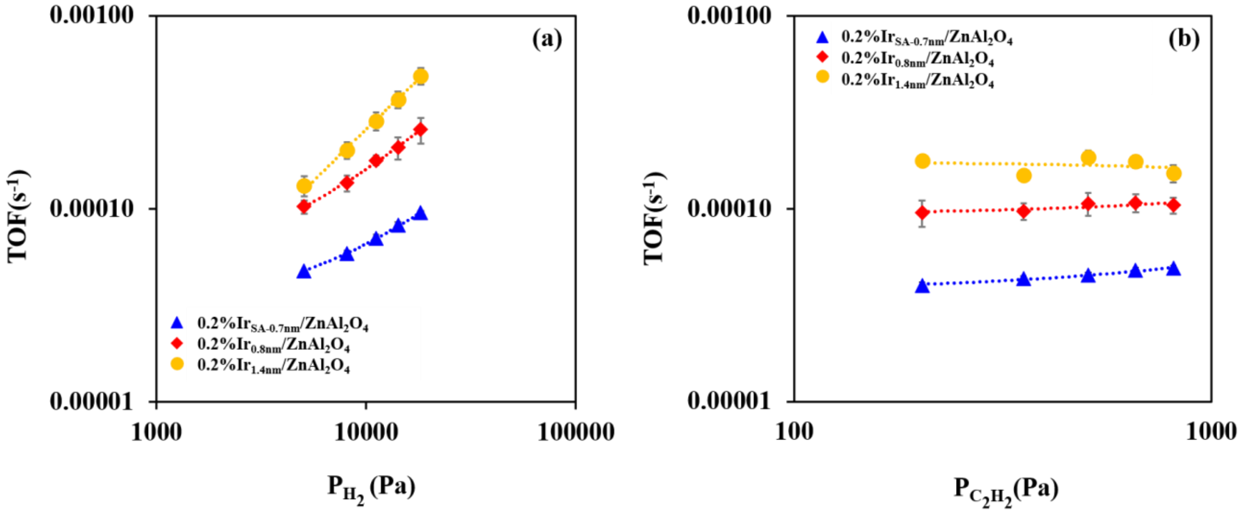

Figure 4.4 Reaction orders of acetylene hydrogenation on Ir/$ZnAl_2O_4$ catalysts at 50 °C. (a) Dependence of TOF on H_2 partial pressure (5.1–18.2 kPa) at 0.5 kPa C_2H_2 partial pressure and (b)

dependence of TOF on C_2H_2 partial pressure (0.2–0.8 kPa) at 5 kPa H_2 partial pressure. The symbols and error bars are the average results and standard deviation from reproduced experiments.

Table 4.2 H_2 and C_2H_2 reaction orders of acetylene hydrogenation on Ir/$ZnAl_2O_4$ catalysts at 50 °C (results in Figure 4.3).

Catalyst	H_2 Order	C_2H_2 Order
0.2%$Ir_{SA-0.7nm}$/$ZnAl_2O_4$	0.55	0.15
0.2%$Ir_{0.8nm}$/$ZnAl_2O_4$	0.72	0.08
0.2%$Ir_{1.4nm}$/$ZnAl_2O_4$	1.02	0

A comparison for the initial TOF and selectivity on the two catalysts of nanoparticles is also summarized in Supplementary Information Table S4.2. The initial TOF on 1%$Ir_{1.4nm}$/$ZnAl_2O_4$ is higher than that on 0.2%$Ir_{1.4nm}$/$ZnAl_2O_4$ but on the same order of magnitude, while the difference in selectivity to C_2H_4 is negligible. Other results from kinetic measurements (Ea, H_2 order and C_2H_2 order) are also very close. The results here clearly show that when the particle size is similar, the difference in electronic properties would not affect the catalytic performance for acetylene hydrogenation. Geometric property (Ir nuclearity) is the factor that plays the critical role for the structure sensitivity of acetylene hydrogenation on the series of Ir/$ZnAl_2O_4$ catalysts.

4.5 Conclusions

Four Ir catalysts were synthesized on $ZnAl_2O_4$ support with different particle size from single atoms to nanoparticles with surface-average particle size of 1.4 nm, which were confirmed by the HAADF-STEM images and volumetric CO chemisorption. The Ir atoms and nanoparticles in the subnanometer regime are catalytically active for acetylene hydrogenation. The decreasing trend of selectivity to C_2H_4 as a function of increasing particle size is consistent with the results in literature, showing the existence of more π-bonded adsorption with less heat of adsorption for acetylene on Ir atoms or small sized clusters than large nanoparticles. While the activity of acetylene hydrogenation on Ir atoms or subnanometer clusters is lower than that on large nanoparticles. The results show that acetylene hydrogenation is structure sensitive on $Ir/ZnAl_2O_4$ catalysts, and the catalytic performance is mainly dependent on the geometric property of Ir (Ir nuclearity) instead of electronic properties. Our work provides fundamental insights on the future study on the metal-support interactions and potential methodologies for catalyst design to optimize the activity and selectivity for the hydrogenation reactions.

Acknowledgment

This research was primarily sponsored by SABIC. STEM imaging was performed in the Oak Ridge National Laboratory and Institute for Catalysis at Hokkaido University in Japan. The XPS characterization was performed in part at the Surface Analysis Laboratory in Department of Chemistry at Virginia Tech, which is supported by the National Science Foundation under Grant No. CHE-1531834.

References

[1] L. Zhang, M. Zhou, A. Wang, T. Zhang, Selective hydrogenation over supported metal catalysts: from nanoparticles to single atoms, Chemical Reviews, 120 (2019) 683-733.

[2] X. Huang, Y. Xia, Y. Cao, X. Zheng, H. Pan, J. Zhu, C. Ma, H. Wang, J. Li, R. You, Enhancing both selectivity and coking-resistance of a single-atom Pd 1/C 3 N 4 catalyst for acetylene hydrogenation, Nano Research, 10 (2017) 1302-1312.

[3] Y. He, Y. Liu, P. Yang, Y. Du, J. Feng, X. Cao, J. Yang, D. Li, Fabrication of a PdAg mesocrystal catalyst for the partial hydrogenation of acetylene, Journal of catalysis, 330 (2015) 61-70.

[4] G.X. Pei, X.Y. Liu, X. Yang, L. Zhang, A. Wang, L. Li, H. Wang, X. Wang, T. Zhang, Performance of Cu-alloyed Pd single-atom catalyst for semihydrogenation of acetylene under simulated front-end conditions, ACS Catalysis, 7 (2017) 1491-1500.

[5] D.V. Glyzdova, T.N. Afonasenko, E.V. Khramov, N.N. Leont'eva, M.V. Trenikhin, I.P. Prosvirin, A.V. Bukhtiyarov, D.A. Shlyapin, Zinc Addition Influence on the Properties of Pd/Sibunit Catalyst in Selective Acetylene Hydrogenation, Topics in Catalysis, (2020) 1-13.

[6] J. Lu, P. Serna, C. Aydin, N.D. Browning, B.C. Gates, Supported molecular iridium catalysts: resolving effects of metal nuclearity and supports as ligands, Journal of the American Chemical Society, 133 (2011) 16186-16195.

[7] C.-T. Kuo, Y. Lu, L. Kovarik, M.H. Engelhard, A.M. Karim, Structure Sensitivity of Acetylene Semi-Hydrogenation on Pt Single Atoms and Subnanometer Clusters, ACS Catalysis, (2019).

[8] M. Ruta, N. Semagina, L. Kiwi-Minsker, Monodispersed Pd nanoparticles for acetylene selective hydrogenation: particle size and support effects, The Journal of Physical Chemistry C, 112 (2008) 13635-13641.

[9] A. Sárkány, A.H. Weiss, L. Guczi, Structure sensitivity of acetylene-ethylene hydrogenation over Pd catalysts, J. Catal.;(United States), 98 (1986).

[10] A.S. Crampton, M.D. Rotzer, C.J. Ridge, F.F. Schweinberger, U. Heiz, B. Yoon, U. Landman, Structure sensitivity in the nonscalable regime explored via catalysed ethylene hydrogenation on supported platinum nanoclusters, Nat Commun, 7 (2016) 10389.

[11] W.-Z. Li, L. Kovarik, D. Mei, M.H. Engelhard, F. Gao, J. Liu, Y. Wang, C.H.F. Peden, A General Mechanism for Stabilizing the Small Sizes of Precious Metal Nanoparticles on Oxide Supports, Chemistry of Materials, 26 (2014) 5475-5481.

[12] Y. Lu, J. Wang, L. Yu, L. Kovarik, X. Zhang, A.S. Hoffman, A. Gallo, S.R. Bare, D. Sokaras, T. Kroll, Identification of the active complex for CO oxidation over single-atom Ir-on-MgAl2O4 catalysts, Nature Catalysis, 2 (2019) 149.

[13] X. Zhang, Y. Lu, L. Kovarik, P. Dasari, D. Nagaki, A.M. Karim, Structure Sensitivity of n-Butane Hydrogenolysis on Supported Ir Catalysts, Journal of Catalysis, (2020).

[14] J.M. Thomas, Handbook Of Heterogeneous Catalysis. 2., completely revised and enlarged Edition. Vol. 1–8. Edited by G. Ertl, H. Knözinger, F. Schüth, and J. Weitkamp, Angewandte Chemie International Edition, 48 (2009) 3390-3391.

[15] Y. Lu, C.-T. Kuo, L. Kovarik, A.S. Hoffman, A. Boubnov, D.M. Driscoll, J.R. Morris, S.R. Bare, A.M. Karim, A versatile approach for quantification of surface site fractions using reaction kinetics: The case of CO oxidation on supported Ir single atoms and nanoparticles, Journal of Catalysis, 378 (2019) 121-130.

[16] L. Nguyen, S. Zhang, L. Tan, Y. Tang, J. Liu, F.F. Tao, Ir1Zn n Bimetallic Site for Efficient Production of Hydrogen from Methanol, ACS Sustainable Chemistry & Engineering, 7 (2019) 18793-18800.

[17] D.M. Ramo, P.D. Bristowe, Impact of amorphization on the electronic properties of Zn–Ir–O systems, Journal of Physics: Condensed Matter, 28 (2016) 345502.

[18] G. Michail, V. Kambylafka, I. Kortidis, K. Tsagaraki, M. Androulidaki, G. Kiriakidis, V. Binas, M. Modreanu, E. Aperathitis, On the growth of transparent conductive oxide ternary alloys Zn–Ir–O (ZIRO) by the means of rf magnetron co-sputtering, Thin Solid Films, 617 (2016) 3-8.

[19] F. Studt, F. Abild-Pedersen, T. Bligaard, R.Z. Sørensen, C.H. Christensen, J.K. Nørskov, Identification of non-precious metal alloy catalysts for selective hydrogenation of acetylene, Science, 320 (2008) 1320-1322.

[20] A.D. Allian, K. Takanabe, K.L. Fujdala, X. Hao, T.J. Truex, J. Cai, C. Buda, M. Neurock, E. Iglesia, Chemisorption of CO and mechanism of CO oxidation on supported platinum nanoclusters, J Am Chem Soc, 133 (2011) 4498-4517.

[21] G.C. Bond, P.B. Wells, The hydrogenation of acetylene: II. The reaction of acetylene with hydrogen catalyzed by alumina-supported palladium, Journal of Catalysis, 5 (1966) 65-73.

[22] G.C. Bond, P.B. Wells, The hydrogenation of acetylene: I. The reaction of acetylene with hydrogen catalyzed by alumina-supported platinum, Journal of Catalysis, 4 (1965) 211-219.

[23] A.N.R. Bos, K.R. Westerterp, Mechanism and kinetics of the selective hydrogenation of ethyne and ethene, Chemical engineering and processing: process intensification, 32 (1993) 1-7.

Supplementary Information

Table S4.1 Summary of pretreatment methods for the series of Ir/$ZnAl_2O_4$ catalysts before DRIFTS, volumetric CO chemisorption and acetylene hydrogenation.

Catalyst	Surface Average Particle Size, d_{SA}	Oxidation	Reduction	Quantity of CO adsorbed (mmol/g)	CO/Ir (mol/mol) Chemisorption
0.2%$Ir_{SA\text{-}0.7nm}$/$ZnAl_2O_4$	SA–0.7 nm	-	20% H_2, 600 °C, 1 h	0.0134	1.3 : 1
0.2%$Ir_{0.8nm}$/$ZnAl_2O_4$	0.8 nm	Air, 500 °C, 4h	20% H_2, 400 °C, 1 h	0.0128	1.23 : 1
0.2%$Ir_{1.4nm}$/$ZnAl_2O_4$	1.4 nm	-	20% H_2, 400 °C, 2 h	0.00727	0.7 : 1
1%$Ir_{1.4nm}$/$ZnAl_2O_4$	1.4 nm	-	20% H_2, 600 °C, 1 h	0.0177	0.34 : 1

- SA is abbreviation of single atoms.
- All the catalysts were dried at 80 °C for 12 hours and 100 °C for 4 hours with a ramp rate of 0.5 °C/min before any calcinations or reductions.
- The ramp rate is 5 °C/min for oxidation steps and 15 °C/min for reduction steps.
- For those catalysts that need higher reduction temperature than 400 °C, the catalysts were first pretreated ex-situ in the reactor and then transferred into the DRIFTS chamber and reduced again at the maximum temperature before DRIFTS measurements (the maximum temperature in DRIFTS chamber is 500 °C).

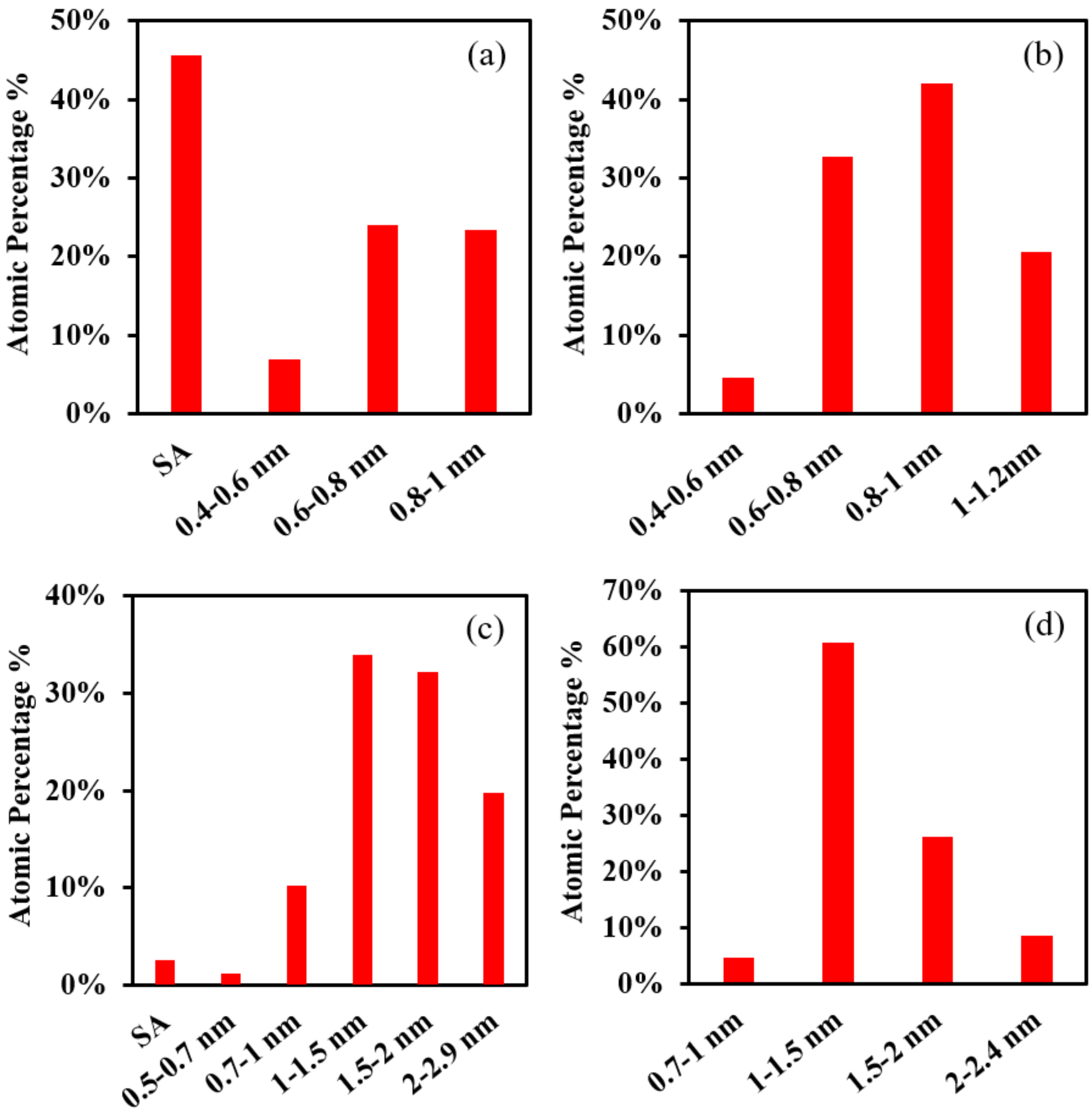

Supplementary Figure S4.1. Particle size distribution for (a) 0.2%$Ir_{SA-0.7nm}/ZnAl_2O_4$ catalyst with 46% of single atoms and subnanometer clusters with surface-average particle size of 0.7 nm based on 286 atoms and 28 clusters, (b) 0.2%$Ir_{0.8nm}/ZnAl_2O_4$ catalyst with surface-average particle size of 0.8 nm based on 213 nanoparticles (c) 0.2%$Ir_{1.4nm}/ZnAl_2O_4$ catalyst with surface-average particle size of 1.4 nm based on and (d) 1%$Ir_{1.4nm}/ZnAl_2O_4$ catalyst with the same surface-average particle size of 1.4 nm based on 288 nanoparticles. The surface-average particle size can be calculated by the equation of $\boldsymbol{d_{SA}} = \frac{\sum \boldsymbol{n_i d_i^3}}{\sum \boldsymbol{n_i d_i^2}}$, where d_i is the diameter of the nanoparticle, n_i is the total number of nanoparticles in the catalyst.

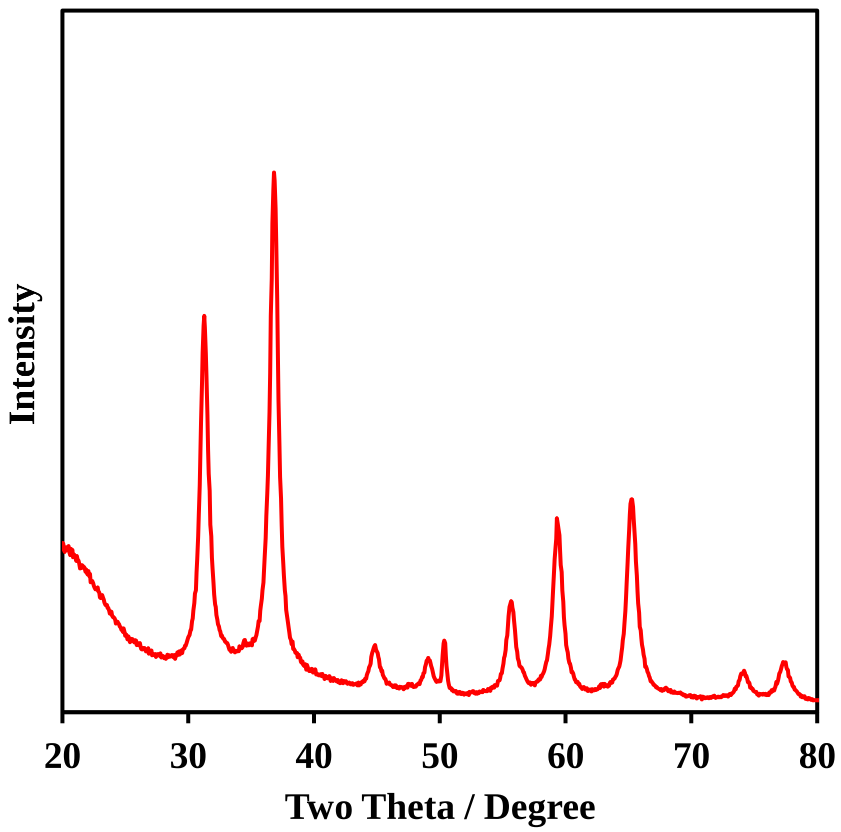

Supplementary Figure S4.2 XRD pattern for $ZnAl_2O_4$ prepared with $Zn(NO_3)_2 \cdot 6H_2O$ and Al(O-i-Pr)$_3$ precursor by sol-gel method and calcined at 700 °C for 12 hours with ramp rate of 5 °C/min.

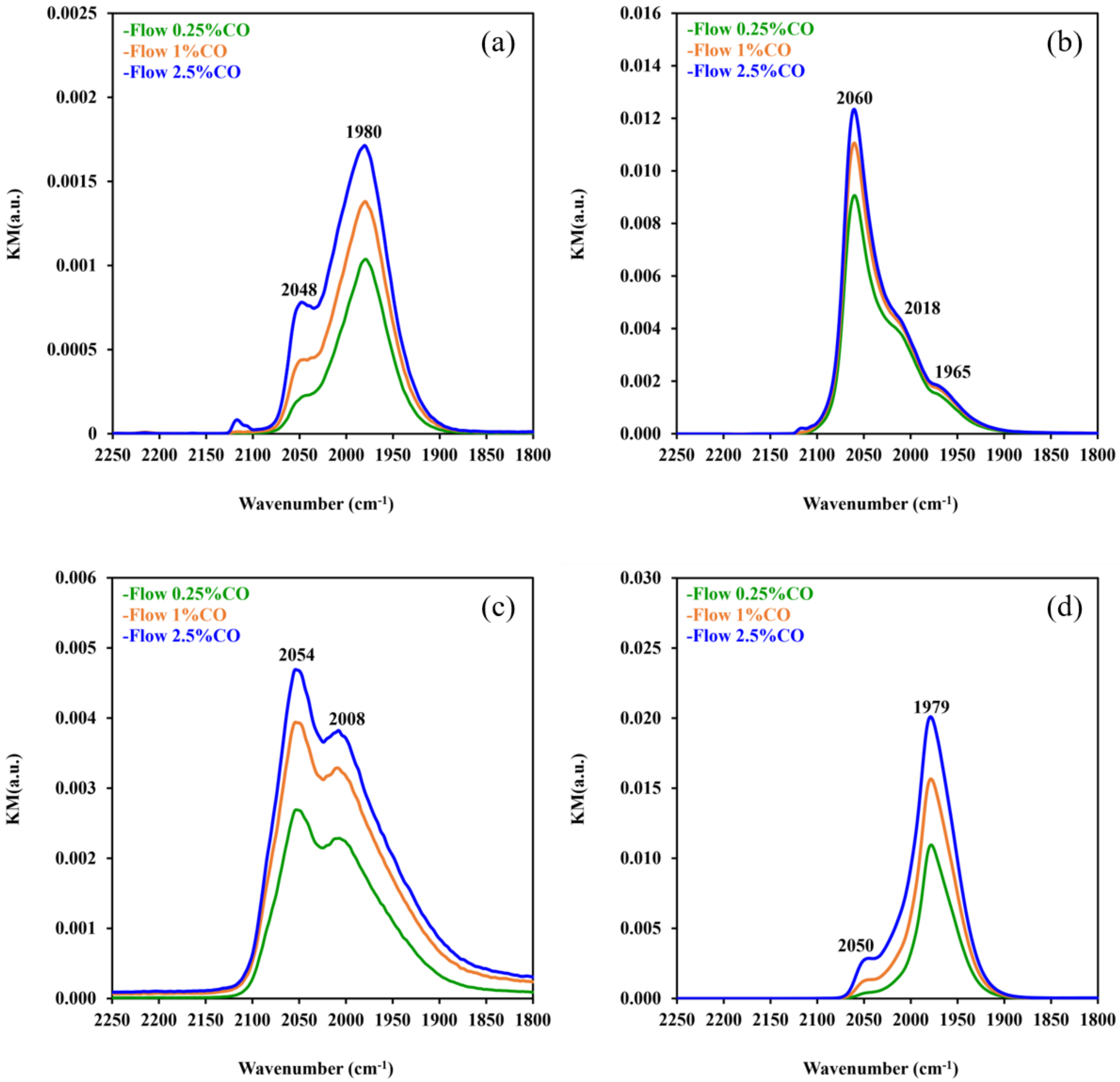

Supplementary Figure S4.3 DRIFTS spectra of CO adsorbed on (a) $0.2\%Ir_{SA-0.7nm}/ZnAl_2O_4$, (b) $0.2\%Ir_{0.8nm}/ZnAl_2O_4$, (c) $0.2\%Ir_{1.4nm}/ZnAl_2O_4$ and (d) $1\%Ir_{1.4nm}/ZnAl_2O_4$ catalysts after flowing 0.25 kPa, 1 kPa and 2.5 kPa CO for 5 minutes at atmosphere. The spectra were collected under N_2 after 5 min flush followed by each CO chemisorption condition.

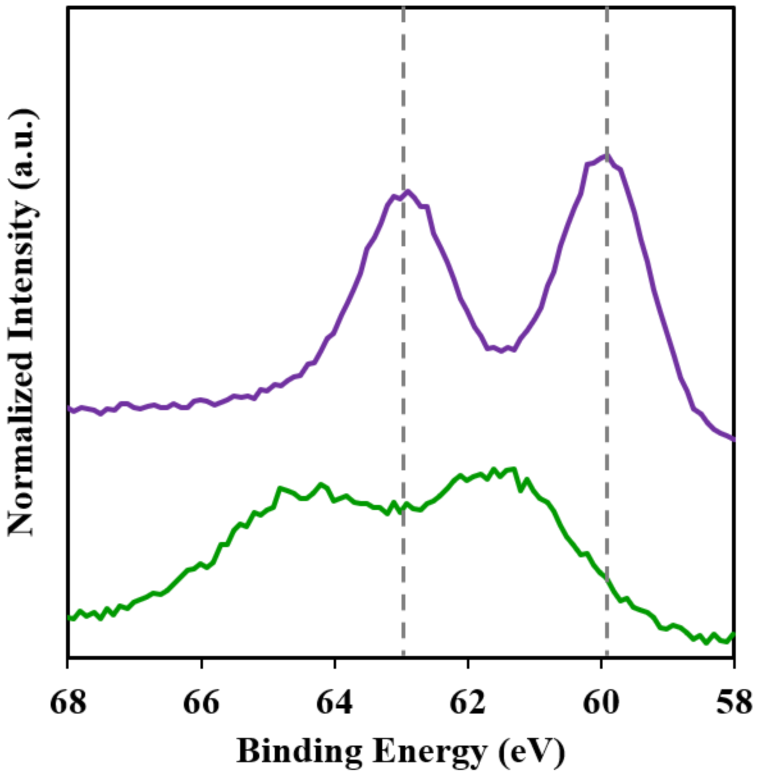

Supplementary Figure S4.4 Ir 4f XPS spectra of (a) 1%$Ir_{1.4nm}/ZnAl_2O_4$ and (b) 0.2%$Ir_{1.4nm}/ZnAl_2O_4$ catalysts (normalized by ×5) with the same surface-average particle size of 1.4 nm after reduction in H_2 at conditions listed in Supplementary Table S4.1. The dashed lines represent the raw Ir 4f peak positions without for 1%$Ir_{1.4nm}/ZnAl_2O_4$.

From the comparison of XPS spectra for Ir 4f in Supplementary Figure S4.4, though the surface-average particle size is the same, the Ir nanoparticles in 1%$Ir_{1.4nm}/ZnAl_2O_4$ catalyst is more reduced than those in 0.2%$Ir_{1.4nm}/ZnAl_2O_4$, indicating a difference of electronic properties (high electron density) in these two catalysts. Because of the higher reduction temperature (600 °C) for 1%$Ir_{1.4nm}/ZnAl_2O_4$, there might be more metal-support interactions that affect the surface electronic properties, resulting in the huge difference shown in Ir 4f XPS spectra.

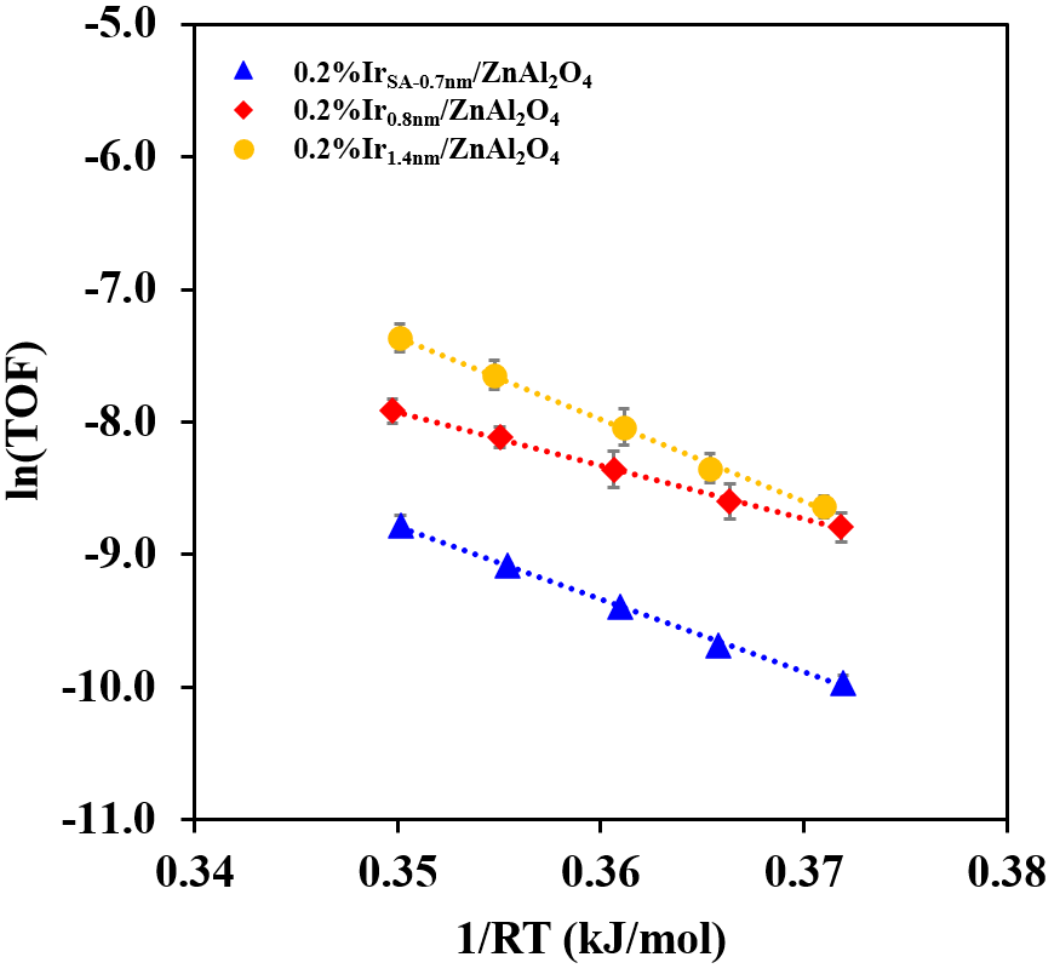

Supplementary Figure S4.5 Comparison of Arrhenius plots for the three catalysts. The activation energy on 0.2%Ir$_{SA-0.7nm}$/ZnAl$_2$O$_4$, 0.2%Ir$_{0.8nm}$/ZnAl$_2$O$_4$ and 0.2%Ir$_{1.4nm}$/ZnAl$_2$O$_4$ catalysts is 55, 40 and 62 kJ/mol, respectively. Reaction conditions: 0.51 kPa C_2H_2 and 5.1 kPa H_2 between 50–70 °C under atmosphere and the conversion was 0.1–1%.

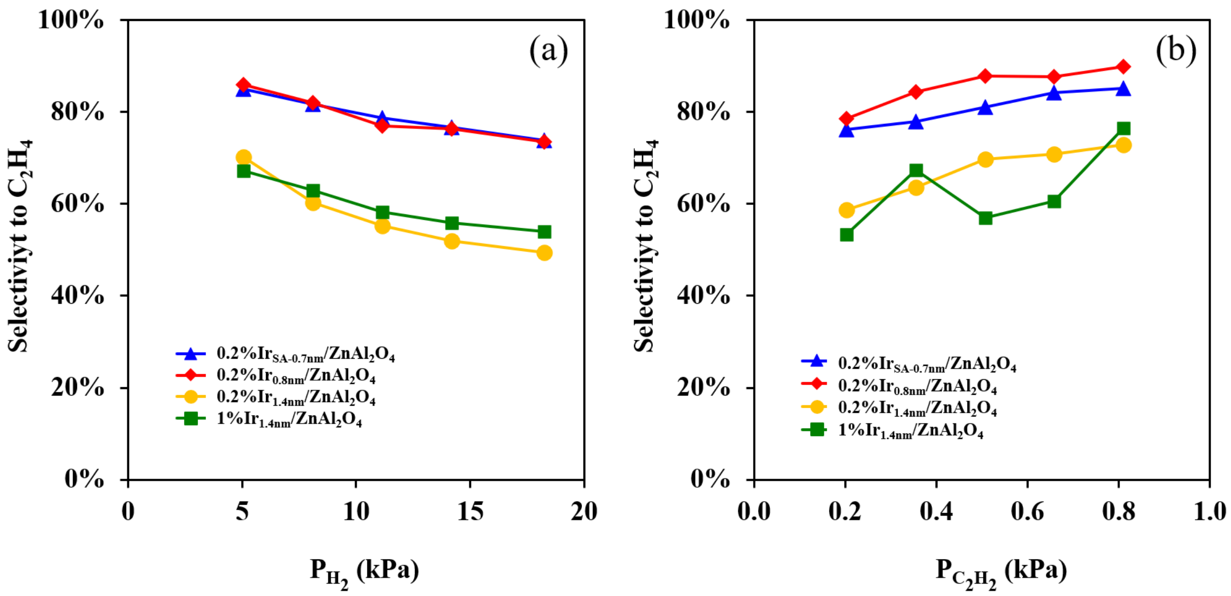

Supplementary Figure S4.6 Comparison of selectivity dependence on H_2 partial pressure (a) and C_2H_2 partial pressure (b) on all the four catalysts. The selectivity to C_2H_4 generally decreases with increasing H_2 partial pressure. Reaction conditions: H_2 partial pressure was changed from 5.1 kPa to 18.2 kPa at constant 0.5 kPa C_2H_2 under atmosphere at 50 °C for H_2 reaction order measurement; C_2H_2 partial pressure was changed from 0.2 kPa to 0.8 kPa at constant 5.1 kPa H_2 under atmosphere at 50 °C for C_2H_2 reaction order measurement.

Supplementary Table S4.2 Comparison of kinetic parameters and selectivity on 0.2%$Ir_{1.4nm}/ZnAl_2O_4$ and 1%$Ir_{1.4nm}/ZnAl_2O_4$ with the same surface-average particle size but different electronic properties (higher electron density in 1%$Ir_{1.4nm}/ZnAl_2O_4$).

	Initial TOF (s^{-1})	Initial Selectivity to C_2H_4	Ea (kJ/mol)	H_2 Order	C_2H_2 Order
0.2%$Ir_{1.4nm}/ZnAl_2O_4$	0.0007	56%	61.9	1	0
1%$Ir_{1.4nm}/ZnAl_2O_4$	0.0012	60.6%	55.2	0.8	0

Calculation for the criterion of transport limitations in acetylene hydrogenation on 0.2% $Ir_{1.4nm}/ZnAl_2O_4$ catalyst [1-3]

The results of acetylene hydrogenation on 0.2%$Ir_{1.4nm}/ZnAl_2O_4$ catalyst are used for the following calculation.

I. Mears Criterion for External Diffusion

The external mass transfer effects could be negligible when $\frac{-r'_A\,\rho_b R n}{k_C C_{Ab}} < 0.15$ (where $-r'_A$ is reaction rate).

The TOF at 50 °C after stabilization overnight is ~$0.00018 s^{-1}$, which is $0.00018\,\frac{\text{mole of } C_3H_2}{\text{mole of Ir}\cdot s}$.

$$r'_A = \left[0.00018\,\frac{\text{mole of } C_2H_2}{\text{mole of Ir }\cdot s}\right]\left[\frac{\text{mole of Ir}}{192\text{ g Ir}}\right]\left[\frac{0.2\%\text{ loading of Ir}}{g_{cat}}\right] = 1.88\times10^{-9}\,\frac{\text{mole of } C_2H_2}{g_{cat}\ \cdot s}$$

n = reaction order (use 1)

$R_p = 9\times10^{-5}$ m (catalyst particle radius)

$\rho_b = \frac{\text{Total amount of catalyst}}{\pi\times(\text{inner radius of reactor})^2\times\text{bed length}} = \frac{0.3\text{ g}}{\pi\times0.35^2\times0.8} = 0.97\text{ g cm}^{-3}$ (bulk density of catalyst bed)

$C_{Ab} = \frac{0.5\%\times10^5\text{ Pa}}{\left[8.3145\text{ Pa}\cdot\frac{m^3}{K}\cdot\text{mol}\right][323K]} = 0.186\text{ mol/m}^3$ (bulk gas concentration of reactant, mol/m^3)

$k_C = 2D_{AB}/R_p$ (mass transfer coefficient, m/s)

$\mathrm{D_{AB}} = \frac{0.001\times \mathrm{T}^{1.75}\mathrm{M}_{\mathrm{AB}}^{0.5}}{\mathrm{P}[(\sum \mathrm{v})_{\mathrm{A}}^{\frac{1}{3}}+(\sum \mathrm{v})_{\mathrm{B}}^{\frac{1}{3}}]^{2}}$ (The Fuller-Schettler-Giddings equation for gas-phase diffusivity between A and B [4, 5])

C_2H_2 is in bath gas of He, then $\mathrm{D_{AB}} = 1.8 \times 10^{-5}\ \mathrm{m^2/s}$ [2].

$$\mathrm{k_C} = \frac{2\mathrm{D_{AB}}}{\mathrm{R_p}} = \frac{2 \times (1.8 \times 10^{-5}\,\frac{\mathrm{m}^2}{\mathrm{s}})}{9 \times 10^{-5}\ \mathrm{m}} = 0.4\ \mathrm{m/s}$$

$$\frac{-\mathrm{r}_{\mathrm{A}}'\ \rho_{\mathrm{b}}\mathrm{R_p}\mathrm{n}}{\mathrm{k_C}\mathrm{C_{Ab}}} = \frac{\left[1.88 \times 10^{-9}\ \frac{\text{mole of } \mathrm{C_2H_2}}{\mathrm{g_{cat}}\ \cdot \mathrm{s}}\right][0.97\ \mathrm{g\ cm^{-3}}][\frac{\mathrm{cm}^3}{\mathrm{m}^3}] \times (9 \times 10^{-5}\ \mathrm{m})|1|}{\left[0.4\,\frac{\mathrm{m}}{\mathrm{s}}\right] \times [0.186\,\frac{\mathrm{mol}}{\mathrm{m}^3}]}$$

$$= 2.2 \times 10^{-6}$$

$$\frac{-\mathrm{r}_{\mathrm{A}}'\ \rho_{\mathrm{b}}\mathrm{R_n}}{\mathrm{k_C}\mathrm{C_{Ab}}} \ll \mathbf{0.15}$$

There is no external diffusion limitation.

II. Weisz-Prater Criterion for Internal Diffusion

The internal mass transfer effects could be negligible when $\frac{-r_A'\,\rho_c\,R^2}{D_e C_{As}} < 1$.

TOF = 0.00018 $\frac{mole\ of\ C_2H_2}{mole\ of\ Ir\cdot s}$, at 50 °C.

$D_e = \frac{D_{AB}\phi_p\sigma_c}{\tau}$ (effective gas-phase diffusivity, m_2/s)

$D_{AB} = 1.8 \times 10^{-5}\ m^2/s$ (gas-phase diffusivity)

ϕ_p= 0.4 (pellet porosity)

σ_c=0.8 (constriction factor)

$\tau = 3$, tortuosity

$$\mathrm{D_e} = \frac{\mathrm{D_{AB}\phi_p\sigma_c}}{\tau} = \frac{1.8\times10^{-5}\ \mathrm{m^2/s}\times0.4\times0.8}{3} = 1.9\times10^{-6}\ \mathrm{m^2/s}$$

$$\mathrm{C_{As}} = \frac{0.5\%\ \times 10^5\mathrm{Pa}}{\left[8.314\ \mathrm{Pa}\cdot\frac{\mathrm{m^3}}{\mathrm{K}}\cdot\mathrm{mol}\right][323\mathrm{K}]} = 0.186\ \mathrm{mol}\ /\mathrm{m^3}$$

$\rho_c = 4.6\ g/cm^3$ (density of solid catalyst, at here it is the density of the support as the loading is only 0.2%)

$$\frac{-\mathrm{r_A'}\ \rho_c\ \mathrm{R^2}}{\mathrm{D_eC_{As}}} = \frac{\left[1.88\times10^{-9}\ \frac{\text{mole of } \mathrm{C_2H_2}}{\mathrm{g_{cat}}\ \cdot \mathrm{s}}\right]\times[4.6\frac{\mathrm{g}}{\mathrm{cm^3}}]\left[\frac{\mathrm{cm^3}}{\mathrm{m^3}}\right]\times[9\times10^{-5}\ \mathrm{m}]^2}{\left[1.9\times10^{-6}\frac{\mathrm{m^2}}{\mathrm{s}}\right][0.186\ \frac{\mathrm{mol}}{\mathrm{m^3}}]} = 2\ \times\ 10^{-4}$$

$$\frac{-\mathrm{r_A'}\ \rho_c\ \mathrm{R^2}}{\mathrm{D_eC_{As}}} \ll \mathbf{1}$$

There is no interphase diffusion limitation.

III. Mears Criterion for Intraparticle Heat Transfer Limitation

The intraparticle heat transfer effects could be negligible when $\frac{|\Delta H_R|\Re R_p E_a}{\lambda_S R_g T_0^2} < 0.75$

Ea = 62000 J/mol (reported in Supplementary Figure S4.4)

$T_0 = 323$ K (temperature of particle surface)

$$\Re = \left[1.88\times10^{-9}\ \frac{mole\ of\ C_2H_2}{g_{cat}\cdot s}\right][4.6\frac{\mathrm{g}}{\mathrm{cm^3}}]\left[\frac{\mathrm{cm^3}}{\mathrm{m^3}}\right] = 0.009 mol/m^3\cdot s$$

ΔH_R= – 296000 J/mol/K (heat of reaction, assuming the acetylene are fully hydrogenated, the heat of reaction is larger than semi-hydrogenation)

$\lambda_S = 7.5\ \mathrm{W/m \cdot K}$ (thermal conductivity of $ZnAl_2O_4$ [6])

R_g = 8.314 $\mathrm{J/mol \cdot K}$ (ideal gas constant)

$$\frac{|\Delta H_R|\Re R_p E_a}{\lambda_S R_g T_0^2} = \frac{\left[296000\,\frac{\mathrm{J}}{\mathrm{mol}}\cdot \mathrm{K}\right]\left[0.009\,\frac{mol}{m^3}\cdot s\right][9\times 10^{-5}\,m]^2[62000\,\frac{\mathrm{J}}{\mathrm{mol}}]}{\left[7.5\,\frac{\mathrm{W}}{\mathrm{m}}\cdot \mathrm{K}\right][323K]^2[8.314\ \mathrm{J/mol\cdot K}]} = 2.06\times 10^{-7}$$

$$\frac{|\Delta \mathrm{H_R}|\Re \mathrm{R_p E_a}}{\lambda_\mathrm{S} \mathrm{R_g T_0^2}} \ll \mathbf{0.75}$$

There is no intraparticle heat transfer limitation.

IV. Mears Criterion for Radical (Interparticle) Heat Transfer Limitation

The interparticle heat transfer effects could be negligible when $\frac{|\Delta H_R|\Re R_t^2}{\frac{\lambda_{eff} T_w^2 R_g}{E_a}}(1+\frac{4\lambda_{eff}}{R_t h_w}) < 0.4$

$\mathrm{R_t}$ = 0.35 cm (reactor radius)

$\mathrm{T_w}$ = 323K (wall temperature)

$h_w = \frac{2\lambda_g}{d_p}$ (heat transfer coefficient at the wall)

$d_p = 1.8\times 10^{-4}\,m$ (catalyst particle diameter)

$$\lambda_g = y_{C_2H_2\times}\lambda_{C_2H_2} + y_{H_2\times}\lambda_{H_2} + y_{He\times}\lambda_{He} = 0.5\%\times 0.02 + 5\%\times 0.187 + 94.5\%\times 0.157$$
$$= 0.16\ \mathrm{W/m\cdot K}$$

$\lambda_{\mathrm{C_4H_{10}}} = 0.021\ \mathrm{W/m \cdot K}$ at 300K, 101.325 kPa.

$\lambda_{H_2} = 0.187\ \mathrm{W/m \cdot K}$ at 300K, 101.325 kPa.

$\lambda_{He} = 0.157\ \mathrm{W/m \cdot K}$ at 300K, 101.325 kPa.

$$\mathrm{h_w} = \frac{2\lambda_\mathrm{g}}{\mathrm{d_p}} = \frac{2 \times 0.16\ \mathrm{W/m \cdot K}}{1.8 \times 10^{-4}\ \mathrm{m}} = 1777.8\ \mathrm{W/m^2 \cdot K}$$

$$\lambda_{eff} = \lambda_g \beta \left(\frac{1-\phi}{\frac{\lambda_g}{\lambda_s} + \psi} \right) = 0.16\ \mathrm{W/m \cdot K} \times 1 \times \frac{1 - 0.4}{\frac{0.16 \frac{\mathrm{W}}{\mathrm{m}} \cdot \mathrm{K}}{7.5 \frac{\mathrm{W}}{\mathrm{m}} \cdot \mathrm{K}} + 0.04} = 1.6\ \mathrm{W/m \cdot K}$$

$where\ \beta = 1, \psi = 0.04, \phi = 0.4, \lambda_s = \lambda_{ZnAl_2O_4} = 7.5\ \mathrm{W/m \cdot K}$

$$\frac{|\Delta H_R| \Re R_t^2}{\frac{\lambda_{eff} T_w^2 R_g}{E_a}} \left(1 + \frac{4\lambda_{eff}}{R_t h_w} \right)$$

$$= \frac{\left| 296000 \frac{J}{mol} \cdot K \right| \left[0.009 \frac{mol}{m^3} \cdot s \right] [3.5 \times 10^{-4} \mathrm{m}]^2}{\frac{\left[1.6 \frac{\mathrm{W}}{\mathrm{m}} \cdot \mathrm{K} \right] [323\mathrm{K}]^2 \left[8.314 \frac{J}{K} \cdot mol \right]}{\left[62000 \frac{J}{mol} \right]}}$$

$$\times \left(1 + \frac{4 \times 1.6 \frac{\mathrm{W}}{\mathrm{m}} \cdot \mathrm{K}}{[3.5 \times 10^{-4} \mathrm{m}] \left[1777.8 \frac{\mathrm{W}}{\mathrm{m^2}} \cdot \mathrm{K} \right]} \right) = 1.65 \times 10^{-4}$$

$$\frac{|\Delta \mathrm{H_R}| \Re \mathrm{R_t^2}}{\frac{\lambda_{\mathrm{eff}} \mathrm{T_w^2} \mathrm{R_g}}{\mathrm{E_a}}} \left(1 + \frac{4\lambda_{\mathrm{eff}}}{\mathrm{R_t h_w}} \right) \ll \mathbf{0.4}$$

There is no intraparticle heat transfer limitation.

V. Mears Criterion for Interphase Heat Transfer Limitation

The interphase heat transfer effects could be negligible when $\left|\frac{-\Delta H_R(-\Re)RE_a}{hT^2R_g}\right| < 0.15$

$\mathrm{h_w} = 1777.8\ \mathrm{W/m^2 \cdot K}$ (heat transfer coefficient between gas and pellet)

$$\left|\frac{-\Delta H_R(-\Re)R_pE_a}{\mathrm{h_w}T^2R_g}\right| = \left|\frac{\left[-296000\,\frac{J}{mol}\cdot K\right]\left[-0.009\,\frac{mol}{m^3}\cdot s\right][9\times10^{-5}\,m]\left[62000\,\frac{J}{mol}\right]}{[1777.8\,\frac{W}{m^2}\cdot K][323K]^2[8.314\,J/K\cdot mol]}\right|$$

$$= 6.7\times10^{-4}$$

$$\left|\frac{-\Delta H_R(-\Re)\rho_bR_pE_a}{\mathrm{h_w}R_g}\right| \ll \mathbf{0.15}$$

There is no interphase heat transfer limitation.

,,

Supplementary Table 4.3 A summary of the calculation results for transport limitation criterion for acetylene hydrogenation on all Ir/$ZnAl_2O_4$ catalysts with or without dilution. The TOFs used for criterion calculation are the first conditions after stabilization overnight right (0.51 kPa C_2H_2, 5.1 kPa H_2, 50 °C, atmosphere) From the results in the table below, the numbers are all several orders of magnitude lower than the criterion. Therefore, there are no transport limitations during the kinetic measurements for all the catalysts.

Catalyst	External Mass Diffusion	Internal Mass Diffusion	Intraparticle Heat Transfer	Interparticle Heat Transfer	Interphase Heat Transfer
	$\frac{-r'_A \rho_b R_n}{k_C C_{Ab}} \ll 0.15$	$\frac{-r'_A \rho_c R^2}{D_e C_{As}} \ll 1$	$\frac{\lvert\Delta H_R\rvert \Re R_p E_a}{\lambda_S R_g T_0^2} \ll 0.75$	$\frac{\frac{\lvert\Delta H_R\rvert \Re R_t^2}{\lambda_{eff} T_w^2 R_g}}{Ea}\left(1+\frac{4\lambda_{eff}}{R_t h_w}\right) \ll 0.4$	$\left\lvert\frac{-\Delta H_R(-\Re)\rho_b R_p E_a}{h_w T^2 R_g}\right\rvert \ll 0.15$
0.2%$Ir_{SA-0.7nm}$/$ZnAl_2O_4$	6.1×10^{-7}	5.5×10^{-5}	4.9×10^{-8}	3.9×10^{-5}	2.3×10^{-6}
0.2%$Ir_{0.8nm}$/$ZnAl_2O_4$	1.9×10^{-6}	1.7×10^{-4}	1.1×10^{-7}	8.7×10^{-5}	5.1×10^{-6}
0.2%$Ir_{1.4nm}$/$ZnAl_2O_4$	2.2×10^{-6}	2×10^{-4}	2.1×10^{-7}	1.65×10^{-4}	6.7×10^{-4}
1%$Ir_{1.4nm}$/$ZnAl_2O_4$ (5× dilution with SiO_2)	1.1×10^{-5}	5.7×10^{-4}	2.8×10^{-6}	4.5×10^{-4}	2.3×10^{-5}

Reference

[1] A.M. Karim, A comparison between packed bed and wall coated reactors for the steam reforming of methanol, (2003).

[2] C.-T. Kuo, Y. Lu, L. Kovarik, M.H. Engelhard, A.M. Karim, Structure Sensitivity of Acetylene Semi-Hydrogenation on Pt Single Atoms and Subnanometer Clusters, ACS Catalysis, (2019).

[3] X. Zhang, Y. Lu, L. Kovarik, P. Dasari, D. Nagaki, A.M. Karim, Structure Sensitivity of n-Butane Hydrogenolysis on Supported Ir Catalysts, Journal of Catalysis, (2020).

[4] E.N. Fuller, P.D. Schettler, J.C. Giddings, New method for prediction of binary gas-phase diffusion coefficients, Industrial & Engineering Chemistry, 58 (1966) 18-27.

[5] H.S. Fogler, M.N. Gürmen, Elements of Chemical Reaction Engineering. 2005, There is no corresponding record for this reference.[Google Scholar], (1999) 741-760.

[6] G. Chen, C. Xu, X. Huang, J. Ye, L. Gu, G. Li, Z. Tang, B. Wu, H. Yang, Z. Zhao, Interfacial electronic effects control the reaction selectivity of platinum catalysts, Nature materials, (2016).

Chapter 5 Conclusions

Supported metal catalysts have been widely used in modern chemical industry and provided prominent catalytic efficiency. In this work, we synthesized a series of supported Ir catalysts in the small particle size range ($\bar{d}$ < 3nm) and characterized the surface structure of geometric properties and electronic properties by multiple techniques including HAADF-STEM, in-situ FTIR, volumetric CO chemisorption and XPS. Alkanes hydrogenolysis and alkynes hydrogenation were applied as probe reactions and the results indicate these reactions are structure sensitive on the supported Ir catalysts, filling up the blank in such small particle size range.

For n-butane hydrogenolysis, our results indicate that the activity increases as the particle size decreases from 2.9 nm to 1.4 nm and then slightly decreases as the particle size further decreases to 0.7 nm in the subnanometer regime. Meanwhile, the selectivity is influenced by both particle size and temperature. The selectivity to the target product of ethane is very weakly dependent on particle size in the small size range of 0.7–1.4 nm and then begin to decrease when the particle size further increases to 2.9 nm. The hydrogenolysis of n-butane was also measured in the kinetic regime to understand the reaction pathways. The molar ratio of CH_4/C_3H_8 is close to 1 when the conversion is controlled <1%, which means the product distribution is determined by the location of C–C bond cleavage without further series reaction on C_3H_8 or C_2H_6. From the comparison of selectivity and molar ratio of CH_4/C_3H_8, central C–C bond cleavage is dominant on the Ir subnanometer clusters and small nanoparticles (<1.4 nm), while on large nanoparticles the selectivity to ethane becomes much lower and the central and terminal C–C bond cleavage are similar and competitive. On the other hand, temperature is a critical factor that affects the reaction pathway. As temperature increases, the selectivity to ethane from central C–C bond cleavage drops and meanwhile the simultaneous terminal C–C bond cleavage increases, resulting in an improvement for the selectivity to methane. When the reaction was proceeding at higher conversion range, series reaction of further hydrogenolysis on propane and ethane intermediates becomes nonnegligible. Our results show that lower reaction temperature and Ir size of ~1.4 nm are optimum for activity and selectivity to ethane (central C–C bond cleavage).

To understand the series reaction pathway of $C_2 \rightarrow C_1$, the series of Ir/$MgAl_2O_4$ catalysts in small size range (0.7–1.3 nm) was also tested for ethane hydrogenolysis. The results show that the activity decreases from nanoparticles (~1.3 nm) to subnanometer clusters (~0.7 nm), and the trend is very consistent with that for n-butane hydrogenolysis. One more Ir/$MgAl_2O_4$ catalyst with > 60% single atoms was also measured and the activity is higher than the subnanometer clusters (~0.7 nm). The higher activity is probably coming from the fraction of nanoparticles within the catalyst. Therefore, the Ir single atoms might not be active for hydrogenolysis since the adsorption of ethane requires more than one single site.

In addition to geometric properties (Ir nuclearity), we also synthesized a series of Ir/$ZnAl_2O_4$ catalysts to understand the effect of electronic properties by changing the metal-support interaction from Ir-Mg to Ir-Zn. 1%$Ir_{1.4nm}$/$ZnAl_2O_4$ catalyst was chosen for n-butane hydrogenolysis as comparison, as the average size of Ir nanoparticles is similar with $Ir_{1.3nm}$/$MgAl_2O_4$ catalyst that shows the highest activity. At elevated temperature, the selectivity to ethane on Ir/$ZnAl_2O_4$ is close to that on Ir/$MgAl_2O_4$. However, the activity of the Ir nanoparticles is extremely low when supported on $ZnAl_2O_4$, and the much lower activity of Ir/$ZnAl_2O_4$ was also observed in the case of CO oxidation when comparing with Ir/$MgAl_2O_4$ (will reported elsewhere). The reason remains unknow and requires further investigation. Because of the much lower activity of hydrogenolysis on Ir/$ZnAl_2O_4$, we chose acetylene hydrogenation as the probe reaction for structure sensitivity study.

Acetylene hydrogenation is structure sensitive on the series of Ir/$ZnAl_2O_4$ catalysts. The key factor that determines the catalytic performance (activity & selectivity) is the geometric properties (Ir nuclearity) of the surface structure instead of the electronic properties. As the particle size increases, the activity of acetylene hydrogenolysis keeps increasing and the selectivity to the target product of ethylene decreases. This might be because of the difference in adsorption methods on the Ir particles with different particle size as reported by literature. On Ir single atoms or subnanometer clusters, the C_2H_2 may adsorb by π-bonded structure with low adsorption energy, and after hydrogenation the adsorbed C_2H_4 molecules can easily desorb from the surface since the adsorption energy of C_2H_4 is also low. While on larger sized nanoparticles, the C_2H_2 may strongly adsorb by di-σ bonds and tend to be further hydrogenated to saturate C_2H_6 since the intermediates of C_2H_4 with high adsorption energy are hard to desorb from the surface. Two catalysts of Ir nanoparticles with the same surface-average particle size but reduced at different temperature were also tested for the effect of electronic properties. The DRIFTS spectra and XPS results clearly indicate the difference in the oxidation state and metal-support interactions, but the activity and selectivity are very close. This means the electronic properties of the surface structure on Ir/$ZnAl_2O_4$ catalysts have very little effect on the acetylene hydrogenation, the Ir nuclearity is the only factor that determines the catalytic performance in the case of Ir/$ZnAl_2O_4$.

For future work, the metal-support interaction can be further analyzed by operando XAFS to investigate the coordination environments of the metal and provide fundamental insights on catalyst design for the catalysts supported on spinel structure material by tuning the interactions based on the electronic properties. Also, the effect of metal identity (e.g. Rh, Pt) can be further studied for structure sensitivity by decouple the effect of geometric properties and electronic properties. After understanding the reaction mechanism on these catalysts, the catalytic efficiencies can be greatly improved for these hydrocarbon reactions in industry.